Dissertation
submitted to the
Combined Faculties for the Natural Sciences and for Mathematics
of the Ruperto-Carola University of Heidelberg, Germany
for the degree of
Doctor of Natural Sciences

Put forward by

Diplom-Physiker Arno Trautmann
Born in: Bad Kreuznach

Oral examination: 19.07.2016

Spin Dynamics and Feshbach Resonances in Ultracold Sodium-Lithium Mixtures

Referees:

Prof. Dr. Markus K. Oberthaler
Prof. Dr. Matthias Weidemüller

To all humans who suffer from war, discrimination, fame, and poverty, and can not enjoy the privilege of fundamental research.

Zusammenfassung

Diese Doktorarbeit zeigt die Untersucheng der Zweikörperstreueigenschaften kalter Atome in Natrium und Lithium-Natrium-Mischungen und deren Effekt auf die Vielkörperdynamik. Da beide Atomsorten Alkalimetalle sind, kann der gemeinsame Drehimpuls der beiden ungepaarten Elektronen entweder null oder eins sein. Dies bietet zwei verschiedene Streukanäle.

Die Kopplung von gebundenen Molekülzuständen in diesen Streukanälen mit den freien Atomasymptoten führt zum reichen Feld der Physik der Feshbach-Resonanzen, wobei die Wechselwirkung zwischen den Teilchen kontrolliert werden kann als einfach einzustellender, experimenteller Parameter. Wir haben das Feshbach-Spektrum in der bosonischen ^{7}LiNa-Mischung untersucht und konnten Vorhersagen bestätigen, die auf den Messungen im ^{6}LiNa-System basierten, mit einer Verschiebung des vorhergesagten Spektrums um etwa 50 G. Ebenso wurden die Möglichkeiten der Einstellung der Wechselwirkungen mittels Feshbach-Resonanzen untersucht.

Der Unterschied in den Streulängen der elektronischen Potentiale verursacht auch eine Kopplung der atomaren Streukanäle, was zu einem Spin-Austausch zwischen den Atomen führen kann. In dieser Arbeit wurden Spin-Austauschprozesse untersucht mittels kohärenter Oszillationen in einem thermischen Gas und einem Bose-Einstein-Kondensat aus Natrium, ebenso wie die Entwicklung dieses Spinorgases zu seinem Grundzustand. Vorbereitende Untersuchungen der heteronuklearen Spin-Austauschprozesse werden ebenso gezeigt, sowohl in der bosonischen ^{7}LiNa-Mischung als auch in der fermionisch-bosonischen Mischung ^{6}LiNa.

Abstract

This thesis presents the investigation of the two-body scattering properties of cold atoms in sodium and lithium-sodium mixtures and their effects on the many body dynamics. Since both species are alkali atoms, the combined spin of both unpaired electrons can be either zero or one, providing two different scattering channels.

The coupling of bound molecular states in these channels with the free atoms asymptote gives rise to the rich field of Feshbach resonance physics, where the interaction between the particles can be controlled as an easily accessible experimental parameter. We have investigated the Feshbach spectrum in the bosonic ^{7}LiNa mixture and could confirm predictions based on ^{6}LiNa measurements, with a shift of the predicted spectrum by about 50 G. Also, the prospects of interaction tuning via Feshbach resonances were examined.

The difference of the scattering lengths of the electronic potentials also causes a coupling of atomic collisional channels, which can enable a spin exchange between the atoms. In this thesis, spin exchange processes have been studied in coherent oscillations in a thermal gas and a Bose-Einstein condensate of sodium, as well as the evolution of this spinor gas into its ground state. Preliminary studies of the heteronuclear spin exchange process in both the bosonic ^{7}LiNa and in the fermionic-bosonic mixture ^{6}LiNa are presented as well.

This thises has been typeset using the LuaLaTeX typesetting system with the fonts Linux Libertine, Linux Biolinum, Linux Libertine Mono and Latin Modern Math, using microtypographical extensions.

Contents

1 Introduction

Many advances in the comprehension of physics were achieved by isolating some smaller parts of a complex problem and investigating these simpler parts. To extend the knowledge, more and more parts of the full system can be considered, finally enabling a deeper understanding of the whole system.

The history of the development of ultracold quantum gases as tools to understand basic quantum mechanics and complex many-body states follows this way. From the first production of Bose-Einstein condensates in cold dilute gases [2, 21, 12, 32], these systems offered highly controllable systems that are well isolated from external influences by magnetic or optical trapping [37], and can be manipulated by a wide range of tools.

For a single atomic species without internal degrees of freedom, possible ways to influence the atoms and to model certain physical systems are the application of external fields, especially optical lattices, which allows the study of a quantum system in periodic potentials with a wide variety of different physical processes. [10, 55, 68, 36]

Besides the influence of external potentials, the second famous tool for ultracold quantum gases is the application of homogeneous magnetic fields to exploit the possibility of magnetically tuneable Feshbach resonances. This allows to change the interaction of the atoms over a wide range, from weakly to strongly interacting regimes, and even allows to invert the sign of the interaction. In the strongly interacting regime, universal physics can be observed and studied in a well controlled enviroment. [82, 57, 54] In the ultracold fermionic systems, the use of Feshbach resonances allowed the formation of molecules, observation of the BEC-BCS crossover, and a wide variety of experiments in the universally interacting regime. [49, 113, 114, 115]

These rich fields of physics could be accessed with only one atomic species without internal degrees of freedom, or in the case of Fermions, two interacting states. But a wide variety of new physical effects could be studied in mixtures of different species, and the exploitation of internal degrees of freedom, namely the spin projection along the quantization axis.

In a state-independent optical trap, bosonic atoms can be described as spinor gases, where the spin degree of freedom opens a wide area for both fundamental physics as well as application-driven techniques. [99, 9, 38, 94] Coherent spin dynamics were not only observed in Bose-Einstein condensates, but also in a thermal bosonic gas [77] and even in an ultracold, degenerate fermionic gas. [58] The advent of atomic species besides the alkali atoms also allowed the observation of spin exchange in a fermionic system between different electronic orbitals. [15]

Extending the ultracold sample to a mixture of different atomic species is nowadays a common and very active subfield of cold quantum gases with many recent advances. One main focus in these systems lies on the production of ultracold fermionic or bosonic polar molecules [45, 16, 43, 76], as the strong polar interaction adds another valuable tool for implementation of further

physical systems. The second focus for mixtures is the physics of impurities, i. e. the combination of a (homogeneous or non-homogeneous) background which influences the properties of a single particle. [90, 56, 109, 17, 83] A very useful tool in this case are species-dependend potentials [61] which allow a confinement for the impurity while leaving the background mostly homogeneous.

Quite recently, also coherent spin exchange between two heterenuclear species was observed, combining several of the tools mentioned above. [62]

To extend this large toolbox even further, this thesis investigates the interactions in the lithium-sodium system in two ways: The first is the study of the ^{7}lithium-sodium Feshbach spectrum, which was predicted based on ^{6}Li-Na Feshbach data. [92] For this, the interspecies Feshbach spectrum is measured, and the possibilities of interaction tuning using both homo- and heteronuclear Feshbach resonances is studied.

The second part of this thesis studies the spin dynamics of sodium and lithium-sodium mixtures. In the case of Bose-condensed sodium, the formation of spin domains could be observed as the system evolves into its equilibrium state. The initial dynamics show coherent spin oscillations – a key ingredient for future experiments in the heteronuclear systems. For the heteronuclear case, clear spin exchange processes could be observed in the Bose-Bose as well as in the Fermi-Bose mixture.

Contents of this Thesis

The presented thesis contains three main parts. After a short chapter about basic atomic physics, which is needed for the understanding of the following chapters, the first main part describes the apparatus used for all experiments in this thesis.

Chapter 3 focuses on the implementation and improvement of important experimental tools, namely a magnetic field stabilization and a versatile frequency source. The magnetic field control covers a wide range from 5 mG up to 1200 G, with an active stabilization for fields below 1 G. The magnetic field is an important parameter to study and control atomic interactions and the full range of fields is applied and used in the later parts of this thesis.

The frequency control tool allows the coupling of all hyperfine states of the sodium and lithium atoms at all accessible magnetic fields, providing both fixed frequencies for coherent state superpositions as well as frequency sweeps for field calibrations and coherent state transfers.

In chapter 4, the Feshbach spectrum of the bosonic ^{7}Li-^{23}Na mixture is investigated. Experimental loss features are used as input for the development of an asymptotic bound state model. This model can cdescribe the s-wave spectrum and confirm the predictions based on earlier Feshbach studies in the Fermi-Bose ^{6}Li^{23}Na system. [92]

The second half of this chapter concentrates on the possibilities of interaction tuning via Feshbach resonances with respect to possible impurity physics. Both intra- and interspecies Feshbach resonances are investigated with respect to the corresponding lifetime and possible experiments.

The third main part in chapter 5 presents studies of spinor dynamics in both homo- and heteronuclear systems. After a theoretical introduction about the underlying physics and the close connection to the Feshbach spectroscopy, a numeric simulation of spin dynamics is presented which can reproduce the analytic results and is useful for the understanding of multimode dynamics.

After the analytic and numeric theory, experimental results for different settings are presented, ranging from the relaxation of an antiferromagnetic spinor gas towards its ground state in a gradient-dominated field setting, over coherent oscillations in both condensed and thermal samples, to heteronuclear spin exchange processes.

The Outlook gives perspectives for future experiments which can use the tools and insights gained from this thesis, with respect to different scenarios of impurity physics in confined geometries.

2 Preliminaries – About Atoms and Interactions

The experiments presented in this thesis deal with the manipulation and investigation of ultracold atoms at phase space densities where the quantum many body properties dominate their behaviour. Therefore, a good understanding of the single atom properties is needed as well as their interaction with each other, the effects of quantum statistics, and the interaction with external fields.

Since these effects are only tools used for investigating further physics, we will only summarize and concentrate on the most important results without a rigorous and detailed derivation here.

2.1 Hyerfine Structure of Alkali Atoms

Our model quantum system for this thesis consists of the three lightest stable alkali atoms, namely ^{6}lithium, ^{7}lithium and ^{23}sodium. All three of these are well-studied work horses in atomic physics and have been used in a wide variety of experiments in ultracold quantum gases, in single-species setups as well as in mixtures. The mixture of ^{7}Li-^{23}Na presented here, however, is realized for the first time up to our knowledge.

Atomic bosons differ from fundamental bosons (like gluons, photons etc.) in that they cannot be created and annihilated. This is because they are compound bosons, consisting of a number of fermions, for which particle conservation is valid. Unless the inner structure of a compound boson can be revealed, it acts like a boson to the outer world; in our case, the interparticle distance typically is so large that the bosonic atoms behave according to the Bose-Einstein statistics discussed below.

The composing particles of the atoms are the protons and neutrons in the nucleus and the electrons in the atom's shell. For neutral atoms, the number of eletrons and protons is always the same, therefore the difference between bosonic and fermionic behaviour is solely given by the number of neutrons in the nucleus – the one neutron difference between ^{6}Li and ^{7}Li has tremendous effects on the many particle behaviour!

In the experiments discussed below, several internal degrees of freedom of the atoms are manipulated: The energetic state of the electron, which can be excited by visible light, and the projection of the nuclear and electronic spin along the quantization axis.

Both bosonic species ^{7}Li and ^{23}Na have a total nuclear spin of $I = 3/2$, and for ^{6}Li, $I = 1$. The total electronic spin is equal to $S = 1/2$, since only the outermost electron has to be taken

into account; the closed inner shells (s for Li and s and p for Na) can be neglected and the atom treated as hydrogen-like.

For most of the time, the atoms in our experiments will be in their electronic ground state, so that the electron's orbital angular momentum will always be $L = 0$. The total angular momentum of the atom can then be expressed by $F = I + S$, and the coupling of the spins will lead to the hyperfine splitting, which is proportional to the product of $\mathbf{I} \cdot \mathbf{S}$. Expressed with the total angular momentum quantum number, one gets

$$\mathbf{I} \cdot \mathbf{S} = 1/2(F(F+1) - I(I+1) - S(S+1)). \tag{2.1}$$

The nuclear and electronic spin can be coupled in parallel or antiparallel direction, leading to $F_{\pm} = I \pm S$; for Na and ^{7}Li the two states are $F = 2$ and $F = 1$, for ^{6}Li $F = 3/2$ and $F = 1/2$. The splitting between these states is given by the hyperfine constant

$$\Delta E_{hf} = (I + 1/2)\, A_{hf}, \tag{2.2}$$

the values for the three species used in our experiments are:

$$^6\text{Li: } \Delta E_{hf} = 228\,\text{MHz}; \quad ^7\text{Li: } \Delta E_{hf} = 804\,\text{MHz}; \quad ^{23}\text{Na: } \Delta E_{hf} = 1772\,\text{MHz}. \tag{2.3}$$

Each hyperfine manifold with total spin F has $2F-1$ Zeeman substates which are degenerate at zero magnetic field but split at finite fields. This will be discussed in detail below.

2.2 Quantum Statistics

There are two fundamentally different classes of particles: Bosons, particles with a spin of an integer multiple of the planck constant (i. e. 0,1,2,...) , and fermions, which have a half-integer multiple (1/2,3/2,...). For high temperatures and low densities, both kind of particles can be described approximately with the Boltzmann distribution which gives the mean occupation number of energy states ε_ν depending on the temperature T of the system:

$$f^0(\varepsilon_\nu) = \frac{1}{\exp((\varepsilon_\nu - \mu)/kT)}, \tag{2.4}$$

where the parameter μ is the chemical potential which ensures particle conservation. This is the classical description of a gas without taking into account the quantum statistics.

For lower temperatures and higher densities, however, the quantum statistics start to play a crucial role, and very different behaviour for bosons and fermions arises, which will be discussed in the following subsections.

2.2.1 Bose Einstein Condensates

The distribution for the bosonic occupation of single particle states follows the Bose statistic[51, 78]

$$f^0(\varepsilon_\nu) = \frac{1}{e^{(\varepsilon_\nu - \mu)/kT} - 1} \tag{2.5}$$

For a given number of particles in a trapping potential, the critical temperature T_c is given by the maximum temperature, where a macroscopic occupation of the ground state arises, also called the onset of condensation. In the case of a three-dimensional harmonic trap, which is realised in most cold quantum gas experiments, with the mean trapping frequency $\bar{\omega} = \sqrt[3]{\omega_x \cdot \omega_y \cdot \omega_z}$, the transition temperature is given by

$$T_c \approx 4.5 \left(\frac{\bar{\omega}/2\pi}{100\,\mathrm{Hz}} \right) N^{-1/3} \mathrm{nK}, \tag{2.6}$$

which is roughly around 1 µK for a typical experiment with sodium atoms in our setup.

The number of atoms in the condensed phase is called the condensate fraction and can experimentally be used to determine the temperature of the atoms:

$$N_0 = N \left(1 - \left(\frac{T}{T_c} \right)^3 \right) \tag{2.7}$$

In order to derive the temperature from the condensate fraction, the momentum spread of the atoms after release from the trap is monitored. In that case, the condensed part has a much lower momentum, which can clearly be distinguished from the thermal expansion. However, if the condensate fraction is so high that no thermal atoms can be detected, or, vice versa, the condensate is too small, this number is not usefull anymore. For intermediate regimes, however, it is a good experimental indicator.

2.2.2 Fermi Gases

The Fermi function which governs the distribution of energy states for a Fermi gas is given by

$$f = \frac{1}{e^{(\varepsilon - \mu)/kT} + 1} \tag{2.8}$$

The chemical potential μ is related to the Fermi temperature T_F and given by

$$\mu = kT_F = (6N)^{1/3} \hbar \bar{\omega} \tag{2.9}$$

This will be of importance for the understanding of some of the observed spin dynamics later on in the Fermi-Bose mixture.

2.3 Interaction with Electromagnetic Fields

While the nature of quantum fields always leads to an interaction between a charged particle and the quantum vacuum, giving rise to the self energy. However, here we will concentrate on a semiclassical description of a quantized atom and a classical field, which is a valid description for large occupation numbers.

Three different cases of external fields will be discussed that have very different applications in our experiments:

1. Static magnetic fields

2. Light fields that couple to electric dipole moments
3. Microwave or radio frequency radiation which couples to magnetic dipole moments

The interaction with static magnetic fields is also used for trapping the atoms as well as inducing Feshbach resonances and an important paramer for the spin dynamics.

The interaction with light is exploited to initially capture the atoms using resonant light, confine them in a far off resonant dipole trap, and image them as the final read out.

Finally, the coupling to magnetic dipole moments is used in evaporative cooling, state preparation and coherent coupling of atomic states.

2.3.1 Atoms in External Magnetic Fields

One of the main tools to manipulate ultracold atoms are magnetic fields. In the scope of this thesis, three different aspects of magnetic field interaction are used:

- Trapping (and cooling) of atoms in inhomogeneous magnetic fields
- Shifting of molecular levels into resonance with atomic levels in homogeneous fields
- Controlling the interaction detuning in spinor physics

Although the nature of these applications are quite different, they all base on the energy dependence of the charged particles and interaction of spins in a magnetic field.

Since the atoms are neutral particles, one has to take a closer look at the constituents to understand the effect of the external field. We will restrict the discussion to the type of atoms deployed in our experiments, which are alcali atoms with a simple electronic structure, and also concentrate on the electronic ground state, as an analytic expression can be found for this case.

With only one valence electron, the electronic spin is $s = 1/2$, which is also the total angular momentum of the ground state $j = 1/2$ since $l = 0$. This leaves only the nuclear spin i and the coupled total spin f as parameters, as well as their projection onto the magnetization axis. So in total the parameters and corresponding quantum numbers for a single atom are:

- total electron spin and its projection j, m_j
- nuclear spin i, m_i
- total spin f, m_f (for low magnetic fields)

We use the lower case letters s, j, i, f for the single-atom variables, reserving the upper case variants for the total spins in the molecular cases, where also the coupling is more complex. This will be detailed in 4.1.3. In case of high magnetic fields, the electron's and the nuclear spin decouple and the total spin is not a good quantum number anymore.

The total energy of an atom in an external magnetic field B is in this case given by the hyperfine coupling and the Zeeman shift [13]

$$H_{\text{hfs}} + H_Z = \frac{a_{\text{hfs}}}{\hbar^2}\mathbf{s}\cdot\mathbf{i} + \left(g_j m_j + g_i m_i\right)\cdot\frac{\mu_B B}{\hbar} \tag{2.10}$$

The first term contains the hyperfine constant a_{hfs}, which depends on the atomic species and is given by the details of the interaction between the nucleus and the single unpaired electron. The

second term indicates the uncoupled spins' Zeeman shift with the corresponding gyromagnetic factors of the electron on its orbit g_j and nucleus g_i and the Bohr magneton μ_B. The factor g_j differs from g_s even for an $l = 0$ orbital in alkali atoms since the many-electron system has a non-negligible impact on the outer electron.

Table 2.1 lists values of the gyromagnetic factors and hyperfine constants for both lithium species as well as sodium, which are all used in the experiments described later. For comparison, also the values for rubidium are listed.

Table 2.1: g-factors and hyperfine constants for different systems. The difference between g_s and 2 is caused by QED corrections; for g_j additional influence from the whole multielectron orbitals contribute to the deviation from g_s. The hyperfine constant E_{hfs} is also called Magnetic Dipole constant. The hyperfine splitting is given by $E_{\text{hfs}} = a_{\text{hfs}} \cdot (i + 1/2)$.

System	value
electron	2.002 319 304 361 82(52) [67]
Na $g_j(3^2S_{1/2})$	2.002 296 0(7)[98]
Na g_i	−0.000 804 610 8(8) [98]
Na a_{hfs}	$h \cdot$ 885.813 064 4(5) MHz [98]
^{6}Li $g_j(2^2S_{1/2})$	2.0023010 [6]
^{6}Li g_i	−0.000 447 654 0 [6]
^{6}Li a_{hfs}	$h \cdot$ 152.136 840 7 MHz [6]
^{7}Li $g_j(2^2S_{1/2})$	2.0023010(7)[6]
^{7}Li g_i	−0.001 182 213 0(6) [6]
^{7}Li a_{hfs}	$h \cdot$ 401.752 MHz [6]
Rb $g_j(5^2S_{1/2})$	$g_S \times (1 + 5.9(1)e - 6)$ [6]
Rb g_i	$-g_J \times 4.9699147(50)e - 4$ [106]
Rb a_{hfs}	$h \cdot$ 6 834 682 610.904 310(3) Hz [75]

For two special states, the Hamiltonian Equation 2.10 is already diagonal, these are the states with parallel electron and nuclear spin, called stretched states; in case of ^{7}Li and Na these are the $|f = 2, m_f = \pm 2\rangle$ states and for ^{6}Li $|f = 3/2, m_f\rangle = \pm 3/2$. The general solution is more involved; following [98], one can reduce the problem to the diagonalization of

$$\begin{pmatrix} (g_i(m_f - \frac{1}{2}) + \frac{g_s}{2})\mu_B B + \frac{a_{\text{hfs}}}{2}(m_f - \frac{1}{2}) & 1/2\sqrt{(i+1/2)^2 - m_f^2} \\ \frac{1}{2}\sqrt{(i+\frac{1}{2})^2 - m_f^2} & (g_i(m_f + \frac{1}{2}) - \frac{g_s}{2})\mu_B B - \frac{a_{\text{hfs}}}{2}(m_f + \frac{1}{2}) \end{pmatrix} \tag{2.11}$$

The eigenenergies and their dependence on the magnetic field B can be expressed by a simple formula which becomes easily readable with the substitution

$$x = \frac{(g_j - g_i)}{a_{\text{hfs}}(i + 1/2)} \mu_B B \tag{2.12}$$

which results in the famous Breit-Rabi formula [14]

$$E(B) = \frac{-a_{\text{hfs}}}{4} + g_i m_f \mu_B B \pm \frac{a_{\text{hfs}}(i + 1/2)}{2} \cdot \sqrt{1 + 2 \cdot x \cdot \frac{m_f}{i + 1/2} + x^2} \tag{2.13}$$

The striking feature of this formula is that it allows an analytic calculation of the energy for all experimentally relevant magnetic fields – but it is limited to the electronic ground state of a $j = 1/2$ atom! This is sufficient for all states used in the final experiments presented below, but for the cooling and imaging of the atoms, the field dependence of the excited electronic states are needed. In those cases, the eigenenergies have to be calculated numerically.

Figure 2.1 shows the field dependence for all sodium states in both $|f = 1\rangle$ and $|f = 2\rangle$ manifolds as calculated with the above formula. The formula Equation 2.13 has one drawback: For higher fields, the square root can take negative values for the negative stretched state $m_f = -f$. In this case, the root has to be replaced by $(1 - x)$. The figure shows the result of neglecting this with the dashed line.

Note that the quantum numbers f and m_f are only well defined at low magentic field. For higher fields, the electron's and nuclear spin decouple and a well defined set of quantum numbers are given by i, j, m_i, m_j. However, throughout this thesis, all states will be labeled with the low-field quantum numbers, indicating the state to which the high-field state adiabiatically connects.

While the full analytic result is very useful for calculations especially at higher fields where the set of good quantum numbers is not given by f, m_f anymore, it is very instructive to investigate the low-field part of the field dependence.

For small magnetic fields, the root in Equation 2.13 can be simplified via

$$\sqrt{1 + ax + x^2} \approx 1 + \frac{ax}{2} + \frac{1}{8}\left(4 - a^2\right) x^2 + O(x^3) \tag{2.14}$$

to the low-field approximation

$$E(B) \approx -\frac{a_{\text{hfs}}}{4} + g_i m_f \mu_B B \pm \frac{a_{\text{hfs}}(i + 1/2)}{2} \tag{2.15}$$

$$\times \left(1 + \frac{1}{2} \cdot 2x \cdot \frac{m_f}{(i + 1/2)} + \frac{1}{8}\left(4 - \frac{4m_f^2}{(i + 1/2)^2}\right) x^2\right). \tag{2.16}$$

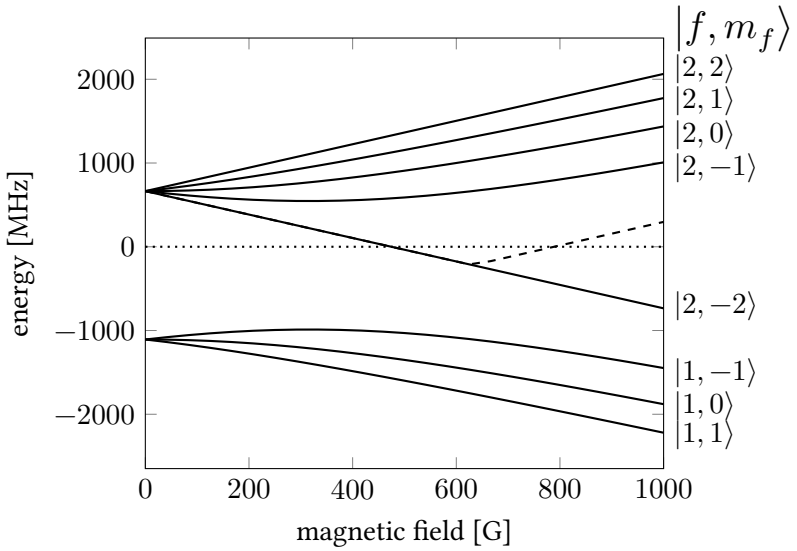

Figure 2.1: Breit-Rabi diagram of sodium. Shown is the magetic field dependent energy of the electronic ground state in both hyperfine manifolds. The dashed line shows the sign problem of the stretched $|f = 2, m_f = -2\rangle$ state.

Sorting the terms depending on the powers of B gives the constant, linear and quadratic dependence:

$$E(B) \approx -\frac{a_{\text{hfs}}}{2}(i+1) \tag{2.17}$$

$$+ \left(g_i \pm \frac{g_j - g_i}{2(i+1/2)}\right) \mu_B \cdot m_f B \tag{2.18}$$

$$+ \left(\frac{g_j - g_i}{4}\right)^2 \frac{1}{a_{\text{hfs}}(i+1/2)} \mu_B^2 \cdot \left(4 - \frac{m_f^2 \cdot 4}{(i+1/2)^2}\right) B^2 \tag{2.19}$$

In the case of $i = 3/2$ as it is for ^{7}Li, Na, and ^{87}Rb, where the latter two are common work horses for spin dynamics that will be discussed later, these factors boil down to the well-known forms

$$E(B) \approx -\frac{a_{\text{hfs}}}{2}(i+1) + p_Z^{i=3/2} m_f B + q_Z^{i=3/2}(4 - m_f^2)B^2, \tag{2.20}$$

$$p_Z^{i=3/2} = \pm\left(\frac{g_j - g_i}{4} \pm g_i\right)\mu_B, \tag{2.21}$$

$$q_Z^{i=3/2} = \pm\left(\frac{g_j - g_i}{4}\right)^2 \frac{\mu_B^2}{E_{\text{hfs}}}, \qquad \text{with } E_{\text{hfs}} = 2 \cdot a_{\text{hfs}}. \tag{2.22}$$

For the fermionic case of ^{6}Li, where $i = 1$, the prefactors of course look different:

$$p_Z^{i=1} = \pm\left(\frac{g_j - g_i}{3} \pm g_i\right)\mu_B, \tag{2.23}$$

$$q_Z^{i=1} = \pm\left(\frac{g_j - g_i}{4}\right)^2 \frac{\mu_B^2}{E_{\text{hfs}}}, \qquad \text{with } E_{\text{hfs}} = 1.5 \cdot a_{\text{hfs}}. \tag{2.24}$$

The prefactors p_Z and q_Z are called the linear and quadratic Zeeman shift, respectively. Since the nuclear gyromagnetic factor g_i is several orders of magnitude smaller than g_j, it is the latter one dominating the energy shifts.

It is important to note that even with identical g-factors the fermionic linear Zeeman shifts differs from the bosonic case by a factor of $^3/_4$, which will be crucial for the discussion of Fermi-Bose heteronuclear spin changing collisions in subsection 5.1.3, where also the effect of different hyperfine splittings on the quadratic term will be highlighted.

2.3.2 Optical Trapping

The realization of optical trapping potentials is a key development to both main topics of this thesis, since it allows the trapping of different hyperfine states in the same trapping potential and leaves the possibility to apply homogeneous magnetic fields as tuning parameters. Since the effect of far off-resonat light on atoms in our setup has been studied extensively before [87, 83], only the basics are discussed here for an understanding of the physical background.

A dipole trap exploits the polarizability of the atoms by using a far off-resonant laser beam. The potential, depending on the light intensity $I(\mathbf{r})$ and the frequency ω, as well as the atomic properties (resonance frequency ω_0, linewidth of the transition Γ), is given by [37]

$$V_{\text{dip}}(\mathbf{r}) = \frac{3\pi c^2}{2\omega_0^3}\left(\frac{\Gamma}{\omega - \omega_0} + \frac{\Gamma}{\omega + \omega_0}\right) \cdot I(\mathbf{r}) \approx \frac{3\pi c^2}{2\omega_0^3}\left(\frac{\Gamma}{\Delta}\right) I(\mathbf{r}) \tag{2.25}$$

Here the term with the sum of the frequencies is neglected since the detuning $\Delta = \omega - \omega_0$ is much smaller; this is known as the rotating wave approximation. One can directly see that the potential is attractive for red detuning, i. e. $\omega < \omega_0$; therefore the experiment uses a 1064 nm laser which is far red detuned for both sodium (589 nm) and lithium (671 nm) D-line transitions.

In previous experiments – and also planned for the future – a species-selective optical potential was used which had a strong influence on lithium atoms but only a small one for sodium. In that case one has to consider the spontaneous scattering rate, since any scattered photon can remove an atom from the trap due to the transferred momentum. The scattering rate is given by

$$\Gamma_{\text{sc}}(\mathbf{r}) = \frac{3\pi c^2}{2\omega_0^3}\left(\frac{\omega}{\omega_0}\right)^3\left(\frac{\Gamma}{\omega - \omega_0} + \frac{\Gamma}{\omega + \omega_0}\right)^2 I(\mathbf{r}) \approx \frac{3\pi c^2}{2\omega_0^3}\left(\frac{\Gamma}{\Delta}\right)^2 I(\mathbf{r}) \tag{2.26}$$

and depends quadratically on the detuning. The ratio of the right-hand side of both equations gives the working point for species-selective lattices; in this thesis, the detuning of the 1064 nm laser is so large that the spontaneous scattering is not the main loss mechanism and therefore does not limit the experiments even for many seconds of hold times.

2.3.3 Atoms Coupled to Radio Frequency Fields

The control over the population of the different hyperfine states at ultralow temperatures is achieved conveniently and with a great control by direct coupling of the states via microwave or radio frequency radiation.

These low-frequency electromagnetic waves can couple to the magnetic dipoles of the atoms and thus drive transitions between the magnetic substates as well as between the hyperfine states.

In the remainder of this work, we will consequently refer to microwave transitions as such between different hyperfine manifolds, i. e. between the $|f=1\rangle$ and $|f=2\rangle$ manifold for the bosonic and $|f={}^1\!/_2\rangle$ and $|f={}^3\!/_2\rangle$ manifold for the fermionic case.

For both kinds of transitions, coherent oscillations can be observed and used to control the hyperfine state of the atoms.

The most relevant processes are the coupling of the spins to an RF field of constant frequency, inducing Rabi oscillations; and a frequency sweep, wich can be used to apply a Rapid Adiabatic Passage (RAP).

Rabi oscillations

A convenient description of Rabi oscillations for a two-level system makes use of the Bloch sphere and denote the population as the z component and the relative phase of the two levels as angle. The states are then depicted as vectors pointing from the center of the sphere onto the surface. The Rabi coupling then corresponds to a rotation around the x axis for the population transfer, and a phase evolution due to an off-resonant couplig corresponds to a rotation around the y axis; both can therefore be displayed by the Pauli matrices:

$$\sigma_x = \begin{pmatrix} 0 & 1 \\ 1 & 0 \end{pmatrix} \quad \sigma_y = \begin{pmatrix} 0 & -i \\ i & 0 \end{pmatrix} \quad \sigma_z = \begin{pmatrix} 1 & 0 \\ 0 & -1 \end{pmatrix} \tag{2.27}$$

This depiction is especially useful since it can be extended to the case of a three level system. Although the picture of a Bloch sphere is more difficult to imagine, the mechanism of rotations using the corresponding matrices can help to understand the phase evolution, which will be important for the spinor phase discussion later on.

The role of the Pauli matrices is played by the Spin 1 matrices:

$$S_x = \frac{\hbar}{\sqrt{2}} \begin{pmatrix} 0 & 1 & 0 \\ 1 & 0 & 1 \\ 0 & 1 & 0 \end{pmatrix} \quad S_y = \frac{\hbar}{\sqrt{2}} \begin{pmatrix} 0 & -i & 0 \\ i & 0 & -i \\ 0 & i & 0 \end{pmatrix} \quad S_z = \frac{\hbar}{\sqrt{2}} \begin{pmatrix} 1 & 0 & 0 \\ 0 & 0 & 0 \\ 0 & 0 & -1 \end{pmatrix} \tag{2.28}$$

The S_x matrix again denotes a rotation around the x axis, corresponding to on-resonance Rabi coupling, while rotation around the y axis via S_y corresponds to the effect of detuned coupling. Applying an RF pulse of a certain length corresponds to the rotation angle on a Bloch sphere. The important example of a spin 1 system for our setup is the coupling of the initial state where all atoms are in one of the side modes:

$$\Psi_{\text{ini}} = \begin{pmatrix} 0 & 0 & 1 \end{pmatrix}^t \tag{2.29}$$

The resulting state is given by the rotation angle:

$$\Psi_{\text{out}} = e^{-i \cdot S_x \cdot \varphi} \cdot \begin{pmatrix} 0 & 0 & 1 \end{pmatrix}^t \tag{2.30}$$

A rotation of π leads to full population in the upper state, while a $\pi/2$ pulse results in equal population of the side modes:

$$\Psi_{\text{out}} = e^{-i \cdot S_x \cdot \pi/2} \cdot \begin{pmatrix} 0 & 0 & 1 \end{pmatrix} = \begin{pmatrix} -0.5 & -i/\sqrt{2} & 0.5 \end{pmatrix}^t \tag{2.31}$$

The same population can be reached by rotating the state with $\pi/4$, but starting in the middle state,

$$\Psi_{\text{out}} = e^{-i \cdot S_x \cdot \pi/4} \cdot \begin{pmatrix} 0 & 1 & 0 \end{pmatrix} = \begin{pmatrix} -0.5i & 1/\sqrt{2} & -0.5i \end{pmatrix}^t , \tag{2.32}$$

however the relative phases of the states are different. This will be of importance later for the discussion of the initial state preparation for the spin changing collisions. It is important to note that the relative phase does not change if the angle of the rotation changes, but is only given by the initial conditions.

Rapid Adiabatic Passages

While a π pulse with a resonant coupling frequency is the most straightforward way to transfer atoms from one state into another, the experimental realization can suffer from four limitations:

1. unstable MW/RF frequency
2. unreliable timing
3. unstable MW/RF power
4. fluctuating magnetic fields

All four of these can lead to incomplete transitions, leaving atoms in undesired states. This can cause problems in the experiment, when e. g. the transfer of sodium into the lower hyperfine state as described below does not work reliably and the remaining atoms cause excess losses in the lithium numbers.

Therefore, for most state transfers, a more robust way of preparation is used, which is where the rapid adiabatic passage (RAP) [65] comes in. The concept of this is to use a dressed state to adiabatically transfer atoms from one state into another (therefore it is typically used in two-level systems). Experimentally, one starts to couple two levels of energy difference ω_0 with a far-detuned frequency ω. In this case, the bare state and the dressed state are close and the atoms are projected basically completely onto the dressed state. By changing the detuning $\Delta = \omega - \omega_0$, the atoms follow the evolution of the dressed state, and if the coupling is turned off far off-resonant on the other side of the resonance, the atoms are projected onto the bare state which again only differs by a negligible factor. Therefore, the atoms are completely transferred.

However, the transfer efficiency depends on the sweep rate, i. e. the change of $\Delta(t) = \alpha t$, since the atoms can tunnel diabatically into the unwanted state if the transfer is done too fast. Quantitatively, the probability P of this tunneling is given by the Landau-Zener formula [60]

$$P = e^{-2\pi \frac{\Omega^2}{|\alpha|}} \tag{2.33}$$

where Ω is the on-resonance Rabi frequency. For the concept of a RAP, it is only necessary to change the detuning, which can be either done by a magnetic field ramp (thus changing ω_0) and applying a constant frequency, or sweep the latter one at a constant magnetic field.

One of the experimental improvements done during this thesis was to enable frequency sweeps for all necessary transitions, therefore all transfers were done at constant magnetic fields. As can be seen from Equation 2.33, a strong Rabi coupling improves the transfer efficiency, as compared to the sweep rate. This does not imply that the slowest possible ramp is the best experimental realization, as external influences can cause decoherence which disturbs the transfer. Therefore one has to scan the transfer time and the detunings to achieve the most reliable scheme.

When you dance with the NaLi, it
doesn't change.
It changes you.

(Losely based on 8mm.)

3 Experimental Setup: Preparation and Control of Ultracold Atomic Clouds

This chapter will present the apparatus used for all experiments discussed in the remainder of this thesis. As the machine itself has been described in previous works [5, 102, 91, 88, 83], the next sections will concentrate on the changes and improvements made during this thesis. These improvements mostly regard the fine control of magnetic fields and microwave radiation, but also other means of increased stability and better atom detection.

The experimental preparation of ultracold atomic clouds consists of three main cooling stages that are applied consecutively and follow the traditional textbook example of the ultracold quantum gas community. [107, 64] Changes between the hyperfine states can be introduced by applying electromagnic radiation tuned to the resonance frequencies of the transitions, either directly driving Rabi oscillations or using a rapid adiabatic passage technique.

The following sections explain the preparation of ultracold ^{6}LiNa and ^{7}LiNa mixtures, the final state preparation as well as the state dependent detecion.

3.1 Preparation of Ultracold Samples

This section will go through the production of ultracold samples of sodium and lithium step-by-step, focussing on the steps which had been changed during the course of this thesis.

Every single step has to work reliable and reproduceable for a stable total setup, and each step has its own characteristic challenges, from the production of stable laser sources, over ultra-high vacuum systems, high-flux atomic sources, to stable magnetic field and microwave or radiofrequency sources.

3.1.1 Lithium Spectroscopy Scheme

The first stage of a laser setup for atomic physics is to provide a reliable frequency reference. The easiest way to get this is the set up of a spectroscopy of the corresponding species. For sodium, a doppler free saturation spectroscopy is used where the pump beam is shifted and modulated by an AOM. The absorption signal is evaluated on a photodiode and fed into a lock-in amplifier which produces the error signal needed for the analog feedback loop. The lock point is the crossover between the hyperfine states of the upper $3^2\mathrm{P}_{3/2}$ manifold, which can be resolved in the case of sodium. Details for this setup can be found in [91, 5]. For sodium, there is only one laser system from which all different beams needed for the whole setup have to be derived.

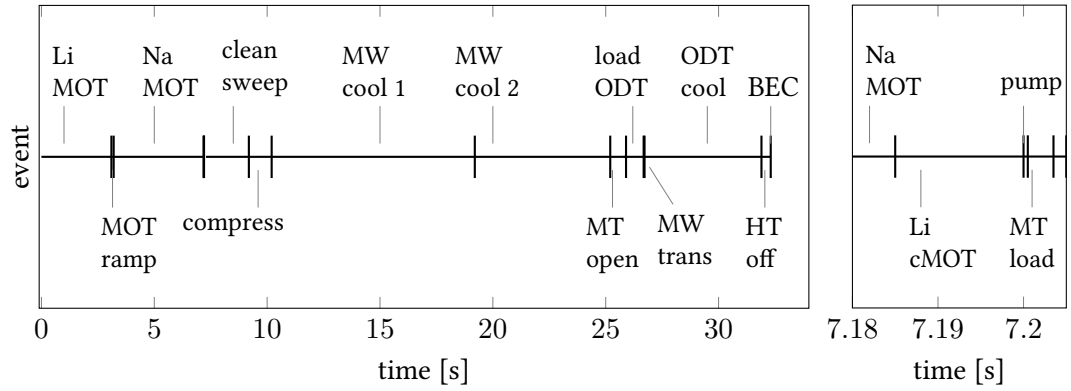

Figure 3.1: Timeline for the production of an ultracold mixture of atomic gases. Starting from the consecutive MOT loading as detailed in the text, the atoms are pumped into the trappable hyperfine states and the magnetic trap is loaded (see zoom-in on the right-hand side). After the clean sweep and compressing, the main cooling steps produce cold thermal samples in the magnetic trap. These samples are loaded into the waveguide, transferred to their absolute hyperfine ground state, and loaded into the dimple trap during the final evaporation, while the hybrid trap is still on. The turn-off of the magnetic confinement marks the final production stage of the Bose-Einstein condensate; from this point on, all different experiments can be conducted.

The lithium laser setup in contrast consists of three laser devices: One master laser for spectroscopy, one MOPA tapered amplifier (TA) for trapping, pumping, and imaging of the atoms, and an additional diode laser for imaging at high magnetic fields.

To allow an easy change between the lithium species, a new spectroscopy cell was used in the setup that contained an approximately equal amount of ^{6}Li and ^{7}Li by using enriched (95% ^{6}Li) as well as natural lithium (95%^{7}Li). Since the isotope shift is just on the order of the (small) fine structure splitting of 10 GHz, the diode lasers can easily be adjusted to either species.

The lock signal is generated by doppler free saturation spectroscopy, using a lock-in scheme, again. As described below, the new implementation in our setup now includes an AOM in the spectroscopy path; this allows to modulate the AOM's frequency instead of the laser frequency, which was done before. This enables a more robust lock scheme and has the advantage that the laser frequency is narrower. Since the two slave lasers, the TA and the high field imaging laser, are locked onto the spectroscopy master laser via a beat lock (described in [102]), the non-modulated reference also reduces the linewidths of the slave lasers.

3.2 shows the absorption spectrum of the overlapping ^{7}Li D2 and ^{6}Li D1 line with the cell and laser setup as now used in the experiment.

In contrast to the earlier setup, the Li laser is not locked onto the crossover between the hyperfine states, but directly onto the resonance line. This scheme allows for a change between the species without further adaption of any frequencies since only the repump beam then has to be different.

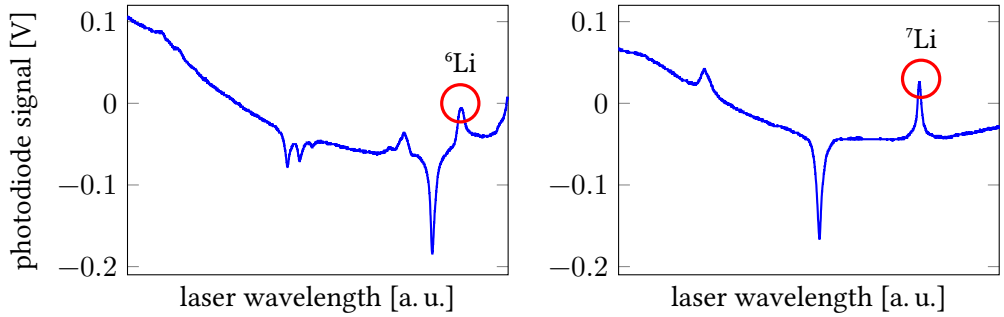

Figure 3.2: Photodiode signal of the Doppler free absorption spectroscopy of the ^{6}Li D2 and ^{7}Li D1 line (left) and the ^{7}Li D2 line (right). The strong triple-feature in the left graph is the ^{6}Li D2 line. The $|F = 3/2\rangle$ Lamb dip is indicated as the lock point, as is the $|f = 2\rangle$ lock point for ^{7}Li.

3.1.2 MOT and Optical Pumping

As both sodium and lithium are in the solid phase at room temperature and have a very low vapour pressure, an oven is needed to heat the atoms and provide a reasonable flux of atoms. The dual-species oven design used in our experiments is based on [96] and described in [88]; in improved version was used after the latest change, and is described in [83]. To compensate for the low natural abundance of ^{6}Li, an equal amount of enriched ^{6}Li and non-enriched Li are used to have the flexibility to choose the species without the need of an oven change.

After leaving the oven, the atoms are decelerated in a Zeeman slower, sharing the same path for both Li and Na, and trapped in a magneto-optica trap (MOT). Since the Li loading rate is very low compared to Na, but the lifetime of the MOT is rather high for Li, the MOT loading takes place in two stages: First, the magnetic field gradient, the Zeeman slower current and the laser detunings are set to optimum lithium loading parameters. The Li MOT is loaded for everal seconds, depending on the needed amount of lithium, then the field gradient and slower current are both lowered to load a large Na MOT. For Na, a dark spontaneous-force optical trap (dark SPOT) MOT is used to increase the initial atom density.

Sodium atoms are transferred into the magnetic trap using a spin polarization and optical pumping scheme [104], for our setup desribed in [5, 102], that pumps the atoms into the $|2, 2\rangle$ stretched state than can be trapped magnetically. An admixture of atoms in the $|2, 1\rangle$ state will also be trapped, since the optical pumping is not 100% effective.

For ^{6}Li, the loading scheme is similar and also described in [5, 102]. In contrast to the sodium loading, a compressed MOT phase is used to increase the Li density directly before the optical pumping.

^{7}Li is loaded analogous to ^{6}Li, with changes in the setup detailed below. However, the pumping scheme was simplified as no separate repumper is applied during the pumping. The necessary population in the upper $f = 2$ manifold is achieved by turning off the MOT beams before the repump beams which populate the upper hyperfine state. The optical pumping then only shuffles the population into the $|2, 2\rangle$ state in which the atoms are trapped.

Alternatively, both Na and ^{7}Li can be trapped in the $|1,-1\rangle$ state, as discussed below. The preparation then is more straightforward since the sodium atoms are already in the lowest manifold and turning off the lithium repumper will also quickly populate that manifold. Without further pumping, one third of the atoms can than be trapped.

3.1.3 Changes for ^{7}Li

The optical setup for ^{7}Li differs from the ^{6}Li MOT only in the repump beam frequency, which makes a change between the species quite easy. The different hyperfine splitting of 804 MHz instead of 228 MHz is done by adding a 290 MHz AOM in double-pass configuration into the repump beam, without the need of any further changes in the beam paths.

Unfortunately, however, the efficiency of the 290 MHz AOM is rather low, which means that after the double-pass the power in the repump path can limit the MOT loading for ^{7}Li. With respect to future experiments, an additional tapered amplifier was set up and will be implemented into the Li repump line after the AOMs to increase the repump power. This also leaves more laser power for the Zeeman slower and the MOT beams.

In total, a change from ^{6}Li to ^{7}Li requires manual relocking of both the master laser and the MOPA, since the tuning range without mode hopping is much lower than the needed 10 GHz. Then, one half-wave plate has to be rotated to send the beam through the double pass AOM, and the setup is ready for ^{7}Li.

3.1.4 Conservative Magnetic Trapping

For efficient trapping of the atoms in an inhomogeneous magnetic field, several contraints have to be taken into account: Magnetic trapping requires a field extremum – either a maximum or minimum – to confine the atoms. Since a magnetic field maximum cannot be produced in free space, the field has to have a minimum of the absoulte field strength. Therefore, only low-field seeking states (i. e. atoms that gain energy with increasingf fields due to the Zeeman effect) can be trapped.

Further, since only the total spin is conserved in the cold collisions, but not the spin of inidividual atoms, spin relaxation has to be prevented. This is the reason why the $|2,1\rangle$ state of Na is problemetic since the process $|2,1;2,1\rangle \rightarrow |1,1;1,1\rangle$ is exothermic and releases a high amount of energy, which causes heating and losses from the trap.

For Na, the natural choice for the trapping state is $|1,-1\rangle$ since the three body loss coefficient for the $|2,2\rangle$ state is about an order of magnitute larger. [35] For ^{7}Li, the $|1,-1\rangle$ state is also trappable, but the scattering length of this state is very small (7 a_0 to 15 a_0 below 140 G) which prevents efficient thermalization. However, the scattering length in the $|2,2\rangle$ state is negative, $-27\ a_0$, which can pose limitations for cold, dense samples and especially condensation in this state. Although both species are inconvenient in the $|2,2\rangle$ state, still Bose-Einstein condensates could be achieved, either by low density, as in [35] for sodium, or for small atom numbers, as in [11].

Trapping of ^{6}Li in the lower manifold ($|F = 1/2\rangle$) is not possible due to the strong quadratic Zeeman shift that prevents $|m_F = -1/2\rangle$ atoms to be trapped above 27 G, corresponding to a low temperature of 0.2 mK, which is much lower than the MOT temperature. So for ^{6}Li, only

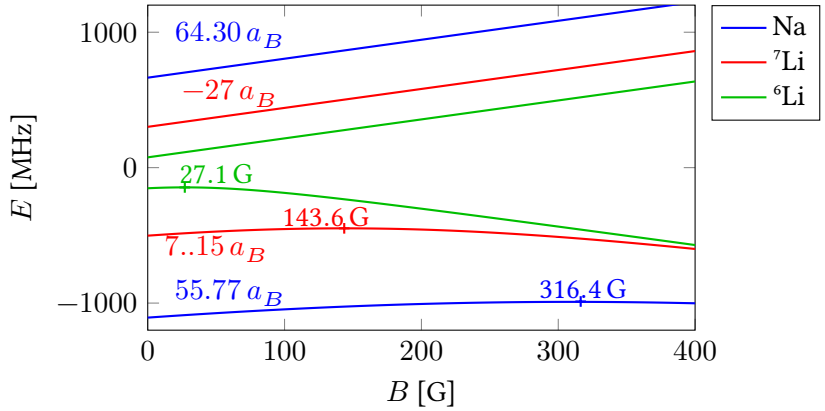

Figure 3.3: Energy dependence of hyperfine states that can be trapped in a magnetic field minimum, with indicated intraspecies background scattering length for the bosonic species The energy maxima of the states in the lower F manifold correspond to temperatures of about 280 mK (Na), 1.7 mK (^{7}Li) and 0.2 mK (^{6}Li). This is far lower than the MOT temperature and thus trapping of ^{6}Li is not possible.

the $|3/2, 3/2\rangle$ state can be used. Figure 3.3 shows the field dependence of the trappable states, calculated via the Breit-Rabi formula (Equation 2.13), of the three species. Also indicated are the maximum fields up to which trapping is possible in the lower manifold and the intraspecies scattering lengths at low fields.

Combining the different atomic species adds, but also solves some problems: The combination of Na in $|1, -1\rangle$ and ^{6}Li in $|3/2, 3/2\rangle$ leads to strong losses in ^{6}Li due to spin relaxation since the combination of $|1, -1; 3/2, 3/2\rangle$ can decay into the $|1, 0; 1/2, 1/2\rangle$ state. Thus, the ^{6}LiNa combination can only be trapped efficiently in the highest hyperfine states for both species. [42]

The ^{7}LiNa mixture can be trapped in both $|2, 2\rangle$ or $|1, -1\rangle$, if both species are in the same state. The convenient ^{7}LiNa scattering length in the order of 20 a_0 allows efficient thermalization, thus lifting the limitation of the ^{7}Li single species setting. This is important since both lithium species are cooled sympathetically, which means that only Na is cooled evaporatively, and the Li atoms are thermalized to the colder sodium temperatures by collisions. [70]

The setup of coils for the cloverleaf type Ioffe-Pritchard magnetic trap has been described in [5] and is still used in the same way. In the remainder of this thesis, the coil pairs will be called *antibias* or *Feshbach coils* for the large coil set in Helmholtz configuration; *curvature* coils for the set that has the same distance as the *antibias* coils but is smaller in diameter, producing a saddle point magnetic field. The *gradient* coils are consisting of four pairs of coils enabling the radial confinement by producing a quadrupole field. An additional set of *finetune* coils is also set up in Helmholtz configuration but with a lower number of windings compared to the *antibias* coils. Figure 3.6 shows a skectch of the coil configuration without the gradient coils.

Additionally, three sets of large *offset* coils are built around the whole setup with diameters and distances of about 1 m. These are used to cancel external fields, apply low, very stable offset fields and might be used in future experiments to cancel gradients, too.

The electronic circuit for driving the coil currents is shown in Figure 3.4. One major change was the addition of the bias current direction switch, indicated by the additional bias line. Note that no additional IGBT was used in this line.

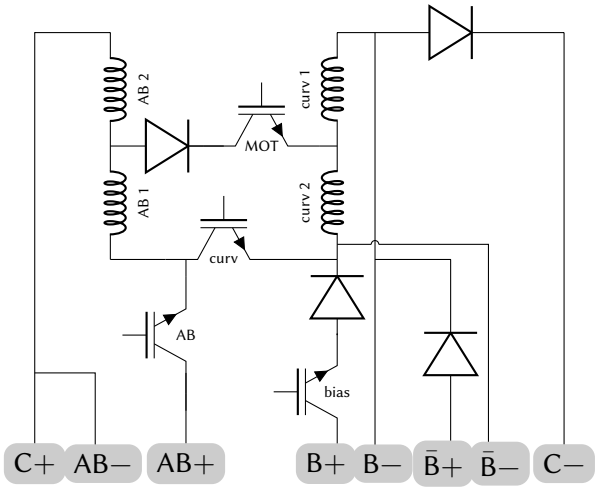

Figure 3.4: Schematics of the electronic circuits for the cloverleaf trap, consisting of the coils, IGBTs and diodes. The power supplies are labelled Curvature, AntiBias and Bias. $\bar{\text{B}}$ indicates the inverted bias circuit for the hybrid trap.

The additional H-bride in the bias circuit allows to turn the current direction which was used in the high-field hybrid trap described below. In some sets of experiments, the passbank in the antibias circuit, described in [102], was connected to the circuit of the 1 m offset coils to provide a stable current source.

In the gradient circuit, the IGBT switch was removed as this switch was not necessary, but limited the maximum current. This allowed for a slightly higher gradient and thus stronger confinement.

3.1.5 Evaporative Cooling

While the atoms in the MOT are already orders of magnitude colder than room temperature, the phase space density is still far away from the one needed for our quantum gas experiments.

To further lower the temperature and increase the phase-space density of the atoms, a standard forced evaporative cooling scheme is applied. Using the microwave source described in section 3.2, Na atoms are driven from the $|2,2\rangle$ state into the anti-trapped $|1,1\rangle$ state. By lowering the frequency from a high initial value, only the hottest atoms are removed, which have enough energy to reach the high-field regions of the trap. This leaves the remaining atoms in a truncated thermal distribution. Collisional re-thermalization leads to a colder sample in thermal equilibrium, until the next atoms are removed. The final temperature of the cloud is then given by the lowest MW frequency applied and the value of the *trap bottom*, that is the lowest magnetic field. In our setup, this is mostly controlled by the *bias* power supply: A higher current through the curvature coils by this supply lifts the field minimum and colder atoms

are transferred. Therefore, this minimum has to be very stable to reliably produce stable atom numbers and temperatures.

For the case of trapping both Na and ^{7}Li in the lower hyperfine manifold, the traditional way of evaporative cooling is to drive the Zeeman transition $|1,-1\rangle \Rightarrow |1,0\rangle$. As our setup is optimized to drive the microwave transitions, we use the $|1,-1\rangle \Rightarrow |2,0\rangle$ transition. This has the advantage that the ^{7}Li transitions are far detuned, which is not the case for the Zeeman transitions, therefore only sodium is removed and the minority ^{7}Li is kept in the trap.

Possible improvements for our cooling scheme have been investigated in [111], but the setup is rather robust and thus fine tuning of the exact ramp form is not necessary. However, the old implementation of the cooling ramp using the programmable frequency list of the microwave source was not very reliable since the timing of the frequency list could differ from the main experiment timing by up to several hundreds of milliseconds, thus inducing changes of the final cooling point which made the preparation unstable.

Table 3.1 lists the cooling frequencies used in most of the experiments presented in this thesis. Also listed are the clean sweep mentioned above as well as the standard transfers of the atoms into the absolute hyperfine ground state.

Table 3.1: List of microwave sweeps in a standard experimental cycle. The clean sweep is done at high offset field of about 60 G, the transfers at low offset field of 1.6 G. Cooling of sodium can be done in the $|2,2\rangle$ state or $|1,-1\rangle$. Note that in the latter case the frequency increases for lower fields.

ramp	f_{start} [MHz]	f_{stop} [MHz]	duration [ms]
clean $\|2,1\rangle \rightarrow \|1,0\rangle$	1870	1810	1900
1$^{\text{st}}$ cooling $\|2,2\rangle \rightarrow \|1,1\rangle$	1900	1800	9000
2$^{\text{nd}}$ cooling $\|2,2\rangle \rightarrow \|1,1\rangle$	1800	1779.3	6000
1$^{\text{st}}$ cooling $\|1,-1\rangle \rightarrow \|2,0\rangle$	1630	1740	9000
2$^{\text{nd}}$ cooling $\|1,-1\rangle \rightarrow \|2,0\rangle$	1740	1761	6000
Na $\|2,2\rangle \rightarrow \|1,1\rangle$ transfer	1774.75	1775.25	32.5
^{6}Li $\|3/2,3/2\rangle \rightarrow \|1/2,1/2\rangle$ transfer	230.178	232.178	32.5
^{7}Li $\|2,2\rangle \rightarrow \|1,1\rangle$ transfer	805.831	807.831	32.5

3.1.6 Dipole Trap

While it is possible to produce quantum degenerate gases in conservative magnetic traps, for many experiments it is more convenient to have a state-independent trap that allows to apply a homogeneous magnetic field as an additional parameter. To be more precise, none of the experiments shown here could have been done in a magnetic trap, or only with major limitations, since the spin degree of freedom would not be accessible. Thus the dipole trap is a central and important part of the setup.

Therefore many typical ultracold atom experiments end their preparation scheme in an optical dipole trap. Depending on the species, experimental circumstances and available laser power, a

magnetic cooling stage might even be skipped and the atoms can be trapped from the MOT directly into the dipole trap.

The trapping is based on the AC stark shift as described in Equation 2.25 and for our case does not depend on the atomic state since the detuning to the resonant D lines (589 nm for Na, 671 nm for both Li species) is very large. We use a 1064 nm industrial welding laser with up to 50 W output power.

For the trapping, the laser beam is split and power controlled as well as frequency shifted by two 80 MHz AOMs. The two resulting beams make up a crossed dipole trap with a horizontal beam piercing the bull's eyes of the coilholders and is tilted by 8° relative to the coil axis. The second beam crosses diagonally from bottom to top with an angle of 42° to the horizontal plane. Figure 3.5 shows the resulting configuration. As the imaging is done from the top view, all absorption pictures presented and all data evaluation rely on this projection.

The trap frequencies are measured by displacing one of the beams using a mirror with piezo mounts and suddenly switching it back, so oscillations are induced. For different waiting times, the resulting position of the atoms after time of flight can be monitored and the frequencies fitted. For typical trap settings we get $\omega_{x,y,z} = 2\pi \times (150, 100, 220)$ Hz, with a mean trapping frequency $\bar{\omega} = \sqrt[3]{\omega_x \cdot \omega_y \cdot \omega_z} = 2\pi \times 150$ Hz. These frequencies are along the main axis as indicated in the figure. The top view corresponds to the imaging direction, as can be seen by the absorption picture of a sodium cloud in-situ, on the left.

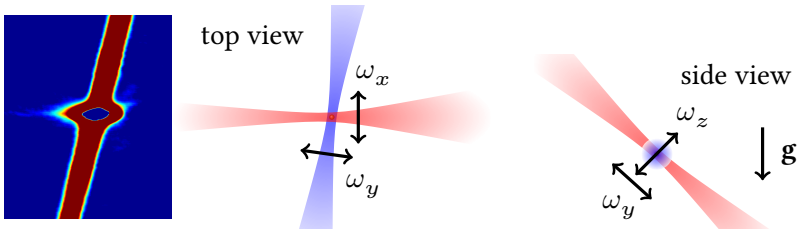

Figure 3.5: Illustration of the crossed dipole trap setup. Both beams are derived from a 1064 nm laser; the colors are used here for better distinction. The blue beam holds the atoms against gravity and will also be called the waveguide, while the red beam confines the atoms along the waveguide, serving as a dimple for the condensation, and comes in under an angle of 42 ° to the horizontal plane. The picture shows a sodium cloud in the crossed trap, with a large part residing in the waveguide. To the left, a small part of the atoms escape the dimple, following the crossed beam along gravity (indicated by **g**). The blue *hole* in the middle of the picture is an imaging artefact due to an optically dense cloud.

The loading scheme of the dipole trap has been changed compared to earlier experiments as the transfer from the magnetic trap into the dipole trap was very unreliable due to several reasons:

- The endpoint of the cooling ramp was unstable due to the microwave timing.
- The trap bottom varied due to temperature changes.
- The magnetic trap center moves when ramping down the currents.
- The ODT position drifts slightly.

- The high density of atoms in $|2, 2\rangle$ leads to fast losses.

These reasons made the direct loading of atoms into the crossed trap very unreliable. Thus, a new scheme was developed, as described in [83] in more detail. The main idea here is to increase the horizontal beam's confinement by reducing its waist and using the vertical beam as a plug. The atoms are then released from the magnetic trap into the horizontal one-beam trap.

In the one-beam trap, the atomic density is low enough to prevent losses, and the transfer to the lowest hyperfine state can be done. For this, an offset field of 1.6 G is applied and two microwave sweeps transfer the atoms. If both species are used, Na is always transferred first, then the Li atoms. section 3.2 gives details about the frequency sources and ramps used for this.

The final cooling stage to reach quantum degeneracy is done by lowering the power of the horizontal beam, leading to losses of the most energetic particles due to gravity, thus cooling the atoms. This is done while the second beam is turned on, so that the atoms will be cooled and pulled into the crossed region. To make this process more efficient, an additional magnetic curvature is applied, but this time with a magnetic field maximum at the trapping point.

This high-field hybrid trap[1] is produced by applying a homogeneous offset field using the finetune coils. Then, the current direction of the bias circuit is turned around using an H-bridge configuration of large relais, so that the resulting magnetic field is opposite to the finetune-field.

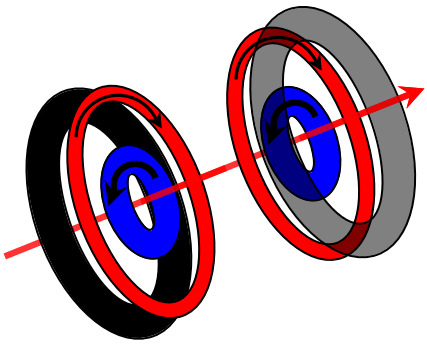

Figure 3.6: Coil configuration for the high-field hybrid trap. The red arrow indicates the dipole trap beam's propagation. Blue coils are dubbed curvature or bias coils, red coils are finetune.

The combined field then produces the maximum that attracts the atoms in the lowest hyperfine state, since those are high-field seekers. The radial anticonfinement is weak enough so the atoms can be held by the horizontal dipole beam. Figure 3.7 shows a sketch of the fields and potentials of the four coils and the two laser beams used for this setup.

After this final evaporation stage, the finetune and bias coils are turned off, and the preparation of the atomic sample is finished. The whole procedure takes about 40 s and can produce Na BECs of up to 1×10^6 atoms with large condensate fraction, or mixtures of Na and Li with varying atom numbers, all in the lowest hyperfine state $|1, 1\rangle$ and $|1/2, 1/2\rangle$ respectively. The lower atom number as compared to [83] is mostly caused by the limited magnetic trap confinement

[1] Dubbed *high-field* because there is a field maximum along the direction of the waveguide, but also because it was used to condense atoms at high fields of 900 G, see chapter 4.

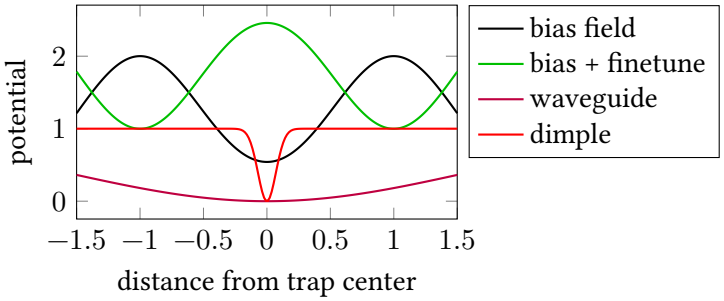

Figure 3.7: Sketch of the high-field hybrid trap. Shown are the magnetic field of the curvature coils (black) and the result of applying the finetune field in opposite direction: A field-maximum in the middle of the trap. The red lines indicate the potential of the waveguide and the diple, where the atoms are trapped after the cooling. Not to scale.

due to the change of the chiller setup as explained below, but also because a big condensate poses more problems for the experiments discussed here, mainly for the spin dynamics.

3.1.7 Cooling Water Temperature Stabilization

The final temperature and the number of remaining atoms after the evaporation depends on two parameters: The lowest magnetic field in the trap and the final frequency of the MW knife.

While the final frequency can precisely be controlled with the new RF setup presented in the next section, the magnetic field suffers from the construction of the trap design: The subtraction of two large fields is sensitive to the exact position and resistance of the coils, which again is dependent on the cooling water temperature. So far, it could not be definitely determined which parameter changes, but the final cooling point is closely related to the water temperature.

Active Water Temperature Stabilization

To reduce this effect, two measures were taken: First, the loading scheme of the dipole trap was changed to be less sensitive to the atoms' temperature, second, the cooling water was actively stabilized. Normally, this would be the chiller's task, but in our setup, the compressor was far overdesigned with a cooling power of about 20 kW. The maximum heat input into the coils is around 12 kW, and this only during about half the time of one experimental cycle. This leads to a fast cooling of the water reservoir, resulting in either strong fluctuations of the water temperature or fast cycles where the compressor is running only for short times.

For a stable experimental setting, one has to choose the short cycles, which strongly reduces the lifetime of the compressor. Therefore, an external heating of the water was implemented that reduced the temperature fluctuations and allowed for a longer lifetime of the compressor.

The rather obvious ansatz of using a flow heater where the water is heated by flowing through a hot pipe turned out to be much too slow to compensate for the temperature changes of the incoming water. This was due to the high pressure and flow rates which lead to a very laminar flow. Therefore the outer layer of the water could be heated, but the energy not be transported to the inside, making this a very slow process – the compressor could cool the water in about 10 s which was faster than the reaction time of the heat pipe on the order of 30 s.

A much faster and more versatile solution was to create a small reservoir of very warm water and add small portions of this to the cool water to achieve the desired temperature. Figure 3.8 shows a sketch of this setup: The main path for the cooling water is above the pipe going straight through the T-piece to the experiment. A small flow is branched off the cool water and flows into the heating pipe from the lower end. Five heat clamps deliver up to 500 W power each to heat the water while it is in the pipe. At the top, below the T-part, is a valve (ASC0 SCG203B002) that can be opened to add a small flow of the hot water to mix it with the cool flow. Since the water just has to be mixed in instead of being heated on-the-fly, this setup has a much faster reaction time on temperature changes.

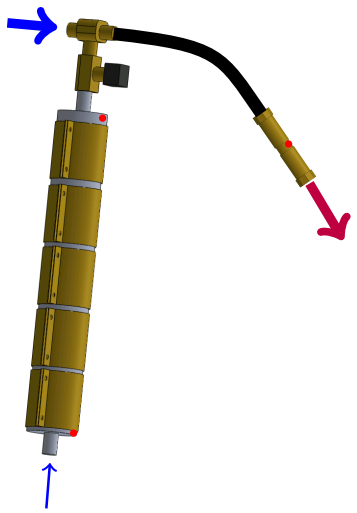

Figure 3.8: Sketch of the heat pipe and the sensor piece. The red dots indicate the position of the thermistors used for temperature regulation of the water output and thermocouples for the monitoring of the heat pipe's temperature. Cold water enters the heat pipe from below, is heated, and mixed with the cold water that is going straight to the outlet.

The mixed water then flows through a brass connector that has a very thin wall where a thermistor is mounted. Using a wheatstone bridge, the resistance is converted into voltage that is read in by an Arduino microcontroller. This value is the input of a digital PID control loop where the output is the opening of the valve in a pulse width modulation setup with a frequency of 2 Hz. The temperature of the pipe is also actively controlled, although with a much simpler readout, to roughly 80 °C.

With this setup, the chiller's hysteresis could be set to at least 1.1 °C, while the cooling water input to the coils was stable to less than 0.1 °C.

Lower Power Chiller Setup

Even with the heat pipe setup, the chiller's compressor broke again and therefore the cooling setup had to be replaced. Instead of a repair or a new design, an old, smaller chiller was used to cool the reservoir of the big one, while the stronger pump of the latter one was still used.

This required changes to the settings for the atomic cooling sequence, since the small chiller's compressor was too weak and could not cool away the heat input during one sequence. To reduce the heat input, the MW cooling of the atoms described to be shortened from 14 s to 9 s and from 12 s to 6 s. Also, an additional pause was added between the runs to allow the chiller to cool down the water. Finally, the current settings for the coils had to be reduced and the corresponding MW frequencies adapted. However, for the loading and clean sweep, the full power was still used to increase the transfer efficiency from the MOT.

Table 3.2 lists the currents and voltages set for the loading/cleaning and the normal trapping. Since the power supplies are in constant current mode, the voltages vary slightly depending on the exact coil temperatures.

Table 3.2: Current settings for the magnetic trap. Reduced values are necessary to compensate the lower chiller power. Normally, only the bias current would be reduced to increase the trapping frequencies.

coil pair	I_{load} [A]	U_{load} [V]	I_{trap} [A]	U_{trap} [V]
gradient	403	13.23	352	11.53
curvature	223	30.60	158	21.60
bias	20.0	13.71	2	8.72

These values were chosen as a trade-off between acceptable atom number and temperature at the end of the cooling and short waiting times between the runs, to reduce the effective cycle time.

3.2 Microwave Control

As described above, our experimental preparation of cold atoms depends on the ability to manipulate their hyperfine states with microwave radiation. This is needed both for the removal of hot atoms for the cooling procedure, but also for the final state preparation.

Furthermore, control over the Zeeman substates of the atoms is an important ingredient to study any spin-dependent physics, starting from Feshbach resonances that occur in different hyperfine states, up to coherent coupling of spinor condensate components.

In total, electromagnetic radiation in frequency ranges from 5 kHz up to 2 GHz and powers up to 100 W are needed. This section describes the development, implementation and useage of a versatile frequency source that, in combination with various amplifiers and antennas, provides all of the desired frequencies and is connected to the experimental control via a simple and robust communication protocoll.

The concept is based on two DDS boards (Direct Digital Synthesis) that give a well-controllable frequency output, different mixers to allow for high frequencies, as well as an adjustable microwave source based on a PLL (Phase Lock Loop) and amplifiers for the final output power. Alle devices are controlled by an Arduino microcontroller.

Figure 3.9 shows a simplified scheme of the whole setup. The following subsections will further explain the single parts and their connections. A list of all components used in this setup can be found in the appendix, Table A.1.

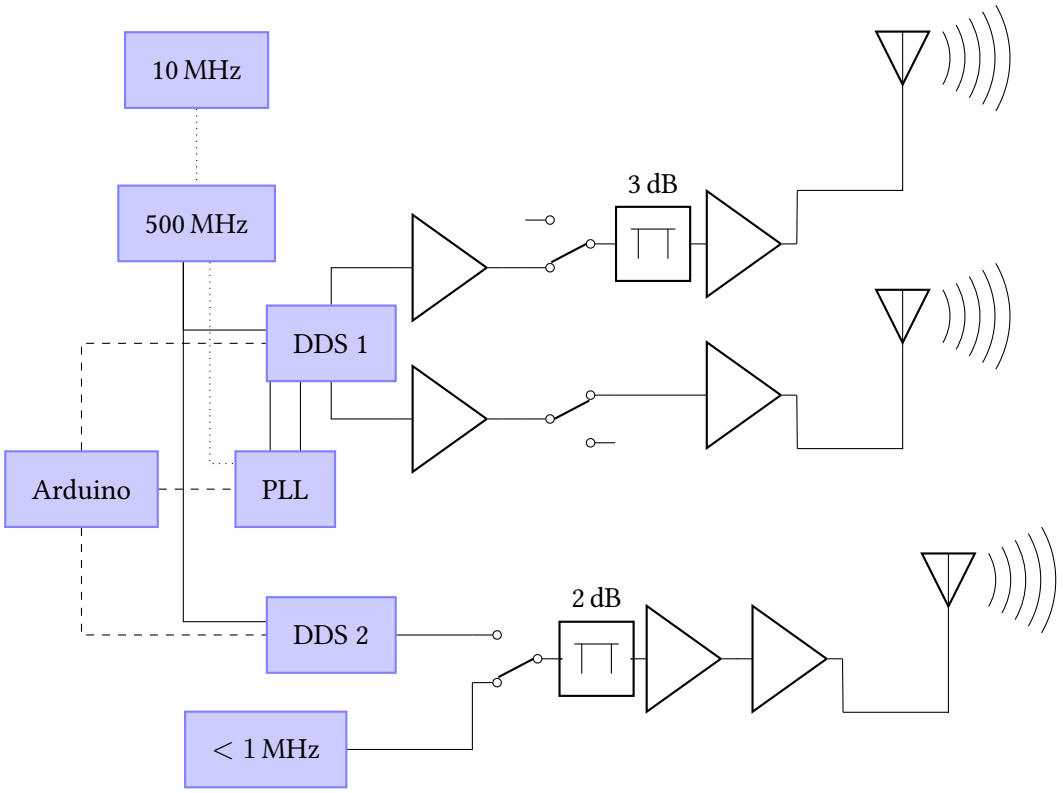

Figure 3.9: Simplified schematics of the whole MW/RF setup including the control/sources. Solid lines depict an MW/RF signal line, the dotted line shows the 10 MHz reference signal, and the dashed lines indicate SPI communication lines.

3.2.1 Fixed-Frequency Sources and PLLs

Since RF and MW transitions are used to determine the absolute magnetic field at the place of the atoms, the frequency of this interrogation also has to be known precisely and accurately.

Therefore the first part in the whole setup is a Rb frequency reference that internally probes a hyperfine transition of Rb atoms and outputs an absolute 10 MHz signal. We use this signal as reference for all further frequency generation.

The next step is a 500 MHz reference that is needed by the DDS boards and offered by an Agilent E4421B microwave source that is locked onto the 10 MHz reference. This device was used as the main microwave source in earlier experiments since it offers a lot more features than just a fixed frequency; if needed, it can easily be replaced by a cheaper solution.

The third device is a Phase-Locked Loop (PLL) board that is locked onto the 10 MHz reference output of the E4421B and thus also stabilized to the Rb reference. This is a standard procedure

for frequency references: The frequency is distributed in a serial way instead of a star-formed distribution. By this, reflections and intereferences causing disturbances of the signal are avoided.

The PLL board consists (simplified speaking) of an oscillator and phase detector. A feedback loop compares the phase of the oscillator with the reference signal and keeps them in lock. This board provides two differential outputs of the same frequency; we use them non-differentially, for which it is sufficient to terminate one of the outputs with 50 Ω. If the terminator is not present, however, a wide variety of reflections causes many spurious signals that strongly disturb the operation.

Figure 3.10 shows the output spectrum of the PLL set to 410 MHz (left) which is used as an input for the mixer for the ^{6}Li microwave transfer and for RF transfers at high magnetic fields. The righ-hand side graph shows the setting for the ^{7}Li transfer with 850 MHz carrier. The Na setting could not be recorded since the frequency is above the spectrum analyzer's range. (HP 4396A)

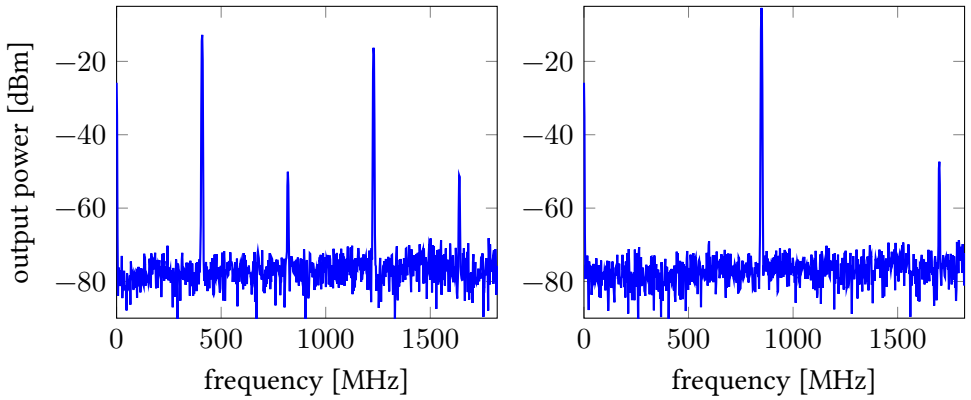

Figure 3.10: Spectrum of the 410 MHz (left) and 850 MHz (right) carrier output from the PLL. Clearly visible are higher harmonics that have to be taken care of. Switching between the settings can be done as quickly as 60 µs. The spectra were taken with a 10 dB attenuator.

Already at this first point of the signal generation, higher harmonics and spurious signals appear in the spectrum that cannot be suppressed directly. However, since the mixers and the final amplifier for the ^{6}Li setup are cut off at 500 MHz, these harmonics do not disturb the experiment and can be ignored. For the 850 MHz setting, the higher frequencies are detuned far enough to have no influence onto the atoms, but they can lead to a saturation of the amplifiers and thus reducing the available power at the desired frequency.

During most of the time of the experiment, the carrier is kept constant: For the cleaning of the $|2, 1\rangle$ atoms as well as the full MW cooling, 1950 MHz are used and the mixing explained below produces all necessary frequencies. The only time critical step is the transfer into the lowest hyperfine states: This is done consecutively for Na, then for Li, although for ^{6}LiNa, this could be done in parallel, since different amplifiers and antennas are used.

Full optimization of the communication between Arduino and PLL bord allows to set the PLL frequency in times as short as 60 µs. This actually would even be short enough to do everything directly with the PLL, without the need for any further processing. But since the PLL board does not have the ability to do ramps itself, the Arduino program would have to store (or calculate, which would be too slow) each frequency step. This is not an option as the memory would be too small; also, the output power of the PLL can only be set to five different values, which is not flexible enough.

Due to all these reasons, the mixing scheme including the DDS boards, was implemented, to gain full control over all frequency ranges.

3.2.2 DDS

The main frequency control is performed by using Direct Digital Synthesis (DDS), readily available via a commercial evaluation board (see Table A.1 for a detailed list of used parts). The working principle of DDS will not be explained here, but we will just take it as a signal source with controllable frequency, amplitude and phase.

The DDS boards can be programmed either using a USB interface to a PC or by an SPI interface. While the USB device is convenient for testing purposes, the SPI interface is used in the experiment and is described below.

Our setup makes use of two DDS boards, with four and two output channels, respectively. All channels can be controlled independently, in frequency, phase, and power. The available frequency range is 0.3 MHz to 200 MHz with sub-Hz resolution. The phase resolution is 14 bit, which is not needed in our setup, since only $\pm 90\,^{\circ}$ are used. For the power, a linear scale of 1024 steps is available.

3.2.3 I/Q Mixer setup

While the DDS offers a highly controllable frequency source, its limited bandwidth does not allow to directly manipulate the atoms in all states. Especially the frequencies for transitions between the hyperfine states are way above the 200 MHz maximum output frequency.

Therefore, an I/Q mixing scheme has been implemented that allows to transfer the control of the DDS output onto a high frequency microwave. While I/Q mixers are standard parts that are commercially available, we did not find an integrated solution for all of our needs. So we decided to set up two discrete I/Q mixers for the different frequency ranges.

Figure 3.11 shows the schematic concept of the I/Q mixing: A fixed microwave signal (local oscillator LO, frequency f_0) is mixed with a controllable intermediate frequency (IF, frequency f_1, although this frequency is the lowest one in the setup) input in two separate mixers. The LO input is split and one of the outputs shifted by 90°.

A simple unbalanced mixer will produce the product of the inputs, resulting in output frequencies $f_+ = f_0 + f_1$ and $f_- = f_0 - f_1$. But also the input signals will be leaking through, so at least four frequencies f_0, f_1, f_+, f_- will be present at the output. While the IF signal can be filtered, the three bands at high frequency can cause major problems in our experiments. Even with a more sophisticated balanced mixer that might suppress the f_1 component, still the two sidemodes f_+, f_- will be present.

To compensate for this, the output radio frequencies (RF) of the mixers are combined without further phase shift. This leads to interference of the mixer outputs and can lead to destructive interference for f_+ while giving constructive interference for f_-. This way, only one sideband will be left and the result is a clear single-frequency signal. Changing the phase of the IF inputs can select the other sidemode or enable both sidemodes to pass, with continuos power distribution between the two frequencies, depending on the relative IF phase.

Of course, any real mixer has more sidebands and the interference is not perfect. We achieve a 20 dB attenuation of the carrier and around 40 dB suppression of the unwanted sideband.

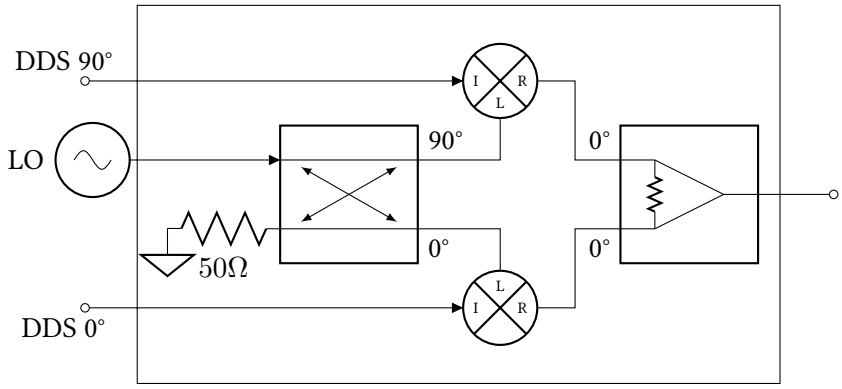

Figure 3.11: Schematics of a discrete I/Q mixer. The local oscillator is split and phase shifted by 90 °, then inserted into the mixers. The IF signal is derived from the DDS with a relative phase of $\pm$90 ° and mixed with the LO. The RF output of both mixers is combined without further phase shift; the interference of the signals in the combiner results in the wanted frequency sidebands.

Since the output of the mixers is limited to (and thus also controlled) by the DDS output power, the signal is by far too weak to drive the atomic transitions. Therefore, in each channel a two-stage amplification is needed, with a low power pre-amplifier in both channels and the final amplifier for the microwave channel (used for 800 MHz to 2000 MHz) and the RF channel (used for 50 MHz to 500 MHz).

The typical output of the whole setup before the final amplifiers is shown in Figure 3.12 for two settings: On the left-hand side, the spectrum of the setting for the sodium $F = 1$ cooling is shown, on the right-hand side the setting for the ^{7}Li microwave transfer.

The numerous sidepeaks show that the sidemode suppression is not perfect. For the 1650 MHz case, the carrier was set to 1600 MHz and is rather well suppressed, while the 1550 MHz signal is suppressed by only about 17 dB, which is still sufficiently weak to be neglected in the experiment.

For the 806 MHz case, the spetral distribution looks really bad, and the desired frequency is not even the strongest one. This is due to an inconvenient setting of the PLL which has a very bad suppression of side modes at the desired frequency. However, no negative influence could be observed in the experiment; the microwave transfer for ^{7}Li works very well and thus no further measures were taken to reduce the side modes.

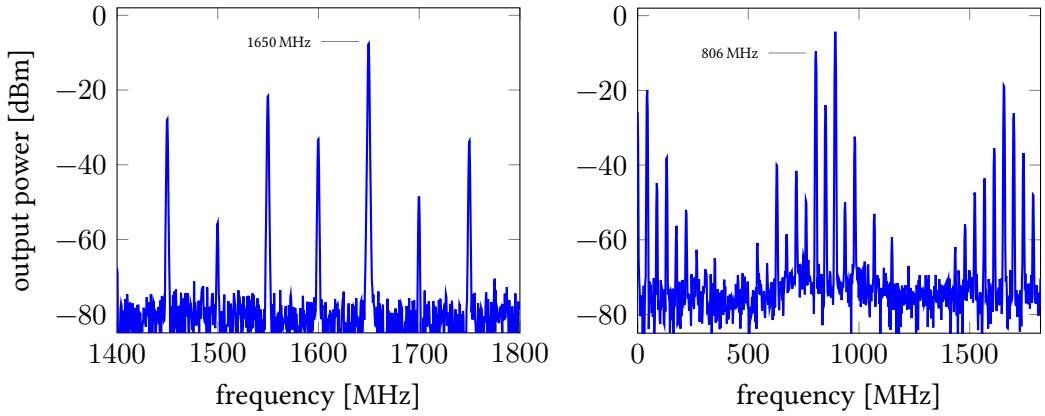

Figure 3.12: Spectra of the microwave source output after the pre-amplifier. The left spectrum shows the output for 1650 MHz, the carrier frequency is 1600 MHz, and the desired frequency has the highest power. The right spectrum is set for 806 MHz, with the carrier at 850 MHz. Spectra were taken with 10 dB attenuation.

3.2.4 External Sources

For Zeeman transitions at very low fields, frequencies down to 5 kHz have to be provided. That's why the third line of amplifiers and antenna is implemented, offering two different possibilities: The second DDS wich has two output channels, is connected directly to the amplifiers without mixers, thus offering the 0.3 MHz to 200 MHz frequency range of the DDS with the full frequency sweep and power flexibilty.

For frequencies below 300 kHz, the DDS cannot be used anymore since the transformers on the board will not work below that frequency. Since in this frequency range, no sweeps are used, but only fixed frequencies for the Rabi coupling, a simple signal source can be used. We used an Agilent 80 Mhz arbitrary waveform generator, but only to produce a sine waveform. Any other (preferably programmable) sine source would be sufficient, too. Since the external source was only installed for a small number of test measurements, the frequency was set by hand. In a final installation, the computer control can set the frequency simply via a GPIB interface, which also allows automatic scanning of the frequency.

For the frequency range of 100 kHz to 300 kHz it turned out that the ZHL-3A amplifiers still worked fine, although they are specified only down to 400 kHz.

Below 100 kHz, the amplifiers could not be used anymore, but the unamplified Agilent signal is strong enough to allow very high Rabi frequencies, up to the driving frequency itself.

3.2.5 Antennas

The end stage of the MW/RF setup are antennas. For the three main frequency output ranges, separate antennas were used. The amplifiers are directly connected to the antennas, so that switching after the amplifier to another antenna or switching between two amplifiers for one

antenna is not possible. This is to avoid the insertion loss of splitters which would reduce the available RF power.

Two of the coils are designed to be as close to the atoms as possible with a low number of windings. One antenna is connected to the microwave amplifier, thus used for the Na and ^{7}Li hyperfine MW transitions. The other antenna is connected to the RF amplifier and thus used for the ^{6}Li MW transfer as well as RF transfers at high fields where the Zeeman splitting gets in the order of 170 MHz (300 G) to 340 MHz (1000 G).

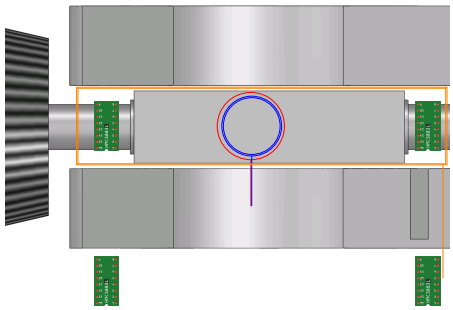

Figure 3.13: Position of the coils in the experiment. The round RF (blue) and MW (red) antennas are centered above the glass cell, with the imaging beam propagating through them. The rectangular low-frequency antenna (orange) is put over the glass cell without blocking any optical access. Also shown are the magnetic field sensors discussed below.

Figure 3.13 shows the position of the antennas in a top view onto the glass cell, embraced by the coil holders. The MW antenna (blue) has only one winding with a diameter of 29 mm, the RF antenna (red) has two windings with a smaller diameter of 23 mm. The low-frequency antenna has two windings and encloses an area of $210 \times 45\,\mathrm{mm}^2$. All coils are connected above the coil holders via coaxial cables to the corresponding amplifiers.

The third antenna in our setup was used with an impedence matching circuit at 16.9 MHz where the Zeeman sublevel preparation was done. This frequency was chosen as in the old setup frequency sweeps were not possible, but the magnetic field had to be ramped. The 16.9 MHz were convenient to selectively transfer Na or ^{6}Li into the corresponding states. Now, the matching circuit is not used anymore and the antenna is typically used at lower frequencies. Still, a prominent resonance feature is present (see Figure 3.16).

At very low frequencies below 1 MHz, the antenna proved to allow very efficient coupling, with Rabi frequencies in the order of the driving frequency, which breaks down the rotating wave approximation.

3.2.6 Control Chain

The control of the microwave signals follows three steps: The graphical user interface running on our main PC sets the parameters and sequence files. These are passed to the control server

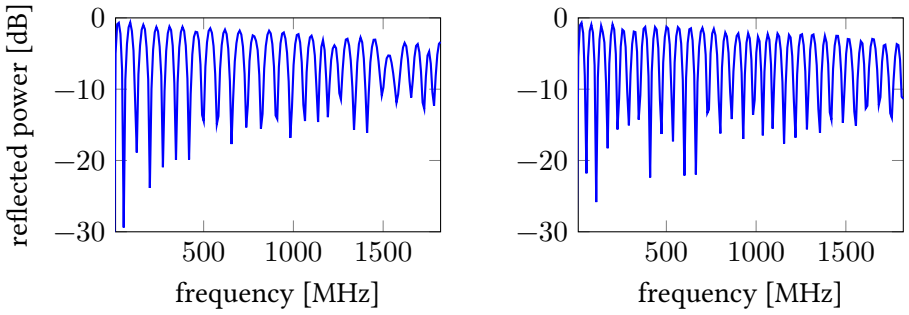

(a) RF antenna.

(b) MW antenna.

Figure 3.14: Reflection spectra of the MW and RF antenna. The spectra show that no clear impedence matching for a broad frequency range is given. The high Rabi frequencies that can be achieved therefore show that the near-field amplitude is more important then the radiated far-field energy.

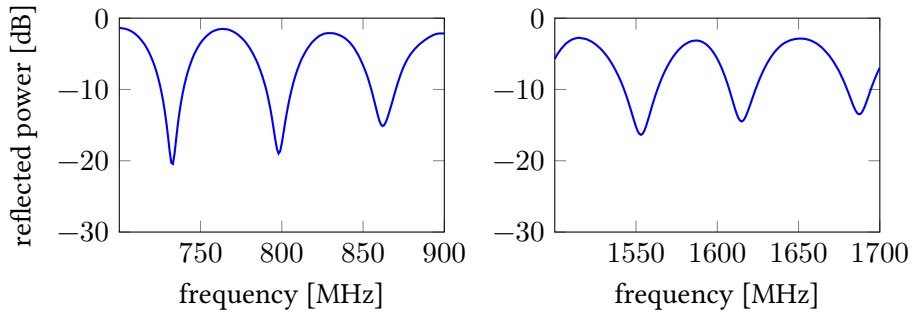

Figure 3.15: Zoom of the frequency dependence of the MW antenna for the relevant frequency range for ^{7}Li (around 800 MHz) and for $|f = 1\rangle$ cooling for Na (around 1600 MHz).

that is evaluating the data, programs the National Instrument cards [59] which control the digital and analog output channels for the whole experiment.

This server also communicates via a serial interface with the Arduino Due microcontroller. The latter one writes the final data onto the DDS boards and is also in charge of triggering the ramps.

The interface between control server and Arduino was chosen to be compact, yet human readable as well as easy to log for later evaluation. Thus, a simple scheme based on the interpretation of ASCII characters was developed. Since the control server setup is not capable of asynchronous tasks, all data have to be written at the beginning of a sequence, evaluated by the Arduino and then hardware-triggered.

The communication protocol starts with the transfer of the character `r` to initialize the `ramp mode`. (For testing purposes, also a *single tone* mode is available, indicated by `s`.) An uppercase R indicates the start of a new ramp, then come the mandatory parameters `t`, `f` and `F` for the ramp time, the start and the stop frequency, respectively. The time is given in microseconds, the

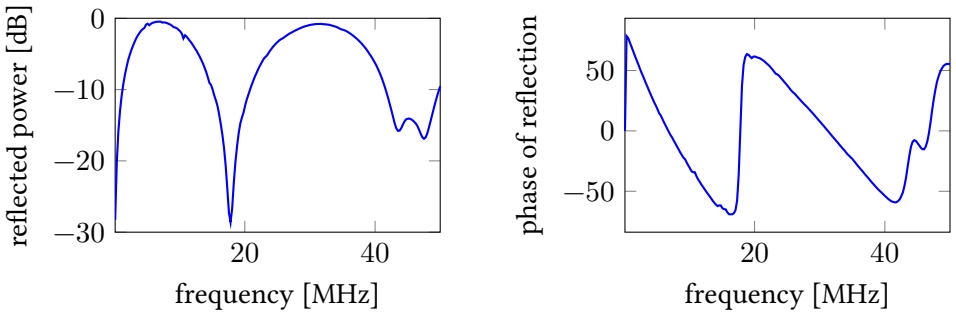

Figure 3.16: Frequency dependence of the low-frequency antenna. Clearly visible is the dip around 17 MHz where the antenna was built for, even without the matching circuit. Also clearly visible is the drop in reflected power for low frequencies < 5 MHz that allows high coupling at low magnetic fields.

Table 3.3: List of source, amplification, antenna and use of radio frequencies in the experiment.

source	frequency [MHz]	amplifier	used for
DDS 1 MW	800 – 2000	MW	cooling, Na & ^{7}Li MW transition
DDS 1 RF	50 – 500	RF	^{6}Li MW transition, RF transitions > 70 G
DDS 2	0.3 – 50	ext	RF transitions < 70 G
Agilent	0.005 – 0.3	ext	RF transitions < 0.2 G

frequencies in Hz. The default amplitude is full scale (1000) of the DDS, but can be changed by the parameter a with a following number between 0 and 1000. A phase can also be defined using p, but typically the Arduino automatically chooses the source and phase relations. The communication is ended with a z; upon receiving this character in the input stream, the Arduino program will start to calculate the ramps, and prepare the PLL and DDS for the first frequency settings.

A standard communication string for the beginning of the experiment would define the MW ramp for the $|2, 1\rangle$ clean sweep and the two RF cooling ramps:

```
rRt1900000f1870000000F1810000000
Rt9000000f1900000000F1800000000
Rt6000000f1800000000F1779300000
z
```

While the communication is very fast due to the lightweight protocol, the ramp calculation takes some time, especially the chopping which is explained below. The calculation is done during the MOT loading, where the microwave setup is not needed. A too short MOT loading will therefore lead to errors since the first cooling ramp will not work – an additional break then has to be added to the sequence.

Depending on the given frequency range, the Arduino code decides which signal source should be taken, with the possible values and chosen carriers listed in Table 3.4.

Table 3.4: List of carrier and amplifier settings for all frequency ranges. The Arduino code decides on its own which configuration is used. For the very low frequencies below 1 MHz no amplifier is used at all, but only the power of the external source.

f_{min} [MHz]	f_{max} [MHz]	source	carrier [MHz]	amplifier
1750	2150	DDS 1 MW	1950	MW
1450	1750	DDS 1 MW	1650	MW
650	1050	DDS 1 MW	850	MW
210	500	DDS 1 RF	410	RF 100 W
20	200	DDS 2	–	RF 100 W
0.3	20	DDS 2	–	RF 1 W
0.005	0.3	extern	–	–

The carrier frequency for the corresponding ramp is written into the PLL and activated as soon as the previous ramp has ended. This allows a very fast switching of the carrier and is an important step to allow quick subsequent transfers of all hyperfine states.

Ramping of the frequency is done automatically by the DDS chip without the need of externally setting each frequency step. Instead, the Arduino just writes the start and end point as well as the ramp time. Additionally, the Arduino sets the frequency increase and the time steps in which the frequency should increase.

Ramp Chopping

For ramps with a small slope, i. e. long ramps with a small frequency change, the finite step size of the DDS leads to complications: Although the frequency resolution is well below the Hertz level (0.1164 Hz for 500 MHz system clock), the finite slope resolution results in a slight offset from the desired frequency in each step. For a long ramp, this can accumulate to a rather large offset. Especially the cooling ramps are problematic in this sense; as has been investigated in [111], these offsets also vary strongly for only a small change in desired frequencies.

This offset change is critical at the end of the cooling ramps, where several kHz frequency offset can have a measurable effect on the final temperature of the atoms, wich limits the reproducibility of the preparation.

Therefore, frequency ramps that take longer than 300 ms are *chopped*, i. e. the ramp is divided into smaller ramps by the Arduino. The program then calculates the best fitting combination of time step and frequency rise by minimizing the deviation from the wanted frequency. For the second part of the ramp, an offset is written so that it starts at the desired frequency, and not at the (slightly off) end frequency of the first ramp. Figure 3.17 shows a sketch to explain the concept of this frequency chopping.

Another reason for the chopping is the frequency dependend output power of the DDS, which varies strongly over the whole frequency range. To compensate for this, a lookup table is created with 200 values. For each frequency setting, the corresponding value is taken to ensure a constant power output. The lowest power at full scale is at the highest frequencies, so the output for lower frequencies is scaled to match the absolute power. This ensures a constant power output over the full DDS frequency range.

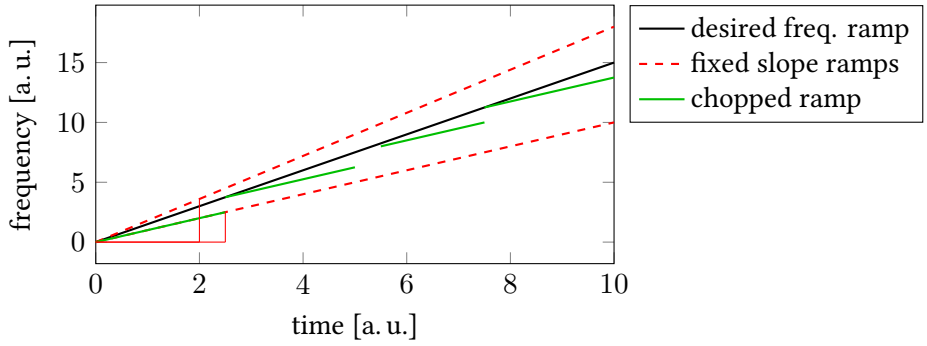

Figure 3.17: Effect of the finite size of the time step and frequency increase. The desired frequency cannot be reached with the possible slopes. Chopping the ramps in short pieces and giving an offset to each piece reduces this effect.

Timing

The data for the first ramp are written into the DDS at the beginning of the sequence. When the first ramp is triggered (via the experiment control), the Arduino takes over the timing and directly after the ramp start writes the data for the next ramp into the DSS buffer. This way, the slow data transfer can already be done during the ramp. The second ramp is then started when the first one has ended, after the data are pushed into the active registers. This is done by an interrupt in the Arduino hardware, which allows the timing to be given by the Arduino hardware clock instead of a software counter. Therefore, long ramps are timed by the Arduino, which is not the highest possible precision, but far better than the old setup or being limited by badly fitting slope parameters.

Finally, also the MW/RF switches are controlled by the Arduino to have the whole MW/RF setup control combined in one device. Again, the Arduino code chooses the necessary switches depending on the desired frequency. The switches serve two purposes: In the paths where only one signal source is connected to one antenna, they block any spurious signal that might get amplified and produce an unwanted parasitic coupling of states or heating of the atoms.

In the path with different sources or different antennas, the switch acts as its name suggests, choosing between the different possibilities. This makes the setup even more flexible and since the switches work even well below 1 kHz, the whole frequency range of the experiment is covered.

50 Hz Trigger

For experiments that are sensitive to magnetic fields, the 50 Hz AC line might cause troubles for high precisions measurements. While it is desirable to cancel the 50 Hz AC field with an active magnetic field control, as will be presented below, it is also an advantage to trigger the experiment onto the 50 Hz line to reduce the influence even further and allow more precise MW/RF couplings.

For this purpose, the Arduino has two further input channels: The 50 Hz `trig` input works similar to the normal trigger channel, but waits for a signal on the 50 Hz `input` signal. The

latter one has to be applied externally, e. g. from a function generator which itself is triggered on the AC line and gives a signal (edge or pulse) at a given phase of the AC line.

This way, the Arduino gets a trigger from the experiment and will start the DDS after it gets the second signal. The other experimental parameters have to be designed in a way that the additional delay of up to 20 ms does not pose any troubles, e. g. for the timing of the imaging.

The effect of the 50 Hz trigger was studied for the magnetic field calibrations. The signal, in terms of measured width of RF/MW transfer as discussed below, was basically the same with and without the trigger. This shows that the setup is not yet limited by the 50 Hz noise, but this might be important in future optimizations.

3.2.7 State Preparation

For all species used in our experiments, the upper hyperfine manifold ($f = 2; {}^3/_2$) is unstable if not in the stretched state and not suitable for further experiments: For sodium, the three-body loss coefficient is too high to achieve a dense Bose-Einstein condensate – although condensation is possible in a more shallow optical trap, as has been shown by [35]. For the trap settings used in our experiments, the losses in the $f = 2$ manifold lead to much too short lifetimes.

Even if the lifetime would not be the limiting factor, the spin relaxation rate is also very high, as mentioned above. This does not only lead to losses in the magnetic trap, but also makes it impossible to investigate spin dynamics in the $f = 2$ state, since only the stretched states are long-lived. This is in stark contrast to the case of rubidium, where both the $f = 1$ ground state and the $f = 2$ upper hyperfine state can be used for spin dynamics and thus allow the study of a richer field of parameters.

In the case of ^{7}Li, the famous negative scattering length makes experiments in the upper hyperfine state very challenging, since only a certain number of atoms can be condensed. [11] As in sodium, the spin relaxation rate prevents experiments in the spin degree of freedom.

The latter is also true for ^{6}Li, which is of course stable if only one Zeeman state is present, but also suffers from strong spin relaxations if not prepared in a pure state.

All these reasons make it necessary to transfer the atoms from the upper manifold, where they are trapped in the magnetic trap, into the lowest hyperfine state, $f = 1$ or $f = {}^1/_2$, respectively.

Microwave Transfer

The microwave transfer of all species into the lower manifold is the first stage in the experiment where the new frequency control based on the DDS brings direct advantages, since it allows arbitrary frequency sweeps. Before the implementation of this setup, it was necessary to ramp the magnetic field while applying fixed frequencies. While this scheme also worked nicely, it is less flexible and the timing of the field ramps is more difficult to realize.

In the new setup, a magnetic offset field of 1.6 G in total is applied after the atoms are loaded into the horizontal dipole trap beam. Then, a frequency sweep for sodium of 32.5 ms from 1774.75 MHz to 1775.25 MHz transfers the atoms from $|2, 2\rangle$ to $|1, 1\rangle$. This rapid adiabatic passage is much more reliable than a π pulse, which could in principle also be applied. If ^{7}Li is also used, the PLL is switched to the corresponding frequency, which takes about 60 µs.

This fast frequency switch allows to start the ^{7}Li ramp 375 µs after the Na ramp has finished, already with a generous time buffer. The ^{7}Li ramp then runs from 805.831 MHz to 807.831 MHz.

For the case of fermionic ^{6}Li, the PLL also has to be set in the same time span, but the second channel is used, going into the lower-frequency mixers. Since everything besides the PLL source is separate from the microwave channel, the ^{6}Li transfer could actually be done in parallel, if a corresponding frequency source was available. Since the consecutive transfer did not pose any limitations, as it is done during a very low density setting, the short time of combining ^{6}Li atoms in $|3/2, -3/2\rangle$ with Na in $|1, 1\rangle$ does not lead to strong losses. Therefore, the ^{6}Li transfer also happens after the Na transfer, with the same sweep duration of 32.5 ms, and a frequency ramp from 230.178 MHz to 232.178 MHz.

The rather large frequency range was chosen in such a way that external influences on the magnetic field could be neglected. For smaller ranges (which allow faster transfer), the transfer sometimes was unstable, due to the strong-field magnet three flors above the lab, as discussed below. In fact, a basic magnetic field sensor was installed on the wall to monitor if the external field changed, so that the frequency of the transfer could be adapted. An active stabilization of the field at this point might be a helpful improvement.

RF Transfers at High Fields

The initial preparation in the absolute ground state $m_f = +1$ or $m_f = +1/2$ defines the start point for all further experiments where other Zeeman states are accessible by a spin flip. For low magnetic fields, this corresponds to a coupling of the total angular momentum Zeeman substates $|m_f\rangle$, while for high fields in the Paschen-Back regime, these transitions correspond to a flip of the nuclear spin while the electron's spin is decoupled and conserved.

The state preparation can be done in two ways, depending on the time scale necessary. If the timing is critical, i. e. the transfer has to be done as fast as possible, Rabi oscillations are driven with a resonant pulse. At high fields, the transitions between the Zeeman substates are far detuned due to the quadratic shift, therefore a resonant π pulse can transfer the whole population of one state to another.

RF Transfers at Low Fields

At low magnetic fields (< 1 G), the frequency difference between the transitions in the bosonic species allows only to couple all three states simultaneously, giving rise to three-level Rabi oscillations. [86] A transfer to a pure $|1, 0\rangle$ state from $|1, 1\rangle$ is thus not possible at low fields. The state evolution of a three-component spinor during a Rabi coupling is shown in Figure 3.18 for the resonant (left) and off-resonant (right) case.

For most of the experiments investigating spin dynamics, this transfer was the final preparation step, since a coherent coupling of all states taking part in the process is needed. Therefore, the ability to drive this preparation reliably, is a key ingredient to the study of the spin dynamics.

Figure 3.19 shows a typical example of the Rabi driving for sodium atoms at 96.9(3) mG, with a driving frequency of 68.060 kHz. At this frequency, the driving can be done directly with the function generator; no amplifier is necessary to achieve a sufficient coupling strength.

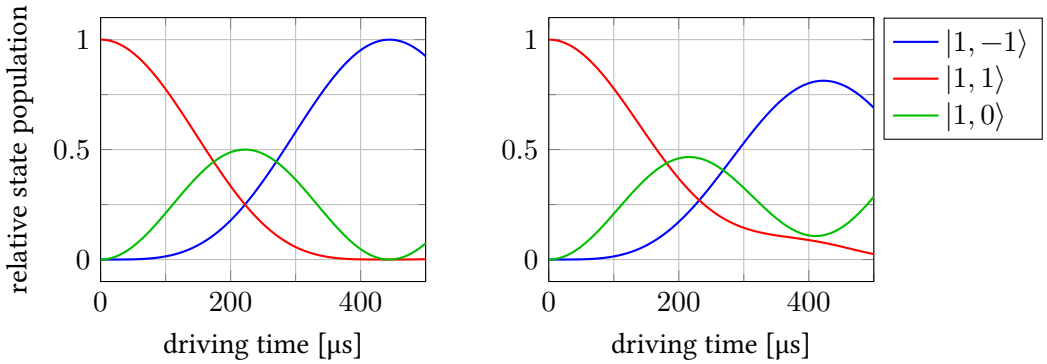

Figure 3.18: Calculated 3-level Rabi oscillations of Na at 500 mG on resonance (left) and with a small detuning (right), starting in $|1,1\rangle$. The chosen Rabi frequency is 5 kHz, driving frequency 351.2 kHz (corresponding to the mean of the Na transition at 500 mG), and the detuning 2 kHz.

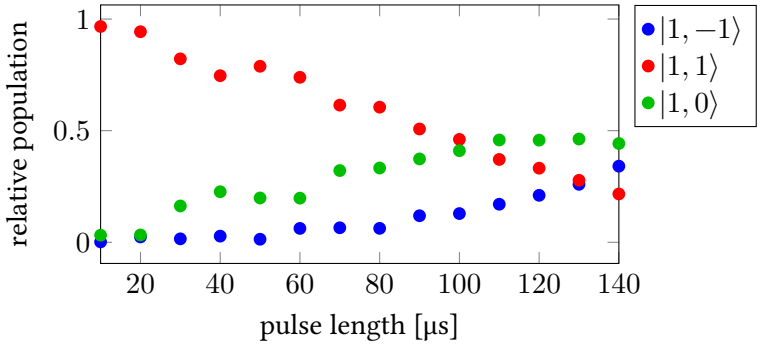

Figure 3.19: Rabi oscillations of Na at 96.9(3) mG, driven with 68.060 kHz and 10 Vpp set. The fitted Rabi frequency is $2\pi \cdot 1.7$ kHz.

Typically, the spin dynamics for sodium was investigated with zero magnetization; this requires a $\pi/2$ pulse which populates the side modes equally. Therefore, Rabi oscillations were driven up to a point of equal side mode population, indepenent of the $|1,0\rangle$ population, which would not be 50 % in the case of detuned driving.

For ^{6}Li, the necessary superposition between $|1/2, 1/2\rangle$ and $|1/2, -1/2\rangle$ requires only a two-level Rabi coupling, wich is a standard application in our setup. At low fields where the splittings of the sodium transitions and lithium transition get close to each other, one can drive both species simultaneously. Such a driving is shown in Figure 3.20, where the resonant driving is for ^{6}Li only, and sodium shows only a small far off-resonant coupling from $|1,1\rangle$ to $|1,0\rangle$, which vanishes already after a short time. This might be due to fluctuating fields and the weak coupling due to the detuning.

During this scan, the lithium atom number fluctuated strongly; still, the relative population shows an excellent coupling behaviour, which shows that with the strong, resonant coupling, a reliable state preparation is possible.

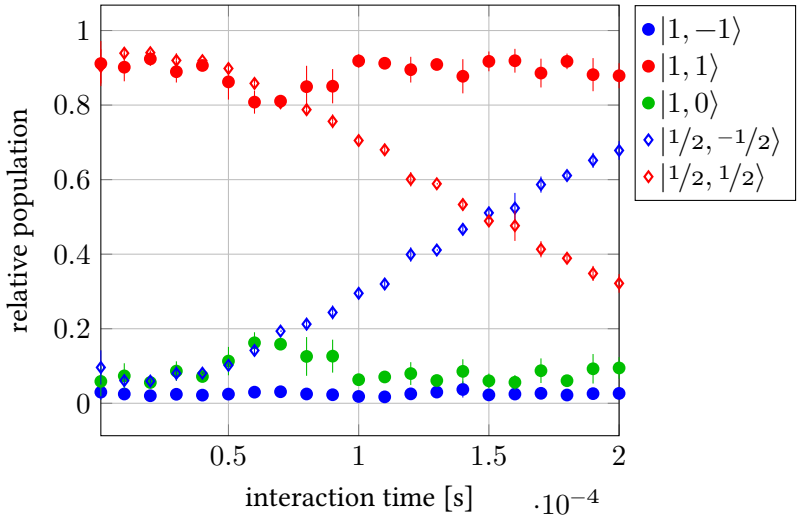

Figure 3.20: Rabi oscillations of both ^{6}Li and Na at 30.4(8) mG with strongly fluctuating ^{6}Li numbers; the Rabi fitted frequency for ^{6}Li is $2\pi \cdot 1.7(1)$ kHz. The relative population of ^{6}Li shows an excellent stability of the coupling. For Na, only a small population chang in the beginning of the driving happens. For coherent coupling of both species, therefore a much lower field is needed. Driving was done with 28.438 kHz, and 5 V_{pp} set on the function generator.

Disturbance of the Dipole Trap

The high power of the 100 W amplifier can induce disturbances onto the optical dipole trap regulation. Even the 1 W RF amplifier already can influence the regulation so strongly that further experiments are not possible.

As the dipole trap beams' power is monitored on photodiodes and actively regulated to this signal, any external influence on these loops will lead to decreased control over the atoms, mostly heating or complete loss. While most external signals can be easily shielded by high-quality cables, the radiation of the RF transfer cannot be shielded. This signal is picked up by the photodiode and detected by the regulation as a sudden rise in signal. The regulation thus reacts by lowering the power of the beams, ultimately even turning them off. After the RF power is off, the beams are turned on again and remaining atoms might be re-trapped. However, this procedure strongly heats the ultracold atoms and prevents further experiments. Figure 3.21 shows the result of the heating after time of flight for sodium.

To prevent this strong heating, a sample-and-hold circuit was implemented based on the LF398 chip. The chip is sampling during the whole sequence, while the hold TTL signal is connected to the RF switch so that it holds the latest signal before the RF pwer is turned on. Although the signal will drift slightly during the pulse, this effect is not detectable on the atoms, and the ultracold cloud is not getting heated. The right plot of Figure 3.21 shows the effect with the sample&hold circuit.

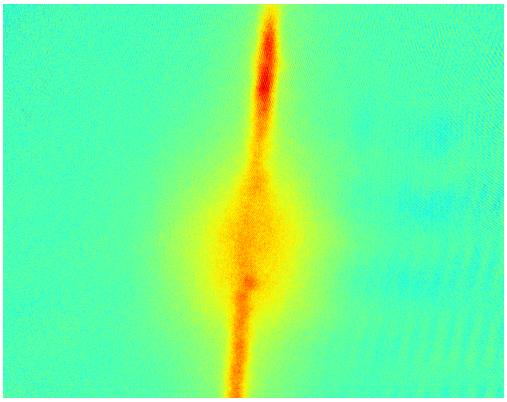

(a) Disturbance of the regulation leads to strong heating of the cloud; the atoms escape the dimple along the strong horizontal beam.

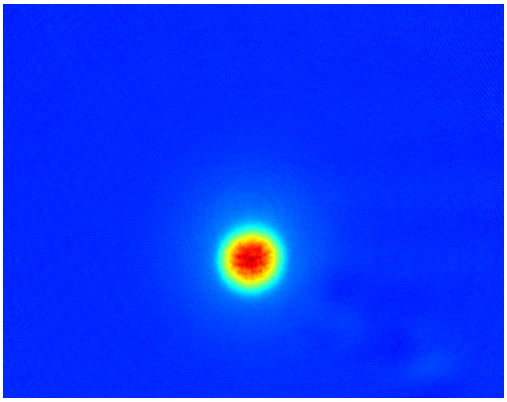

(b) Constant laser power with passive sample & hold prevents heating due to power fluctuations.

Figure 3.21: Effect of the strong RF radiation on the dipole trap regulation and heating of the atoms. Using sample & hold circuits, the disturbance can be greatly reduced.

3.3 Magnetic Field Control

One of the key ingredients for ultracold quantum gas experiments is the control over magnetic fields. In our case, there are two very different scales of field strengths: The Feshbach resonances studied in this thesis are at fields which are several orders of magnitude higher than the earth's magnetic field (roughly 0.5 G in Heidelberg), ranging up to 1000 G.

The quadratic Zeeman shift, which plays a role in the spin changing collisions, however, requires much lower magnetic fields: For the experiments of coherent spin exchange, the required magnetic field is on the same order as the earth's field, or even orders of magnitude smaller, with the lowest field used in our experiments of 6 mG.

The main challenge for stable high fields is a very precise control of high electric currents (electro magnets have to be used, since permanent ones are not flexible enough) which requires a coupling of fine regualtion electronics with high power currents that range up to 400 A.

For the low fields, the currents are in a less demanding range of about 10 A, but external influences are much more critical. These external factors range from temperature drifts in the lab, over relatively large gradients from ion pumps' magnets, to a residual magnetic field caused by a 17 T (170 kG) magnet located in a lab three floors above our experiment.

The following section presents the techniques used to produce, characterize and apply the magnetic fields in the different scenarios.

3.3.1 Precise Stabilization of High Magnetic Fields

Our setup is an improved version of the one described in [102] which was already used to study NaNa and ^{6}LiNa Feshbach resonances [53, 92]. However, the field stability in that setup was rather bad, which made it impossible to resolve the narrow Feshbach resonances. The width could only be estimated indirectly by comparing the lifetimes around the resonances.

One of the main reasons to investigate the ^{7}LiNa resonances was a potential application for tuning the interspecies interaction. For this, the rough stabilization of the previous setup was far too bad, so a new, flexible and very stable implementation was needed. This new setup uses the same high-power parts as before, i. e. the same power supplies, coils, the current transducer sensor and the passbank.

Four main improvements increased the overall performance of the regulation circuit:

- New analog PID controller
- Digitally controlled gain factor
- Digital set value with high resolution
- Highly stable read-out resistors

A sketch of the new setup is shown in Figure 3.22. The principle of the setup is rather simple: Two power supplies connected in series provide the needed voltage to drive the coils. In total, 33 V are available. The current is measurend by a current transducer; this signal is read by the analog control circuit and the manipulated variable is the voltage on the gates of 32 power MOSFETS in parallel.

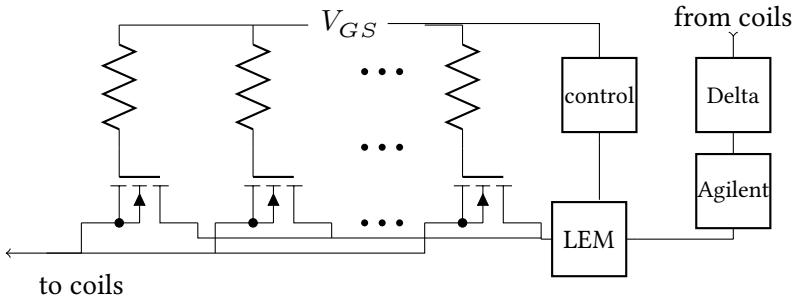

Figure 3.22: Setup of the passbank control with current sensor (LEM), control box including the Arduino, DAC board, sensing circuit and PID board, power supplies and connections to the coils. The circuit is capable of driving the embedded antibias coils for high fields or the offset coils for low magnetic fields. In the latter case, only the Delta power supply is used.

Digital Gain Setting

A major challenge for the optimization of the PID parameters is the highly non-linear response of the MOSFETs in the way they are used in our circuit. In the normal useage, one would adjust the voltage of the whole setup in such a way that the current through the MOSFETs is directly proportional to the applied voltage, resulting in a voltage-controlled current source. However, in our setup this would require a higher voltage drop over the MOSFETs, resulting in high power dissipation in the devices which can easily destroy them. Therefore, the voltage is chosen such that only a small voltage drop occurs over the passbank, reducing the dissipation to a manageable amount. Using the MOSFETs in this configuration, however, changes their response strongly while ramping the current up and down. Thus, the parameters for a stable PID loop would have to be adjusted for the different current stages. Elsewise, either the stability during the hold time is compromised, or the ramps become highly unstable.

Therefore, the fixed resistor of the final gain in the PID loop was replaced by a digital potentiometer. This way, the resistance and thus gain can be chosen low during the ramps, allowing a smooth increase and decrease of the current. During the hold time, the gain can be increased to stronger suppress fluctuations and thus increase the stability of the regulation. Figure 3.23 shows the regulation box with the analog PID control board and the digital potentiometer on the left side, attached to the board as replacement of the gain resistor. The rainbow colored flatband cable is the connection to the Arduino which resides outside the closed box to reduce the influence of the digital circuit.

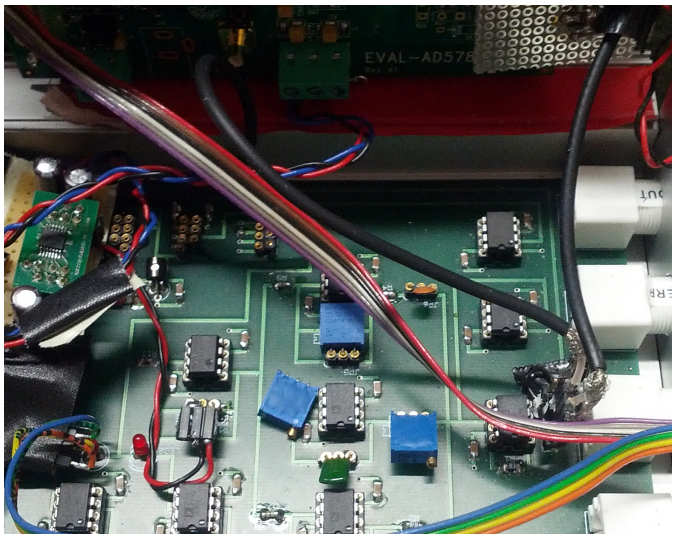

Figure 3.23: Photograph of the new passbank control circuit, showing the analog PID board below, the digital 10 Bit potentiometer on the left side, and the 20 Bit ADC on the top. Flatband cables connect the digital parts to the Arduino control.

DAC setpoint

The set signal for the PID control was improved in several steps compared to the old setup. In the original configuration, an analog signal from the experiment control was lead to the next room (the power supplies and passbank are in the *wohlfühloase* together with all high power electronics) and isolated from the common ground by DC/DC converters. These parts induced strong fluctuations on the signal, in addition to noise picked up by the long signal cable. Thus the first improvement was to use a stable fixed-voltage chip which was set a given value once for a sequence. The ramp-up was then still done using the analog channel, but for holding the signal was switched to the fixed voltage. This increased the stability greatly, but was not a very flexible implementation.

An improved solution was using a 10 Bit digital potentiometer for the set signal. The two ports of that potentiometer were connected to a positive voltage reference and the inverted negative voltage, which suppresses fluctuations of the reference. The output port then can give a very stable signal, which can be set by a microcontroller. Changing this signal quickly enables ramps of the current.

The full scale of the digital potentiometer for the set value should cover the maximum magnetic field achievable in the experiment, roughly 1200 G. The 10 Bit resolution then corresponds to a step size of 2.3 G since the potentiometer starts at maximum negative voltage, effectively reducing the resolution by 1 Bit. For any precise measurement of Feshbach resonances, this resolution is by far not sufficient, which is the reason that a 20 Bit analog to digital converter (ADC) was implemented, allowing a resolution of 2.3 mG per step.

High Precision Readout Resistors

The final improvement was the replacement of the sense resistor: The current is measured using a current transducer LEM IT600-S that gives a secondary current proportional to the primary one in the ratio of 1:1500. This smaler secondary current can be transferred into a voltage by a resistor. For a primary current of up to nearly 400 A, this means a current of up to 250 mA in our setup. The largest possible resistor, limited by the transducer's ability to drive the secondary current, is 20 Ω. This also means a dissipation of over 1 W which leads to heating of the resistors. Thus special resistors with very low temperature dependence (Vishay Dale Y1746-10ACT-ND, 0.05 ppm/°C) were used, and five of them with 100 Ω are installed in parallel to distribute the total power.

All these improvements lead to a strongly increased field stability for offset fields of up to 1200 G with a FWHM of the spectroscopy signal as low as 2 mG over the whole range. The long-term stability is on the order of 10 mG and might be given by external influences.

Control and Programming

The control chain starts with the experiment control which transmits the desired DAC value, ranging from 524,288 (corresponding to 0 V set voltage) to 1,048,576 (10 V); negative voltages are not meaningful since the current is uni-directional. Due to the necessary ground isolation, the normal serial interface could not be used, thus a one-channel digital interface with an optocoupler transmits both the value and serves as trigger for the ramps during the experiment. Figure 3.24 shows a sketch of the control chain. Both the DAC and the digital potentiometer are programmed via standard SPI commands, transmitted through high-speed optocouplers (HCPL-2631). Due to their high bandwidth, the communication is only limited by the calculations for each voltage step in the Arduino loop.

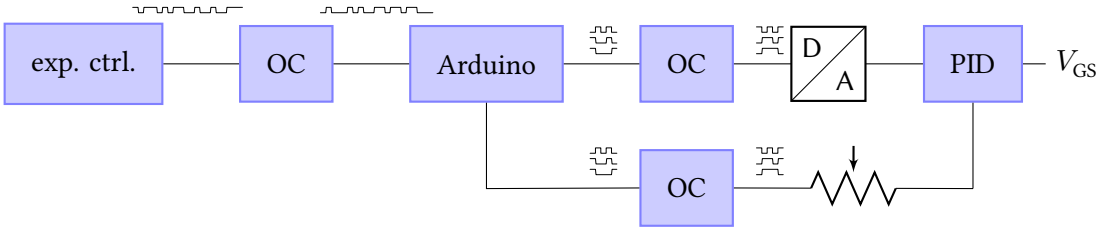

Figure 3.24: Sketch of the signal chain for the passbank control. The experiment control transmits one number to the Arduino, which controls the DAC and the digital poti that sets and adjusts the PID loop. The output voltage V_{GS} is the gate voltage of the passbank MOSFETs. The optocouplers invert the signals which has to be taken into account for the Arduino programming.

Once the Arduino is triggered, it writes a voltage ramp to the ADC, one value about each 100 µs. The ADC is also decoupled from the Arduino via optocouplers, as is the digital potentiometer. The latter one is set to a low value before the ramp, and to a high value after the final voltage has been reached. For the downward ramp to turn off the currents in a controlled way, the potentiometer is again set to a lower value to allow a smooth ramping behaviour. The rampdown typically happens within 5 ms to 20 ms.

3.3.2 Active Stabilization of Low Magnetic Fields

Now, we will turn to the other extreme of magnetic fields: The stabilization and control of fields up to 5 orders of magnitude smaller than the ones discussed in the last subsection.

The simplest approach of achieving a very low magnetic field would be the complete shielding by high-permeable alloys (Mu-metal), which can provide a nearly field-free region. But it would also block the complete optical access and would not allow any further manipulation of the atoms. Therefore, this standard approach in other scientific machines cannot be applied to our setup. This leaves only coils as tools again, which have to compensate the external fields.

For the low magnetic fields, there are several challenges that have to be overcome in comparison to the high-field case. The easiest challenge is a stable current source, since only around 10 A of current are needed, which is a convenient order of magnitude for a home-built current source. Assuming the same order of current stabilization of about 10^{-5}, as has been achieved for the high-field circuit, this implies a current-noise limited stability of 10 µG at an absolute field of 1 G.

However, spectroscopic measurements of the magnetic fields result in much broader signals of up to 2 mG in width, and long-term drifts of even larger values. The widths of the spectroscopy is partly given by the 50 Hz field that is always present near any AC line and cannot be shielded easily.

Flux Gate Sensor

Since 50 Hz is comparably very slow for the electronic circuit used to control the coils, an active compensation of this influence is possible, as implemented and shown in [33]. This setup consists of a highly precise three-axes flux gate sensor (MAG-03MS1000) which gives an analog voltage signal proportional to the magnetic field. The circuit to read out this sensor consists of an offset subtraction, as well as filters and an amplifier, all optimized for lowest noise, so that the limitation stems from the magnetic fields and not the electronics.

The results of this implementation are shown in Figure 3.25, where the signal of the sensor is plotted with and without the active regulation. The 50 Hz AC field is clearly suppressed; the step answer at the beginning shows the time scale on which the circuit can react.

The remaining parts of the setup are similar to the high-field regulation: An analog PID controller regulates the voltage of power MOSFETs on a passbank. Only this time both p- and n-channel MOSFETs are used to provide positive as well as negative currents. Four devices in parallel are sufficient to drive the rather low current of 10 A, with one additional channel that can drive up to 30 A and is used for larger fields. Details of the performance of this setup can be found in [33]; an improved circuit for the readout was also developed and will be used in future experiments.

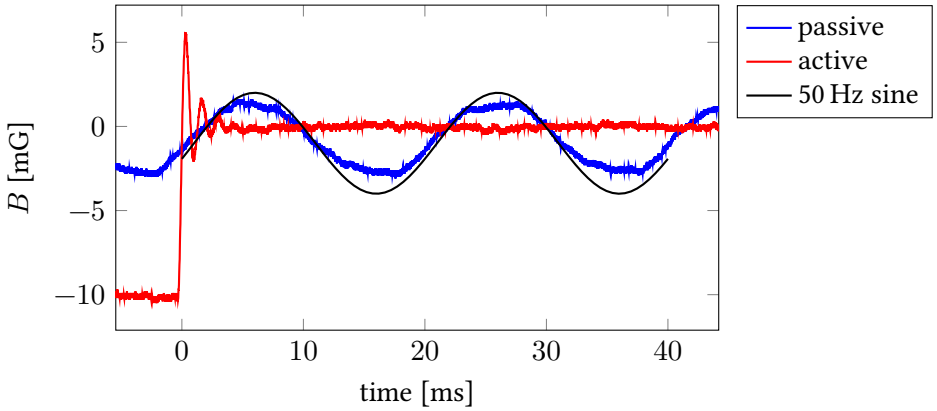

Figure 3.25: Measured magnetic field without (red) and with (blue) active field stabilization. The jump at 0 ms indicates a step answer of the stabilization and shows the reaction time. The 50 Hz signal that is clearly visible in the passive measurement is strongly suppressed with the active regulation. For comparison, a 50 Hz sine is added. Data from [33].

Integration Into the Experimental Cycle

While the active regulation was working very well, it is rather difficult to integrate into the full experiment, since the coils used for the active regulation are also used passively in several steps of the experiment: At the very beginning of the MOT loading, they are used to adapt the MOT position to the minimum of the magnetic trap to improve the loading and reduce heating of the atoms. At a later stage, the offset coils are used to provide the field for the microwave transfer to the ground states, and they were also used to provide additional sweeps for the Feshbach studies.

This list of passive regulations made it necessary to include a switch between passive and active regulation. For the passive regulation it turned out to be the most stable operation if the experiment control's analog output was directly connected to the gates of the MOSFETs, without any current sensing and regulating. This results in a non-linear response of the field to the applied voltage, which did not impose any problems.

The combination of the passive and active control was implemented using a box with four relays switching between the experiment control and the analog PID output. The moment of switching is critical since the analog PID typically will be saturated during the sequence as the magnetic trap produces fields way above the range of the sensor and the amplifying circuit.

In the final version of the coil control used for most of the spin dynamic experiments, only two directions were actively controlled and set to values that cancelled the magnetic field in these directions. For the third direction, z, the passive control was sufficient, since in this direction (conveniently it is the one along the horizontal dipole beam which already is the quantization axis for all experiments) external disturbances were the lowest. This allowed to set the z direction to a high value to define the quantization axis, then switch the x and y directions to active field cancelling, and finally ramp to the desired total offset field.

Field Gradients

One of the most challenging influences is given by magnetic field gradients. So far there is neither a direct measurement of gradients possible, nor is a compensation implemented in the setup. The existence of a large gradient could easily be found with a standard Hall probe that showed field difference of about 300 mG from the lower right to the upper left corner of the glass cell, translating to a gradient of roughly 30 mG/cm.

This gradient has an indirect and a direct influence on the experiments: Indirect, as the sensor is not at the position of the atoms. Therefore, a cancelling of the fields using the sensor signal would produce some different field for the atoms. This means that the compensation has to be set to some finite fields where the values have to be found using time-consuming spectroscopies.

The direct effect of the gradient regards the inhomogeneity of the field over the extend of the atomic cloud. This can directly be seen by the formation of domains as discussed later, which would not be possible in the antiferromagnetic sodium in homogeneous fields. Also, for the planned spin dynamics in the combined Fermi-Bose mixture of ^{6}LiNa, this gradient can induce a large energy scale, preventing any coherent dynamics.

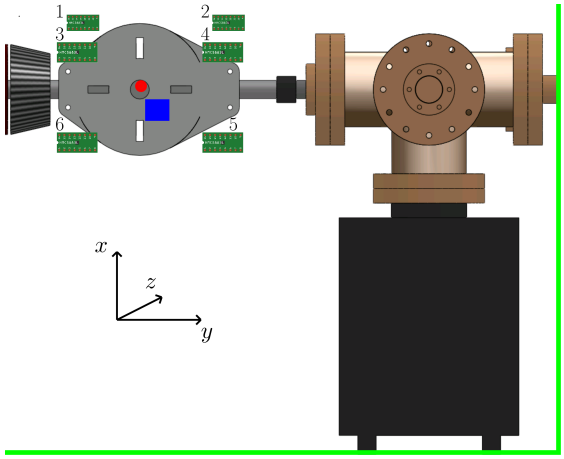

Figure 3.26: The large magnet (black) of the ion pump near the glass cell (between the grey coil holders) causes a strong magnetic field gradient at the place of the atoms (red circle). Active stabilization is based on the fluxgate sensor (position indicated in blue) and monitored with the six magneto-resistive sensors. The bias coils, indicated by the green lines, are larger than all other length scales and cannot compensate a gradient. The coordinate system indicates the axes as referred to in the text.

Several sources for gradients could be found, but one is dominating the whole setup: The strong permanent magnet of the ion pump which is rather close to the glass cell; the setup is shown in Figure 3.26. When the system was built, it was not designed for low-field experiments, therefore no special care was taken about this magnet, as it did not interfere with any previous experiments so far. For further, better-controlled spin dynamics, this magnet's field has to be compensated or shielded – this will be implemented in the next few months.

The figure also shows the coordinate system used to denote the magnetic fields. For both the Feshbach studies as well as the spin changing collisions, the quantization axis is given in the z

direction. This is done by either applying a high field using the *antibias* coils, thus all other magnetic fields can be neglected, or by actively cancelling the latter ones, as is needed for the low-field studies.

3.3.3 Calibration

To get a knowledge about the magnetic field at the place of the atoms, spectroscopy between different states is the standard tool in cold quantum gases. This spectroscopy makes use of the magnetic field dependence of the hyperfine transitions, which are mostly very well known. The concept is then to ramp to the field which should be calibrated, apply a microwave/RF pulse or sweep and detect the ratio of transferred atoms. For the latter one we use typically the Stern-Gerlach imaging explained below, at low field.

Since the field range applied in the experiments of this thesis spans about five orders of magnitude, the corresponding spectroscopy tools have to be equally versatile.

For the spectroscopy of high magnetic fields, typically the transition from $|1,1\rangle$ to $|1,0\rangle$ in sodium is driven, except for the 905 G resonance. In that case the spectroscopy is between $|1,-1\rangle$ and $|1,0\rangle$ since the $|1,1\rangle$ state suffers from the resonant losses. A transition to the $|f=2\rangle$ manifold is not possible for these fields as already above 190 G the necessary frequencies are too high for the microwave setup.

For fields below 0.1 G, on the other hand, Zeeman transitions are not useful for calibrations since the frequencies get very low, and the two transitions $|1,1\rangle \Longleftrightarrow |1,0\rangle \Longleftrightarrow |1,-1\rangle$ are not clearly separated, making the evaluation problematic. Therefore, at low fields the $|1,1\rangle$ to $|2,2\rangle$ transition is more convenient. However, one has to take care not to hit the $|1,1\rangle$ to $|2,1\rangle$ transition which is also very close for small frequencies. Figure 3.32 shows the effect of coupling to all three possible upper states from $|1,1\rangle$.

For all calibrations, the spectroscopies are done iteratively, where the first scan uses high power and a rather broad frequency sweep, which can cover a large range of fields so that the resonance can be found easily even if the field is not well-known yet. Both the power and sweep range are then reduced until the transition frequency is clear enough. By reducing the sweep range by more than a factor of 2 in each iteration, the rough field settings can be found quite fast, since only one transfer has to be detected to go to the next-lower sweep range.

The final scan then uses no or only a small sweep; the power and pulse time are adjusted in a way that the transition is not saturated and the signal is not Fourier limited. This means if a resolution of 1 mG is wanted, which corresponds to 2.1 kHz, the pulse duration must be longer than 500 µs. Vice versa, a shorter pulse can be used to achieve a clearer signal if the field fluctuates too strongly.

A gaussian is fitted to the transferred ratio of atoms; the center value is attributed to the central field, while the widths of the gauss curve gives the fluctuations or scattering. Throughout this thesis, we use the full width at half maximum to indicate the width, instead of the variance.

The field is then calculated by inverting the Breit-Rabi formula; for all fields given in this thesis, the notation $901(2)$ mG means that the center field corresponding to the gaussian fit to the transferred atoms is 901 mG and the full width at half maximum is 2 mG.

An example for the very low-field calibration is shown in Figure 3.27. This setting shows the active stabilization with the offset coils as described below.

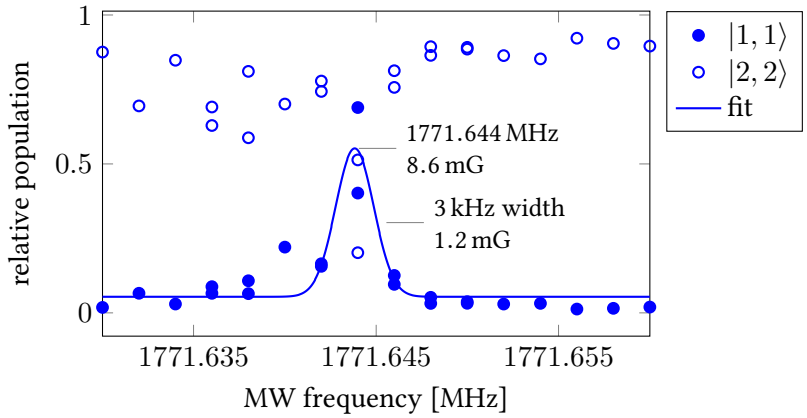

Figure 3.27: Microwave spectroscopy for one of the lowest field used in the experiments. Peak transfer is at 1771.644(3) MHz, corresponding to 8.6(12) mG. A 2 kHz sweep was applied during the 2 ms pulse. The uncertainty in the frequency denotes the full width at half maximum, not the error of the peak which would be ±1 kHz.

For intermediate fields of 3 G, using the offset coils passively-driven and the antibias passbank for the comparatively large field, spectroscopy can still be done with the RF transitions. Figure 3.28 shows an example where both Na and ^{7}Li were probed. The small difference in resonance positions is exactly the difference in the quadratice Zeeman shifts, as expected and calculated from the Breit-Rabi formula. This scan therefore also gives a direct measure for the detuning of spin changing collisions in the corresponding channels.

Note that the whole spectroscopy for all fields is done conveniently by the new microwave setup; with the old setup, frequency sweeps could not easily be applied. In that case, additional magnetic field sweeps were used to find the resonances.

The last example for a magnetic field calibration is given in Figure 3.29 to show the stability of high magnetic fields, in this case 120 G. This field was produced with the antibias circuit and used for the study of one of the Feshbach resonances of ^{7}LiNa.

3.3.4 Field Monitoring With Independent Sensors

Any active stabilization's performance can be increased – or at least monitored – with an independend set of sensors. In our case, additionally to the very precise, but costly, flux gate sensor, which requires a complex readout, we added a set of very cost efficient and still rather precise magnetoresistive sensors that can easily be read.

The Magnetoresistive Sensors

These sensors are based on the Honeywell HMC5883L sensor on a GY-273 breakout board and can be controlled and read out using a standard I²C interface. Each sensor has three perpendicular axes, so that the field direction and strength can be determined. Unfortunately, each chip and each channel has its own offset. It was not possible to calibrate each channel reliably, therefore absolute values could not be measured, but only relative changes in the field

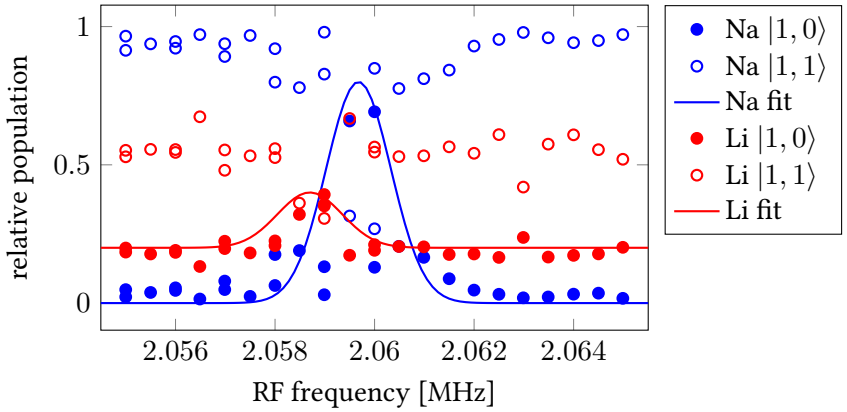

Figure 3.28: RF Spectroscopy of $|1,1\rangle$ to $|1,0\rangle$ in both Na and ^{7}Li in one run. The fit for Na results in a center frequency of 2.0597 MHz, for Li 2.0587 MHz. Both correspond to $B = 2.9358$ G. Full width at half maximum is for Na 0.34 mG, one of the lowest widths measured in our setup. Lithium suffers from a very high background noise and bad imaging quality, therefore the large offset in the $|1,0\rangle$ signal.

strength could be monitored. Still, a lot of important information could be drawn of these cost efficient sensors that were not accesible with only one very precise fluxgate sensor. The step size of one digital step is roughly one milligauss, so that at least the changes can be understood in absolute scales.

One of the drawbacks of the cheap sensors, however, is the communication protocoll: The sensors are read by an Arduino microcontroller, which only has one hardware I²C port. We did not want to rely on a software-based I²C, therefore the readout of the six sensors was switched using relays, again controlled by the Arduino. After getting a trigger from the experiment control, the microcontroller reads the values from each sensor as quickly as possible, switching the hardware I²C channel to each of the chips. This takes about half a second, meaning that only one value for each sensor can be read during one sequence.

The digital values read by the Arduino are saved together with all other data from the scan, as well as the analog value from the flux gate sensor. These voltages are taken by using a sample&hold chip which samples the voltage at the relevant time and holds it until the experiment control can read them at the end of the sequence. A synchronous reading during the sequence is not possible so far. Since the S&H chips suffer from a small decay of the voltage, the monitored signal at the end is not exactly the one measured at the sampling, but this does not pose any limitations.

Sampling an Over-Night Scan

Letting the machine run over one night and day and monitoring all sensors provided the data shown in Figure 3.30, where several features can be seen. The x-axis is the number of experiment cycles, which is roughly one minute each. For this scan, the field regulation was alternatingly active and passive. This means that each second shot is controlled by the flux gate circuit, while for the other ones just the passive control of the current was applied. Therefore two

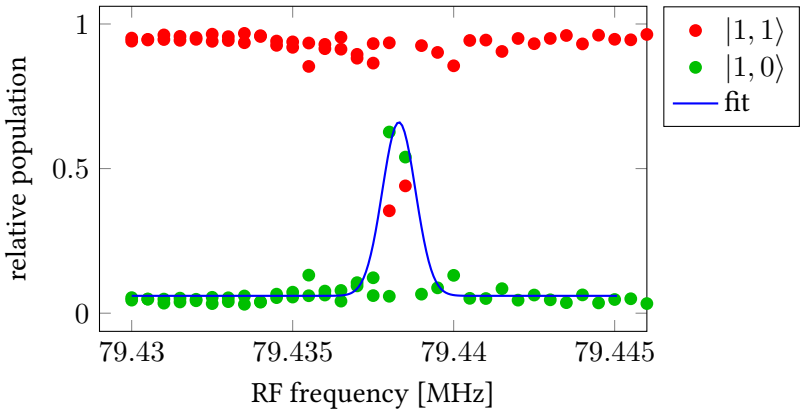

Figure 3.29: RF spectroscopy of sodium around 120 G where one of the ^{7}LiNa s-wave Feshbach resonances is located. The center frequency of the fit is 79.438 MHz, corresponding to a field of 120.174(1) G. The width of 1 mG is again given by the FWHM of the gaussian fit.

curves with the same color are shown, which are actually one dataset. The offset between these curves has no further meaning since it is just the difference in the set points. Unfortunately, the communication to some sensors or at least one of their axes broke after their installation, thus not all directions at all places could be monitored.

The Ion Pump

The most striking feature are the two peaks around shot number 1700. This feature was produced on purpose to prove a hypothesis: The big magnet of the ion pump strongly influences the field near the glass cell and the field depends on the temperature. For this, the magnet was heated with a band heater by about 3 °C over a few minutes, then the heater was turned off. Clearly visible is the fast increase of the field in all dimensions and on all sensors. The following decrease gives a rough time scale on which this part of the experiment thermalizes. This signal clearly shows that the magnet is a big problem and has to be shielded and, if possible, temperature stabilized. In fact, a temperature stabilization for the room air has been installed after observing this strong influence.

It is also clear from the sensor signals that the magnet causes a gradient since the different sensors are affected more or less strongly, with the most obvious signal in the sensor closest to the magnet. See Figure 3.26 for the position of the sensors relative to the magnet. Also, while the flux gate shows a complete compensation for the actively-regulated shots, the sensors clearly show a remaining effect or even an overcompensation.

The Magnet Three Floors Above

The second feature with a similar structure are the peaks around shots 1400 and 1500, which show the ramping of the strong-field magnet in our institute three floors above our experiment. While the disturbing influence is clearly visible in the passive data, the active regulation can mostly compensate the effect in the x direction. In the y-direction, on the other hand, it looks

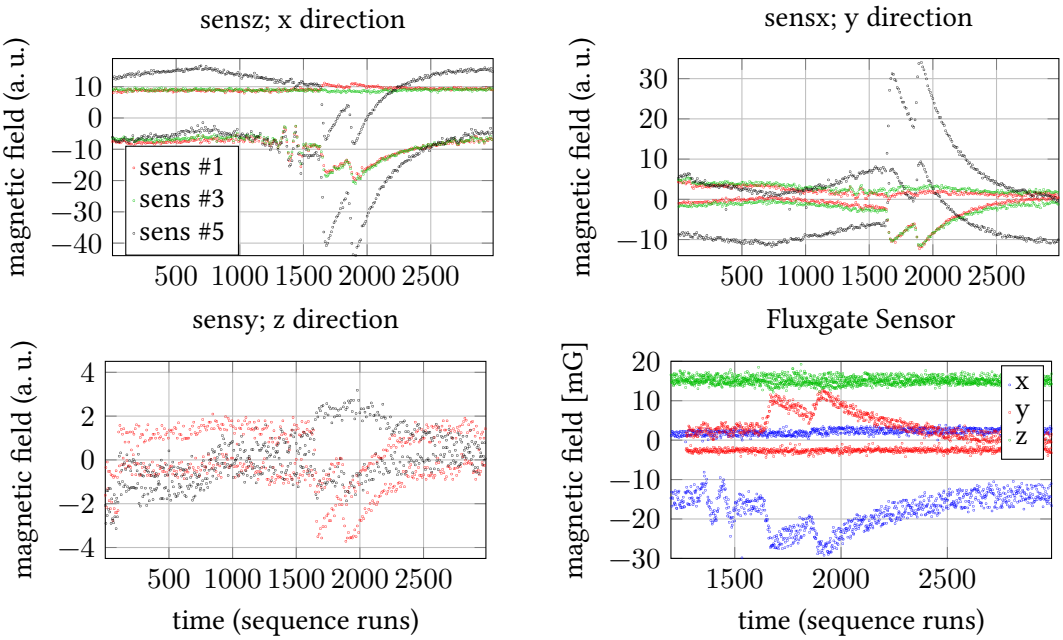

Figure 3.30: Data of the GY-273 HMC5883L magnetometers and the flux gate sensor over a time of more than 3000 experimental cyles. Data are shifted towards zero offset for better comparison. The four striking features are clearly visible: The jump around shot 100, the ramp of the 17 T magnet around 1400 to 1500, the heating of the ion pump's magnet starting around shot 1700, and the very slow drift over the whole measurement time with a peak around shot 700.

like the regulation over-compensates the influence and actually makes the influence stronger. This indicates a gradient, since the flux gate sensor shows a complete compensation.

Drift and Jumps

Finally, there are two less obvious features, which still limit the performance of the experiment. These are a jump at the beginning of the measurements, most prominently in the z direction. The reason for this jump is not known, but similar effects have been observed several times. We suspect an external influence that we did not yet find.

The second feature is a slow drift over the whole measurement time. This drift has been observed over several days, clearly following the room temperature. While one influence clearly is the ion pump, other sources of varying fields cannot be excluded. These drifts give another clear motivation for a more stable room temperature.

In total, these monitoring data show that the active stabilization is working well but is limited due to gradients. For a better performance, these gradients have to be eradicated at all or actively compensated by using another sensor so that gradient measurements and thus compensations are possible.

3.4 Atom Detection

As in most ultracold atom experiments, all information about the experiment is drawn from absorption pictures of the atoms. For this, a resonant laser beam is shone onto the cloud and imaged onto a CCD camera. The shadow gives space-resolved information about the atomic density, integrated along the beam path. For our two-species experiment, both beams come from the same fibre, go through the glass cell from above, and then are split using a dichroic mirror after the imaging lens. The reflected 589 nm light for sodium is detected by the first camera; the transmitted 671 nm light for lithium is reflected onto the second camera by another mirror. Only the objective lens system is used, without additional imaging optics in front of the cameras. This two-camera setup allows easy detection of both species independently.

For all experiments presented here that deal with spinor physics, the hyperfine state has to be resolved, but also for the Feshbach resonance measurements, where the state preparation has to be checked, as well as for the field spectroscopies.

This state-dependend detection could be done at high magnetic fields, where the imaging transition for the different hyperfine states is detuned. More convient, however, is using a Stern-Gerlach seperation where a magnetic field gradient splits the states with different magnetic moments spatially and allows simultaneous imaging of all states. In this way, relative counting of the atom numbers is possible and fluctuations of the total atom numbers have no impact on the relativly measured populations.

3.4.1 Absorption Imaging

Detection of the atoms is done using a standard absorption imaging technique. [51, 52] The atoms scatter photons from the beam, leaving a shadow image. A second laser pulse is used as a reference, and by taking the logarithm of the divided picture, one gets a signal that is proportional to the atomic column density, which is integrated along the imaging beam direction.

Normally, the imaging is done at low magnetic offset field, especially for the spin-dynamics, since then all magnetic hyperfine substates can be imaged simultaneously. For the investigation Feshbach resonances, in contrast, it is useful to be able to image the atoms directly at the high offset field, without the need to ramp down, which takes time and can cause additional strong losses (in case of a broad resonance in-between) or blurr any further structure that one wants to observe.

Therefore, in addition to the normal low-field imaging, for both species a high-field imaging is present. For lithium, it consists of an additional diode laser that can be offset-locked to the spectroscopy laser. [102] This setup is very flexible and allows imaging of lithium atoms at all accessible magnetic fields in all states.

In the case of sodium, laser sources are very expensive, therefore a different approach is used: By shifting the frequency only with an AOM and using the right transition, one can enable an imaging around the 905 G resonance in the $|1, 1\rangle$ channel, which is one of the reasons for the longer investigation of this resonance instead of the somewhat broader 1202.6 G resonance in the $|1, -1\rangle$ state. For both high-field imaging systems, a repump beam is not necessary, since the transitions are mostly closed and enough photons can be scattered for a sufficiently clear signal.

3.4.2 Stern-Gerlach Separation

The state-dependend mapping relies on the spatial separation of the different Zeeman substates. The easiest way to achive this is to apply a gradient magnetic field, since as mentioned in subsection 5.4.2, the energy of an atom with total spin **F** depends on an external magnetic field. Therefore, an inhomogeneous field exerts a force on the atoms:

$$E_Z = -\mu \cdot B \Rightarrow \mathbf{F} = -\nabla E = \mu \nabla B \tag{3.1}$$

So by applying a field gradient onto the atoms, different spin states experience a different force and can be separated during the free expansion after release from the trap.

Finetune Gradient Mapping

In the experiment, there are two possible ways to apply a field gradient perpendicular to the imaging direction: In the first configuration, only one of the finetune coils is used. This method also directly offers a finite and defined offset field which prevents uncontrolled spin flips. Since the inductance of the finetune coils is rather low, this gradient can be turned on (important to observe fast spin dynamics) and off (important for zero-field imaging) quite fast and has been used for many years in previous experiments of our setup.

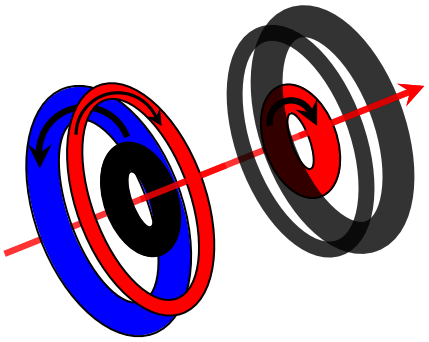

Figure 3.31: Finetune (inner large coils) and MOT (small curvature coil on the right-hand side and outer large antibias coil on the left-hand side) gradient configuration for Stern-Gerlach separation. Arrows and color indicate the current direction. Black coils are not used in these configurations. The red arrow indicates the propagation direction of the horizontal dipole trap beam.

MOT Gradient Mapping

While the finetune mapping has certain advantages, it suffers from the low gradient which does not allow for a very clear separation especially of the ^{6}Li atoms. The limitation stems from the connected power supply and the maximum possible current. Using the second coil would be possible, but the gradient would only increase by a factor of two, while the advantage of the offset field would vanish and the switching circuit would become more complex.

Therefore, another scheme was used, exploiting the readily available MOT configuration. Contrary to the MOT situation, where only a few amps are applied, a high current can be used

in this circuit, since the limiting element is only the diode (see Figure 3.4) which can withstand short peak currents of much higher value than the constant current limit.

The high gradient that is possible in this configuration allows a very clear separation of all spin states of the three species. The gradient is roughly 1 G/cm/A, and up to 225 A can be applied. A typical setting would result in a calculated gradient of about 45 G/cm, compared to a maximum of 3.9 G/cm that can be produced by the finetune configuration.

But of course this high gradient setting also comes with a price: Due to the high inductance of the curvature and antibias coils, the current cannot settle during the short pulse duration of a few ms. Also, since the coils are not symmetric, the field is neither a pure gradient, nor pointing directly in the direction of the offset field that defines the spin dynamics. This causes problems at very low fields since the atoms can undergo spin flips, making a clear mapping impossible. Third, turning off the field also is slow and thus can cause a detuned imaging. Since the detuning then is different for the magnetic substates, this may even have an influence on the measured magnetization.

Figure 3.32 shows a typical picture of the MOT gradient mapping. Clearly separated are four clouds of atoms, resulting from a microwave spectroscopy that coupled the $|1,1\rangle$ ground state to the three possible upper states $|2,0\rangle$, $|2,1\rangle$ and $|2,2\rangle$ via a 2 ms frequency sweep from 1771.65 MHz to 1771.75 MHz at an offset field of 50(3) mG. The ring-shaped structure results from a detuned imaging cause by residual magnetic fields.

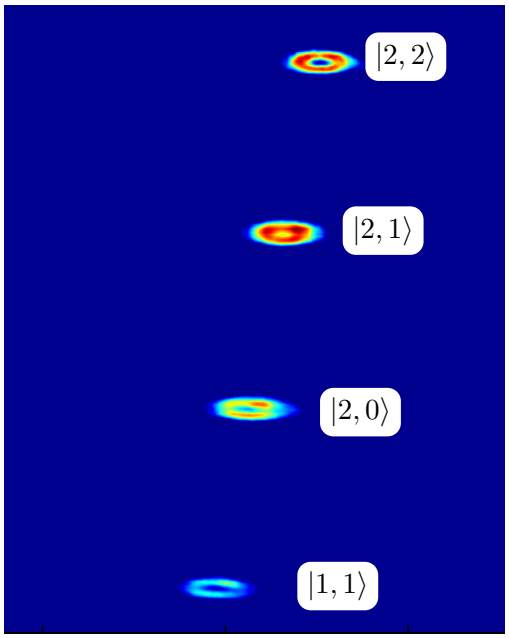

Figure 3.32: Stern-Gerlach separation of sodium atoms after coupling from $|1,1\rangle$ to all possible $|f=2\rangle$ states. Clearly visible is the vertical as well as slight horizontal shift. The spatial distribution of each cloud indicates a detuned imaging.

The mapping sequence for this shot was the following: Directly after the MW pulse has finished, first the horizontal optical dipole trap beam is turned off to reduce the optical density for Na as much as possible into the now free direction, leading to the ellipitical shape of the cloud. Since the second ODT beam is diagonal to the imaging direction, the atoms actually propagate along this tilted axis, and are pulled by gravity to the left side of the picture.

The vertical dipole trap beam actually runs under an angle of 45 ° into the picture plane, thus the atoms also expand under this angle and not perpendicular to the imaging axis.

After 1 ms of expansion, also the second dipole trap beam is shut off, and the MOT gradient is turned on for $t_{\text{grad}} = 1.125\,\text{ms}$ and turned off again. Here, the current was set to 20% of the maximum value, allowing for a longer time of flight than with the full current. After the turn off, the sodium atoms expand freely for $t_{\text{tof}} = 7.875\,\text{ms}$ before imaging starts with optical pumping into the $|2,2\rangle$ state and imaging 125 µs later.

To verify that the currents in the coils can follow the applied set voltages, one can calculate the expected seperation of the clouds and compare with the observation. The atoms are only accelerated during the application of the gradient, and flying freely after that; taking a gradient of $B' = 45\,\text{G/cm}$, the total displacement due to the gradient can be calculated as

$$\Delta x = \frac{\mu B'}{2m}\left(\left(t_{\text{grad}} + t_{\text{tof}}\right)^2 - t_{\text{tof}}^2\right) = 1\,\text{mm} \tag{3.2}$$

with the Bohr magneton μ. The observed separation of the $|1,1\rangle$ and $|2,0\rangle$ state in Figure 3.32 is about 810 µm in (from the point of view) vertical direction, i. e. along the horizontal dipole trap beam. Comparison of these two values leaves three different interpretations:

1. The gradient is only 35 G/cm,
2. the gradient is not only in the direction of the dipole trap beam, but also perpendicular and possibly also along the imaging axis, which cannot be resolved,
3. the coils are not fast enough to allow the strong current in the short time where the voltage is applied.

None of these possible effects has a direct impact on the performance of the experiment, but one has to keep them in mind if the settings are changed. Especially for the lithium mapping, where an even greater gradient is applied, the coil current might be too slow to vanish after the set turn off, which might lead to additional detuning in the imaging.

For most experiments, the parameters of coil current ramps and time of flight could be chosen in a way that a reliable mapping was possible. Unfortunately, a strong gradient that clearly separates the lithium atom clouds, accelerates the sodium too strongly, driving it out of the field of view of the camera too fast. Therefore, the possible time of flight of sodium is too short and the cloud becomes too optically dense, preventing a precise atom counting. This is one of the reasons why in the heteronuclear experiments, the effect of lithium onto sodium is not detectable and thus all experimental results on magnetization transfer from one species to the other can only be found in lithium.

To improve the situation, one could apply a second gradient opposing the first one to decelerate the sodium atoms strongly enough. This was tested with the finetune gradient, since it points against the MOT gradient, but the effect was much too weak.

3.4.3 Mapping Problem

Achieving a stable operation at very low magnetic fields poses a set of challenges, even if the field itself can be precisely stabilized. The main problem is to reach this field from a higher offset field, to keep the atoms in the prepared state, and being able to state-selectively detect the atoms, without influencing the state population in any unwanted way.

Ramping to and from the Final Field

The first and third point of this list boil down to the ability of adiabatically ramping magnetic fields. Especially at very low fields, zero-crossings have to be avoided, which is especially challenging if the coils are not in perfect Helmholtz configuration and therefore the different directions are (at least slightly) coupled.

For the initial preparation of a state at low fields, this is not a very crucial problem, since any field ramps can be executed very slowly, allowing the atoms' spins to follow any change of field direction adiabatically.

More demanding, however, is the mapping at the end of the investigated time scales. In the case of slow dynamics, it is possible to ramp up the gradient for the mapping, and the atoms again can follow, without changes of the populations. However, looking at the short-time dynamics is more critical, since then the field has to be ramped up fastly, might cross a zero point or change the direction too fast for the atoms to follow.

This was the case for offset fields below about 50 mG. For these fields, first the homogeneous offset field had to be increased, before the mapping gradient could be applied. Only then a reliable state detection was possible. Unfortunately, this prevents the observation of any short-time dynamics at the very low fields, which might be interesting for the ^{6}LiNa heteronuclear spin exchange process.

For the most successfull observations in the spin exchange processes which were done with sodium, however, the dynamics do not change critically below these fields, so that no important information would be lost. More sophisticated mapping sequences are possible, of course, where the gradient would be ramped more slowly up and down – also, a completely different state mapping without a spatial separation might be a future solution.

Parasitic Coupling

A major problem which was very time-consuming were stray RF fields in the lab that coupled the different Zeeman states unintentionally: For quite many magnetic field settings, a clear state preparation could be achieved, but after holding times of several hundreds of milliseconds – a typical time scale where the magnetic fields are allowed to settle before the experiment proper starts – atoms in other Zeeman states were detected. We dubbed this effect *parasitic coupling* and it will play a role in discussing the results of the spin dynamics experiments.

This effect clearly depends on the hold time and makes experiments with longer evolution times nearly impossible. Examples for this effect are shown in Figure 3.33 for fields of several hundreds of milligauss, and in Figure 3.34 for lower fields down to below 100 mG. Spectroscopies could only be done at the indicated fields, where no parasitic coupling was present or where it could be neglected.

Many RF sources in the lab were investigated, additional shieldings for several sources of radiation were installed, but none of these measures could reduce the observed effects. Several

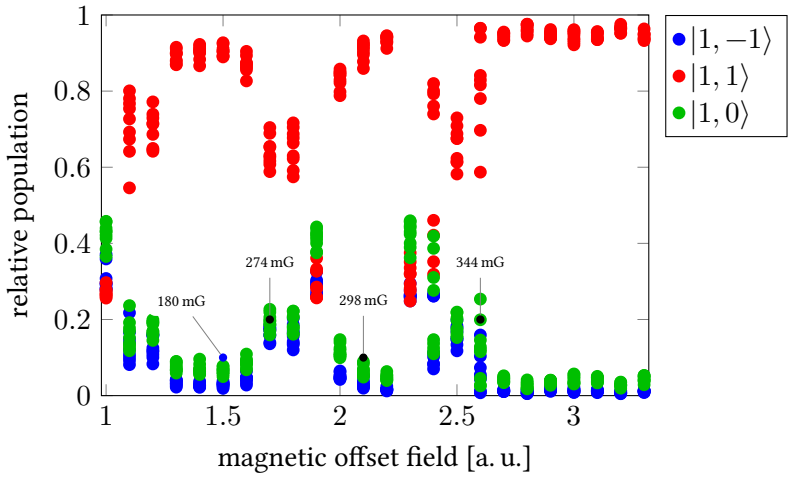

Figure 3.33: State population after a short hold time at different magnetic fields, showing the mapping problem; the fields roughly correspond to about 100 mG to 350 mG. Single fields are calibrated with the shown values; the fields with strong mapping problems could not be calibrated since a clear readout is needed for that.

power supplies of the coils were exchanged to also exclude influence from the applied magnetic fields, but in the end only avoiding certain offset fields could offer a stable state during longer hold times.

The main change between the data of Figure 3.33 and Figure 3.34 were different settings of the actively regulated coils in x and y direction. This shows that for the same absolute field value, the parasitic coupling can be stronger or not present at all. All of this made it especially challenging to find the right settings for very low absolute fields since the normal procedure of iteratively changing and scanning the fields was disturbed by the parasitic state populations.

Finally, one setting for the x and y coils could be found which nearly cancelled the fields in these directions and a scan with low offset fields could be done. Figure 3.35 shows the parasitic coupling effects at these fields, with the lowest spectroscopically measured field in our setup of 6 ± 2 mG.

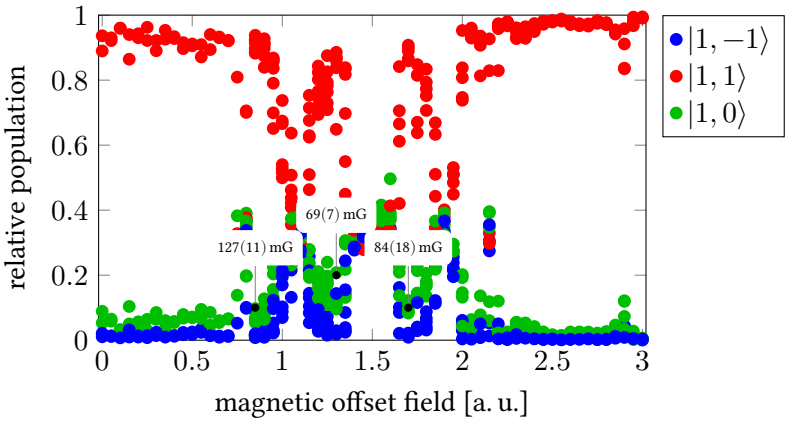

Figure 3.34: Mapping problem for lower offset fields in x and y direction. The scan shows that neither the absolute field nor the z value can directly be related with the mapping problem.

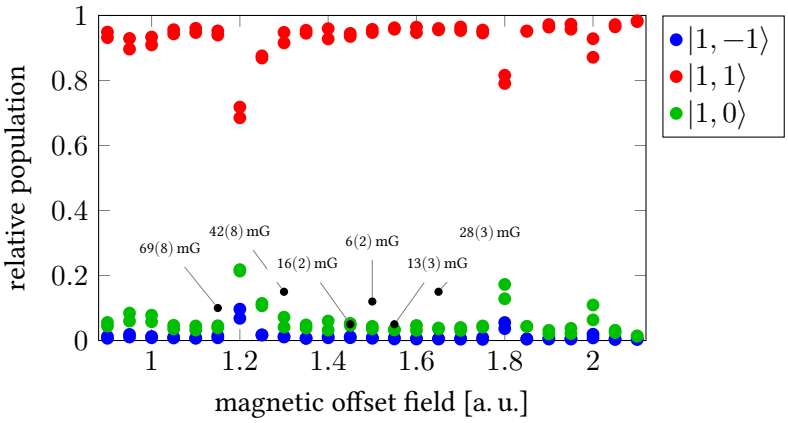

Figure 3.35: Mapping at the lowest fields realized, with fixed, actively regulated fields in x and y direction, scanning the passively regulated z direction. The lowest field calibrated in this sequence was at $6(3)$ mG. Finally, there are many low-field points with a reliable state preparation, holding, and detection possibility.

In the darkest times, hope is something you give yourself. That is the meaning of inner strength.

(Uncle Iroh)

4 Feshbach Resonances

The investigation of Feshbach resonances is an interesting field, since fundamental concepts of the quantum scattering theory can be shown and applied in a straightforward way, and it can provide very precise input for the calculation of interaction potentials. But in most cases in the field of ultracold gases, the search for Feshbach resonances is driven by the great amount of possibilities they offer for experimental atomic physics.

Due to the ability to tune the scattering length between atoms, Feshbach resonances provide a tool to investigate strongly interacting systems, suppress the interaction, or to reverse their sign. This enables the investigation of further few-body states as the Efimov physics, where the strong interactions cause three-body bound states without two-body bound states, or even higher few-particle states.[57, 19, 29, 80, 103]

Also moderate tuning can be of great use, as in [69], where a small change in the scattering length of one channel induces interesting non-classical many body physics.

Finally, the crossing of molecular levels with the atomic threshold that causes the resonance can be used to associate molecules, which enabled the study of the BEC-BCS crossover, and offers an intermediate step on the way to ultracold molecules, where especially the fermionic case opens a wide range of possible applications.

In this chapter, the first observations of the Feshbach spectrum of the bosonic mixture of ^{7}Li and Na will be presented. Additionally, the possibilities and limitations of interaction tuning in both homo- and heteronuclear Feshbach resonances is studied in respect to possible future use for tuneable impurity physics or spin dynamics.

Besides from this, the Feshbach studies provide important parameters for the fine tuning of the modelling of the interaction potential and therefore offer a more rigorous calculation of the scattering lengths which are an important parameter for the spin dynamics discussed in the next chapter. Finally, an understanding of the physical background of Feshbach resonances helps to understand where the coupling of the spin degrees of freedom comes from and how it could be influenced.

4.1 Physical Background

The diluteness and low energy of ultracold alkali atoms allow a very simple description of their scattering properties that can be expressed by one single number, the s-wave scattering length a: Since the interaction potential is spherically symmetric, any scattering can be decomposed into spherical waves. The discussion of this decomposition and the resulting properties of the

scattering are topic to each standard quantum physics textbook, therefore this section will point out the most important steps needed for the basic understanding.

4.1.1 s-Wave Scattering

The eigenstates of a spherically symmetric scattering potential of a point-like particle can be decomposed into the spherical harmonics

$$\Psi_k(\mathbf{x}) = \sum_{l=0}^{\infty} i^l (2l+1) R_l(r) P_l(\cos\vartheta), \tag{4.1}$$

with the angular momentum l in units of the Planck constant, R_l the amplitude of the partial wave with angular momentum l and the Legendre polynomials P_l. These polynomials provide an orthogonal set of eigenstates, thus coupling between the different harmonics is not possible.

The description of the scattering is based solely on elastic processes, therefore the amplitude R_l of each angular momentum has to be conserved, and the scattering can only affect the relative phase η_l of the incoming and outgoing waves. Due to the small extent of the scattering potential compared to the typical interatomic distance, the details of the potential do not play a crucial role. Therefore the phase evolution can be described by one effective number, and thus be compared to the scattering in a box potential, which results in the same phase shift, but offers a much simpler description.

In the asymptotic limit for the interatomic distance R, each scattering channel's wave function can be expressed by

$$\Psi_{l,k}(R,E) \to c\frac{\sin(kR - \pi l/2 + \eta_l(E))}{R\sqrt{k}} e^{i\eta_l(E)} \text{ for } R \to \infty, \tag{4.2}$$

where the phase shift η_l generally depends on the particle's kinetic energy $E = \hbar^2 k^2/2\mu$ and $c = \sqrt{2\mu/(\pi\hbar^2)}$ is a normalization constant with the reduced mass μ. k is the wavevector of the incoming particle.

For $l > 1$, i. e. scattering with a non-vanishing angular momentum, the rotation introduces an energetical barrier, preventing atoms with low energy to reach the scattering center; this is sketched in Figure 4.1. In the remainder of this thesis, we follow the usual convention to name rotational states with the labels $s, p, d, f, g, \ldots$ known from atomic spetroscopy, although their meaning *sharp*, *principal*, *diffuse*, *fundamental*, have no meaning here whatsoever.

This rotational barrier suppresses collisions with $l > 0$ for very low relative momenta, which is the case in the ultracold quantum regime that dominates basically all experimental stages discussed in this thesis. Therefore, the most important scattering channel is the $l = 0$ s-wave scattering. For the low momenta, corresponding to small wavevectors k, the phase shift parameter $\eta_0(E)$ depends on the kinetic energy via [78]

$$k\cot\eta_0(E) = -\frac{1}{a} + \frac{1}{2} r_0 k^2 \tag{4.3}$$

where r_0 is the extension of the potential and a is a constant. For small k, this expression can be simplified even further by neglecting the quadratic k^2 term, leading to

$$\tan\eta_0(E) = -ka. \tag{4.4}$$

Depending on the potential depth, η_0 can take any value from 0 to 2π, thus the so-called scattering length a can diverge from $-\infty$ to $+\infty$ and take any value in between. Even with a purely attractive potential, a positive scattering length can appear, which results in a repulsive interaction.

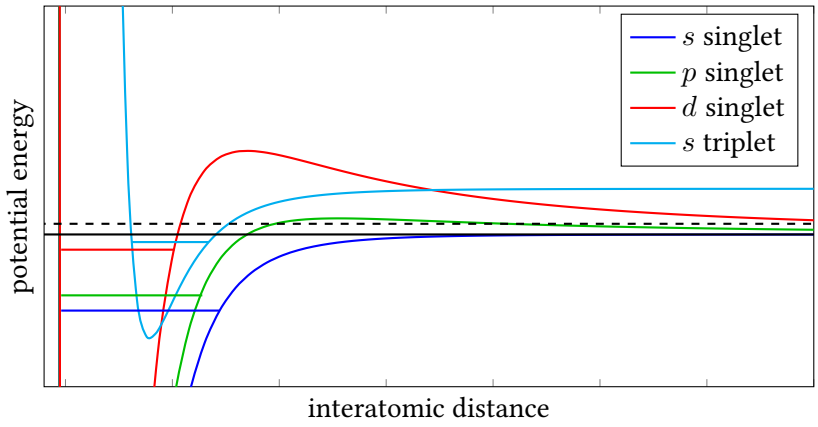

Figure 4.1: Illustration of the different molecular potential types causing Feshbach resonances: Atoms can enter in the lowest-lying open channel, inducing singlet s-wave or d-wave Feshbach resonances. p-wave resonances occur due to the coupling to the $l = 1$ continuum. The higher-lying triplet can cause resonances as closed channel.

Open and Closed Channels, Coupling

If the potential has a bound state, a Fano-Feshbach resonance can occur [31, 30, 27], in the remainder just called Feshbach resonance for brevity.

The crucial formula for the dependence of the scattering length on an externally applied magnetic field connects the background scattering length with the universal scaling which occurs near a Feshbach resonance, and gives a simple scaling:

$$a = a_{\text{bg}} \cdot \left(1 + \frac{\Delta\delta\mu}{-E_0 + i(\gamma/2)}\right) \tag{4.5}$$

The background scattering length a_{bg} depends on the full potential depth and is normally not easily accessible a priori, but can be calculated if the potential is well-known. The position of Feshbach resonances can be an important input parameter for the fine-tuning of the potential modelling.

E_0 is the position of the resonance threshold, and in the case of magnetically-induced resonances can be tuned by a magnetic field. Δ is the width of the resonance, defined as $\Delta = -\hbar^2/(2\mu r_0^2 \delta\mu)$.

Speaking about Feshbach resonances, two terms are often used in two different contexts: Narrow and broad. Typically one uses them to characterize the parameter Δ as the magnetic field difference between the zero-crossing of the scattering length and the divergence point. In this sense, both the famous ^{6}Li and the ^{7}Li resonances are very broad, since both show a

significant change in the scattering length over several hundreds of gauss. Examples for narrow resonances, in contrast, would be the ^{6}LiNa resonances with $\Delta < 10\,\mathrm{mG}$.

However, a more rigorous definition of *narrow* and *broad* is given by the resonance strength and depends on the universal behaviour shown by the resonance. Taking the lithium resonances again as example, one sees that for the ^{6}Li case the universal scaling is valid for a wide range between the resonance and the zero-crossing, while for ^{7}Li this is true only for a very small part. Quantitatively, the resonance strength is defined as

$$s_{\mathrm{res}} = \frac{a_{\mathrm{bg}}}{R_{\mathrm{vdW}}} \frac{\delta\mu\Delta}{E_{\mathrm{vdW}}} \tag{4.6}$$

with the van der Waals radius R_{vdW} of the interaction potential and the corresponding energy $E_{\mathrm{vdW}} = \hbar^2/(2\mu R_{\mathrm{vdW}}^2)$. A large parameter $s_{\mathrm{res}} \gg 1$ denotes a broad resonance, which is largely dominated by the open channel. In contrast, narrow resonances are closed-channel dominated and show the universal scaling only over a small range of Δ, which in turn also often is rather narrow itself.

This constraint about the universal scaling has to be kept in mind when the tuneability of the resonances is discussed below. For simplicity, for that discussion the resonance strength parameter is neglected and a universal behaviour is assumed to estimate an order of magnitude for the tuning possibilities. A rigorous measurement or full coupled channels calculation would be needed to provide a more reliable prediction of the scattering length dependence on the magnetic field.

4.1.2 Connection of Scattering Lengths

The exact numerical values of each scattering channel have to be calculated using the full interaction potential. But for a basic understanding of the underlying physical properties and mechanisms and also approximate results, one can project the molecular states F, M_F onto the electronic basis states $S = 0, 1$. The scattering lengths of these states then add up according to the relative decomposition and give an approximate scattering length for this molecular state. This results in the $a_{F=0,1,2}$ parameters often used to describe spinor physics, as will be the case in chapter 5.

From these molecular state scattering length, the interaction strength for each single atomic channel can be calculated by another decomposition using the commonly known Clebsch Gordan coefficients.

To calculate the decomposition of the molecular states into the electronic singlet/triplet states, one has to couple four spins. The well-known case of coupling two spins makes use of the Clebsch-Gordan coefficients. In analogy to this, for four-spin coupling, the Wigner 9-j symbols [47] have to be used, given by:

$$\sqrt{(2j_3+1)(2j_6+1)(2j_7+1)(2j_8+1)} \begin{Bmatrix} j_1 & j_2 & j_3 \\ j_4 & j_5 & j_6 \\ j_7 & j_8 & j_9 \end{Bmatrix} \tag{4.7}$$

$$= \langle ((j_1 j_2) j_3, (j_4 j_5) j_6) j_9 \,|\, ((j_1 j_4) j_7, (j_2 j_5) j_8) j_9 \rangle \tag{4.8}$$

In our case, the coupling involves two nuclear spins i_1, i_2 and two electronic spins s_1, s_2 that are coupled to the atomic hyperfine states f_1, f_2. The three sets couple to the total nuclear spin I with projection M_I, total electronic spin S with projection M_S and total angular momentum F, $M_F = M_S + M_I$.

Using this notation, the molecular state $|f_1, f_2, F, M_F\rangle$ can be decomposed into the sum over all S,I,M_F:

$$|f_1, f_2, F, M_F\rangle = \sum_{S,I,M_F} \langle S, I, M_S, M_I \,|\, f_1, f_2, F, M_F\rangle \tag{4.9}$$

and the coefficients can be calculated by using Equation 4.8 with $j_1 = s_1 = 1/2$, $j_4 = s_2 = 1/2$, $j_3 = f_1$, $j_6 = f_2$, $j_7 = S$, $j_8 = I$, $j_9 = F$:

$$\sqrt{(2S+1)(2I+1)(2f_1+1)(2f_2+1)} \begin{Bmatrix} s_1 & i_1 & f_1 \\ s_2 & i_2 & f_2 \\ S & I & F \end{Bmatrix} \tag{4.10}$$

The numerical calculation of these values is rather involved and error-prone, but fortunately a ready-made Matlab script[74] can be used to solve this problem.

Given the singlet and triplet scattering length a_s and a_t e. g. from the full coupled channels calculation, the scattering length a_F is directly given by

$$a_F = \sum_{S=0,1} \sum_{I=0}^{i_1+i_2} a_S \cdot \left(\sqrt{(2S+1)(2I+1)(2f_1+1)(2f_2+1)} \begin{Bmatrix} 1/2 & i_1 & f_1 \\ 1/2 & i_2 & f_2 \\ S & I & F \end{Bmatrix} \right)^2 \tag{4.11}$$

As a side remark we want to emphasize that the scattering in the stretched states (i. e. for Na the $|2, 2\rangle$ atomic state or for ^{6}LiNa $|3/2, 3/2, 2, 2\rangle$) is directly given by the electronic triplet scattering length since there is no coupling to the singlet channel.

The decomposition of the F, M_F base into the f_1, m_{f1}, f_2, m_{f2} base is shown in detail in chapter 5. Table 4.1 shows a list of scattering lengths calculated by this method. As input for the calculation, we only take the known electronic singlet and triplet scattering lengths, and compare, if possible, to the full numerical calculation.

Obviously, some of the shown values deviate more or less strongly from the full calculations. In case of small deviations (as e. g. for NaNa) this can be explained by the oversimplification of the potential: Since the scattering potentials are not point-like, the simple decomposition cannot give correct results, but these finite size effects have to be taken into account. The scattering takes place neither in the pure electronic triplet/singlet base nor the molecular base, therefore the projections onto these bases are strictly speaking wrong.

For larger deviations, especially for ^{7}Li, the scattering properties are dominated by resonant effects.

An interesting case can be seen in the case of ^{7}LiNa $|1, 0; 1, -1\rangle$. While the explanations above would assume that this channel can only be projected onto the three $F = 0, 1, 2$ states and therefore the scattering length must be a mixture of them, the actual value is larger than the largest molecular channel, a_2. This can be understood from the full description since even though the atoms are both in the $f = 1$ state, they can couple to the $f = 2$ manifold which changes the scattering properties accordingly.

Table 4.1: List of scattering lengths of different channels relevant for this thesis. The values in the third column are calculated according to Equation 4.9 and Equation 4.11 from the electronic singlet and triplet potentials.

species	channel	calc. value [a_B]	lit. value [a_B]
NaNa	triplet	64.30	64.30 [53]
NaNa	singlet	18.81	18.81 [53]
NaNa	$\|2,2,0\rangle$	35.87	–
NaNa	$\|2,2,2\rangle$	44.39	–
NaNa	$\|2,2,4\rangle$	64.30	64.30 [53]
NaNa	$\|1,1,0\rangle$	47.24	48.91 [53]
NaNa	$\|1,1,2\rangle$	55.77	54.54 [53]
^{7}Li^{7}Li	$\|1,1,0\rangle$	–	23.9[95]
^{7}Li^{7}Li	$\|1,1,2\rangle$	–	6.8 [95]
^{6}LiNa	triplet	–	-76.0 [92]
^{6}LiNa	singlet	–	-73.0 [92]
^{6}LiNa	$\|1/2,1,1/2\rangle$	-75.0	
^{6}LiNa	$\|1/2,1,3/2\rangle$	-75.4	
^{7}LiNa	triplet	–	21(2) [24]
^{7}LiNa	singlet	–	6.8(10)[24]
^{7}LiNa	$\|1,1,0\rangle$		18.9 [24]
^{7}LiNa	$\|1,1,1\rangle$		19.3 [24]
^{7}LiNa	$\|1,1,2\rangle$		20.0 [24]
^{7}LiNa	$\|1,0;1,-1\rangle$		20.2 [24]
^{6}Li^{7}Li	$\|1/2,11/2\rangle$	36.7 [24]	
^{6}Li^{7}Li	$\|1/2,13/2\rangle$	38.2 [24]	

4.1.3 Asymptotic Bound State Model

The precise calculation of the scattering lengths is possible with the coupled channels calculation and provides very good results regarding the background scattering length, Feshbach resonance positions, and determination of their strength. While this model can deliver coarse calculations rather fast on a moderately powerful computer, the necessary data for the full potential modelling may not be readily available in all cases, and the useage and understanding of the numerics are very challenging.

A rather simple, but still very powerful tool for determining Feshbach resonance positions and assigning them to molecular states is offered by the Asymptotic Bound State Model, ABM. [66, 101] While an advanced version of this model can even calculate resonance widths, the calculations presented here are only using a rather basic modelling. An in-depth discussion of the ABM can be found in [34] and an application to the ^{6}LiNa system in [91].

For the ABM, one exploits the fact that the resonant scattering is caused only by the least bound molecular states closely below the disossiation energy and therefore can neglect the complex details of the full scattering potential.

These least bound states are so-called halo states [48, 84] that all share a common property: The most weight of the wavefunction is outside the potential, while only a small part is contained inside the classical turning point. Close to the dissociation, the wave function can then be described by the asymptotic behaviour $\Psi(r) \propto e^{-\kappa r}$. This ansatz allows a simple description of the magnetic field dependence of the states and thus the crossing of the molecular and the atomic energies, as well as their coupling. This determines the resonance position as well as their strength.

The Hamiltonian of the molecular states depends on both external and internal parameters:

$$H = T + H_Z + H_{\text{hf}}(R) + U(R) + V_{\text{SS}}(R), \tag{4.12}$$

where the meaning of the terms is:

$$T = -\hbar^2\nabla/(2\mu) \qquad \text{kinetic energy,} \tag{4.13}$$

$$H_Z = \sum_\alpha (g_{s\alpha} s_{z\alpha} + g_{i\alpha} i_{z\alpha})\mu_B/\hbar \cdot B \qquad \text{Zeeman shift,} \tag{4.14}$$

$$H_{\text{hf}} = \sum_\alpha a_\alpha \mathbf{s}_\alpha \cdot \mathbf{i}_\alpha/\hbar^2 \qquad \text{the hyperfine interaction,} \tag{4.15}$$

$$U(R) = U_X(r)P_X + U_a(r)P_a \qquad \text{interatomic potential} \tag{4.16}$$

$$V_{SS}(R) = \frac{2}{3}\lambda(R)(3S_Z^2 - S^2) \qquad \text{electron spin-spin coupling} \tag{4.17}$$

$$\lambda(R) = -\frac{3}{4}\alpha^2\left(\frac{1}{R^2} + a_{\text{SO}} e^{-b_{\text{SO}}R}\right) \tag{4.18}$$

The summation over $\alpha = 1, 2$ is for the two atoms. The g-factors are of the electrons g_s and the nuclei g_i, with the corresponding spins $\mathbf{s}$ and $\mathbf{i}$ and their z-projections; μ_B is the Bohr magneton.

The interatomic potential $U(R)$ can be projected onto the electron singlet $S = 0$ (labeled X in accordance with the spectroscopy literature) and triplet $S = 1$ (labeled a) Born-Oppenheimer potentials, using the projection operators $P_{X/a}$.

The electron spin-spin interaction V_{SS} includes in the first term in λ the magnetic dipole-dipole interaction, while the second part comes from a second-order spin-orbit contribution. [22] α is the fine structure constant.

Diagonalization of Equation 4.12 first requires a suitable basis. A good set of eigenvalues are the rovibrational eigenstates in the singlet or triplet potentials, with their spin projections of the uncoupled and coupled spins. We denote the states as

$$|\nu l, \sigma\rangle = \left|\Psi_\nu^{S,l}\right\rangle \tag{4.19}$$

where ν, l are the vibrational and rotational quantum numbers of the molecular state in the $S = 0$ singlet or $S = 1$ triplet potential. $|\sigma\rangle = \left|SM_S m_i^{\text{Na}} m_i^{\text{Li}}\right\rangle$ denotes the total electron spin, its z-component and the nuclear spin projection of the two atoms in case of heteronuclear

systems. For a homonuclear system, one could choose $|\sigma\rangle = |SM_S IM_I\rangle$ for the total nuclear spin I and its projection.

In these states, the Hamiltonian can be written as

$$\mathcal{H}_{\nu' l' \sigma', \nu l \sigma} = \langle \nu' l' \sigma' \,|\, H \,|\, \nu l \sigma \rangle \tag{4.20}$$

$$\begin{aligned} &= \varepsilon_\nu^{S,l} \delta_{\nu\nu'} \delta_{ll'} \delta_{\sigma\sigma'} \\ &\quad + \mu_B B \left(g_s M_S + g_i^{\mathrm{Na}} m_i^{\mathrm{Na}} + g_i^{\mathrm{Li}} m_i^{\mathrm{Li}} \right) \delta_{\nu\nu'} \delta_{ll'} \delta_{\sigma\sigma'} \\ &\quad + a_{\mathrm{hf}} \delta_{ll'} \eta_{\nu\nu'}^{SS'}(l) \left\langle \sigma' \left| \sum\nolimits_\alpha \mathbf{s}_\alpha \cdot \mathbf{i}_\alpha \right| \sigma \right\rangle / \hbar^2 \end{aligned} \tag{4.21}$$

Here, δ denotes the Kronecker delta; $\varepsilon_\nu^{S,l}$ is the eigenenergy of the molecular level in the vibrational state ν with angular momentum l in the singlet ($S = 0$) / triplet ($S = 1$) potential. For a given molecular state, this represents the binding energy for $B = 0$, if no couplng to other states is given.

For finite magnetic fields, the Zeeman term shifts the energies proportional to the electron and nuclear spin projections and the gyromagnetic factors.

The hyperfine coupling term $\langle \sigma' | \sum_\alpha \mathbf{s}_\alpha \cdot \mathbf{i}_\alpha | \sigma \rangle$ in Equation 4.21 influences the splitting of the molecular levels at low magnetic fields. The operator does not commute with the total electron spin, therefore it induces the coupling between singlet- and triplet states.

The last expression in Equation 4.21 also contains the overlap integral $\eta_{\nu\nu'}^{SS'}(l)$ between the molecular states with the same angular momentum l: $\eta_{\nu\nu'}^{SS'}(l) = \langle \Psi_\nu^{S,l} | \Psi_\nu'^{S',l} \rangle$. For $S = S'$, this is given by $\delta_{\nu\nu'}$, since the states in each electronic potential are forming an orthogonal set. For different electronic spin, this integral gives the coupling strength between singlet and triplet states, which can cause avoided crossings in the level schemes and thus change the structure of the Feshbach spectrum and the magnetic field of the resonances.

A simplification of the Hamiltonian in Equation 4.20 can be found by using the approximation

$$\sum_\alpha a_\alpha \mathbf{s}_\alpha \cdot \mathbf{i}_\alpha \approx {}^1\!/_2 \, \mathbf{S} \cdot \mathbf{I} \tag{4.22}$$

which decouples the singlet and triplet states as the expression on the right-hand side commutes with the total spin S. By this, the coupling term vanishes from the Hamiltonian, leaving only the eigenenergies $\varepsilon_\nu^{S,l}$ as free parameters, while the Zeeman terms are fixed by the gyromagnetic factors and the spin projections.

This model will be called the Moerdijk model [66] and allows a coarse understanding and assignment of observed Feshbach resonances with only the binding energies as free parameters. The remaining deviations can then be explained and taken into account by including the singlet-triplet coupling and the overalap integrals as fit parameters, in total allowing for a sufficiently accurate description of the observed resonance spetrum.

4.2 ^{7}LiNa Measured Resonances and Modelling

This section will describe the measuement and modelling of newly observed Feshbach resonances in our system. However, before discussing the results, one has to know how Feshbach resonances can be studied experimentally at all.

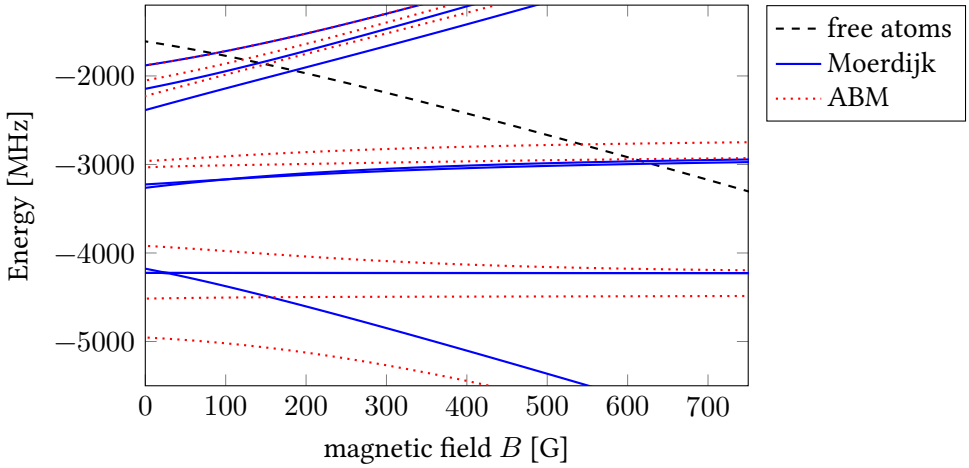

Figure 4.2: Effect of the singlet-triplet coupling for the ^{7}LiNa molecular spectrum. Without coupling (*Moerdijk*), the lower singlet and lowest triplet branch overlap at low fields. The coupling induces a shift in all triplet states but the uppermost which has purely triplet character. The detailed effects of these shifts will be elaborated below.

The effect of Feshbach resonances on ultracold atoms are twofold: While the change of the elastic s-wave scattering length has been discussed so far, this parameter is difficult to measure. Detection possibilities of the change in scattering length include an in-situ imaging, detecting a change of the atomic cloud size as the chemical potential changes. But this requires a high-resolution imaging and the possibility to image at all magnetic fields resonantly. Both is not available in our system.

The second option is the study of time-of-flight images, since the change in the chemical potential changes the expansion speed. This method does not need a high imaging resolution, but still an imaging at the field of the resonance. Also, for the mixture, the overlap of the clouds plays a role, making these measurements very demanding.

Instead, we used a standard technique that exploits an increased three-body interaction in the vicinity of a Feshbach resonance, namely three-body recombination.

4.2.1 Experimental Signature: Losses

Several processes can reduce the atom number during the experiment. The density-independent processes are caused by collisions with the background gas in the vacuum chamber, since the residual atoms in the glass cell have the thermal velocity of the room temperature. This is much higher than the trap depth, thus any collision with an ultracold atom will kick that one out of the trap. This vacuum-lifetime is the reason why great care has to be taken to reduce the pressure in cold quantum gas experiments, typically below 10×10^{-11} mbar. Also, in the dipole trap, atoms can off-resonantly scatter photons, and the momentum transfer can remove the atom from the trap, too.

Loss mechanisms involving two atoms are also possible, but not if both atoms are in their respective ground state. For our experiments, these processes are not dominating, but the

mechanism is a spin exchange process, where the coupling of singlet and triplet potentials can cause different molecular states with the same total angular momentum to couple. The atoms can then undergo spin flips to the lower state, gaining enough energy to leave the trap.

The relevant loss mechanism for the Feshbach spectroscopy, however, is the three-body channel. For a dense Bose-Einstein condensate in our setup, this is typically the dominating loss process and the reason for the transfer of sodium from $|2,2\rangle$ to $|1,1\rangle$, since the combination coefficient for the upper hyperfine manifold is about 10 times higher than for the lower one. In the typical three-body recombination process, two atoms can be scattered into a bound molecular state instead of elastically bouncing off. The bound state typically has a binding energy much larger than the trap depth, which is on the order of 10 µK, or 0.2 MHz. As will be shown later, the molecular binding energy of the least bound state in the ^{7}LiNa molecular at zero magnetic field is on the order of 500 MHz. To fulfill both energy and momentum conservation, a third collisional partner is needed, therefore this process transfers a large amount of energy to three atoms, and all three will be lost from the trap due to their high momenta.

In the vicinity of a Feshbach resonance, the binding energy can be much less, in fact the molecular and atomic states are degenerate at the resonance. On the bound-state side of the resonance, the energy of the molecular state scales with the universal law

$$\varepsilon_b = -\frac{\hbar^2}{2\mu a^2} \tag{4.23}$$

which means that for large scattering lengths the binding energy can be small enough that the released energy is not sufficient for the atoms to escape from the trapping potential. However, the overlap with deeper-lying molecular states is larger than the free atom's wave function, thus this weakly-body molecule can undergo a relaxation if a third atom is present, again leading to losses.

In total, this does not mean that a Feshbach resonance suppresses losses – quite the contrary is true: From a qualitative argument, [28] shows that the recombination rate for the three-body process is proportional to a^4.

This now gives the tool needed to allocate the position of a Feshbach resonance: At a magnetic field where a strongly enhanced loss happens, the resonance occurs. The strongest losses are expected at the exact resonance position, at least for the simple description for the narrow resonances that are important for the mixtures studied in this thesis.

It is important to keep in mind that the a^4 scaling does *not* mean that atom losses would be strongly suppressed at the $a = 0$ crossing of the scattering length. This scenario is more involved and will be discussed further in the context of the sodium 905 G resonance.

Most of the resonances in the ^{7}LiNa spectrum are too narrow, anyways, to clearly resolve the loss curve to distinguish the exact loss mechanisms involved.

4.2.2 Detection Procedure

The measurement procedure for the detection of all resonances was the same and is depicted in Figure 4.3: The investigated hyperfine combination of both species is produced at low offset fields after the final evaporation step in the dipole trap. Then, the current through the antibias coils is ramped up, controlled by the Arduino microcontroller as described in section 3.3.

The initial negative set value is to avoid uncontrolled jumps or small currents during the rest of the sequence. Unfortunately, it also causes an uncontrolled jump, as soon as the set point is set to some positive value. Therefore care has to be taken to not heat up the atoms due to uncontrolled currents. A possible improvement would be the addition of a switchable short circuit for the analog integration part of the regulation. Preliminary tests with such a switch were not successfull and did not give a clear improvement of the turn-on conditions.

From microwave spectroscopy we know that the magnetic field drifts over about 1 s, partly due to warm-up effects of the coils and magnetization of any material around the glass cell.

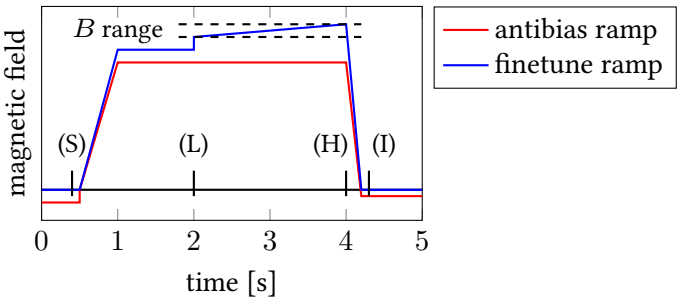

Figure 4.3: Scheme for the detection of Feshbach resonances. The red and blue lines indicate the set points for the currents of the *antibias* and *finetune* coils, respectively. The negative value is explained in the text. Both currents are ramped up in parallel; and the final field is set with finetune ramps. After the desired hold time, all fields are turned off. The indicated points on the timeline are: State preparation, Lowest field in the ramp range, Highest field in the ramp, Imaging. The antibias ramps in the experiment are actually faster than shown in this sketch, typically 100 ms up and 5 ms down.

After this waiting time, the finetune coils are used to add an additional field, as those coils can be ramped more conveniently, although their field stability is very bad, with a measured width of 30 mG. This limits the field determination when this coil pair is used.

For a coarse search of loss features, the finetune field is ramped generously by up to 8 G. The time of the ramp is varied depending on the loss strength and ramp width, and may be between 10 ms and 1 s. After the final ramp point has been reached, both the finetune and the antibias currents are ramped down, and the remaining atoms are imaged at low offset field.

The final position of the resonances given below depends on this ramping scheme. In the errors of the field determination, this ramp widths is either included or given explicitly; in most cases the ramp width limited the resolution, as the aim was not a high-precision measurement.

To make use of the resonances to tune the interaction, this scheme is not useful due to the large fluctuations of the finetune coils. For these cases one tries to hold the atoms at the final field only with the antibias coils or add, if necessary, a small field with the equally stable large offset coils which can deliver additional fields of up to 2 G.

4.2.3 s-Wave Resonance Spectrum

In the course of this thesis, the interspecies Feshbach spectrum of the bosonic ^{7}lithium-sodium mixture was investigated and a total of 11 s-wave resonances in four different hyperfine state combinations were found and identified. Additionally, 10 loss features were observed that could partially be identified as p- and d-wave resonances. The correct identification of these loss features is not conclusive and will be discussed below.

Table 4.2 lists the observed s-wave resonances with the prepared hyperfine states, the center field of strongest loss as calibrated with MW or RF spectroscopy, and, if possible, the assignment by coupled channels calculations including the width, as well as the estimated resonance position according to an asymptotic bound state model.

The detection of the first s-wave resonances was rather straightforward, since the coupled channels calculations published in [92], based on the ^{6}LiNa resonances measured in our setup, could predict the spectrum with a rather broad resonance at – comparably – low magnetic fields. Figure 4.4 shows the first observation of heteronuclear losses in the new mixture.

Due to the strong imbalance in atom numbers, it is not possible to see a clear loss in the sodium numbers, so the whole information is given by lithium.

For fields above 220 G, Li atoms are lost without obviously assignable interspecies resonances. We assign these losses to the intraspecies scattering length of ^{7}Li which becomes negative for fields above about 150 G.

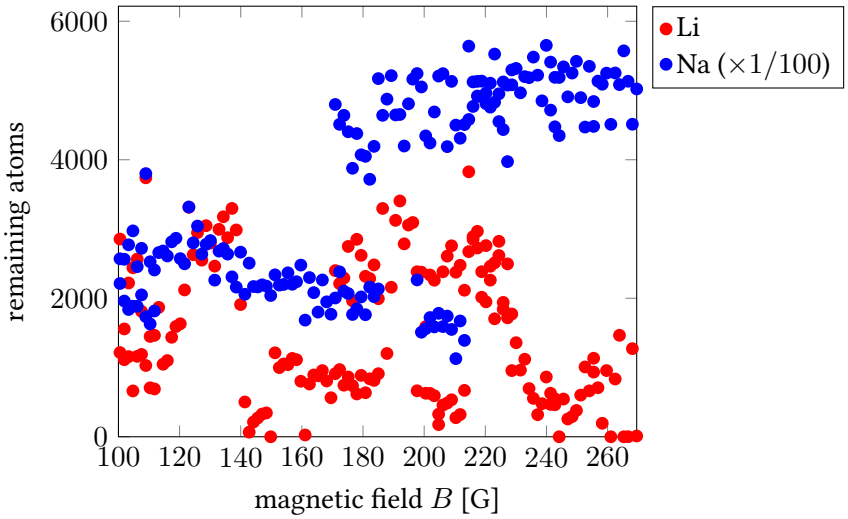

Figure 4.4: Coarse scan in the $|1,1;1,1\rangle$ channel for detection of the first Feshbach resonances. With a 8.4 G sweep for each point, the width of the loss features are exaggerated. We attribute the losses around 120 G and 150 G to the corresponding Feshbach resonances. The different Na atom numbers are caused by bad laser performance and increased after re-adjustment during the scan run. This also shows the challenges of an unstable experimental preparation. The losses above 220 G start when the ^{7}Li^{7}Li scattering length becomes negative, showing that experiments in the $a_{\mathrm{LiLi}} < 0$ regime are challenging.

After the detection of these first resonances, it was clear that the whole spectrum had to be shifted by about 50 G towards smaller fields as compared to the predictions in [92]. From this point on, it was rather straightforward to find further resonances, following the field ramping procedure explained above.

As soon as a loss feature could be identified, the field ramp was reduced iteratively to minimize the uncertainty of the resonance position. The results of these scans are listed in Table 4.2 for the four hyperfine combinations which were experimentally investigated. For the hyperfine ground state of both species, also the predictions for higher field resonances are listed which could not be investigated experimentally.

Table 4.2: List of s-wave Feshbach resonances in the ultracold ^{7}LiNa mixture. B_{meas} is the magnetic field of the strongest losses. For data where only one error is given, it is the combined uncertainty of a magnetic field ramp and the calibration error. If two errors are given, the first one is the calibration error, the second one shows the ramp width. The given value corresponds to the middle of the magnetic field ramp. For comparison, the coupled channels results and the Moerdijk and ABM calculations are listed.

state	B_{meas} [G]	B_{CC}	B_{Moerdijk}	B_{ABM}
$\|1,1;1,1\rangle$	85.18(02)	85	85.1	85.1
$\|1,1;1,1\rangle$	$121.50(05)_{\text{cal}}(10)_{\text{sweep}}$	121	142.1	121.8
$\|1,1;1,1\rangle$	150.2(1)	150.0	184.8	149.6
$\|1,1;1,1\rangle$	543.2(4)	543.0	617.7	542.7
$\|1,1;1,1\rangle$	609.3(4)	609.4	629.0	609.1
$\|1,1;1,1\rangle$	−−	1095	1101.1	1096.0
$\|1,1;1,1\rangle$	−−	1188	1101.2	1192.5
$\|1,0;1,1\rangle$	127.05(04)	127	126.9	126.9
$\|1,0;1,1\rangle$	172.16(04)	172	193.4	172.6
$\|1,0;1,1\rangle$	202.27(16)	202	232.6	201.7
$\|1,1;1,0\rangle$	130.00(16)	130	130.0	130.0
$\|1,1;1,0\rangle$	176.93(10)	177	198.8	177.4
$\|1,1;1,0\rangle$	207.77(10)	207	239.7	207.3
$\|1,0;1,0\rangle$	208.36(10)	208	208.7	208.3
$\|1,0;1,0\rangle$	262.90(16)	263	287.2	263.4

Moerdijk Model

Neglecting the coupling between the molecular levels gives already important information about the overall structure of the Feshbach spectrum, especially if the resonances tend to be narrow. Figure 4.5 shows an overview of measured resonances in the $M_F = 2, 1, 0$ channels for positive magnetic fields, corresponding to the atomic asymptotes of $|1,1;1,1\rangle$, $|1,0;1,1\rangle$ and $|1,1;1,0\rangle$, and $|1,0;1,0\rangle$. This plot contains much information: Each cross indicates an observed loss, induced by a Feshbach resonance at the given magnetic field, and was assigned

to a molecular $l = 0$ state. The dashed lines show the energy of the free atom pair at the given magnetic field. The open circles show the coupled channels predictions, while the solid lines shown the molecular states and their field dependence according to the Moedijk model.

The parameters for the model are the energies of the least bound states, and for this scenario were chosen to be

$$\varepsilon_\nu^1 = h \cdot -2846.5\,\text{MHz} \tag{4.24}$$
$$\varepsilon_\nu^0 = h \cdot -4210.4\,\text{MHz} \tag{4.25}$$

for the triplet and singlet energy, respectively. The vibrational level ν is not yet assigned; for the ABM, this number is not important.

Note that the energetic zero point is chosen for the atomic case without hyperfine interaction, therefore the zero-field energy for the free atoms is at

$$E_{\text{atoms}} = -5/4 \cdot (a_{\text{hfs,Na}} + a_{\text{hfs,Li}}) = -1.609\,\text{GHz} \tag{4.26}$$

with the hyperfine constants a_{hfs}.

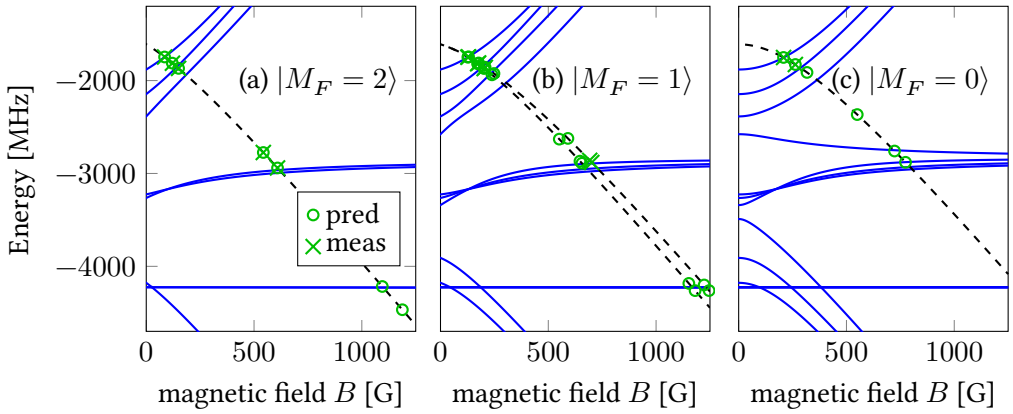

Figure 4.5: Basic Moerdijk model of the ^{7}LiNa Feshbach spectrum, based on one triplet and one singlet molecular level. While the overall structure of the spetrum can be modelled, strong disagreements are obvious for resonances caused by different hyperfine levels of the same molecular branch. The atomic asymptotics are (a) $|1,1;1,1\rangle$, (b) $|1,1;1,0\rangle$ (upper) and $|1,0;1,1\rangle$ (lower), and (c) $|1,0;1,0\rangle$. The open circles show the positions of resonances predicted by coupled channels calculations; the crosses indicate measured resonances.

For low fields, this model can qualitatively describe and assign the character of the observed resonances: In the $M_F = 2$ channel (a), the three lowest s-wave resonances are caused by the three uprising branches of the least bound molecular triplet level. But the spacing between the resonances is far off the experimental errors and cannot be altered in the modelling since there is no free parameter; the splitting is purely determined by the hyperfine interaction and the Zeeman shift.

The same kind of deviation is found in the $M_F = 1$ (b) and $M_F = 0$ (c) manifold, also for the resonances at lowest fields. In the $M_F = 1$ case, six resonances were found, three in both the $|1, 1; 1, 0\rangle$ and $|1, 0; 1, 1\rangle$ channel, that are caused by the three highest molecular levels, while the fourth one could not be investigated experimentally in both scenarios. The interesting feature in the $M_F = 1$ channel is that the same molecular levels couple to two different atomic asymptotes, therefore measurements in these different channels can complement each other, e. g. if one channel cannot be accessed due to the negative scattering length of ^{7}Li.

Also, in case the structure was completely unknown, the relative position of resonances in different atomic channels could directly indicate whether the resonances are caused by an $M_S = 1$ or $M_S = 0$ multiplet due to the slope of that molecular level.

Even more dramatic than in the low-field cases is the splitting in the $M_F = 0$ spectrum between the resonances around 500 G where only one of them in each channel could be explained by the corresponding triplet branch, while the other one is at far too low fields. The same is true for the $M_F = 1$ case, but here the resonances around 500 G could not be investigated. Only the two resonances around 700 G were found, which could still be in accordance to the Moerdijk model.

Finally, the coupled channels calculations agree very well with the experimental findings and show the same deviations, also for further resonances that were not observed.

Asymptotic Bound State Model

The fitting of resonances can be greatly improved by taking coupling between the molecular levels into account. For this, the Frank Condon-overlap between the states is used as a fit parameter for the resonance positions. This leads to different fractions of singlet and triplet part, providing additional insight into the overall spectrum.

For the three lowest-field resonances in the $|1, 1; 1, 1\rangle$ channel, the triplet character is dominating, but the 120 G and 150 G resonances already show clear singlet admixtures, which is also connected to their larger width. Therefore, the triplet level energy can already be fixed by the 80 G resonance, while the position of the other two resonances help determining the singlet energy without the need of explicit singlet resonances. Indeed, no Feshbach resonance caused by the lower lying singlet level could be measured due to the strong losses of the ^{7}Li intraspecies resonance and the negative scattering length of this species for higher fields.

The results of the best fit using all experimentally observed Feshbach resonances in the $|1, 1; 1, 1\rangle$, $|1, 1; 1, 0\rangle$, $|1, 0; 1, 1\rangle$ and $|1, 0; 1, 0\rangle$ atomic states is shown in Figure 4.7. This rather complex presentation provides a lot of information and needs some further explanations:

The graphs again show the energy dependence of the atomic states on the magnetic field. The extension to negative values here allows an easy comparison of states with the same absolute M_F, i. e. states with $M_F = \pm 2, \pm 1, 0$. For the atomic states this means that the channel which is $|1, 1; 1, 1\rangle$ for positive magnetic fields, shows the $|1, -1; 1, -1\rangle$ state for negative fields. So at -1000 G the resonance is not in the $|1, 1; 1, 1\rangle$, but at a positive field in the $|1, -1; 1, -1\rangle$ channel.

This is also the reason why in the $M_F = 1$ channel, four combinations of atomic states can be compared, namely $|1, 0; 1, 1\rangle$, $|1, 1; 1, 0\rangle$ on the positive-field side, and $|1, 0; 1, -1\rangle$ and $|1, -1; 1, 0\rangle$ on the negative-field side. For the $M_F = 0$ case, there is no dependence in the $|1, 0; 1, 0\rangle$ channel, but the $|1, 1; 1, -1\rangle$ and $|1, -1; 1, 1\rangle$ channels are asymmetric.

In the lines that indicate the free atoms' energy, there are also the scattering properties of ^{7}Li encoded: For magnetic fields with positive intraspecies scattering, a green line is drawn, while the dotted red line indicates fields with negative scattering lengths. For many cases, this negative scattering length prevented measurements at these fields, therefore the red area does not indicate that no resonances are present, but that their detection is more challenging. For sodium, the background scattering length is only very slightly field dependend, and does not play any role here, since sodium can be prepared easily at any field – at least below the strong 905 G resonance in the $|1,1\rangle$ channel.

The final information shown in the graph are additional atomic states that open for higher magnetic fields and provide additional loss channels. While these states were not investigated, their loss-induced broadening of resonances can have strong influence on the interpretation of loss spectra. For the $M_F = 2$ case, this is the $|2,-2;1,0\rangle$ state from the upper ^{7}Li hyperfine manifold, which is lower in energy than the $|1,-1;1,-1\rangle$ channel above 500 G.

In the $M_F = 1$ manifold, the situation is again more complex, since the $|1,-1;1,0\rangle$ state is already below the $|1,0;1,-1\rangle$ state. But additionally, the $|2,-2;1,1\rangle$ crosses $|1,0;1,-1\rangle$ at 439.9 G and $|1,-1;1,0\rangle$ at 639.9 G, adding a second and third inelastic loss channel for high fields.

Figure 4.6 shows a closer look at the mentioned features that support the coupled ABM levels.

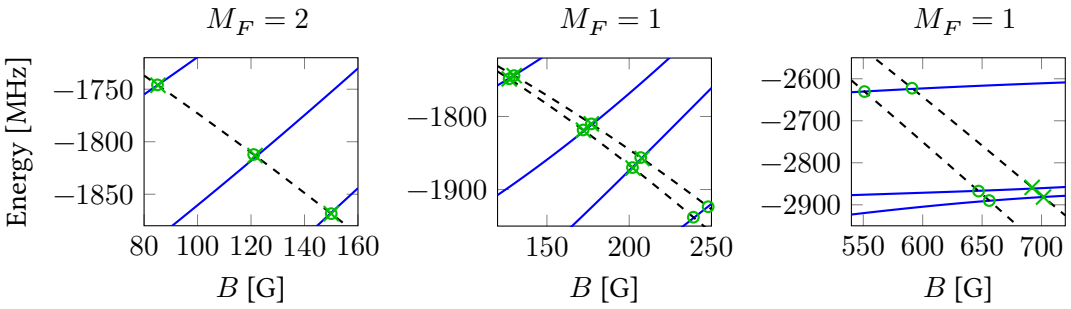

Figure 4.6: Most important resonances supporting the ABM scenario: The three s-wave resonances in the $|1,1;1,1\rangle$ channel with the 1 G broad resonance around 150 G; and in the $M_F = 1$ channel resonances in the different atomic states caused by the same molecular level.

The binding energies of the molecular states are the same as shown above (in fact, they were fitted to the resonance positions with the coupling taken into account), and the parameters for the model are

$$\varepsilon_\nu^1 = -2846.5\,\text{MHz} \cdot h \tag{4.27}$$
$$\varepsilon_\nu^0 = -4210.4\,\text{MHz} \cdot h \tag{4.28}$$
$$\eta^{01} = 0.978 \tag{4.29}$$

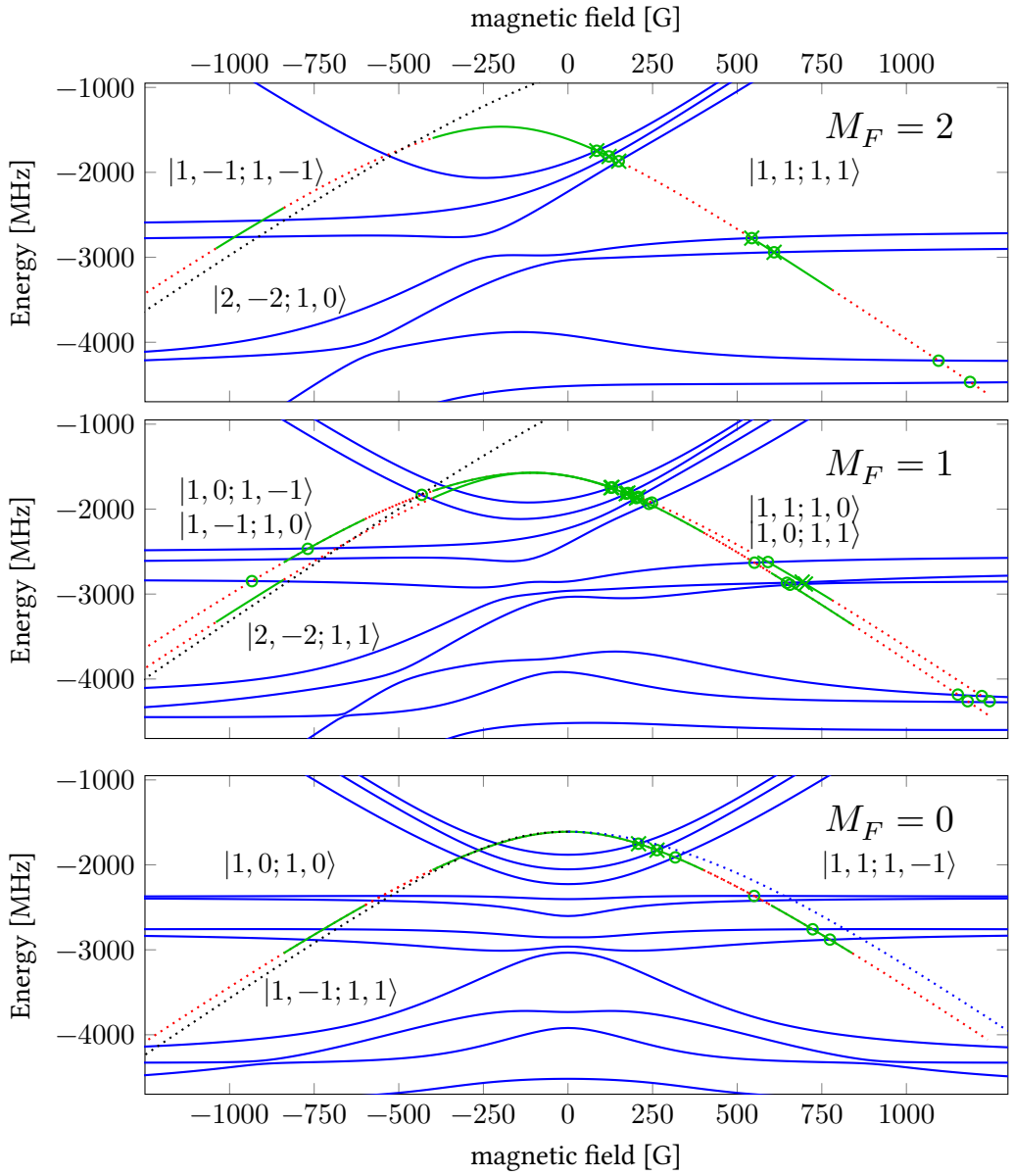

Figure 4.7: Improved asymptotic bound state model taking into account the coupling between the molecular branches. The model contains two singlet and two triplet states, while only one of each is mainly causing the resonances. The other two states can be used for fine-tuning of the resonance positions by fitting the coupling parameters and are not essential for the resonances studied here. For the color coding see text.

4.2.4 Higher Partial Wave Resonances

For identical bosonic particles, the scattering at a central pontential is limited to even numbers of quantized angular momentum, therefore p-wave scattering is not possible. For distinguishable particles, however, this restriction does not exist and a richer scattering spectrum can be investigated.

p-wave resonances

In the heteronuclear scattering, the parity restriction due to particle exchange symmetry is not given, and odd partial wave scattering is possible. This is also true in the case of identical fermions, whereas s-wave scattering is not possible in the latter system. But even if p-wave scattering is possible, it is normally strongly suppressed in cold quantum gas experiments, since the rotational barrier is much higher than the atom's temperature, as described in subsection 4.1.1.

In the vicinity of a Feshbach resonance caused by an $l = 1$ molecular state, however, the scattering can be strongly enhanced and thus also shows a stronger interaction and increased three-body loss. Since the scattering happens in another channel, the s-wave scattering length is not a useful parameter for the scattering properties anymore, and the resonance strength depends on the temperature, too. In the experiment, we measured three p-wave resonances in the lowest hyperfine state, where two of them originate from the same molecular level and its splitting into the $M_L = 0$ and $M_L = \pm 1$ states. These two resonances are at $268.29(10)$ G and $270.35(10)$ G, respectively. The third loss feature we assign to a p-wave resonance that was measured at $237.50(40)$ G, where the theoretical description is not in good agreement. Table 4.3 shows an overview of observed loss features that could not be explained in the s-wave spectrum and are thus assigned to higher partial waves.

d-*Wave Resonances*

The rotational barrier for higher partial wave scattering also prevents resonances for relative angular momentum $l \geq 2$, which is why there is no scattering and also no resonance features in these higher angular momentum channels. But due to the magnetic dipole-dipole interaction which can couple $l = 0$ and $l = 2$ states, the scattering properties of the s wave continuum can be influenced by molecular states of even angular momentum larger than zero. In our experiment, we could find seven loss features in two hyperfine channels that we assigned to be caused by d-wave molecular states, see Table 4.3.

In earlier experiments in our setup, also g-wave resonances in the NaNa system could be observed, where molecular states with $l = 4$ couple to the $l = 0$ atomic continuum. However, for the ^{7}LiNa mixture, molecular states with $l > 2$ were not studied.

The vast amount of molecular states with $l = 2$ makes their modelling using the ABM much more complex. Especially since the number of possible resonances is much higher than in the s-wave molecular spectrum, it is not easily possible to assign the observed resonances clearly to a given molecular state, as there are too many fit parameters to choose. Figure 4.8 shows a calculated spectrum of d-wave states in the $M_F = 2$ channel.

This assignment was not achieved doing a fit to experimental data, since only a few loss features could be observed that were assigned to d-wave resonances. While the model reproduces the experimental loss features nicely and also fits to the coupled channels calculations, one has

Table 4.3: List of loss features assigned to higher partial wave resonances. For data where only one error is given, it is the combined width of a magnetic field ramp and the calibration error. If two errors are given, the first one is the calibration error, the second one shows the ramp width. The given value corresponds to the middle of the magnetic field ramp.

state	l	B_{meas} [G]	B_{CC}	B_{ABM}
$\|1,1;1,1\rangle$	p	268.24(10)	267	–
$\|1,1;1,1\rangle$	p	270.30(10)	269	–
$\|1,1;1,1\rangle$	p?	327.3(4)	327	–
$\|1,1;1,1\rangle$	d	42.96(10)(05)	40	40.8
$\|1,1;1,1\rangle$	d	54.72(10)(05)	54	54.7
$\|1,1;1,1\rangle$	d	X	162	159.0
$\|1,1;1,1\rangle$	d	X	301	301.1
$\|1,1;1,1\rangle$	d	321.8(4)	322	321.7
$\|1,1;1,1\rangle$	d	353.6(4)	353	352.1
$\|1,1;1,1\rangle$	d	410.7(4)	407	405.8
$\|1,0;1,1\rangle$	d	58.820(087)(160)	–	
$\|1,0;1,1\rangle$	d	81.396(54)..81.316(50)	–	

to keep in mind that the number of possible assignments is so high that also other scenarios could be possible, therefore these models are just preliminary.

An additional loss feature at $327.50(40)$ G was observed but could not clearly be assigned to the d-wave spectrum. Thus we do not claim that this feature is caused by a Feshbach resonance, but cannot explain it so far.

Figure 4.9 shows the effect of an unstable RF transfer that could be used as a tool: While trying to prepare lithium in the $|1,0\rangle$ state, a large part of atoms remained in the $|1,1\rangle$ ground state. The magnetic field scan then shows two loss features, both not saturated, as only atoms of one of the two states are lost and the imaging is not state-selective.

This scan therefore gives a direct measure for the distance of the two resonances without the need of calibration for each of them separately. The drift to lower atom numbers for higher fields has no physical reason, but might be caused by the stronger field ramping of the finetune coils, causing heating and thus increased loss of the atoms from the trap.

4.2.5 Inelastically Broadened Feshbach Resonances

Although in many cases a direct connection can be made between the two body elastic scattering and the three body inelastic losses around a Feshbach resonance, as shown in subsection 4.2.1, it is also possible that a resonance is strongly dominated by inelastic scattering into other atomic channels. Such a case was found in the ^{7}LiNa $|1,1;1,0\rangle$ state around 702 G. There, an over 5 G broad loss feature was observed, while the coupled channels calculation for the elastic scattering predicts a much narrower feature.

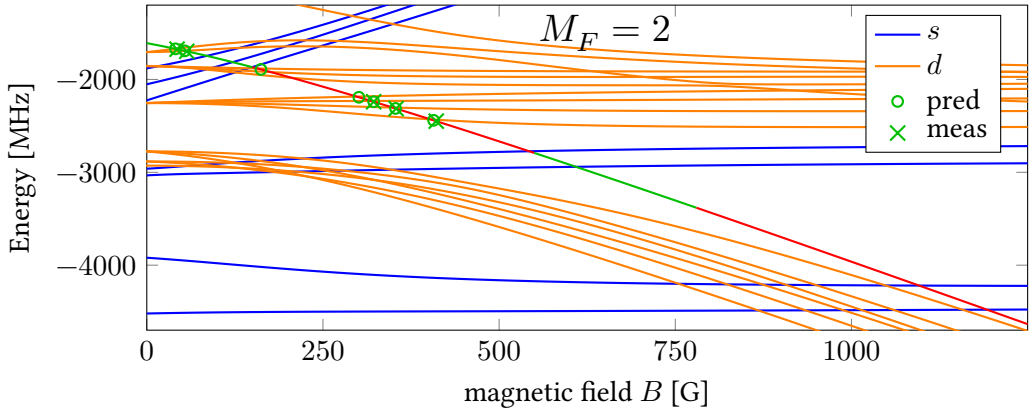

Figure 4.8: Asymptotic Bound State Model including the d-wave molecular states (orange) for the $|1,1;1,1\rangle$ channel. The rotational shift was chosen to be 2010 MHz for the triplet potentials and 2310 MHz for the singlet potential, respectively, relative to the s-wave spectrum (shown in blue). The crosses indicate measured loss features; the open circles coupled channels predictions for d-wave resonances. Due to careful preparation of a small ^{7}Li sample, the range of negative scattering lengths was still accessible.

Taking the inelestic scattering channels into account, the calculations can reproduce the loss feature and thus explain the apparent deviation: The two-body inelastic process $|1,1;1,0\rangle \Longrightarrow |1,0;1,1\rangle$ releases about 120 MHz energy, and is strongly enhanced around the Feshbach resonance. The calculated width of 3 G at 1 µK temperature fits well to the observed roughly 5 G since the loss is saturated and thus broadened, and a field sweep of about 840 mG was used.

This inelastic process also means that the broad resonance here is not suited for any interaction tuning and instead has to be avoided to prevent too strong losses.

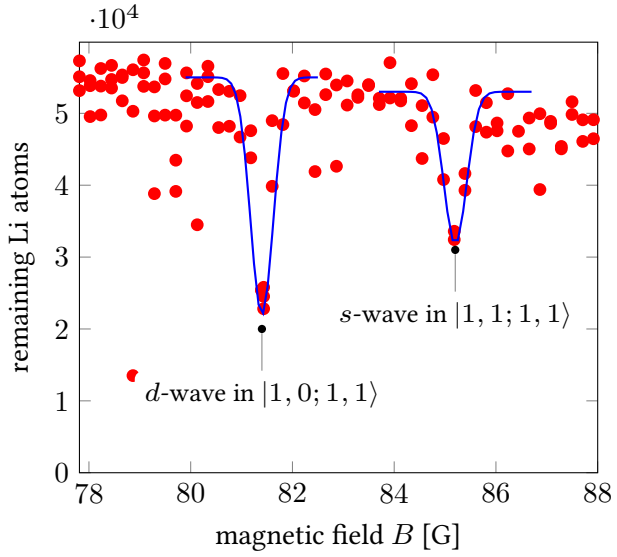

Figure 4.9: Scan of magnetic field showing two loss features in the lithium atom numbers. Due to an insufficient RF transfer, lithium atoms of both $|1,1\rangle$ and $|1,0\rangle$ states are present, allowing to observe the 85 G s-wave resonance in $|1,1\rangle$ and the 81 G d-wave resonance in the $|1,0\rangle$ channel. The blue curves are guides to the eye.

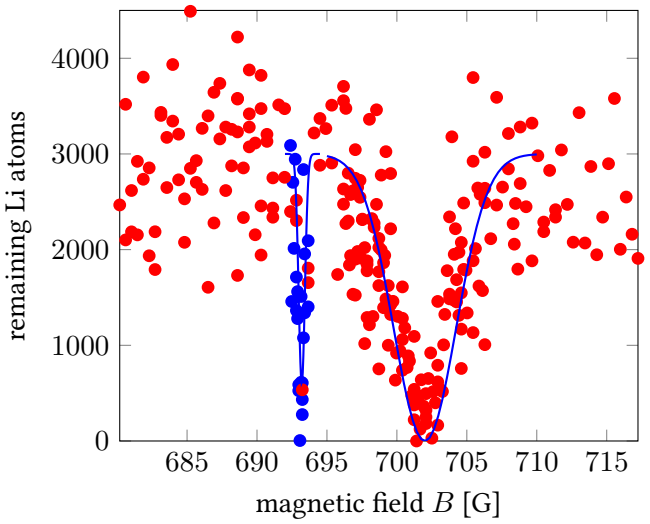

Figure 4.10: Two loss features in the $|1,1;1,0\rangle$ channel of very different widths, both caused by the $M_S = 0$ triplet s-wave branch. While the 693 G resonance is very narrow, the 703 G resonance shows a > 5 G broad loss feature. Coupled channels calculations show that this resonance is dominated by inelastic scattering, thus it is not suited for tuning the elastic cross section. The blue curves are guides to the eye; the blue data were taken with a smaller field sweep to resolve the narrow feature.

4.3 Tuning of Interaction Strength

Since the existance of Feshbach resonances is long known in both homonuclear and heteronuclear ultracold quantum mixtures, the investigation of these resonances here is not the main interest itself. The resonances are mostly considered one of the main tools for cold quantum gas experiments, as the tuning of the interaction by application of an external field is a very convenient way to build a model system for interesting physics.

During the course of this thesis, different scenarios for interaction tuning have been studied, mostly with the aim of influencing the polaronic coupling constant

$$\alpha = \frac{a_{\mathrm{IB}}^2}{a_{\mathrm{BB}}\xi} \tag{4.30}$$

which is an important parameter for impurity physics. [100, 40, 41, 83] α here depends on the scattering length of the background (a_{BB}) and the interaction between the impurity and the background (a_{IB}). The healing length ξ of the background condensate denotes the length scale on which the condensate can react onto spatial structures, and is given by

$$\xi = \frac{\hbar}{\sqrt{2mnU_0}} = \frac{1}{\sqrt{8\pi na}}. \tag{4.31}$$

Thus, ξ also depends on a_{BB}, and α in total scales only with the square root of sodium scattering length, but also with the density.

The tuning possibilities thus include the change of the background's scattering length, here sodium, or the change of the interspecies scattering length, with ^{6}LiNa or ^{7}LiNa. The following subsections will present the results of these investigations and discuss future possibilities.

4.3.1 Sodium Resonance

The strong Feshbach resonance in the sodium ground state is famous as it was one of the very first observed ones [46, 53], triggering the research on and application of Feshbach resonances with a wide range of important experiments.

However, up to our knowledge, no experiment so far made use of this specific resonance to tune the interaction strength. This is mostly due to the strong losses associated with Feshbach resonances in bosonic systems, especially if a strong tuning of the scattering length is desired. Losses can be prevented in special geometries, e. g. in a lattice where no more than two atoms per lattice side are prepared. Energy and momentum conservation then prevent losses.

In a free geometry, however, as it was planned for our experiments with a bath of very high density, the losses are not suppressed. Therefore, we studied the possibilities of experiments in a short-lived Na BEC close to the 905 G resonance. Unfortunately, the lifetime indeed was too short to be usefull for the planned experiments on impurity physics.

Several approaches were used to try and use the resonance for background interaction tuning. Figure 4.11 shows the results of a spin-flip into the $|1,1\rangle$ state: The atmos were transferred from the $|2,2\rangle$ state from the magnetic trap into $|1,1\rangle$ and subsequently to $|1,0\rangle$ at low field. Then the strong offset field was ramped up, and at high field, the $|1,0\rangle$ atoms were cooled to

condensation using the high field hybrid trap. The magnetic curvature is shut off and a wait time of 50 ms makes sure that the final field is well settled.

After the wait time, a 5 ms RF sweep transferred the atoms into the resonantly interacting $|1,1\rangle$ state. These experiments were done before the microwave setup presented in section 3.2 was completed, therefore the frequency generator (Agilent 8657B) was used via the ability to modulate its output frequency proportional to an analog input voltage.

Using a π pulse instead of the RAP turned out to be too unreliable. Thus, the 5 ms were the fastest transfer possible. Directly after the pulse is finished, the atoms are released from the dipole trap and imaged after 20 ms of free expansion using the high-field imaging set up in [8].

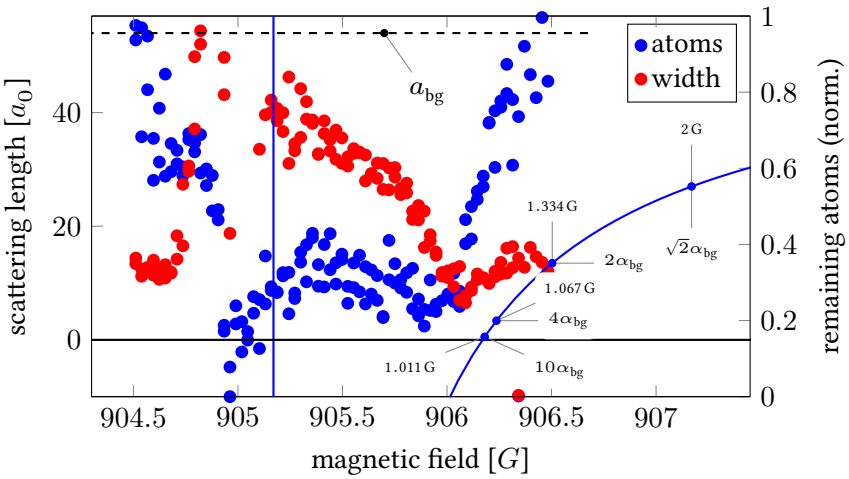

Figure 4.11: Atom loss around the 905.17 G resonance after RF transfer into the $|1,1\rangle$ state. Shown are the number of remaining atoms and the width of a gauss fit to the atomic cloud. The latter one has been scaled for better comparison; the off-resonant width is about 100 µm. The blue line indicates the change of the scattering length due to the resonance. Blue dots indicate the possible changes of the interaction parameter $\alpha \propto \sqrt{a_{\mathrm{NaNa}}}$ (see text). Atom signals have been shifted by 0.3 G to fit the theoretical resonance form, accounting for residual magnetic fields from the hybrid trap.

As there was no additional hold time, the remaining fraction of atoms is the highest that could be achived. Since the interaction parameter is proportional to the inverse square root of the background interaction as mentioned above, the sodium-sodium scattering length has to be tuned to one fourth of its background value $a_{\mathrm{bg}} = 54.45\, a_0$ to increase α by a factor of two. But already at this interaction change, we observe a loss of atoms, for higher values correspondingly stronger. Since the planned experiments deploying the motional Ramsey sequence take several milli seconds, this hold time is already too long and too many sodium atoms will be lost.

A somewhat improved situation could be achieved by adding a delay after the ramp of the hybrid trap. It is known that the turn off of the bias coils is rather slow, therefore the field was given 10 ms to reach the final value. The result of this changed ramping is shown in Figure 4.12, which shows less losses around the zero crossing of the scattering length.

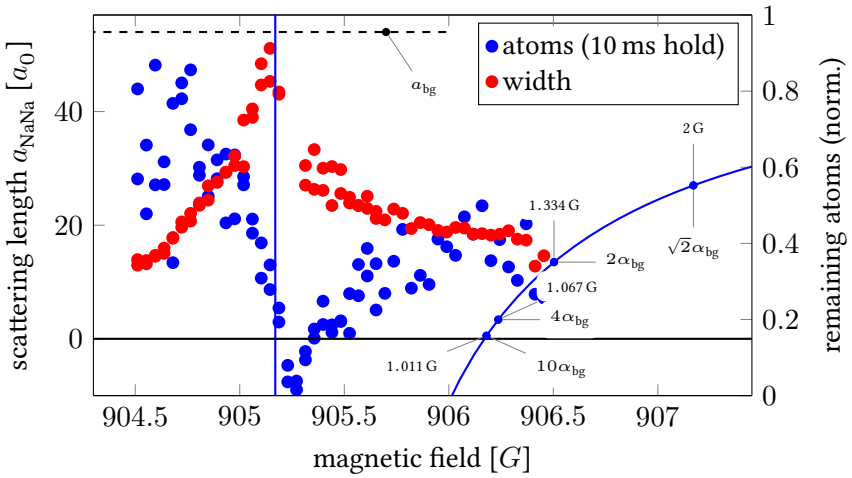

Figure 4.12: Atom loss feature as in Figure 4.11, but with less cooling and a stronger confinement. An additional delay after the hybrid trap ramp and before the RF pulse allows a longer life time of the sample; the data shown are taken after 10 ms.

Even if the atoms were not lost from the BEC, the sudden change of interaction and thus mean field shift will cause oscillations of the BEC density on the time scale of the trap frequency, which is also on the order of the Ramsey interferometry. This changing background density would make the interpretation of the results even more challenging.

The structure of the atom loss and especially the fitted width of the atomic cloud requires a further explanation: A striking feature in the loss spectrum is that right in the middle of the strongest losses a bulk of atoms remains, although with a larger width, corresponding to a higher temperature and thermal fraction.

We explain this feature by a *bosenova* explosion,[85, 23] where the BEC collapses due to the sudden change to negative scattering length. We expect a high three-body collision rate, leading to strong losses that heat the sample and cause the increased width of the cloud. For strongly negative scattering length, this process can happen so fast that a thermal cloud remains, while for weaker interaction all atoms are lost in a somewhat slower process.

The decreased cloud size at small but positive scattering length can be associated with the decreased mean field energy, leading to smaller momenta of the released atoms, thus decreasing the spread after time of flight.

To prevent the sudden quench of the scattering length and allow a smooth change, one can also ramp the magnetic field while the atoms are kept in the resonantly interacting state. Unsurprisingly, the increased three body recombination causes even stronger losses, again preventing the usability of this resonance. Figure 4.14 shows the results of such a ramping ansatz.

In this setting, the atoms were condensed in the high field hybrid trap for fields above the resonance. Since the hybrid trap adds an offset field, turning off the trap leads to a decrease in the field, leading to a ramp towards the resonance. For fields below the resonance, the finetune

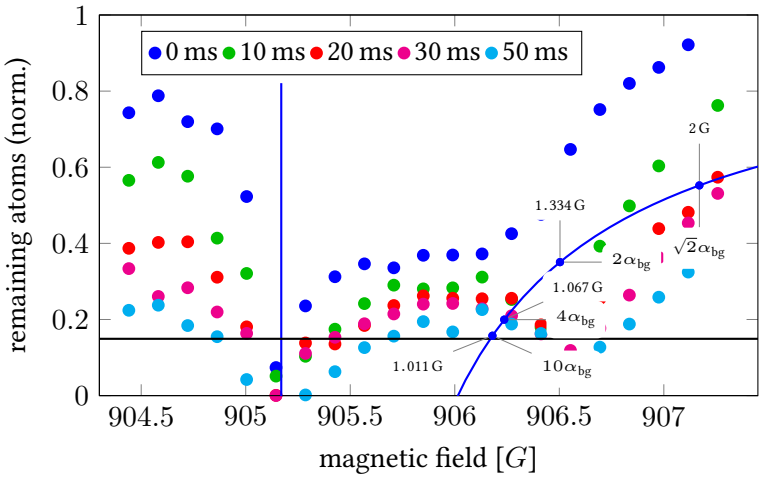

Figure 4.13: Scanning the hold time around the 905 G sodium resonance. Again, the strong losses for sodium prevent any tuning toward small scattering lengths.

coils were off, leading to a total negative offset. In this scenario, turning off the bias current leads to an upwards ramp.

In both scenarios, the fields were turned off with a rather slow linear current ramp of 20 ms, and the atoms were imaged directly at the final field without additional hold time.

Another possibility of background interaction tuning could be the -1.473 G broad resonance in the $|1,-1\rangle$ state at $1202.6(6)$ G that was reported in [92]. This resonance is caused by a molecular state coming from *above* the atomic threshold, thus showing the inverse scattering length dependence: The zero-crossing is below the resonance, while a bound state appears at higher fields. This makes the experimental preparation much easier since the sample can conveniently be cooled at low field and the final field could be ramped easily from below.

In this work, this resonance has not been investigated since a high-field imaging for this field is more challenging than for the more convinent 905 G. The necessary detuning can not easily be achieved with standard AOM or EOM techniques. Since laser sources at 589 nm are still very expensive as no direct laser diodes are available, it is also not possible to copy the simple offset-lock scheme that can be used for lithium.

Two final remarks regarding the reduction of the background scattering length has to be made: While the plots above assume a scaling of α with $1/\sqrt{a_{\mathrm{BB}}}$, one has to take into account the density increase for smaller scattering lengths: The atoms in the condensate will repel each other less, leading to a smaller interparticle spacing, which in turn *increases* the healing length ξ. Therefore, the scaling of α is even worse than the assumed inverse square root.

A second remark regards the physics involved in the polaron coupling picture: The impurity couples to the excitations of the BEC, which vanish for $a_{\mathrm{BB}} \to 0$. This means a break down of the whole description, which of course is again an interesting case requiring a new formalism.

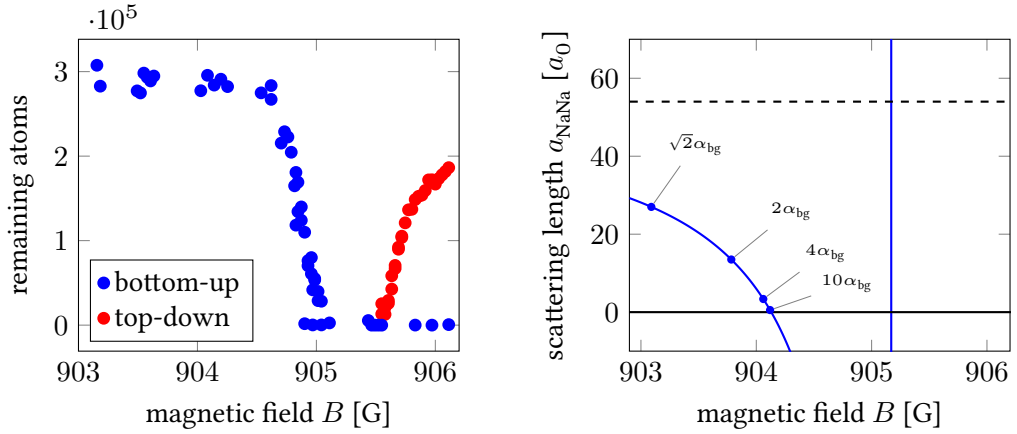

Figure 4.14: Magnetic field ramp towards the 905 G Na resonance from above and below and that shows the strong losses. The hybrid trap was ramped down from its full value during 20 ms. For the bottom-up ramp, only the bias coils were used, for top-down both finetune and bias were active. The right-hand sketch shows the corresponding scattering length, assuming the resonance position to be at 905.17 G.

4.3.2 ^{6}Lithium-Sodium resonances

The extremely narrow interspecies Feshbach resonances of the ^{6}LiNa mixtures renders it nearly impossible to use them for any interaction tuning to a strongly interacting mixture. However, it has been shown in [43] shown that it is possible to create Feshbach molecules by ramping over the 745 G d-wave resonance. Although Feshbach resonances caused by higher angular momentum molecular states tend to couple much less to the atomic spectrum and thus lead to very narrow resonances, this resonance is the broadest in the ^{6}LiNa spectrum at experimentally accessable magnetic fields.

Even though strong tuning will not be possible with the standard experimentally achievable magnetic field stability of a few milli gauss, the resonance could be used for moderate tuning of interaction, since the bath-impurity interaction parameter is proportional to the square of the impurity-bath scattering length

$$\alpha \propto \frac{a_{\mathrm{IB}}^2}{a_{\mathrm{BB}}\xi} \tag{4.32}$$

Figure 4.15 shows the scattering lentgh dependence of this 10 mG broad resonance and the possible tuning parameters. A 10 % increase in α can be achieved already 200 mG away from the resonance; at this field, no increased losses have been observed. This moderate tuning, however, could provide additional insight on the impurity problem. An increase of 50 % would require to go 44 mG close to the resonance. This field might already show stronger losses, but should still allow a lifetime long enough for the motional interferometry.

Stronger interaction changes could be achieved assuming a magnetic field stability of 2 mG, but the steep derivative closer to the resonance will lead to stronger fluctuations during the

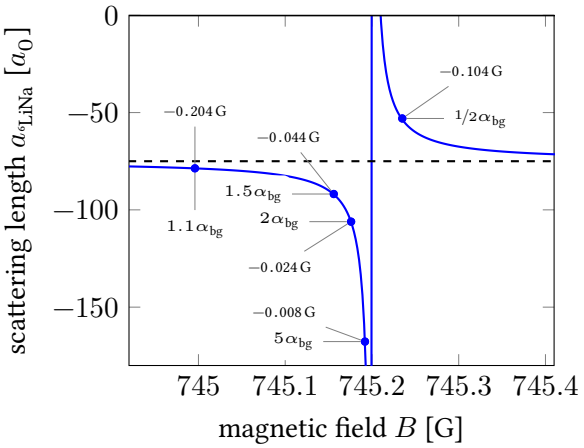

Figure 4.15: Possible interaction tuning scenario for the ^{6}LiNa resonance at 745 G. Although the resonance is very narrow ($\Delta = 10$ mG), the field stability would allow for a moderate tuning of about 50% or even 100%, depending on the lifetime.

measurement, possibly limiting the precision. So far, no experiments deploying the motional Ramsey spectroscopy have been done at magnetic fields close to any resonance.

4.3.3 ^{7}Lithium-Sodium resonances

In contrary to the ^{6}LiNa resonances, the ^{7}LiNa spectrum offers several broader Feshbach resonances which could be used for interaction tuning. The most convenient one is the 150 G resonance, as the magnetic field is still rather low for a good field control, and the width is far above the experimental field stability.

Figure 4.16 shows the scattering length in the ^{7}LiNa system between 110 G and 170 G with the two broadest resonances observed. The right-hand picture shows the tuning possibilities.

If the predicted resonance around 1095 G would be accessible, the width of 5 G of course could offer even better possibilities for a strongly-interaction system.

4.3.4 ^{7}Li-^{7}Li Resonance

The ^{7}Lithium interaction is over a large range of magnetic fields dominated by a strong Feshbach resonance, in effect similar to the very broad ^{6}Li resonances. [82] reported on the use of this resonance for a tuning of interaction over several orders of magnitude. Figure 4.17 shows a sketch of the scattering length for the $|1,1\rangle$ and $|1,0\rangle$ intraspecies channels.

In our experiments, the strong resonance and corresponding losses limited the maximum magnetic field where interspecies Feshbach resonances could be investigated. Especially the predicted 5 G broad resonance around 1095 G which might offer good interaction tuning abilities could not be reached without too strong losses of ^{7}Li.

While a more sophisticated cooling and ramping strategy might allow to investigate and use the high-field interspecies resonance, also the lower field properties might be interesting

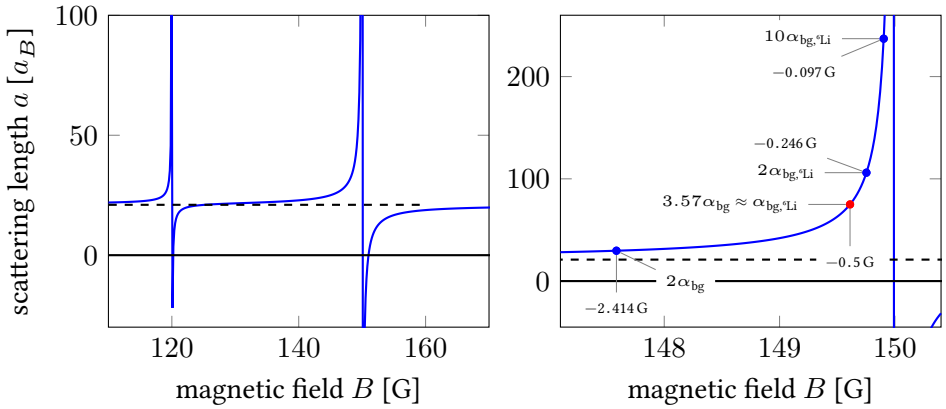

Figure 4.16: Left: Scattering length in the lowest hyperfine states for ^{7}LiNa near the two broadest observed resonances. The resonance at 150 G has a calculated width of about 1 G and might be suitable for interaction tuning. Right: Possible interaction tuning scenario for the ^{7}LiNa resonance at 150 G.

for impurity physics: [82] report on the observation of ^{7}Li^{7}Li scattering lengths below 0.1 a_0 with more than 10×10^5 atoms remaining. So since the sodium as background is not strongly tuneable due to the high losses, changing the role of impurity and background gas might allow to immerse a sodium atom in a very weakly interacting background. This gives rise to a rather large interaction parameter α, allowing to investigate the effects of strong effective interaction with a very weakly interacting background.

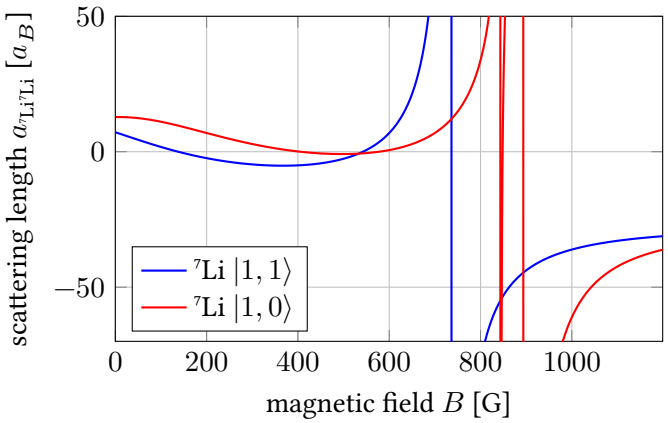

Figure 4.17: Intraspecies scattering lengths of ^{7}Li. [24] In both spin channels, the scattering properties are dominated by a strong Feshbach resonance. The $|1,0\rangle$ state shows two resonances close to each other.

Mîn úngemach, daz ich durch si erlitten hân,
swenne ich mit senenden sorgen alsô sêre rane, sol mich daz alsô kleine wider si vervân?

(Walther von der Vogelweide)

5 Spin Dynamics

In this chapter, the physical cause for the coupling of spin states and the dynamics induced by this process will be discussed. Analytic models of increasing complexity will be introduced, followed by a numerical simulation. For the latter one, the one-dimensional Gross-Pitaevskii equation for a spinor gas is utilized to gain understanding of the observed dynamics, and is especially useful to discuss the multimode effects.

The second part of this chapter will present the experimental results of homo- and heteronuclear spin dynamics, with quantitative comparisons to the simulations and analytical results if applicable.

5.1 Theoretical Background

Several levels of complexity can be adressed when looking at coherent spin dynamics. For didactical reasons, to gain an understanding of the coupling mechanism, it is instructive to look at the description of the two-body system first, where no many-body properties and spatial degrees of freedom are involved which allows a basic analytic model of oscillations.

5.1.1 Two-Body Theory

We will start the discussion here with the heteronuclear system because only two states are involved and an easy analogy to the Rabi oscillations of coupled hyperfine states can be made. After that, the homonuclear case involving three states will be discussed.

Heteronuclear Spin Dynamics

The interaction Hamiltonian for two distinguishable spin-1 particles $|f_1, m_1\rangle$ and $|f_2, m_2\rangle$ (the case of ^{7}Li and Na) is given by the possible molecular states and their respective interactions:

$$H_I = \sum_F g_F \left|F, M\right\rangle \left\langle F, M\right|, \tag{5.1}$$

where $g_F = 2\pi\hbar^2/\mu \cdot a_F$ is the interaction parameter for the molecular channel with total spin F and reduced mass μ. The scattering length a_F for the molecular channels has been discussed in chapter 4 in the context of the electronic singlet and triplet channels and the corresponding scattering in the coupled channels.

Again, $F = f_1 + f_2$ and $M = m_1 + m_2$ is the projection onto the quantization axis. The collision is spin-conserving, therefore the total projection equals the sum of the single particle z-components.

In contrast to the homonuclear case, several spin channels can possibly undergo spin dynamics; for the ^{7}LiNa case the most relevant one is $|M_F = +1\rangle$ with the atomic states $|1, 0; 1, 1\rangle$ and $|1, 1; 1, 0\rangle$, where the first entries denote the total spin and the projection for ^{7}Li, the third and fourth correspondingly for sodium. In the case of ^{87}RbNa, it would be the $|M_F = -1\rangle$ channel with $|1, 0; 1, -1\rangle$ and $|1, -1; 1, 0\rangle$. This is given by the differential Zeeman shift and will be detailed in subsection 5.1.3.

Since the atoms are prepared in the free atom base $|f_1, m_1; f_2, m_2\rangle$, one has to project these states onto the molecular ones. The trivial case would be the preparation in the hyperfine ground state $|1, +1; 1, +1\rangle$ where $|F = 2, M = 2\rangle$ and the interaction is solely given by g_2. Obviously, this state is stable and no dynamics will happen. For the experimentally relevant case of $|F = 1, M_F = +1\rangle$, the two states $|1, 1; 1, 0\rangle$ and $|1, 0; 1, 1\rangle$ are taken into account, which are distinguishable in the heteronuclear case. In this case, both the $|F = 2\rangle$ and $|F = 1\rangle$ channel contribute, while $|F = 0\rangle$ is not involved:

$$H_I = g_2 \left|2, 1\right\rangle \left\langle 2, 1\right| + g_1 \left|1, 1\right\rangle \left\langle 1, 1\right| \tag{5.2}$$

The projection onto the atomic basis via the projection operators $\mathcal{P}_2$ and $\mathcal{P}_1$ allows to write the Hamiltonian in the atomic basis as

$$H_I = \frac{1}{2} \begin{pmatrix} g_2 + g_1 & g_2 - g_1 \\ g_2 - g_1 & g_2 + g_1 \end{pmatrix}. \tag{5.3}$$

The diagonal elements give the state-independent interaction, while the off-diagonal elements lead to a coupling of the states. Since $g \propto a$, the scattering lengths give a direct indication about the coupling strength – the bigger the difference in a_2 and a_1, the stronger the spin exchange.

For the total Hamiltonian, the Zeeman shift also has to be taken into account, in general form as $E_{1,2}(B)$, where $E_{1,2}$ is the energy of the configuration $1 : |1, 0; 1, 1\rangle$ and $2 : |1, 1; 1, 0\rangle$ which differ for the heteronuclear case. The dependence of $\Delta E(B) = E_1(B) - E_2(B)$ on the magnetic field for different combinations of species is shown below in Figure 5.2. For homonuclear cases, one parameter (q) can describe the dependency, while for the heteronuclear cases, the dependency is more complex.

These energies give an offset on the diagonal elements, such that

$$H = \begin{pmatrix} 1/2(g_2 + g_1) + E_1(B) & 1/2(g_2 - g_1) \\ 1/2(g_2 - g_1) & 1/2(g_2 + g_1) + E_2(B) \end{pmatrix} \tag{5.4}$$

This system now looks exactly as the coupling of two atomic states via a light field or a microwave, and one can calculate a generalized Rabi frequency:

$$\Omega_{\text{SCC}} = \sqrt{\Delta E(B)^2 + (g_2 - g_1)^2}\hbar \tag{5.5}$$

This model would predict oscillation of a minimum frequency given by the difference of the $g_{2,1}$ at $\Delta E = 0$, which can be the case at $B = 0$ or at finite magnetic field for heteronuclear atoms, see Figure 5.2. However, as also pointed out by [62], this simple model gives a wrong prediction: At $\Delta E = 0$ they observe a suppression of spin oscillations, and the full many body theory predicts vanishing oscillations at this point.

Therefore, a more rigorous model has to be applied, which accounts for the interactions in the many body system.

5.1.2 Mean-Field Description

The full despription of the many body system of a condensed spinor gas includes, besides the coupling terms and the Zeeman detuning, also all state-dependend interactions as well as spatial degrees of freedom, which was missing in the previous section.

For simplicity, we will now discuss the homonuclear case of indistinguishable spin-1 particles. The full Hamiltonian in this system is given by [44, 73]:

$$\begin{aligned}\mathcal{H} = \int \mathrm{d}\mathbf{r}\Bigg(&\frac{\hbar^2}{2M}\nabla\hat{\Psi}_i^+ \cdot \nabla\hat{\Psi}_i + U\hat{\Psi}_i^+\hat{\Psi}_i \\ &+ \frac{c_0}{2}\hat{\Psi}_i^+\hat{\Psi}_j^+\hat{\Psi}_j\hat{\Psi}_i + \frac{c_2}{2}\hat{\Psi}_k^+\hat{\Psi}_i^+\mathbf{F}_{ij}\cdot\mathbf{F}_{kl}\hat{\Psi}_j^+\hat{\Psi}_l^+\Bigg)\end{aligned} \tag{5.6}$$

Here Ψ_a^+ (Ψ_a) is the creation (annihilation) operator for an atom in the state a; the atom's mass is M. The external potenial U consists of the trapping potential V which is the same for all states in the optical dipole trap. For small magnetic fields, the Zeeman energy E_i will consist only of the quadratic shift, since the linear one cancels in the homonuclear case.

The atomic interaction can be expressed by the two simple parameters c_0 and c_2, depending on the scattering lengths of the molecular channels as

$$c_0 = 4\pi\hbar^2(2a_2 + a_0)/3M \tag{5.7}$$

$$c_2 = 4\pi\hbar^2(a_2 - a_0)/3M, \tag{5.8}$$

and are similar to the previously used numbers g_1 and g_2 or their sum and differences, respectively, up to prefactors.

The vector $\mathbf{F}$ contains the spin-1 matrices, in explicit form:

$$\mathbf{F}' = \begin{pmatrix}S_x & S_y & S_z\end{pmatrix} = \frac{\hbar}{\sqrt{2}}\left(\begin{pmatrix}0&1&0\\1&0&1\\0&1&0\end{pmatrix}\quad\begin{pmatrix}0&-i&0\\i&0&-i\\0&i&0\end{pmatrix}\quad\begin{pmatrix}\sqrt{2}&0&0\\0&0&0\\0&0&-\sqrt{2}\end{pmatrix}\right) \tag{5.9}$$

This rather complex and very compact notation of $\mathcal{H}$ contains a lot of information; two examples shall help to clarify the situation:

The scattering of two particles in $|1,1\rangle$ is given by a_2. This can be seen by setting $i = j = 1$. The matrix entries for x and y are zero, while for z it equals $\sqrt{2}$. Therefore the interaction is

$$a_{11} \propto c_0/2 + c_2/2 \propto (a_0 + a_2)/3 + (a_2 - a_0)/3 = a_2, \tag{5.10}$$

in agreement with the projection onto the molecular state.

For the case of two atoms colliding in the $|1,0\rangle$ state, the direct interaction is given by $c_0/2$, since the matrix entries all vanish, therefore

$$a_{0,0} \propto c_0/2 \propto (2a_2 + a_0)/3. \tag{5.11}$$

The other scattering lengths are given by:

$$a_{11} = a_{-1-1} = a_{10} = a_{-10} = a_2 \tag{5.12}$$

$$a_{00} = (2a_2 + a_0)/3 \tag{5.13}$$

$$a_{1-1} = (a_2 + 2a_2)/3 \tag{5.14}$$

For the experiments presented below, we are only interested in large occupations of the states. Therefore quantum fluctuations play no role and the creation/annihilation operators $\hat{\Psi}$ can by replaced by the macroscopically occupied wave functions Ψ. This has an important effect in the case of non-seeded coherent spin changing collisions induced by quantum fluctuations as will be mentioned below, but those are not investigated experimentally here.

With these values one can re-write the Hamiltonian using the wave functions Ψ_1, Ψ_2, Ψ_3 of the single components. We will neglect all additional proportionality factors here, which means that we set $4\pi\hbar^2 = 1, M = 1/9$, so that $c_0 = 2a_2 + a_0$, $c_2 = a_2 - a_0$. This reduces the complexity of the matrix and allows to concentrate on the scattering length entries:

$$H_{\text{int}} = \begin{pmatrix} 3a_2(\Psi_1^2 + \Psi_2^2) + (a_2 + 2a_0) \cdot \Psi_3^2 & (a_2 - a_0) \cdot \Psi_2 \cdot \Psi_3^* & 0 \\ (a_2 - a_0)\Psi_2^* \Psi_3 & 3a_2 \cdot (\Psi_1^2 + \Psi_3^2) + (2a_2 + a_0)\Psi_2^2 & (a_2 - a_0) \cdot \Psi_2 \Psi_1^* \\ 0 & (a_2 - a_0) \cdot \Psi_2^* \Psi_1 & 3a_2 \left(\Psi_3^2 + \Psi_2^2\right) + (2a_2 + a_0) \cdot \Psi_1^2 \end{pmatrix} \tag{5.15}$$

We choose this explicit depiction of the matrix form for didactial reasons, since it allows to directly plug in the scattering lengths known from the Feshbach studies, and it is also used in this form for the numerical simulation discussed at the end of this chapter. In terms of c_0 and c_2 the matrix representation reads

$$H_{\text{int}} = \begin{pmatrix} (c_2 + c_0)\left(\Psi_1^2 + \Psi_2^2\right) + (c_0 - c_2)\Psi_3^2 & c_2 \cdot \Psi_2 \cdot \Psi_3^* & 0 \\ c_2 \Psi_2^* \Psi_3 & (c_2 + c_0)(\Psi_1^2 + \Psi_3^2) + c_0 \Psi_2^2 & c_2 \Psi_2 \Psi_1^* \\ 0 & c_2 \cdot \Psi_2^* \Psi_1 & c_2 + c_0 \left(\Psi_3^2 + \Psi_2^2\right) + (c_0 - c_2)\Psi_1^2 \end{pmatrix} \tag{5.16}$$

Here the diagonal terms give the mean-field shift of the different states with the corresponding intra- and interstate scattering properties. The non-zero off-diagonal terms give rise to the spin-coupling, as atoms in one state are annihilated and created in another one. The structure thus is of the form:

$$H = \begin{pmatrix} MF & SCC & 0 \\ SCC & MF & SCC \\ 0 & SCC & MF \end{pmatrix} \tag{5.17}$$

This notation is also helpful to understand the effect of the seeding as mentioned above: If one or both states in the coupling terms (SCC) are zero, i. e. all atoms are perpared in $|1,0\rangle$ or in a superposition of $|1,0\rangle$ and $|1,1\rangle$, all SCC-terms vanish as $\Psi_{-1} = 0$, and no dynamics will happen at all.

This also shows a limitation of the mean field approach wich is of course wrong for low occupation numbers, especially for zero occupation, since the quantum fluctuations then dominate. Indeed, quantum fluctuation-driven spin changing collisions without seed can and have been studied. [93, 20, 79, 26, 38]

The operators for the wave functions evolve according to the Heisenberg operator equation of motion

$$\frac{\mathrm{d}}{\mathrm{d}t}\Psi(t) = \frac{\partial}{\partial t}\Psi(t) + \frac{i}{\hbar}[H(t), \Psi(t)], \tag{5.18}$$

which for our case results in a set of coupled Gross-Pitaevskii equations. This is the point where the numerical simulation starts, which also takes the external potential and the (spatially-dependend) Zeeman shift into account, and allows for spatial degrees of freedom.

For an analytic treatment and many experimental realizations, however, an important simplification can be made, which is the single mode approximation. Here, the spatial mode function is the same for all three spin states and can be adapted from the Hamiltonian neglecting the spin-dependend c_0 part. This approximation is valid if $c_2 \ll c_0$ which is the case for the work horse rubidium ($c_0 > 300 \cdot c_2$) as well as for sodium ($c_0 > 15 \cdot c_2$). For ^{7}Li, however, they differ only by a factor of 2.

We will not provide the full analytic solution here which is rather involved, but refer to [105], where the equations are solved for both ^{87}Rb and Na in the $|f = 1\rangle$ manifold, i. e. for the ferromagnetic and antiferromagnetic case, respectively.

In contrast to the purely sinusoidal oscillations one would expect from the simple approach in Equation 5.5, the solutions have the form of a classical non-rigid pendulum. We will concentrate on the Na case as we can compare this to our experimental findings. Two scenarios have to be distinguished which depend on the spinor phase, which is mainly given as the relative phase between the $|1,0\rangle$ and the side modes, as discussed below. In our experiments, this phase is zero. Also, in the experiments the magnetization is chosen to be zero, meaning equal population in the side modes. As the coupling is done via a resonant three-level Rabi pulse, the initial state preparation is about 50% in the $|1,0\rangle$ mode and 25% in each of the side modes.

For this initial preparation, one gets the resonance feature of the non-rigid pendulum, where the magnetic offset field is the scanned parameter. For zero field, where all states are degenerate and only the scattering lengths differ, the oscillation amplitude vanishes for a spinor phase $\vartheta = 0$. It increases then up to the resonance where $q = c_2 \cdot \bar{n}$, with the mean density $\bar{n}$ and the quadratic Zeeman detuning parameter q, i. e. at a point where the Zeeman shift is the same as the spin coupling term. Up to this point, the oscillation period also rises, meaning slower oscillations. This regime corresponds to the periodic oscillations of the pendulum.

For higher magnetic fields, both the amplitude and oscillation period drop, and small, fast oscillations remain, corresponding to the running phase solutions of the pendulum. The numeric simultations shown in Figure 5.1 can reproduce this behaviour and are shown here for reference.

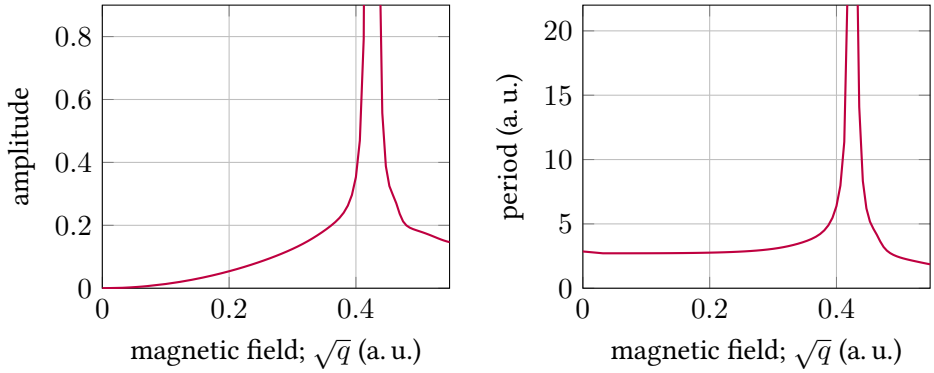

Figure 5.1: Amplitude and period for numerically simulated spin changing collisions vs. detuning, with initial $|1,0\rangle$ state population of 50% and spinor phase $\vartheta = 0$. The divergence in the amplitude is due to fit problems. Details will be explained in section 5.2. The x axis is the square root of the detuning, thus linear in the magnetic field.

In the experiment, the coupling pulse might be off-resonant, leading to a smaller population in the $|1,0\rangle$ mode; this shifts the point of zero oscillation amplitude to finite magnetic fields, which can also be seen in Figure 5.6.

5.1.3 Detuning in Finite Magnetic Fields

As mentioned above, the energy shift due to the (quadratic) Zeeman shift is an important parameter which controls the detuning and resonance behaviour of spin dynamics. For the homonuclear case, this parameter mostly is rather simple, as in the spin 1 systems it is only one number related to the process of $|1,0;1,0\rangle \Longleftrightarrow |1,1;1,-1\rangle$: The quadratic Zeeman shift, see subsection 5.4.2. For ^{87}Rb, this shift is rather small with 71.9 Hz/G^2, while Na shows a larger shift of 277.3 Hz/G^2 and ^{7}Li has the strongest quadratic shift[1] of 611.5 Hz/G^2. For typical trap parameters and atom numbers, the resonance condition $q = c_2\bar{n}$ is met in the range of a few 100 mG which is a very convenient scale where active magnetic field stabilization can be used and external influences are still comparatively small, see subsection 3.3.2.

For the heteronuclear case, the shift in the magnetic field offers more possibilities. This stems from the larger number of possible spin combinations and the difference in quadratic shifts. In these systems, the dependence on the magnetic field is more complex. Fortunately though, one can easily calculate the full Breit-Rabi formula for all states if the numbers for hyperfine splitting, nuclear g factors etc. are known well enough. The possible scenarios for spin changing collisions and the respective detunings are shown in Figure 5.2.

In most calculations and discussions about spin dynamics, the parameter q is mostly given per atom; since always two atoms are taking part in the spin exchange processes, the numbers in Figure 5.2 are twice as high as this parameter, since the energy for the total process is plotted. For the heteronuclear processes, this is a clearer depiction, since the total energy differences enter the calculations. Therefore, for $B = 1$ G, the homonuclear curves show the values $\delta E = 2 \cdot q$.

[1] It is interesting to note that the ratio of the quadratic Zeeman shifts for ^{87}Rb and ^{7}Li equals $e \cdot \pi$ to within 0.4%.

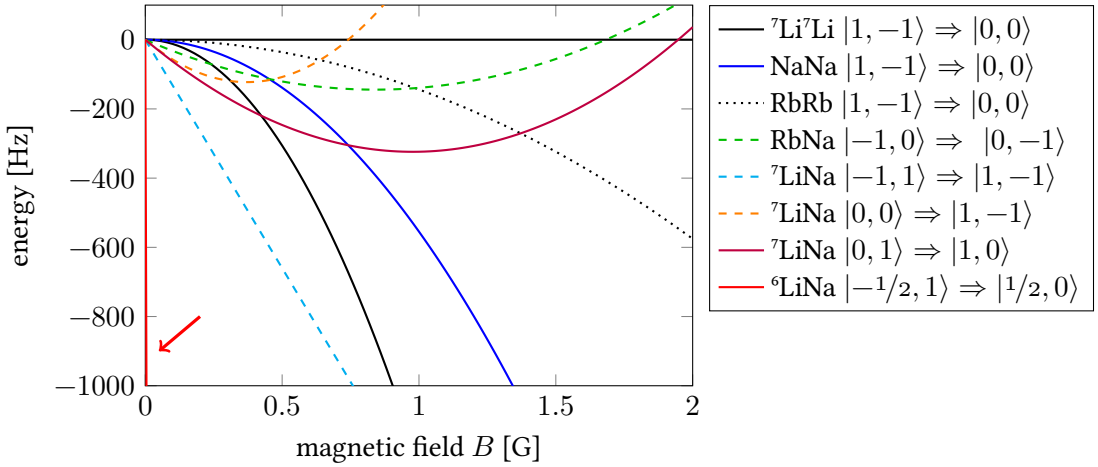

Figure 5.2: Possible scenarios for spin changing collisions. The first ket in the legend entries denotes the state combination with the higher energy. This means that the process $|1,1;1,-1\rangle \Longrightarrow |1,0;1,0\rangle$ is exotherm, releasing the plotted energy. All processes are in the $|f=1\rangle$ or $|f=1/2\rangle$ manifold, respectively. The dashed-plotted state combinations have not been investigated and are shown for comparison and future possibilities. The ^{6}LiNa line is nearly invisible in this scale due to the huge differential *linear* Zeeman shift. Shown is the energy of the pairs, so the q parameter used in the homonuclear SCC is half of this.

For the successful observation of heteronuclear spin changing collisions, the bosonic mixtures are more promising than the Fermi-Bose mixture. In case of ^{7}LiNa or RbNa, one can choose between different spin combinations. The advantage is that the zero detuning is at a rather large field where the homonuclear dynamics can already be suppressed, especially if the density is chosen low enough, so that only the interspecies effects should dominate. Also, preparing the single species in a superposition of only $|1,1\rangle$ and $|1,0\rangle$ will suppress the homonuclear dynamics strongly since there is no seed in the $|1,-1\rangle$ state.

The Fermi-Bose mixture, on the other hand, provides a huge challenge, which is obvious from the fact that the red ^{6}LiNa line nearly is not visible on the scale of the other species and combinations: The (comparatively) huge differential linear Zeeman shift gives an immense energy scale which is far beyond any other scale in the system for even a total field of a few milligauss and will only allow very far detuned dynamics if at all. So the main challenge here is to reduce the offset field. On the other hand, the very low field will again suppress the homonuclear spin dynamics of the bosonic component, similar to the high field on the other side of the homonuclear resonance. Of course, the RF coupling to the Bosons will always populate all states.

5.1.4 The Spinor Phase

The initial phase of the spin dynamics is determined by the sign of the interaction parameter c_0 (i. e. ferromagnetic, $c_0 < 0$, or antiferromagnetic, $c_0 > 0$) and also by the spinor phase, given by

$$\vartheta = \vartheta_1 + \vartheta_{-1} - 2 \cdot \vartheta_0, \tag{5.19}$$

i. e. the relative phase between the side modes and the $m_f = 0$ mode. For most of the homonuclear measurements shown here, the atoms are condensed in the $|1, 1\rangle$ state, followed by a Rabi coupling with a $\pi/2$ pulse to the superposition of equal side mode population, with 50% in the $|1, 0\rangle$ mode. This pulse corresponds to rotation of the vector (001) by $\pi/2$ around the x axis with the spin-1 matrix S_x.

$$\vartheta_1 = 0, \vartheta_0 = -\pi/2, \vartheta_{-1} = \pi \Rightarrow \vartheta = 2\pi = 0. \tag{5.20}$$

The same phase would result from a start in $|1, -1\rangle$, which is common in experiments that trap the atoms directly in the $|1, -1\rangle$ state in a magnetic trap, just inverting the role of $|1, 1\rangle$ and $|1, -1\rangle$, resulting in the same dynamics.

The alternative way of preparing a $(0.25, 0.5, 0.25)$ superposition, which was not reliable in our experiments, would have had a step in-between: The preparation of all atoms in $|1, 0\rangle$. This can be done via a rapid adiabatic passage, which must happen at a higher magnetic field where the quadratic shift clearly separates the transitions. Then, a magnetic field ramp to the final field is needed.

Another approach would be a transition to the $|2, 1\rangle$ or $|2, 0\rangle$ state and then to $|1, 0\rangle$, but this requires a stable upper state, which is not available for sodium. A STIRAP process where the upper state is never populated, but the population can be adiabatically shifted to $|1, 0\rangle$ could be a possible solution, but requires very precise control over the microwave radiation. In principle, the DDS setup presented in section 3.2 could provide the necessary frequency and power ramps, but this was not further investigated.

After preparation of the $|1, 0\rangle$ state, a $\pi/4$ pulse then will also result in 50% of the population remaining in the $|1, 0\rangle$ mode, with 25% population in each of the side modes. The resulting spinor phase is then

$$\vartheta_1 = \pi/2, \vartheta_0 = 0, \vartheta_{-1} = \pi/2 \Rightarrow \vartheta = \pi. \tag{5.21}$$

While 0 and π are the only spinor phases that can be produced by the Rabi coupling, arbitrary phases can be realized if the spinor gas is held for example at a high magnetic field, where the single components have different energies and thus different phase evolutions. After the corresponding hold time, the field can be ramped to the final field where the dynamics start. As the ramping of fields is rather slow and uncontrolled, a better way to achieve this is applingy a microwave dressing to one of the states, to induce the phase shift. This radiation can be very well controlled and turned on and off instantaneously.

Finally, a less controlled way of changing the spinor phase depends on the initial population of the Zeeman substates. In our preparation scheme, where only $|2, 2\rangle$ atoms are in the magnetic trap, which are transferred to $|1, 1\rangle$, the initial preparation in this state is very clearly defined. Another approach of cooling sodium is to load the atoms into the dipole trap directly from the MOT. The atoms are then distributed in all Zeeman states. Applying a magnetic field gradient during the cooling changes the magnetization of the sample, as e. g. the $|1, 1\rangle$ atoms are expelled

from the trap, leaving the $|1,-1\rangle$ atoms as energetically lowest state. However, in this scheme small populations of $|1,0\rangle$ can remain and thus change the spinor phase; this has been reported in [9]. The spinor phase can be used as a fit parameter to the experimental results, since the magnetic field dependence of oscillations amplitude and frequency depends on the phase.

The effect of the initial spinor phase onto the spin dynamics is experimentally easily distinguishable: Starting from the superposition with 50% population in the $|1,0\rangle$ state, this population will increase for $\vartheta = \pi$ and decrease for $\vartheta = 0$. For the first experimental signature of spin changing collisions therefore one expects a decrease in the $|1,0\rangle$ mode, while an increase would not suit the predictions and indicate additional, uncontrolled, spin dynamics. Also, for both settings the $|1,0\rangle$ population always stays below ($\vartheta = 0$) or above ($\vartheta = \pi$) the initial preparation; any deviation from this can only result from multimode dynamics and incoherent drifting into the ground state, as will be explained later.

5.1.5 Coherent Dynamics in a Thermal Gas

The quantum degerenate state of a Bose-Einstein condensate is often thought of as a textbook example for coherent many body dynamics. This is most obviously true for the external degree of freedom, where collective oscillation modes show the coherence of the process.

On the other hand, the internal degrees of freedom do not necessarily depend on the external ones and thus coherent spin dynamics are also possible in a purely thermal gas. This has been shown just surprisingly recently, considering that the production of a single mode Bose-Einstein condensate is much more challenging than the preparation of a cold thermal cloud.

[77] nicely showed coherent oscillations in cold thermal sodium and compared the findings to a single-mode as well as a multi-mode BEC. [63] investigated the effects of the interaction between a thermal and a condensed spinor gas with the result of an increased domain separation due to large spin waves in the thermal part.

The theoretical description shown here closely follows the experimental paper [77]; in-depth theoretical discussions can be found in [25, 72, 71].

For the description in second quantization of an atomic spinor gas with a quadratic Zeeman shift given by q, the Hamiltonian has been shown in Equation 5.6.

For a thermal gas of spin-1 Bosons, none of the condensate modes is macroscopically occupied, thus $\left\langle \hat{\Psi}_i \right\rangle = 0$ for all spin states, and the spatial and momentum distributions are constant, given by the trap potential only. With this, one can introduce the Wigner density operator [108]:

$$\hat{f}_{ij}(\mathbf{r},\mathbf{p}) = \int \mathrm{d}\mathbf{r}' \, e^{i\mathbf{p}\cdot\mathbf{r}'/\hbar} \hat{\Psi}_j^\dagger(\mathbf{r}-\mathbf{r}'/2)\hat{\Psi}_i(\mathbf{r}-\mathbf{r}'/2) \tag{5.22}$$

The further derivation uses the assumption that the momentum and spatial degree of freedom are given by a Boltzmann distribution, therefore separating from the spin states. Integration over the spatial and momentum coordinates, gives the equation of motion

$$i\hbar\partial_t \sigma = [\sigma, M_{\mathrm{TG}}] \tag{5.23}$$

with $\sigma_{ij} = \sqrt{\rho_i}\exp(-i\vartheta_i)\sqrt{\rho_j}\exp(i\vartheta_j)$ containing the spinor information. ρ_i is the population of the state $|i\rangle = |1,1\rangle$, $|1,0\rangle$, or $|1,-1\rangle$, and ϑ_i the corresponding phase. The matrix

M_{TG} contains the coupling and quadratic Zeeman shift for the thermal gas:

$$M_{\mathrm{TG}} = 2c_2\bar{n}\mathrm{Tr}(S_i n)S_i + qS_z^2, \tag{5.24}$$

with the mean density

$$\bar{n} = \int \mathrm{d}\mathbf{r}[Tr(n(\mathbf{r}))]^2/N, \tag{5.25}$$

and the density distribution

$$n(\mathbf{r},t) = \int \mathrm{d}\mathbf{p}/(2\pi\hbar)f(\mathbf{r},\mathbf{p},t). \tag{5.26}$$

Note that the *mean density* for a thermal gas cannot just be calculated by summing over all atoms and dividing by the volume; this would result in zero.

For the BEC case, the analog formulation is given by

$$i\hbar\partial_t\tau = [\tau, M_{\mathrm{BEC}}] \tag{5.27}$$

with $\tau_{ij} = \psi_i^*\psi_j$, and

$$M_{\mathrm{BEC}} = c_2\bar{n}\mathrm{Tr}(S_i n)S_i + qS_z^2. \tag{5.28}$$

Comparing Equation 5.24 with Equation 5.28, one finds that the thermal dynamics are similar to the BEC case, just with a factor of 2 in the coupling term. This allows an easy comparison of the two cases experimentally by scaling the density correspondingly.

5.1.6 Multimode Dynamics

For the physics discussed so far, the external degrees of freedom were not considered, since the SMA for a BEC and the Boltzmann distribution for the thermal gas assume a time independent density distribution which is the same for all components. But for a dense Bose-Einstein condensate in a rather shallow trap, this approximation is not given anymore. The number of merit for this case is the spin healing length ξ_s given by [9]

$$\xi_s = \frac{2\pi\hbar}{\sqrt{2m|c_2|n}}. \tag{5.29}$$

This gives a length scale on which the condensate can react in the spin degree of freedom, very much like the ordinary healing length [78]

$$\xi = \frac{\hbar}{\sqrt{2mnU_0}} = \frac{1}{\sqrt{8\pi na}} \tag{5.30}$$

gives the length scale on which the condensate can react on spatial disturbances.

For the typical *large* sodium BEC in our setup, the mean spin healing length is about 17 µm, and the healing length at the maximum density about 11 µm. Both numbers are smaller than the diameter of the cloud, calculated as twice the Thomas-Fermi radius, in our system:

$$2 \cdot r_{\mathrm{TF},x,y,z} = 2 \cdot (10\,\mu\mathrm{m}, 14\,\mu\mathrm{m}, 6\,\mu\mathrm{m}). \tag{5.31}$$

Therefore the BEC cannot react on the spin dynamics as a whole, but will start forming domains where the spincomponents separate, which is energetically favourable for the antiferromagnetic interaction present in the sodium gas.

Without damping and decoherence effects, these domains will oscillate spatiall in a rich variety of frequencies; this will be discussed shortly in the numeric simulations. For the experiment, the damped case is more important, as the system evolves into equilibrium by forming domains in the presence of a magnetic field gradient.

5.2 Numerical GPE Simulation

Since the full description of the many body spin dynamics is rather involved, the following section presents the resuls of a quite simple numerical calculation for a spinor condensate with three components in one dimension. This can easily be extended to higher dimensions and also to more than one species.

For simplicity, only a pure BEC (that is, a gas with temperature far below the critical temperature) is considered, since the combination of a thermal gas and a BEC makes the description much more involved. In the BEC case, the ground state in the trap is given by the time-independent Gross-Pitaevskii equation (GPE) [81, 39], and the whole dynamics are goverend by the time-dependent GPE:

$$i\hbar\frac{\partial\psi}{\partial t} = \left(-\frac{\hbar^2}{2m}\frac{\partial^2}{\partial x^2} + V(x) + (N-1)\frac{4\pi\hbar^2 a}{m}|\Psi|^2\right)\Psi, \tag{5.32}$$

where the external potential $V(x)$ is here taken as constant in time, and N is the particle number.

In numeric simulations, it is useful to translate this equation containing physical units into a purely numeric version. This makes the interpretation of the results easier and avoids problems with very small numbers that might be limiting due to the finite precision of the software.

To this end, one can first define a natural length scale L from which most other transformations follow. In the case of BECs, the typical extensions are a few to several tens of micrometers, so we choose $L = 1\,\mu\text{m}$. This determines an energy scale

$$E_R = \frac{\hbar^2}{mL^2} = 2.915 \times 10^{-31}\,\text{J} = h \cdot 440\,\text{Hz} \tag{5.33}$$

with the particle's mass m chosen for sodium. Dividing both sides of Equation 5.32 gets rid of the energy unit, leaving all energy scales in units of E_R.

The term on the left-hand side of Equation 5.32 then reads

$$\frac{i\hbar\frac{\partial}{\partial t}}{E_R} = i\frac{mL^2}{\hbar\tau}\frac{\partial}{\partial\tilde{t}}, \quad \text{with a time scale } \tau = \frac{\hbar}{E_R} \tag{5.34}$$

and $\tilde{t}$ the time in units of τ.

For the remaining terms of the right-hand side of Equation 5.32, one gets the expression

$$\frac{\hbar^2}{2mE_R}\frac{\partial^2}{\partial x^2} = \frac{L^2}{2}\frac{\partial^2}{\partial x^2} = \frac{1}{2}\frac{\partial^2}{\partial\tilde{x}^2}, \tag{5.35}$$

with $\tilde{x}$ as the scaled spatial coordinate. The potential is also expressed in E_R:

$$\frac{V(x)}{E_R} = \tilde{V}(\tilde{x}) \tag{5.36}$$

In the numerics, the wavefunction is normalized to 1, therefore the whole expression for the nonlinearity, depending on the particle number N and the scattering length a will be expressed by one parameter η, in units of E_R.

With these substitutions, the numbers for the conversion are:

$$x = 1\,\mu\text{m} \times \tilde{x} \tag{5.37}$$

$$t = 0.36\,\text{ms} \times \tau \tag{5.38}$$

$$E = 2.915 \times 10^{-34}\,\text{J} \cdot \tilde{E} = 2\pi \cdot 440\,\text{Hz} \cdot \tilde{E} \tag{5.39}$$

To get a realistic simulation, the trap parameters and particle numbers are adjusted in the numerics in such a way that the scaled extension and chemical potential are close to the experimental realization, i. e. in dimensionless units a BEC Fermi radius of about 5, and a chemical potential on the order of 5, corresponding to 5 µm and 2.2 kHz, typical numbers for our experiment.

For all numeric simulations here, we make use of the very flexible GPElab code [3, 4]. This toolbox for the Matlab software allows both the numerical calculation of ground state wave functions as well as the dynamics of arbitrary states in 1, 2, or 3 dimensions. Here, only a small part of the possibilities is used to find the ground state for a scalar BEC, and the dynamics for a spinor BEC with spin coupling. As in the formulation of the GPE above in Equation 5.32, the potential is assumed to be time-independent, as well as the Zeeman shift. A drift of the magnetic field in the experiment could easily be implemented by adding it to a time-dependent potential.

5.2.1 Ground State Calculation

The first step for the simulations is the calculation of the ground state for only one component. This copies the experimental ansatz of producing a BEC at given field and trap frequencies and then applying the coupling pulse, which is thought of being instantaneous. This leads to a quench of the system into a non-equilibrium state and induces the dynamics.

This ground state is calculated using the imaginary time method [1], also called projected gradient method [7], which is implemented in the GPElab software.

Since this thesis is experiment-based, only a one dimensional simulation was done, which can be calculated fast enough on a regular personal computer to allow a quick qualitative comparison to the experimental results.

To be able to compare the results as good as possible, the chemical potential and trapping frequencies were chosen in a way that after the scaling shown above, they are on the order of the real experimental data. The most interesting point for a numerical simulation is not directly the coherent oscillation dynamics, as these can be calculated analytically in the SMA, but mostly in the multimode behaviour and the phase separation, as these cannot easily be described by the analytic solutions. Therefore, especially the cases of a high chemical potential are most

interesting here, since the small spin healing length starts to induce spatial dynamics of the different spin states.

The following code shows the full Matlab input needed to get the ground state computation using the GPElab code.

```
%% Setting the method and geometry
Computation = 'Ground'; Ncomponents = 1; Type = 'BESP';
Deltat = 1e-1; Stop_time = []; Stop_crit = {'MaxNorm',1e-9};
Method = Method_Var1d(Computation, Ncomponents, Type, Deltat,
    Stop_time, Stop_crit);
xmin = -18; xmax = 18; Nx = 2^8+1;
Geometry1D = Geometry1D_Var1d(xmin,xmax,Nx);
Potential = @(Z) Z.^2/2;
Delta = 1; Beta = 1;
Physics1D = Physics1D_Var1d(Method, Delta, Beta);
Physics1D = Potential_Var1d(Method, Physics1D, Potential);

aB = 5.29e-11; a2 = 52*aB; a0 = 46*aB; N = 1; eta = 8e8;
lambda_s = 4*pi*N*(a0+2*a2)/(3)*eta;
Nonlinearity = @(Psi,Z) lambda_s*abs(Psi).^2;
Physics1D = Nonlinearity_Var1d(Method, Physics1D, Nonlinearity);
%% Setting the initial data
InitialData_Choice = 1;
Phi_0 = InitialData_Var1d(Method, Geometry1D, Physics1D,
    InitialData_Choice);
%% Setting informations and outputs
Outputs = OutputsINI_Var1d(Method);
Printing = 1;
Evo = 15;
Draw = 1;
Print = Print_Var1d(Printing,Evo,Draw);
%-------------------------------------------------------------
% Launching computation
%-------------------------------------------------------------
[Phi_1, Outputs] = GPELab1d(Phi_0, Method, Geometry1D, Physics1D,
    Outputs, [], Print);
```

5.2.2 Preparing the Dynamics

As mentioned above, the dynamics are induced experimentally by a short coupling pulse. For the numerics, this is simulated by initializing the dynamic calculation with a three component spinor. The side modes are populated with 27.5% each, with 45% in the $|1,0\rangle$ mode, as is experimentally observed, instead of the (0.25 0.5 0.25) population which would result from a clear $\pi/2$ pulse. As the experimental realization starts in $|1,1\rangle$, the spinor phase is

$$\vartheta = \vartheta_1 + \vartheta_{-1} - 2 \cdot \vartheta_0 = 0, \tag{5.40}$$

therefore no additional phase offset has to be given to the initial state.

However, for comparison to the case starting in $|1,0\rangle$, a $\pi/4$ pulse leads to a spinor phase $\vartheta = \pi$ which can be distributed to the $|1,0\rangle$ mode or the side modes. This phase also determines the initial dynamics, i. e. an increase or decrease of the $|1,0\rangle$ mode.

The quadratic Zeeman shift is taken into account by adding a constant q to the potential for the side modes, the linear shift cancels in a homogeneous magnetic field.

Since the method is completely flexible, any magnetization, spinor phase, population and potential can be investigated, also magnetic gradient fields which shift the outer parts of the side modes due to the linear Zeeman shift.

Below is the code listing for the dynamic calculation. After setting the calculation method and the parameters, the interaction Hamltonian (`CoupledSpinNL`) is defined. The initial state preparation is performed by setting the three components of `Phi_0` equal to the ground state calculated above, `Phi_1`, times the population.

```
%% Setting the method and geometry for dynamics
Computation = 'Dynamic'; Ncomponents = 3; Type = 'Relaxation';
Deltat = 1e-2; Stop_time = 20; Stop_crit = [];
Method = Method_Var1d(Computation, Ncomponents, Type, Deltat,
    Stop_time, Stop_crit);
xmin = -18; xmax = 18; Nx = 2^8+1;
Geometry1D = Geometry1D_Var1d(xmin,xmax,Nx);

Delta = 1; Beta = 1;
Physics1D = Physics1D_Var1d(Method, Delta, Beta);
Physics1D = Dispersion_Var1d(Method, Physics1D);

q = 0.1; %% homogeneous field
p = 0;   %% gradient field
Potential = cell(3);
Potential{1,1} = @(t,Z) Z.^2/2 + q + Z.*p;
Potential{2,2} = @(t,Z) Z.^2/2;
Potential{3,3} = @(t,Z) Z.^2/2 + q - Z.*p;
Physics1D = TimePotential_Var1d(Method, Physics1D, Potential);

aB = 5.29e-11; a2_Na = 52*aB; a0_Na = 46*aB;
lambda_a = 4*pi*(a2_Na-a0_Na)/(3)*eta;
lambda_s = 4*pi*(a0_Na+2*a2_Na)/(3)*eta;

CoupledSpinNLCoupledSpinNL = cell(3);
CoupledSpinNL{1,1} = @(Psi, Z) (lambda_a+lambda_s)*(abs(Psi{1}).^2+
    abs(Psi{2}).^2) + (lambda_s-lambda_a)*abs(Psi{3}).^2;
CoupledSpinNL{1,2} = @(Psi, Z) lambda_a*Psi{2}.*conj(Psi{3})
CoupledSpinNL{2,1} = @(Psi, Z) lambda_a*conj(Psi{2}).*Psi{3}
CoupledSpinNL{2,2} = @(Psi, Z) (lambda_a+lambda_s)*(abs(Psi{1}).^2+
    abs(Psi{3}).^2) + lambda_s*abs(Psi{2}).^2;
CoupledSpinNL{2,3} = @(Psi, Z) lambda_a*conj(Psi{2}).*Psi{1};
CoupledSpinNL{3,2} = @(Psi, Z) lambda_a*Psi{2}.*conj(Psi{1});
CoupledSpinNL{3,3} = @(Psi, Z) (lambda_a+lambda_s)*(abs(Psi{3}).^2+
    abs(Psi{2}).^2) + (lambda_s-lambda_a)*abs(Psi{1}).^2;
```

```
32
   Physics1D = Nonlinearity_Var1d(Method, Physics1D, CoupledSpinNL);
34 %% Setting the initial data, state preparation
   load Phi_1
36 Phi_0{1} = Phi_1{1}*sqrt(0.275);
   Phi_0{2} = Phi_1{1}*sqrt(0.45)*exp(i*pi);
38 Phi_0{3} = Phi_1{1}*sqrt(0.275);
   %% Setting informations and outputs
40 Save = 0;
   Output_function{1,1} = @(Phi,Z,FFTZ) sqrt(Geometry1D.dx)*sqrt(sum(
      abs(Phi).^2));
42 Output_name{1} = 'L2-Norm␣';
   Outputs = OutputsINI_Var1d(Method,1,1,Output_function,Output_name);
44 Printing = 1;
   Evo = 100;
46 Draw = 1;
   Print = Print_Var1d(Printing,Evo,Draw);
48 %-------------------------------------------------------------
   % Launching computation
50 %-------------------------------------------------------------
   [Phi, Outputs] = GPELab1d(Phi_0, Method, Geometry1D, Physics1D,
      Outputs, [], Print);
52 Draw_Timesolution1d(Outputs,Method,Geometry1D,Figure_Var1d)
```

5.2.3 Single Mode Dynamics

The case where the single mode approximation is valid can be simulated by using a small atom number, resulting in a small nonlinearity. Comparison with analytic results are then benchmarking the simulations, and deviations can be attributed to multimode dynamics.

Figure 5.3 shows the results of this simulation run for different detunings q by plotting the time evolution of the $|1,0\rangle$ population. With an initial preparation of (0.275,0.45,0.275), this setting is in the regime where for $q = 0$ oscillations are expected, in contrast to the case of $\rho_0 = 0.5$.

This is clearly visible, shown by the red curve. The initial feature is the *increase* in the $|1,0\rangle$ mode, which can be intuitively understood as a *negative* amplitude. This amplitude then increases, which means that the absolute value decreases, until it reaches zero for $q = 0.035$. From that on, the amplitude increases again and the oscillations become slower, until the critical detuning is nearly reached around $q = 0.2$. Above the critical point, the amplitude and period decrease again, in accordance with the anayltical expectation.

A striking deviation, however, appears for a certain detuning regime, here shown for $q = 0.5$, where a clear multimode oscillation appears. Figure 5.4 shows the evolution of the density distribution for this case. On the left-hand side, the side modes are shown, as $|1,1\rangle$ and $|1,-1\rangle$ share the same wavefunction in this calculation. The right-hand side shows the $|1,0\rangle$ distribution. The vertical axis is the spatial coordinate, while the abscissa shows the evolution time.

The deviation from the single spatial mode approximation is obvious already after two oscillations, and the change in density and overlap of the components explains the deviation

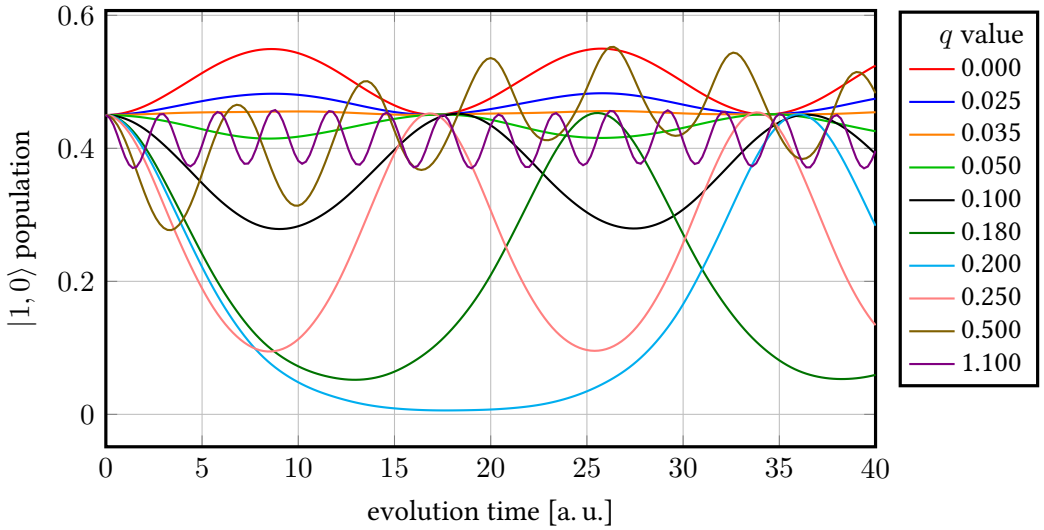

Figure 5.3: Numerically simulated dynamics of the $|1,0\rangle$ population. The initial population preparation is (0.275,0.45,0.275). For $q = 0$, a finite oscillation amplitude is visible, with an *increase* of $|1,0\rangle$. The oscillation amplitude is reduced as q goes to 0.035; from this point on, the amplitude increases again until the $q = 0.2$, close to the divergence, corresponding to the critical $\delta(B_c)$. Above the divergence, period and amplitude of the oscillations are reduced, as expected. For certain detunings, e. g. $q = 0.5$, clear multimode oscillations occur.

seen in Figure 5.3. Note that these spatial structures only appear in a certain range of detunings, while for smaller and larger values the single mode approximation works very well.

To simulate the magnetic field dependence of the oscillation amplitude and period, several numerical runs are executed and the resulting oscillations fitted with a sine curve. For q close to $\delta(B_c)$, this fit of course gets worse, since the functional form deviates strongly from a sine, but still a measure for the important numbers can be extracted. The results of such scans are shown in Figure 5.6, where the field dependence of the oscillations is plotted for different initial populations of ρ_0.

As expected from the analytic results, for $\rho_0 = 0.5$, no oscillations happen at $q = 0$, then the amplitude increases while the period stays constant over a wide range of detunings. Only close to the critical point, the oscillations become slower, ultimately diverging.

The divergence point depends on ρ_0 and increses (decreases) with higher (lower) initial population. For $\rho_0 \neq 0.5$, a finite oscillation appears even for $q = 0$.

In the period in the graph on the right-hand side, the fit does not work if the amplitude is too small, since no meaningful frequency can be fitted. The points that deviate from the expected function are the ones with vanishing amplitude.

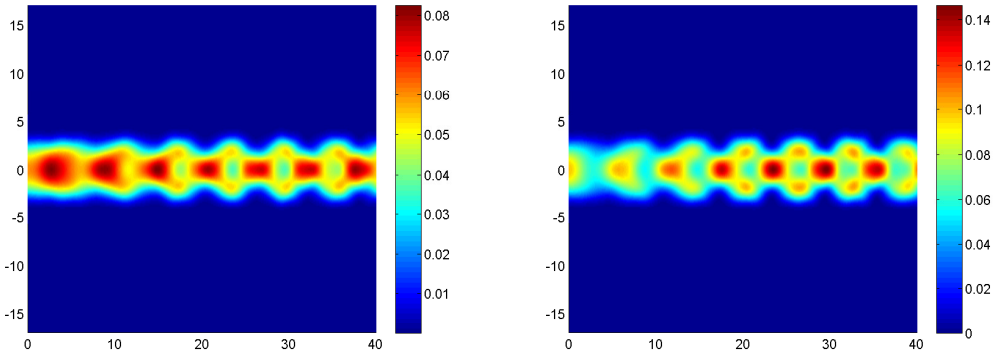

Figure 5.4: Density distribution for the $q = 0.500$ setting. Shown are the probability amplitudes for the $|1, \pm 1\rangle$ mode (left) and the $|1, 0\rangle$ mode (right) vs. the evolution time. Already after two oscillations, a clear spatial structure forms where the side modes are separated from the $|1, 0\rangle$ mode.

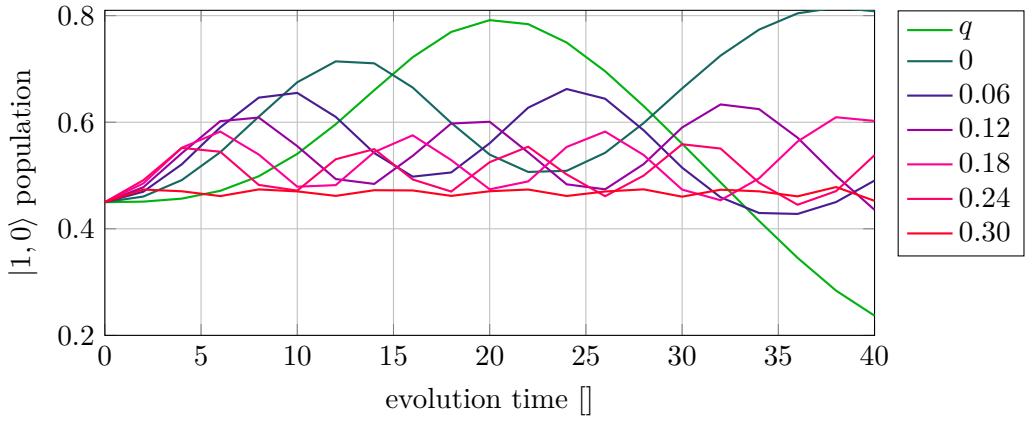

Figure 5.5: Numerical simulation of an antiferromagnetic spinor gas with spinor phase $\vartheta = \pi$. For all detunings, the initial dynamics is an increase of the $|1, 0\rangle$ mod.

5.2.4 Influence of the Spinor Phase and Magnetization

A change of the spinor phase is easily implemented in the numerics by changing the relative phase of the spinor components. From the analytical solution, one finds that the critical field, or rather the corresponding detuning $\delta(B_c)$, depends on the three parameters ρ_0, m, ϑ and the coupling strength $c = c_2\bar{n}$ by

$$\delta(B_c) = c \cdot ((1 - \rho_0) + \sqrt{(1 - \rho_0)^2 - m^2} \cos\vartheta. \tag{5.41}$$

For the experiments, the magnetization was chosen to be zero, achieved by equally populating the side modes, and the $|1, 0\rangle$ population was set to 0.5. Equation 5.41 then takes the simple form

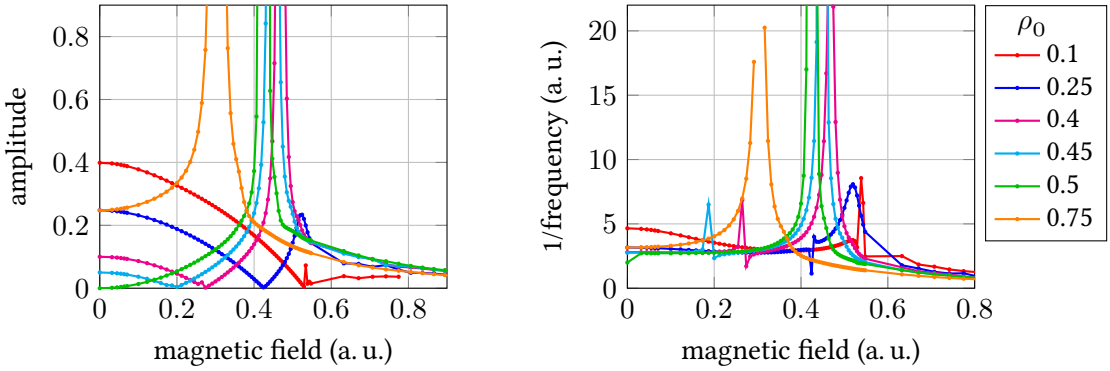

Figure 5.6: Amplitude and period of a sine fit to numerically simulated spin changing collisions in a near-single mode setting. For each simulation run, a sine is fitted to the $|1,0\rangle$ population to get a measure for the amplitude and period, although the exact form deviates from a sine.

$$\delta(B_c) = c \cdot (0.5 + 0.5 \cdot \cos\vartheta). \tag{5.42}$$

Thus, for $\vartheta = 0$, one gets the highest critical field, while for $\vartheta = \pi$, the frequency diverges at $B = 0$. This behaviour is shown in Figure 5.7, where the spinor phase is changed from zero to π and above; due to the periodicity of the cosine, the setting of $\vartheta = 1.2\pi$ equals $\vartheta = 0.8\pi$. The data clearly reproduce the expected scaling, and also show that for larger spinor phases the resonance peak does not only shift, but also broadens. The exact shape of the curve deviates from the analytic calculations especially for large periods, since the fit with a sine then is not good enough; also, small deviations from the SMA start to play a role for these cases.

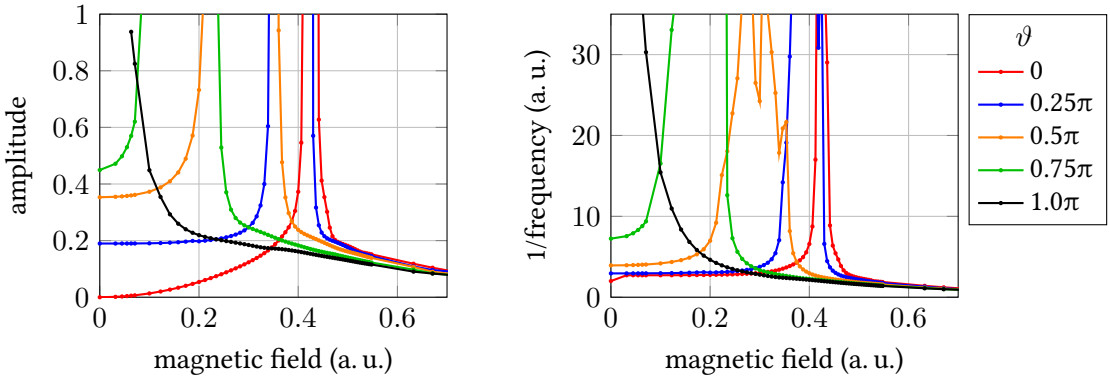

Figure 5.7: Amplitude and period of a sine fit to numerically simulated spin changing collisions in a near-single mode setting. Here, the influence of the spinor phase is shown, as it is varied from $\vartheta = 0$ to $\vartheta = \pi$. For the latter case, the oscillation period diverges for $q \to 0$.

For a fixed populiton of $|1,0\rangle$ of 0.5, one can investigate the effect of the magnetization. (Of course any other population can be chosen, too.) The most interesting feature here is for a magnetization of $m = 0.5$: In this case, only the $|1,0\rangle$ and $|1,1\rangle$ states are populated, but still spin dynamics appear. This clearly shows that the seeding does not have to be in both sidemodes; in the case where all atoms are in $|1,0\rangle$, however, no dynamics happen, as expected. Figure 5.8 shows the field dependence of the oscillations for different values of m.

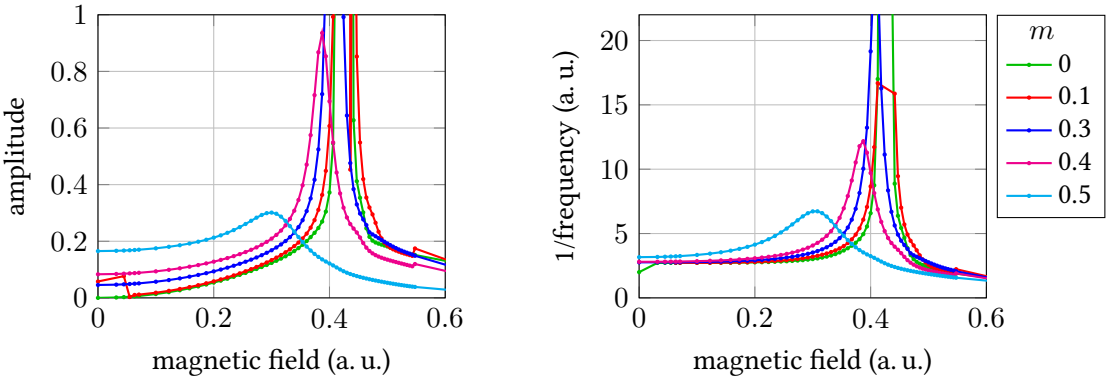

Figure 5.8: Numerically simulated effect of the magnetization on the spin oscillations. For all data, the initial population of $|1,0\rangle$ was 0.5. Larger magnetization leads to a reduction of the critical detuning, according to the analytical result for $\delta(B_c)$.

5.2.5 Multimode Dynamics

The term *multimode* here shall here be used for any spatial dynamics that deviate strongly from the initial ground state preparation. This can be deviations from the initial BEC mode, complete separation of the $|1,0\rangle$ and side modes, up to a seemingly chaotic distribution where numerous small islands of the phases develop.

An interesting case of the spatial deviation is shown in Figure 5.9, where the dynamics initially looks close to single mode, but after reachig a certain density of the $|1,0\rangle$ population, a spatial separation happens, followed by ongoing oscillations.

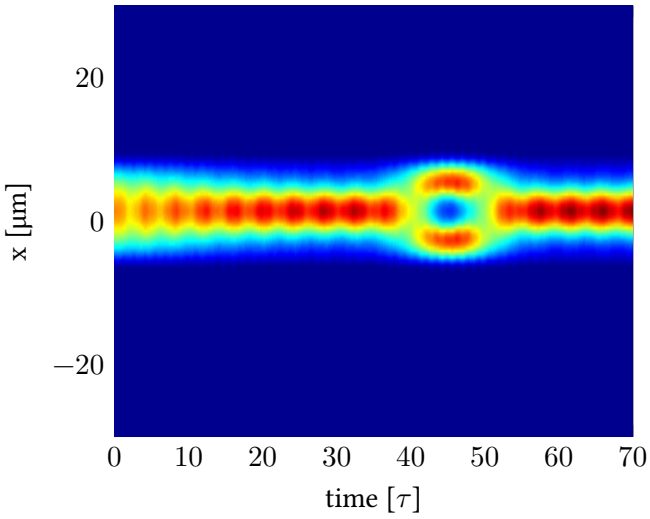

Figure 5.9: One dimensional simulation of spin changing collisions showing multimode dynamics after some evolution time of near-single mode oscillations.

Since the single mode approximation depends on the ratio of spin healing length ξ_s and the condensate extension, a simple way to show strong multimode behaviour is to increase the atom number. This leads to a smaller ξ_s, while the condensate size increases. Figure 5.10 shows this in a dramatic manner: For the same settings as in Figure 5.4, where a separation of both the $|1,0\rangle$ mode and the side modes showed up, the atom number here is increased by a factor of ten.

The behaviour gets very complex, and no clear oscillation structure can be seen. This setting shows dramatically, why an experimental setting where the single mode approximation is valid is important for the observation of coherent oscillations. However, if the imaging resolution of an experimental realization is high enough, the diverse spatial structure offers interesting physics per se.

As a final graphic representation, Figure 5.11 shows the influence of a gradient on the side modes. Without a surprise, the side mode evolves into the direction of the gradient, where the energy is minimized. If any damping or dissipation was implemented in the simulation, the separation would be the final state, as is observed in the spin domain formation experiments. Here, however, the dynamics remain coherent, and the probability distrubution evolves back into the trap center.

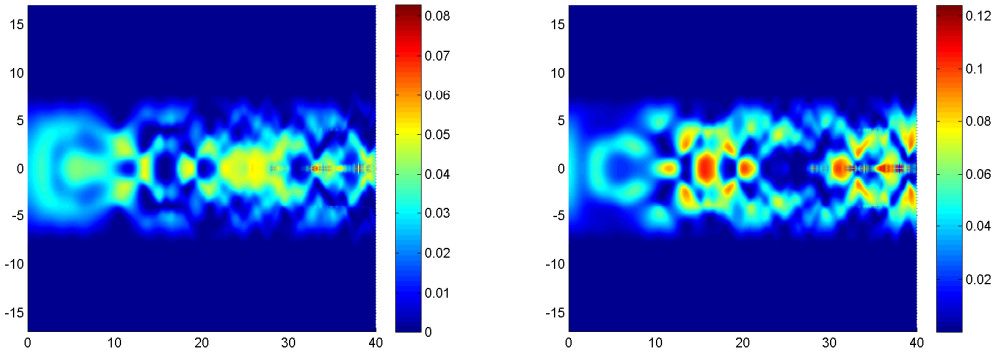

Figure 5.10: Density distribution for the $q = 0.500$ setting with larger atom numbers.

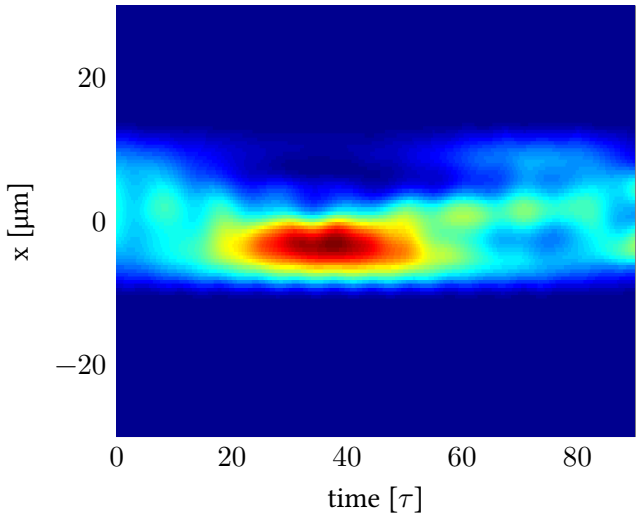

Figure 5.11: One dimensional simulation of spin changing collisions showing clear phase separation, with a finite magnetic field gradient.

5.3 Experimental Results of Homonuclear SCC

This section will present, summarize, and explain the observed spin dynamics in the homonuclear cases. Several different cases ware studied that lead to qualitatively different behaviour:

- Large sodium BEC. Here *large* refers to a high atom number in a rather strong confinement, at high temperatures. Therefore, the thermal part of the cloud can play a role. Also the single spatial mode approximation is not valid as the spin healing length is smaller than the Thomas-Fermi radius in at least one direction.
- Small sodium BEC. Cooled to lower temperatures with smaller atom numbers in a shallower trap, the thermal part can be neglected. The requirements for the single mode approximation are met better.
- Thermal cloud of sodium. The atoms' temperature is close to, but above the critical temperature, in a tighter trap setting, without detectable condensate fraction.
- Condensed ^{7}lithium, which has ferrogmagnetic interaction properties, in contrast to the antiferromagnetic interaction in sodium. In this case, sodium can act as a passive bath, meaning that it only cools the external degree of freedom, while not influencing the internal spin evolution, if it is in the correct hyperfine state.

5.3.1 Non-Seeded Case of a Sodium BEC Evoling Into Equilibrium

One of the first experiments done to observe spin dynamics in Bose-Einstein condensates [99] was the preparation of a pure $|1,0\rangle$ state at a high offset field. Then, the magnetic field was ramped down to different offset fields, and the spin-distribution was observed.

We dub these measurements *non-seeded* since no population was put into the side modes deliberately. However, no special cleaning was done to ensure that no atoms are in the side modes which might be present due to a non-ideal preparation of the $|1,0\rangle$ mode. This is in contrast to experiments with a better atom number detection and cleaning, where the *seed* might contain just a few atoms. For our case, *seeded* always means a macroscopic number and a large relative population in the corresponding modes.

The rate and final offset of this decay depends on the magnetic offset field; the endpoint is given by the equilibrium state of the antiferromagnetic sample. For these measurements, the spatial degree of freedom could not be resolved, so no information is available about phase separation or similar effects, as will be presented below.

But already at this point it should be mentioned that the ground state of an antiferromagnetic spinor gas in a homogeneous magnetic field is the $|1,0\rangle$ state. So the observations can only be explained by assuming a magnetic field gradient over the cloud. This will become more obvious below, where data with spatial resolution are discussed.

The inset shown in Figure 5.12 is a small reminder of the process taking place, where the three lines correspond to the Zeeman levels, with $|1,+1\rangle$ on the left side with the lowest energy, $|1,0\rangle$ in the middle and the $|1,-1\rangle$ state which shifts upwards in a magnetic field. The spheres indicate the population of the states; a large sphere means a large occupation. The arrows indicate the

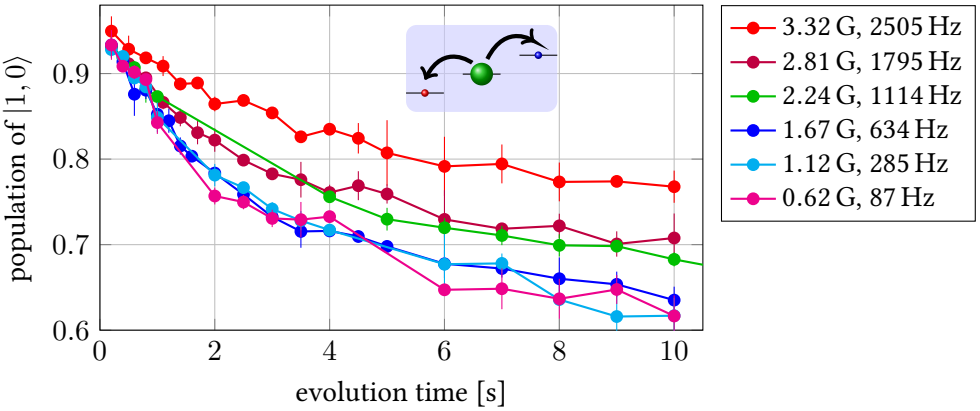

Figure 5.12: Decay of the $|1,0\rangle$ mode of sodium without seeding for different magnetic fields. Only the $|1,0\rangle$ mode population is shown; the side modes are always symmetric as far as our imaging can resolve them. The trend clearly shows a suppression of the spin relaxation for higher magnetic fields; altogether the process is very slow and saturates at different finite populations for different magnetic fields. In the legend, the offset field and the corresponding q_{Na} are listed.

flow of population. All datasets in the remainder of this chapter will be supplemented with these sketches, which will be helpful especially in the combined homo- and heteronuclear dynamics.

Since for the very long hold times shown here the trap losses play an important role, one has to rule out that the relative increase of the side modes is not just due to a reduction of the signal and increased relative noise – without any atoms left, the calculated population in all states would be equal! Therefore Figure 5.13 shows the total atom numbers for the 621 mG case, where the strongest increase in the side modes occurs. For better visibility, the side modes have been magnified by a factor of ten.

During the first about 2 s, a clear increase in the total number of atoms in the side modes is seen, while the $|1,0\rangle$ mode strongly decreases; after that, the total losses dominate and all states loose atoms. Still, the $|1,0\rangle$ mode has the strongest losses, which leads to the further relative increase of the side modes.

For the losses, one has to take care about the condensate fraction: Since the atom numbers in the side modes are small, only the $|1,0\rangle$ mode stays condensed, while the outer modes become thermal. The lower density of this thermal cloud reduces the three-body losses, so that the final state equilibrium overestimates the side modes.

5.3.2 Large Sodium BEC

For the following experiments, a large Bose-Einstein Condensate of around 8×10^5 atoms was prepared in a rather tight dipole trap with trapping frequencies in the order of $\bar{\omega} = (212, 183, 341)$ Hz, with the mean trapping frequency of 236 Hz.

Considering the single spatial mode approximation, one has to estimate the spin healing length as introduced in Equation 5.29. For the numbers mentioned above, the mean density of

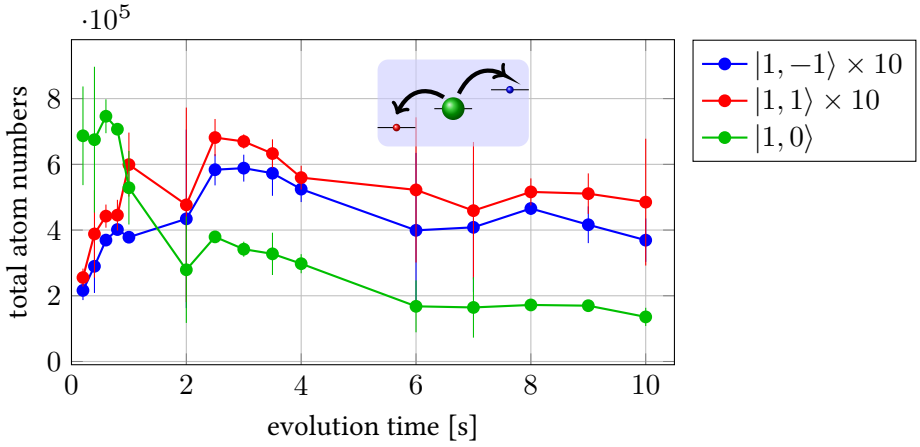

Figure 5.13: Absolute atom numbers durin the decay of the $|1,0\rangle$ mode. The side modes are multiplied by 10 for better visibility. Overall, a clear total decay is visible due to the lifetime in the trap and three-body losses. This decay is the same for all magnetic fields and indicates that the spin relaxation is not the main cause for the losses, which would be field-dependent. The shown case for 621 mG gives the larges increase in the side modes, but a clear signal is visible for all fields.

the BEC is $\bar{n} = 1.4 \times 10^{14}\,\mathrm{cm}^{-3}$ with a maximum density at the center of $n_0 = 3.5 \times 10^{14}\,\mathrm{cm}^{-3}$. The Thomas Fermi radii are

$$r_{\mathrm{TF},x} = 10\,\mu\mathrm{m}, \quad r_{\mathrm{TF},y} = 12\,\mu\mathrm{m}, \quad r_{\mathrm{TF},z} = 6.5\,\mu\mathrm{m}. \tag{5.43}$$

The spin healing length depends on the difference of the a_2 and a_0 scattering lengths, which we take here to be $a_2 = 54.54\,a_B$ and $a_0 = 48.91\,a_B$, as results from the improved NaNa Feshbach spectrum and Coupled Channels calculations by [53]. This gives

$$\xi_s = \frac{2\pi\hbar}{\sqrt{2m|c_2|n}} = 10.6\,\mu\mathrm{m} \tag{5.44}$$

with $c_2 = 4\pi\hbar^2 \cdot (a_2 - a_0)/3m = 5.5 \times 10^{-13}\,\mathrm{Hz/cm^3}$. This indicates that we are in an intermediate regime where the spin healing length is similar, smaller, and larger than the different Thomas-Fermi radii. But since the important number is rather the diameter than the radius, one would expect that the single mode approximation is not valid at the outer parts of the condensate. Therefore, a clear oscillatory behaviour is not visible, but in this regime one can rather study the phase separation dynamics as the system tends into its ground state equilibrium.

Figure 5.14 shows the time evolution of a large Bose-Einstein condensate, prepared from the $|1,1\rangle$ state via a $\pi/2$ pulse into a superposition with equal side mode population. The $|1,0\rangle$ mode does not show an occupation of 50%, which can either indicate detuning or additional, very fast dynamics that cannot be resolved, which drives the system from the (0.25,0.5,0.25) preparation quickly into the observed (0.3,0.4,0.3) state. A similar effect was measured for

the smaller BEC, see for example Figure 5.22. Therefore we assume that the initial dynamcs already happened before the mapping could resolve any effects, and the RF pulse did prepare 50% in $|1,0\rangle$.

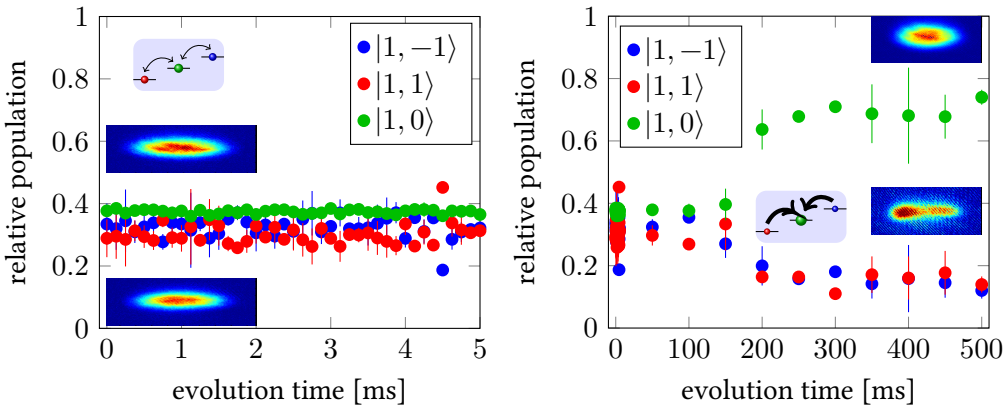

Figure 5.14: SCC of a large Na condensate of 0.6×10^6 to 1.2×10^6 atoms at $q = 21\,\mathrm{Hz}$, $B = 307(3)\,\mathrm{mG}$, showing phase separation. The short-time evolution shows no population changes, while after longer times the $|1,0\rangle$ mode population clearly increases. The insets show absorption images of the atoms after short time of flight, revealing partially the in-situ distribution. The upper pictures show the $|1,0\rangle$ mode, the lower pictures are typical examples of the side mode populations. For this scan, atoms were prepared in $|1,-1\rangle$ before the $\pi/2$ pulse.

The plot shows two distinct features: First, on a long time scale of over 150 ms (right-hand side), there is a clear rise of the $|1,0\rangle$ mode to a large population of about 60% to 80%, while the side modes are equally populated with 10% to 15%.

On a much shorter time scale, starting directly after the coupling pulse (as well as resolved here) to 150 ms, there is no visible change of the $|1,0\rangle$ population, shown on the left-hand side. This is in direct contrast to the expected oscillations, but also in contrast to any non-coherent decay which describes the slow drift into the equilibrium state for longer times, as discussed above.

Of great importance here are the insets showing the absorption pictures of the $|1,0\rangle$ and the side modes, here $|1,1\rangle$ as example. For the short time scales, nothing obvious can be seen, as the clouds have the standard appearance after the Stern Gerlach mapping: No additional spatial structure or displacement can be seen. This is true for all pictures up to the 150 ms time mark. After this, there is a very clear spatial structure on the atoms: The $|1,0\rangle$ mode typically shows a bit smaller extension in the left-right direction.

The side modes, on the contrary, show a clear separation in the same direction, with nearly complete extinction in the middle. This is true for both side modes; further examples are shown in the insets of Figure 5.16.

This phase separation cannot be understood for a homogeneous magnetic field, as an antiferromagnet with zero magnetization is miscible and does not show any phase separation.

However, magnetization or – important for our setup – a magnetic field gradient will lead to a lower free energy if the phases separate, where the $|1,1\rangle$ and $|1,-1\rangle$ phase are miscible. This has been shown in early experiments, also in sodium, by Stenger et al. [99]

The long-time dynamics show the system relaxing into its ground state. The free energy

$$K = \int \mathrm{d}r^3 n \left(V + \frac{1}{2} c_0 n + \frac{1}{2} c_2 4 \langle \mathbf{F} \rangle^2 + E_z - p_0 \langle F_z \rangle \right) \tag{5.45}$$

has to be minimized for this, where the kinetic terms are neglected due to the Thomas-Fermi approximation. V is the external potential and E_z the Zeeman energy; p_0 is a Lagrange multiplier accounting for the spin conservation.

The spin-dependent part of the free energy can be minimized and leads to a spin domain diagram as sketched in Figure 5.15 for the antiferromagnetic case.

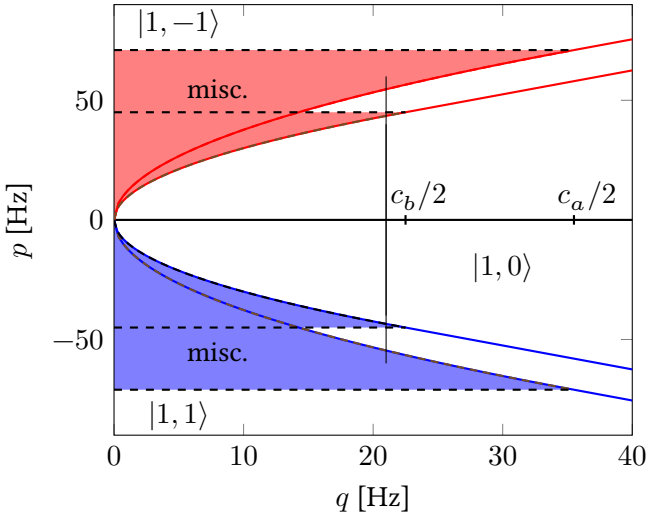

Figure 5.15: Spin domain diagram for an antiferromagnet ($c_2 > 0$). Shown is the spin configuration that minimizes the free energy depending on the quadratic Zeeman shift and the parameter p, see text. Changing c leads to a change of the borders. Inside the lines, the $|1,0\rangle$ state is the ground state; outside, it is $|1,1\rangle$ or $|1,-1\rangle$. In the shaded region, mixing of the side modes is possible, where the ratio of populations is given by $\rho_1/\rho_{-1} = (2c+p)/(2c-p)$. For the parameters c_a and c_b and the vertical line see explanations in the text.

A systematic investigation of the phase separation and population dynamics depending on the density is presented in Figure 5.16. From the left upper to the lower right subfigure, the final trap depth of the cooling ramp is reduced. This leads to a coupling of different effects, as a lower final power of the horizontal laser beam means:

- lower trap frequencies
- lower atom numbers
- higher condensate fraction due to lower temperature
- lower densities for equal condensate fraction

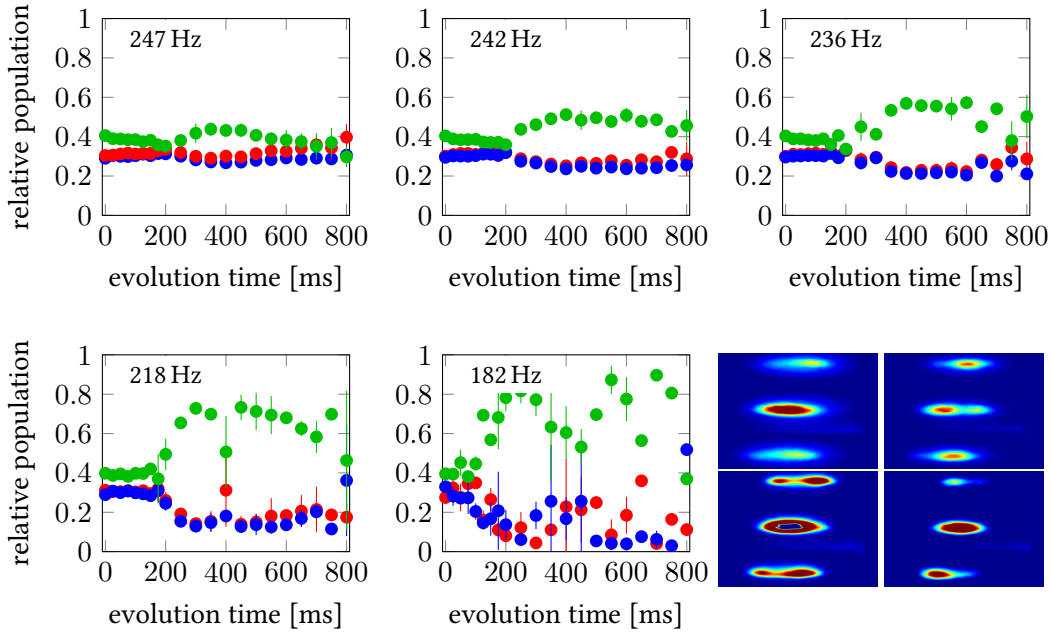

Figure 5.16: Preparation of a sodium BEC for different final trap depths; the mean frequencies are given in the graphs. $q_{\mathrm{Na}} = 26\,\mathrm{Hz}$, $B = 307(3)\,\mathrm{mG}$. For all settings, a clear phase separation is visible at least after 250 ms, while for the lower trap setting (lower left) already after 125 ms a separation occurs. The absorption pictures shown are taken after 300 ms for 247 Hz, 250 ms for 242 Hz, 200 ms for 236 Hz and 150 ms for 182 Hz (top left to bottom right).

Comparing the total atom numbers, however, shows that the effect of further evaporative cooling on the atom number is rather small since the scattering of the numbers for one setting is mostly stronger than the difference between the different trap setting, with $7(2) \times 10^5$ atoms for the largest power and $4(1) \times 10^5$ for the lowest one. A list of the trap frequencies, the calculated Thomas-Fermi radii, mean density, interaction parameter c and the spin healing length ξ_s for all trap settings above is shown in Table 5.1 for comparison.

The first observation to be made in Figure 5.16 is that the overall structure is the same for all trap parameters: For the first about 100 ms to 250 ms no oscillations can be observed. But the $|1,0\rangle$ population decreases slowly, until it reaches about 33%, where all three states are equally populated. From this point on, the phase separation starts, in the same manner as in Figure 5.14, and the spin population increases in the $|1,0\rangle$ mode.

It is a coincidence that the timing steps were chosen narrower up to 200 ms (25 ms steps) and wider after that (50 ms steps). The experimental sequence was exactly the same for the data taken for the shorter and the longer times. No connection can be made between the time steps and the increase in $|1,0\rangle$.

The phase separation shows a distinctly different behaviour for the various trap settings; for a stronger confinement, the side mode population after the phase separation stays rather high,

Table 5.1: Condensate parameters for the trapping frequency scans. Listed are the trap frequency settings, the calculated Thomas-Fermi radii, the mean density, the parameter $c = c_2 \cdot \bar{n}$ and the spin healing length.

$\bar{\nu}$ [Hz]	$r_{\mathrm{TF}}; x, y, z$ [µm]	$\bar{n}$ [$\frac{10^{13}}{\mathrm{cm}^3}$]	$c \cdot h$ [Hz]	ξ_s [µm]
247	(10,11,6)	13	71	11
242	(10,11,6)	13	69	11
236	(10,11,6)	12	67	11
218	(9,12,6)	10	56	12
182	(8,17,6)	8	45	14

at roughly 30%. The data for the longest hold time even suggest that the side modes rise above the $|1,0\rangle$ mode after 800 ms. For the weaker confinement, the population of $|1,0\rangle$ atoms rises strongly, until for the weakest confinement the side modes vanish nearly completely, but also the data scatter very strongly.

Finally, the weakest confinement settings show a reversal of the flow into the $|1,0\rangle$ mode: After about 250 ms, the side mode population rises again, so that overall this looks like an oscillation. The time scale and initial phase of this oscillation, however, show that it cannot be the coherent dynamic expected for a single-mode BEC, but that a completely different description is needed.

Comparing these results with the findings of [99], we conclude that the system is not yet in its equilibrium state, but that still some dynamics are happening. The time scales do not fit to any other known time scale of the experiment, though; neither the trapping frequencies nor the lifetime in the dipole trap are on the same order.

An important information is that in very few cases the $|1,0\rangle$ mode shows a depletion in the middle, which does not fit into the description for the ground state. An example of this is shown in the upper right absorption picture in Figure 5.16. Also, the spatial distribution of the side modes varies strongly from shot to shot, which should not happen for the equilibrated state.

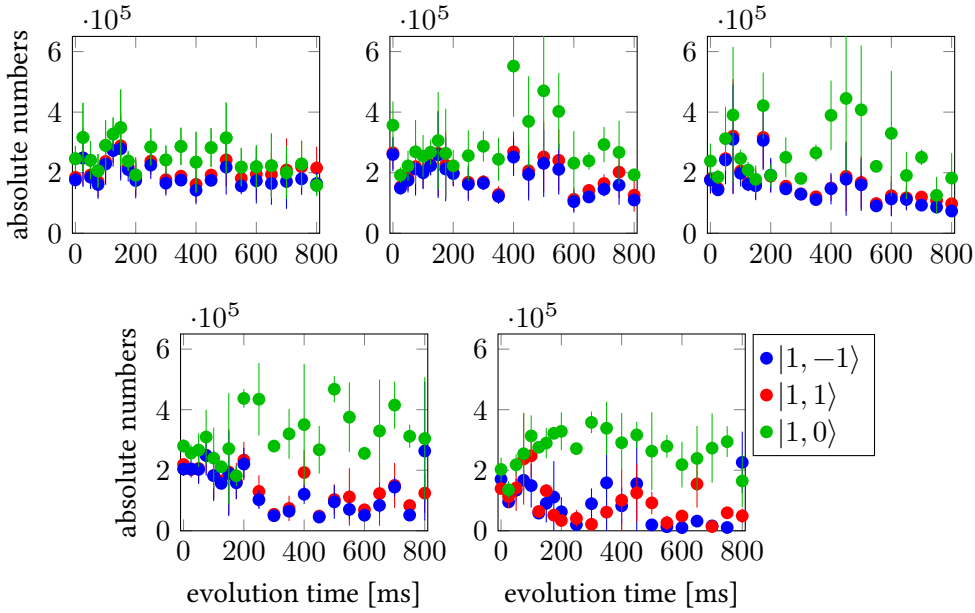

Figure 5.17: Preparation of a sodium BEC for different final trap depths. Here, the same scans are shown as in Figure 5.16, with the total atom numbers. Although the data scatter strongly, the basic features are also visible in the absolute numbers.

5.3.3 Small Sodium Condensate

The preparation of *small* BECs was done by simply lowering the trap depth of the dipole trap further down which realized lower temperatures, a higher condensate fraction and lower atom numbers. Here, the term *small* of course has to be taken relative to the samples shown above where around 1×10^6 atoms were prepared; the following data still contained more than 1×10^5 atoms. This ist a rather large number, stemming from the fact that the machine was built and optimized for the production of large BECs and is less stable for smaller atom numbers. Also, the detection is not suitable and optimized for small atom numbers – the imaging turned out to be detuned, which was not obvious from the pictures of the large clouds. One reason for this is that the BECs with higher atom numbers required longer time of flights to reduce their optical density; after this expansion, the curvature of the density is lower and thus the lensing effect caused by the refraction is weaker. For the small BEC after short time of flight, the lensing has a strong effect. Still, the pictures are useful to determine the relative atom numbers in a meaningful way.

However, the reduction of the atom number allowed to study at least the initial dynamics further than in the denser cloud, with signs of low-multimode oscillations for certain settings. Another important difference and one of the reasons why we differentiate here between the *large* and *small* cases is that in these *small* BECs no spatial structure was observed, in contrast to the results presented above.

One of the first observations of spin population oscillations were done in ^{87}Rb [18], where also the spin mixing was investigated. In contrast to our case, the preparation was not done with a Rabi coupling, but with an incoherent population preparation integrated in the cooling scheme. Still, as the system was not prepared in its equilibrium, some oscillations could be observed.

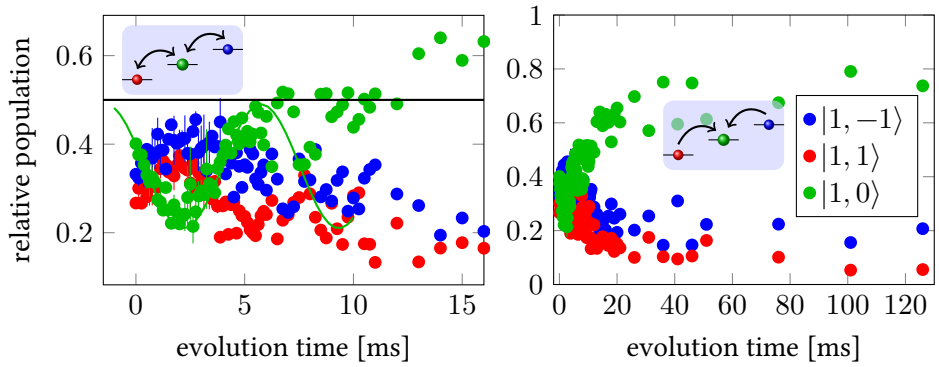

Figure 5.18: SCC of a small Na condensate of 1×10^5 to 5×10^5 atoms at $q_{\mathrm{Na}} = 107\,\mathrm{Hz}$, $B = 621(3)\,\mathrm{mG}$. Clearly visible is the initial coherent dynamics. After around 10 ms, the population of the $|1,0\rangle$ state rises, while the data scatter more strongly, and settles again at around 80% in the $|1,0\rangle$ mode. The green sine curve is discussed in the text. Mean trapping frequency is $\bar{\omega} = 2\pi \times 122Hz$, $c = c_2\bar{n} = 43\,\mathrm{Hz}$.

The typical behaviour for the lower trap parameters and atom numbers is shown in Figure 5.18 where the sample was prepared at 621(3) mG.

The dynamics here can be split into three time scales: For short times, one can see a clear decrease of the $|1,0\rangle$ mode, while the side modes rise equally, followed by the reverse process. This very much resembles at least the beginning of an oscillation as is expected from the single mode approximation picture.

The green sine curve is not a fit, but a guide to the eye, containing several assumptions: First, the RF preparation was done with a frequency calculated from a precise spectroscopy of the field. Therefore it is highly unlikely that the coupling is detuned so strongly that the initial $|1,0\rangle$ population is far below 50%. Therefore, we assume that the initial dynamics are too fast to be covered by our readout, and thus the maximum of the sine starts at 0.5.

After one cycle of sinusoidal behaviour, the population of $|1,0\rangle$ stays rather constant for several milliseconds, which reminds of the results for the *large* BEC. At this point, one can make the connection, assuming that in the large BEC the initial dynamics were even faster than here and could not be monitored at all, leaving the flat line as the first observable feature.

Longer time scales also show the same evolution as the large condensate, where the $|1,0\rangle$ mode rises strongly above the initial level and an equilibrium population is reached after about 50 ms. This rise above 50% is important, since for coherent spin changing collisions of an antiferromagnet with initial spinor phase $\vartheta = 0$, the $|1,0\rangle$ population should not go above the initial preparation.

Note that this scale for the rise is now faster, but also at a higher magnetic field of 620(3) mG instead of the 307(3) mG discussed above. Therefore, the detuning is higher and one would expect faster dynamics for the same densities.

Very similar behaviour can be seen at other magnetic offset fields, with more or less clear initial structure. At 512(3) mG, for example, a single sine curve can still be laid over the data with rather low deviations from the $|1,0\rangle$ population, as shown in Figure 5.19

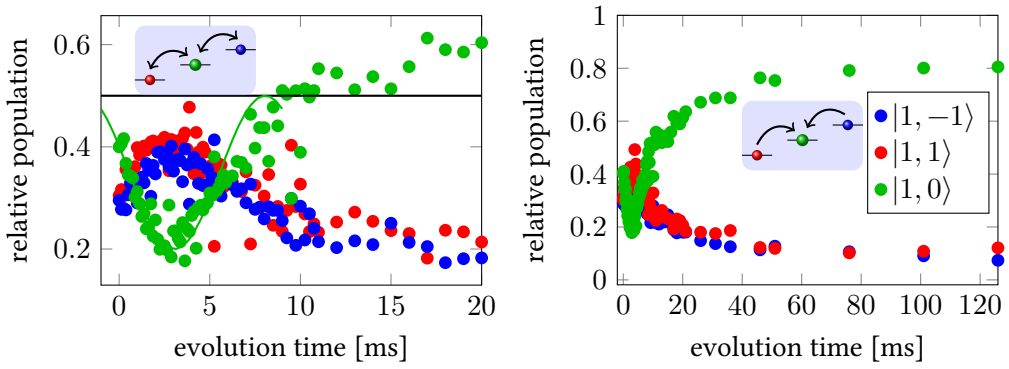

Figure 5.19: SCC of a small Na condensate of 0.5×10^5 to 2.5×10^5 atoms at $q_{\mathrm{Na}} = 73\,\mathrm{Hz}$, $B = 512(3)$ mG. Clearly visible are the initial coherent dynamics while after 8 ms the population of the $|1,0\rangle$ state rises above the initial preparation.

Here again, the population stagnates for several milliseconds at 50% of $|1,0\rangle$ population and then increases.

The same behaviour for a lower magnetic field of 470 mG can be seen in Figure 5.20, with higher statistics. For this detuning, the initial decrease of the $|1,0\rangle$ mode is somewhat slower, but the overall structure very similar.

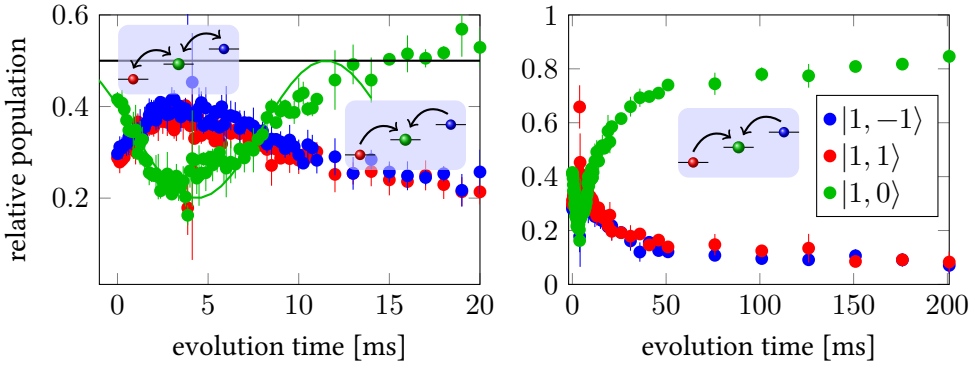

Figure 5.20: SCC of a small Na condensate of 0.5×10^5 to 2.5×10^5 atoms at $q_{\mathrm{Na}} = 61\,\mathrm{Hz}$, $B = 470(2)\,\mathrm{mG}$. Around 5 ms, deviations frmo the single-mode sinusoidal behaviour appear, indicating a second oscillation mode.

The initial dynamics can be even more rich in features, as is shown by the data in Figure 5.23, presenting spin dynamics in a Bose-Einstein condensate at $407(3)\,\mathrm{mG}$. While the long time dynamics show the same evolution into the $|1,0\rangle$ state, the short time shows two minima, indicating oscillations with several frequencies.

To understand the signal and estimate a number for the oscillation period, three curves are added to the data in Figure 5.23: The green and red curve are sine functions with frequencies of 63 Hz and 95 Hz, respectively. They aim to fit two different features: The green curve indicates an oscillation given by the initial decrease and increase after 12 ms, assuming that the minimum has been *cut* by damping or multimode dynamics, while the red curve fits the faster dynamics at the beginning, but strongly deviates after that.

Damping of the spin oscillations has been discussed theoretically in [25]; the details are highly complex and far beyond the scope of this thesis. As the exact experimental parameters are not yet under full control (especially regarding magnetic field gradients, but also a thermal cloud that influences the BEC dynamics and possibly external disturbances), the damping will not be further investigated here.

A fit to the data using two sine functions with all parameters free is shown in the blue curve, resulting in two sine functions with 104 Hz and 66.4 Hz, respectively. Due to the number of free parameters, the error bars are huge, so this fit is also rather a guide to the eye. It is obvious that this function, too, cannot reproduce the data very well, indicating that the real dynamics are much more complex than just the addition of two or even more sine curves. All this makes it hard to estimate an oscillation period for the comparison with theory.

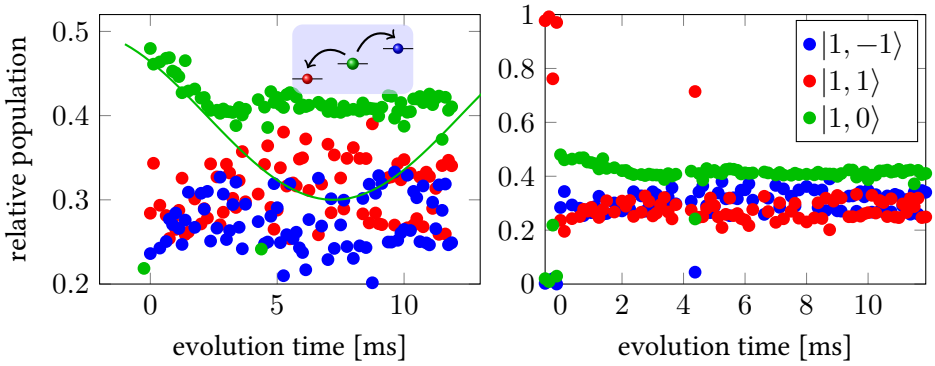

Figure 5.21: SCC of a small Na condensate of 0.9×10^5 to 4.0×10^5 atoms at $q_{\mathrm{Na}} = 13\,\mathrm{Hz}$, $B = 218(3)\,\mathrm{mG}$. The fast damping makes it hard to fit a reliable curve. As the order of magnitude for the frequency can be estimated from the theoretical prediction for the single mode, the fit was chosen with a large amplitude, assuming that the damping cuts already after less than quarter an oscillation period. The data at the very beginning were taken before the RF pulse was applied to cover the full dynamics. Therefore, atoms are still in $|1,1\rangle$ in these shots.

Slow Oscillations

At a rather low magnetic field of only $97(3)\,\mathrm{mG}$, corresponding to $q_{\mathrm{Na}} = 2.6\,\mathrm{Hz}$, the slowest oscillation-like structure could be resolved, shown in Figure 5.24.

This is the only dataset so far where the initial dynamics is not a steep slope, but the slow exponential growth could be observed. The first minimum is clearly resolved, while after that the data are not stable enough to clearly detect further oscillation cycles. Again, a sine fit is laid over the data to indicate the oscillation period here, a maximum population of 45% in the $|1,0\rangle$ mode definitely is the best choice.

To justify the use of a sine although the initial dynamics deviates from that, Figure 5.25 shows the same dataset with a numerical simulation superimposed. The red curve is calculated as detailed in section 5.2. This simulated curve has been scaled and phase-shifted to fit the data.

This procedure does not give quantitative information, as it is neither a fit nor a calculation with the corresponding atom number. The intention here is to show the expected oscillation structure of a single-mode BEC, which does not depend critically on the exact parameters. With this curve added, the second minimum in the data seems more convincing, as all data points are lying close to the simulation.

The sine deviates for initial dynamics: As the phase is determined by the dynamics between 20 ms and 70 ms, it would show an initial increase of the $|1,0\rangle$ mode, which is not in accordance with the theory. The data scatter by several percent, which allows no clear distinction between increase, decrease or nearly constant $|1,0\rangle$ population. Still, the oscillation period for both the simulation and the sine are the same, which justifies to use a sine for the estimation of the periodicity. Therefore, although all other data sets show only one minimum, the sine gives a rough measure for the time scale.

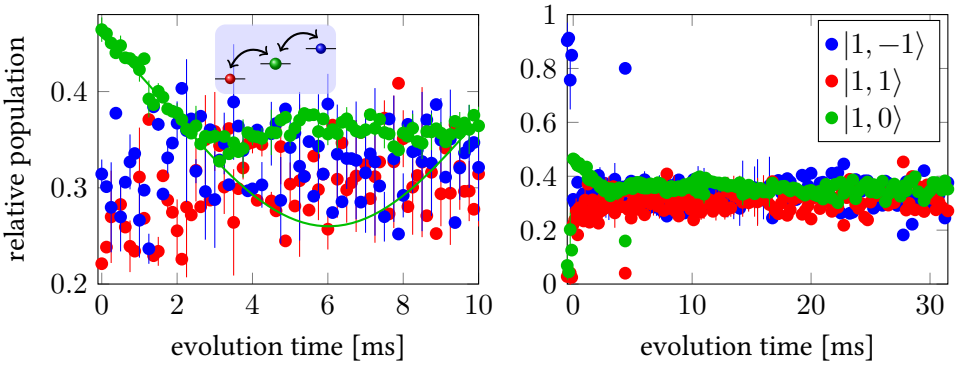

Figure 5.22: SCC of a small Na condensate of 0.5×10^5 to 2.0×10^5 atoms at $q_{\mathrm{Na}} = 25\,\mathrm{Hz}$, $B = 300(2)\,\mathrm{mG}$. Data at the very beginning are again taken before the pulse.

Influence of Trapping Frequency

The spin dynamics obvioulsy depend on the density of the atoms, therefore, for the same number of atoms, on the trapping frequencies. Unfortunately, our preparation scheme leads to a direct coupling of atom number and trapping frequencies, since the final number of remaining atoms depends – as the frequency – on the laser powers. In Figure 5.26, three different trap parameters are shown with the effect on the spin dynamics.

While the mean trapping frequency is changed by a factor of 1.7, the mean atom numbers changed by roughly a factor of 4, so the main effect indeed is in the atom numbers. Thus the density changes strongly, with calculated mean densities of $\bar{n} = 2.3, 5.7, 7.5 \times 10^{13}\mathrm{cm}^{-3}$, respectively. The corresponding $c = c_2\bar{n}$ are 13 Hz, 32 Hz, 40 Hz.

The tendency here is very clear: A lower trap potential leads to lower atom numbers, and allows a clearer onset of the dynamics. From the calculated coupling strengths c, one can infer the magnetic field where the resonant behaviour appears, from $q_{\mathrm{res}} = c_2 \cdot \bar{n}$, which is for the three cases shown in Figure 5.26 a field of 420 mG, 370 mG, and 240 mG for the case of the weakest confinement.

As the measurements were done at 343 mG, this means that only the lowest trap setting was done *below* the resonance. It is not sure if there is a physical reason that the oscillation is less damped in this case or if the expected larger amplitude is the only reason that the signal is clearer than in the other cases.

Summary of the Results of the Small Condensate

Table 5.2 lists the results of the small condensate preparation for different fields. The listed frequency is the one of the sine curves shown in the single measurements; it is important to keep in mind that these are neither fits to the data nor the correct functional dependence. Still, they give a time scale for the oscillation period which is the relevant information here.

As the functional form of the oscillation period is known from the analytic solution for the SMA and could be reproduced by the numeric simulation, one can compare the observed dependence on the magnetic field with the results of a simulation run. This is shown in the right-hand side plot in Table 5.2, where the oscillation period of all scans presented above are

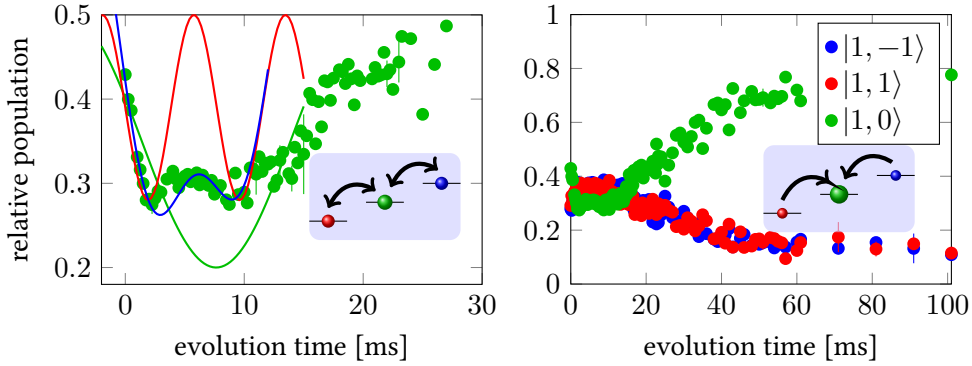

Figure 5.23: SCC of a small Na condensate of 1.5×10^5 to 4×10^5 atoms at $q = 45\,\mathrm{Hz}$, $B = 407(3)\,\mathrm{mG}$. The short-time evolution shows two minima, indicating oscillations with several modes. After the second minimum, the system drifts to the equilibrium with 80% in $|1,0\rangle$ again. The red and green sine curves are guides to the eye; the blue curve is a fit of two sines onto the data up to 12 ms. Further explanations are given in the text.

plotted. The blue curve shows a simulation and was scaled to fit the points. This is rather a guide to the eye, but the data are in accordance with the expected form.

For a quantitative comparison, one has to calculate the coupling strength for these settings, which gives the critical field B_c where the divergence of the oscillation is expected. Since the atom numbers scatter rather strongly in all measurements, an estimate of the coupling strength $c = c_2\bar{n}$ is difficult. For the given trap settings, one can calculate the parameter for 0.5×10^5, 1×10^5, 2×10^5 and 4×10^5, where 1×10^5 is about the mean number in the measurements. The corresponding values for c are listed below the plot in Table 5.2.

The minimum and maximum values of B_c, 211 mG and 321 mG, are added in the plot in Table 5.2 as vertical black lines; the calculated divergence point for the oscillation should therefore lie in the red-shaded area between the lines.

Obviously this contradicts the data, since the two data points in this region show a short period. The red line is a scaled numeric simulation which shows that a shift of the peak cannot reproduce the rest of the data set. This leaves as only explanation that the density is strongly overestimated, maybe due to a smaller condensate fraction than assumed, lower trap frequencies, or a badly calibrated imaging.

Another possible explanation for the low B_c would be that the constant c_2 is smaller then expected; but as the values of c_2 reported in [77] and, from a completely independend method, in [53], agree well, we exclude that our observation would correct this value by a factor of 2.

Finally, if the spinor phase were greater than zero, this could also shift the critical field to lower values due to the $\cot\vartheta$ dependence of $\delta(B_c)$, as shown in Figure 5.7. This was the case for the experiments of [9], where a small population of 2% in the $|1,-1\rangle$ state is mentioned as an explanation for an observed $\vartheta = 0.5(3)$. We cannot exclude such a population due to the imaging quality, but our preparation scheme with the initial trapping in $|2,2\rangle$ and the transfer

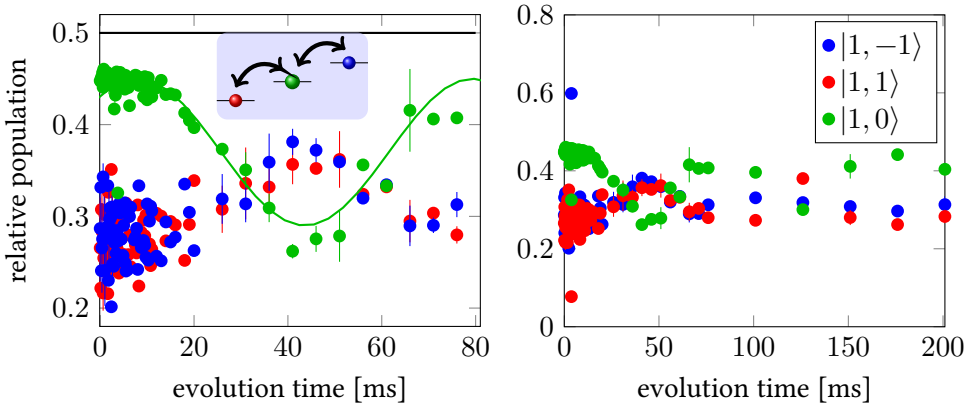

Figure 5.24: SCC of a small Na condensate of 0.25×10^5 to 2.5×10^5 atoms at $q_{\mathrm{Na}} = 2.6\,\mathrm{Hz}$, $B = 97(3)\,\mathrm{mG}$. During the first about 15 ms, only a slow dynamic occurs, while from 20 ms to 60 ms half an oscillation is visible. At 125 ms and 200 ms, further minima of the $|1,0\rangle$ state might be present.

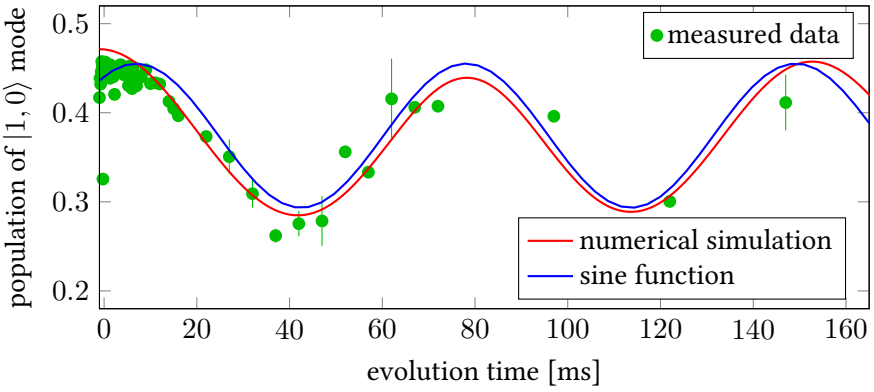

Figure 5.25: Comparison of experimental data as shown in Figure 5.24, with a numerical 1D simulation and a sine function. The simulated data are shifted and scaled to fit the data. For longer times, the simulation shows spatial dynamics and thus deviates from the sine.

to $|1,1\rangle$ should provide a very clear preparation as compared to the cooling in the $|F=1\rangle$ manifold as in [9]. The Rabi pulse itself cannot produce a spinor phase other than $\vartheta = 0$, as shown in subsection 2.3.3. This leaves the overestimated density as the most likely explanation so far. A greater set of data points of course could clarify the situation.

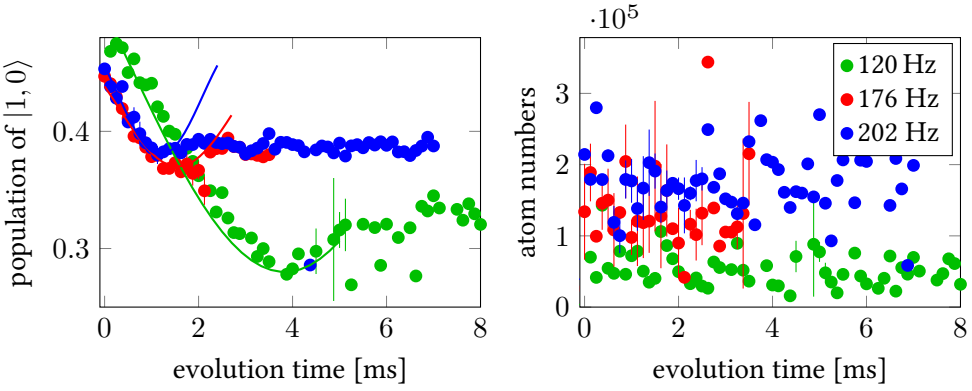

Figure 5.26: For the same magnetic field, a change in the trap parameters can have a tremendous effect on the frequency, but especially on the visibility and damping of the oscillations. The data show only the $|1,0\rangle$ population and were taken at $q_{\mathrm{Na}} = 33\,\mathrm{Hz}$, $B = 343(3)\,\mathrm{mG}$, at $\bar{\omega} = 2\pi \cdot 120\,\mathrm{Hz}, 176\,\mathrm{Hz}, 202\,\mathrm{Hz}$. Only at the lowest mean trapping frequency, a clear minimum can be observed. For higher frequencies, the damping is strong and leads to a fast equilibration.

Table 5.2: Summary of observed spin dynamics in the small Na condensate case. From the calibrated magnetic field, the q_{Na} value is calculated. The listed frequencies are given by the sine curves shown in the graphs. The three bottom entries are for the same field, but different trap settings. On the right-hand side, the oscillation periods are plotted against the magnetic field for these measurements. The blue curve is a numeric simulation scaled to fit the data to show the expected behaviour. The critical field B_c, with $c_2 n = q(B_c)$, depends on the density and therefore the atom number. Since these fluctuate strongly, a list of B_c for different atom numbers is given below the plot. 1.0×10^5 is an average atom number for most scans; the corresponding oscillation period is plotted in red.

field [mG]	q_{Na} [Hz]	freq [Hz]
97	2.6	14
218	13	40, damped
300	25	60
343	33	–
407	46	63
470	61	70
512	73	100
620	107	140
	$\bar{\nu}$ [Hz]	
343	120	75
343	176	200
343	202	280

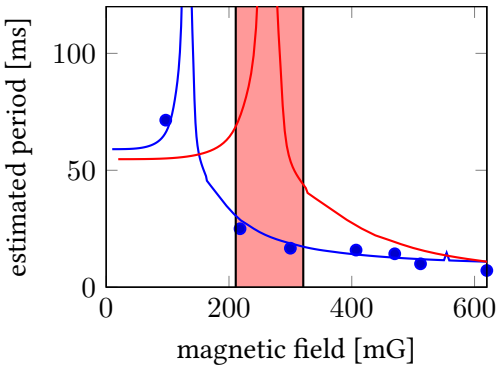

atom number	$c_2 \cdot \bar{n}$ [Hz]	B_c [mG]
0.5×10^5	12	211
1.0×10^5	16	243
2.0×10^5	22	279
4.0×10^5	29	321

5.3.4 Thermal Sodium Gas

As described in subsection 5.1.5, also a cold thermal gas can show coherent oscillations in the spin degree of freedom.

Since our experimental apparatus is optimized for the production of a large BEC, the preparation of a cold, but not condensed sample is challenging and needs some changes in the sequence. The cooling scheme with the dimple condensation leads to a strong increase of the phase space density for all trapped atoms. So either the atoms are very cold and dense – thus at least partly condensed – or they are not yet trapped in the dimple and remain in the waveguide.

To overcome these limitations, several changes in the sequence were implemented, aiming at a thermal gas with still rather large atom numbers. These changes included:

- Reduction of the MOT loading time down to 2 s instead of 4 s to reduce the initial atom numbers.
- Much deeper MW knife cooling down to 1777.95 MHz instead of 1779.3 MHz.
- Final cooling in the crossed dipole trap only to $2\pi \times (212, 200, 356)$ Hz.
- Ramping up the horizontal dipole beam in 100 ms to heat the sample, with final trapping frequencies of $2\pi \times (212, 316, 465)$ Hz, with a mean trapping frequency of $\bar{\omega} = 2\pi \times 464$ Hz.
- Stern-Gerlach mapping with only 4 ms time of flight and current control set to full value in the gradients to separate the thermal clouds as clearly as possible.

A thermal sample could also be produced by shortening the MOT loading time even further, but this approach is unstable since the MOT only gives reliable atom number stability after a certain loading time when it starts to saturate. Therefore, the shortest time that still produces acceptable atom number fluctuations was chosen.

Further reduction of the atom number was done with the decreased MW knife frequency, as the deeper cut does not lead to an increased phase space density at the end: The lower temperature is increased again by the dipole trap loading, so that the main effect in this regime of the MW knife is just removing atoms. This approach is much more stable than a further reduction of the MOT loading time. Also, the stronger three-body losses in the $|2, 2\rangle$ state decrease the atom number, while also compensating to a small degree for fluctuations, since larger samples also suffer from stronger losses.

Still, due to fluctuations in the atom numbers, a small condensate fraction could occur due to a shot with more than the average atom number. This small condensate fraction could not be monitored during the SCC measurements and might be one cause for damping or reduced visibility of any fringes.

Some results of a thermal gas preparation are shown in Figure 5.27, at a magnetic field of 343 mG, corresponding to $q_{\mathrm{Na}} = 33$ Hz. The solid line is a guide to the eye, given by a sine with a frequency of 57.3 Hz. While the first decrease of the $|1, 0\rangle$ mode is convincing, the data scatter strongly after the first minimum. As mentioned above, this might be caused by a non-vanishing condensate fraction, but also again by magnetic field gradients or other uncontrolled influences.

At lower magnetic fields, it was not possible to see clear oscillations, but again hints at oscillatory behaviour could be shown, presented in Figure 5.28. At these fields, the lower detuning leads to slower oscillations with a larger amplitude. Still, as the data scatter strongly,

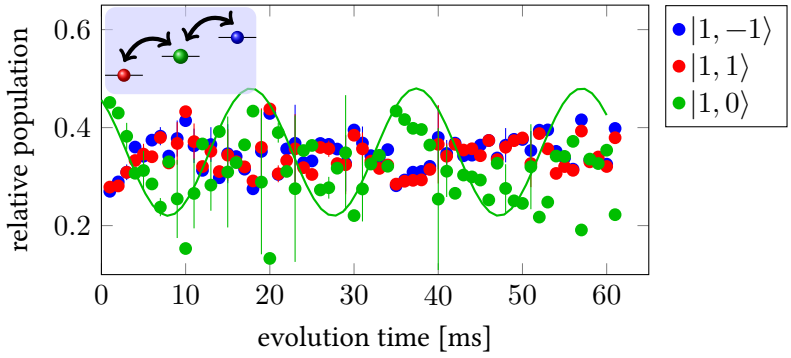

Figure 5.27: Spin Changing Collisions in a thermal Bose gas at $q_{\mathrm{Na}} = 33\,\mathrm{Hz}$, $B = 343(3)\,\mathrm{mG}$. The sine is a guide to the eye with a frequency of 50.9 Hz.

no simple fit to the data can be obtained. Additionally challenging is a drift into the side modes that occurs even before one full oscillation cycle.

The data for 197(3) mG on the left-hand side of Figure 5.28 show a small increase of $|1,0\rangle$ for very short times directly after the coupling pulse, which could not be explained. We assume an artefact from the imaging, where it is difficult to clearly distinguish the thermal clouds after time of flight due to their fast expansion.

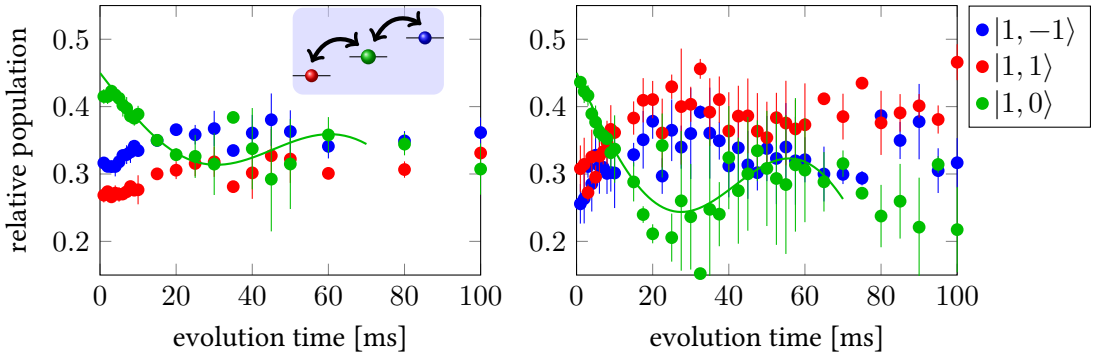

Figure 5.28: SCC in a thermal Bose gas at $q = 10.8\,\mathrm{Hz}$, $B = 197(3)\,\mathrm{mG}$ (left) and $q = 5.4\,\mathrm{Hz}$, $B = 139(3)\,\mathrm{mG}$ (right). The solid lines are guides to the eye, consisting of a sine with a frequency of 12 Hz and 11 Hz, respectively, and a linear slope to include the drift into the side modes.

Summary of Thermal Spin Dynamics

In summary, the investigation of thermal spin dynamics was the most successful given that several oscillation periods could be observed. However, the data quality is still very bad and the data scatter strongly after the first minimum for all data sets. This might be related to the unstable preparation process leading to varying temperatures and atom numbers. Also, the

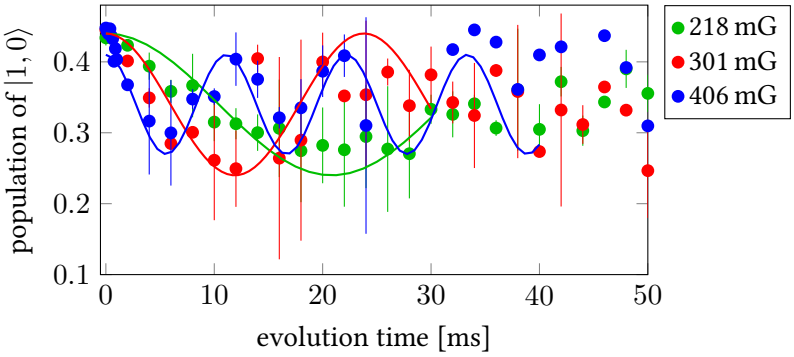

Figure 5.29: SCC in thermal sodium at different magnetic offset fields. The corresponding q parameters are $q_{\mathrm{Na}} = 10.8\,\mathrm{Hz}; 20.6\,\mathrm{Hz}; 37.5\,\mathrm{Hz}$. Again, sine curves are laid in as guide to the eye and rough estimates of oscillation frequencies. The plotted frequencies are 24 Hz, 42 Hz and 90 Hz, respectively.

mapping was not optimized for thermal clouds, therefore the read out was suboptimal and can be improved.

Table 5.3 shows a summary of the results, mainly the estimated frequency given by the sine curves in the plots, as for the BEC case in Table 5.2.

In contrast to the BEC case, two points with longer oscillation periods are available, which makes the comparison with the theory somewhat easier: These two data points could be around the resonance peak, while the data at higher fields are already above the resonance, where the oscillation frequency quickly rises.

Table 5.3: List of observed spin dynamics in the thermal sodium gas. The offset fields are calibrated within the experimental error of 3 mG; the corresponding q_{Na} is calculated. Frequencies listed here are taken from the sine curves that are laid into the data. The plot shows the corresponding oscillation period depending on the magnetic field. For the coupling parameter and the verticall lines in the plot see discussion in the text.

field [mG]	q_{Na} [Hz]	freq [Hz]	$2c_2\bar{n}$ [Hz]
139(3)	5.4	11	5.6
197(3)	10.8	12	5.8
218(3)	13.2	24	6.2
301(3)	25.1	42	5.7
343(3)	32.6	51	6.9
406(3)	45.7	90	7.0

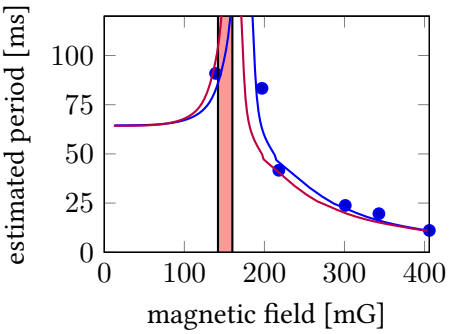

For a quantitative comparison, from each scan the mean number is taken and the mean density of the gas calculated for this value. The trapping frequencies for all cases are $\omega_{x,y,z} = 2\pi \times (212, 408, 561)\mathrm{Hz}$.

From the mean density, the coupling parameter (remember to include the factor 2 for the thermal case) $2 \cdot c_2 \bar{n}$ is calculated and listed in the last column of Table 5.3.

In the plot, the critical field B_c for the extreme cases of the coupling parameters of the table are indicated by the vertical lines, with $\delta(B_c) = 2 \cdot c_2 \bar{n}$.

As in the case of the BEC oscillations, two curves are laid over the data: The blue one is adapted to fit the data points without restrictions regarding B_c, while the red one shows the dependence for the maximum calculated B_c. Both curves fit the data very nicely, taking into account that the estimation of the oscillation period was done only very roughly. The exact position of B_c of course depends on too many unknown factors, but the function dependence and order of magnitude for the critical field seem to agree very well with the expectations.

5.3.5 ^{7}Lithium

As in sodium, also bosonic lithium can show homonuclear spin dynamics. The ratio of scattering lengths is even more favourable than in sodium, but the sign of the coupling is negative, therefore ferromagnetic behaviour is expected. For the scattering lengths of the coupled $|F = 0\rangle$ and $|F = 2\rangle$ channels for the $|f_1 = f_2 = 1\rangle$ manifold, coupled channels calcuations give values of $a_0 = 23.9\, a_B, a_2 = 6.8\, a_B$. [95]

This gives for the parameters c_0 and c_2:

$$c_2 \approx 6 \times 10^{-12}\,\mathrm{Hz/cm^3} \tag{5.46}$$

$$c_0 \approx 1.2 \times 10^{-11}\,\mathrm{Hz/cm^3} \tag{5.47}$$

which gives a coupling constant c_2 about 10 times larger than the one for sodium. For this ratio of scattering lengths, the single mode approximation is not valid anymore.

While using the upper hyperfine manifold is experimentally challenging due to the negative scattering length, the hyperfine ground state offers a convenient system to work with.

In our system, we have an additional degree of freedom since we can choose to perform experiments on ^{7}Li without any sodium background, or to add sodium in different hyperfine states. By choosing a state where spin changing collisions between the species are energetically forbidden, the sodium can just provide a cold bath for the lithium atoms without changing the internal spin dynamics.

Dynamics in ^{7}Li have only been investigated with a large population in the $|1, 0\rangle$ state instead of coherent coupling as in the sodium case. Figure 5.30 shows the results of such a preparation after different waiting times. This is in close analogy to the measurements done with sodium, as shown in Figure 5.12.

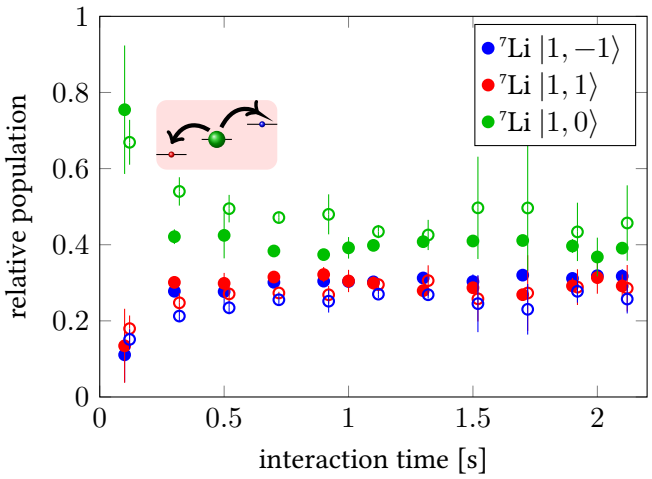

Figure 5.30: Homonuclear spin changing collisions of ^{7}Li while Na is present in the $|1, -1\rangle$ state (full circles) compared to no sodium background (empty circles). The data without sodium have been shifted by 0.02 s for better visibility. All coils were off, giving an offset field of 477.6 mG, where $q_{\mathrm{Li}} = 140$ Hz.

The dominant feature in these data is the very rapid decrease of the $|1,0\rangle$ mode. In the case of sodium background present, the main dynamics happen during the first 250 ms, and after that only a small further drift into the side modes can be seen. Without sodium, this process seems to be slower; this might be caused by a higher temperature of the sample: The RF pulse which populates the $|1,0\rangle$ state heats up the sample, and the sodium can act as a cooling bath, therefore increasing the density of the ^{7}Li atoms, leading to faster dynamics.

While for sodium the spatial structure of the single components could be resolved, the ^{7}lithium imaging is not good enough to observe any spatial features. Thus possible phase separations or changes in the cloud's form could not be monitored.

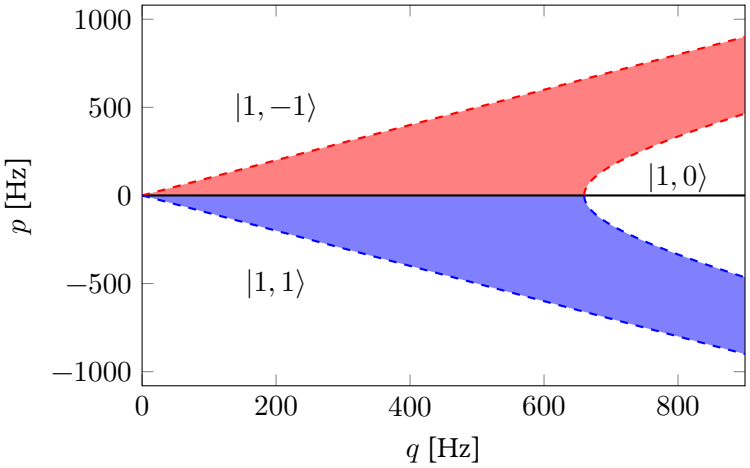

Figure 5.31: Spin domain diagram for an ferromagnet ($c_2 < 0$). Shown is the spin configuration that minimizes the free energy depending on the quadratic Zeeman shift and the parameter p. Inside the lines, (right side) pure $|1,0\rangle$ domains can form; the same is true for $|1,1\rangle$ or $|1,-1\rangle$ outside the shaded region. Inside the shaded regions, $|1,0\rangle$ is mixed mostly with only one of the side modes. All states are miscible in all regimes; the boundaries are not sharp. The parameters for the plot are given in the text.

As for the antiferromagnetic case, a spin domain diagramm for the ferromagnetic behaviour can be calculated, and the structure is shown in Figure 5.31. In contrast to the antiferromagnet, all spin states are always miscible, indicated by the smooth boundaries between the regions. Pure domains exist in the white regions, for the $|1,-1\rangle$ (above the shaded regions), for $|1,0\rangle$ (around the x-axis for high fields) and for $|1,1\rangle$ (below the shaded region). The shaded areas show a regime where the $|1,0\rangle$ component mixes with one of the side modes, while the other side mode has only a small population.

Using the mean atom number of about $5(1) \times 10^4$ atoms and calculating the c_2 parameter using the scattering lengths $a_2 = 6.8\,a_B$, $a_0 = 23.9\,a_B$, the coupling parameter is $c = c_2\bar{n}/2 = 442$ Hz and the corresponding magnetic field is 850 mG. The date shown above were taken at a smaller field, indicating that the atoms are well in the miscible regime. This might explain the fast decay into the equal distribution of the substates.

Since there is no change in the overall magnetization, meaning that the number of atoms in the side modes is symmetric within the experimental uncertainty, there is no interspecies spin exchange, unlike the measurements presented in the next section.

5.4 Results Heteronuclear SCC

As in many other aspects of ultracold atomic gas experiments, the addition of a second species does not increase the complexity of the system linearly, but many additional challenges have to be overcome. That is one of the reasons why the extension of any effect shown in a single species experiment takes several years to be ported onto a mixture experiment.

In the case of Feshbach resonances, this process took six years, from the very first observation of Feshbach resonances in sodium [46] to the first two-species observations in the ^{6}lithium-sodium mixture. [97]

For spin dynamics, this is true as well, and just recently the first coherent spin-exchange dynamics between two heteronuclear bosonic species has been reported by Li et al. [62] in the sodium-rubidium system. This system shows very favourable scattering properties and allows the authors to observe several coherent oscillation periods of spin exchange between the species.

In our setup, the Bose-Bose case was also studied, but only as a preliminary effort to enable the investigation of the Fermi-Bose mixture, which imposes very demanding requirements on the experimental setup. The following sections will present our findings in both mixture systems and will detail their limitations and future possibilities.

5.4.1 Bose-Bose Mixture ^{7}Li-Na

While the fermionic lithium discussed below shows no dynamics without sodium, the bosonic lithium shows a rather rich variety of spin dynamics since the homo- and heteronuclear collisions can influence each other.

On the other hand, this combination prevents us from seeing a clearly heteronuclear influence alone. There are two possible start points for the $M_F = +1$ channel, namely Li in $|1,1\rangle$ and Na in $|1,0\rangle$ (denoted again as $|1,1;1,0\rangle$), or the other way, $|1,0;1,1\rangle$. Both cases suffer from the strong intraspecies dynamics shown in the last sections.

Due to the usual approach of our apparatus to treat lithium as an impurity, we chose the preparation of $|1,0;1,1\rangle$, since the lithium density should be smaller than the sodium density. Figure 5.32 shows this preparation and the time development of the ^{7}Li populations.

The sketched insets show the dominating process, where the red-shaded one is for ^{7}Li, and the blue-shaded one for Na.

Clearly visible are the initial dynamics of ^{7}Li where the $|1,0\rangle$ atoms tend into the side modes for about 500 s. But, after this time, a clear imbalance between the $|1,-1\rangle$ and $|1,1\rangle$ state in lithium are observed, which can only be due to the influence of sodium. This is in contrast to the data shown in Figure 5.30 where sodium is in the $|1,-1\rangle$ state.

In the latter case, the process $|1,0;1,-1\rangle \Rightarrow |1,-1;1,0\rangle$ is energetically forbidden and thus only the ^{7}Li homonuclear dynamics is observed. But for the case of $|1,0;1,1\rangle \Rightarrow |1,1;1,0\rangle$ energy is released, allowing the ^{7}Li atoms to change their total magnetization.

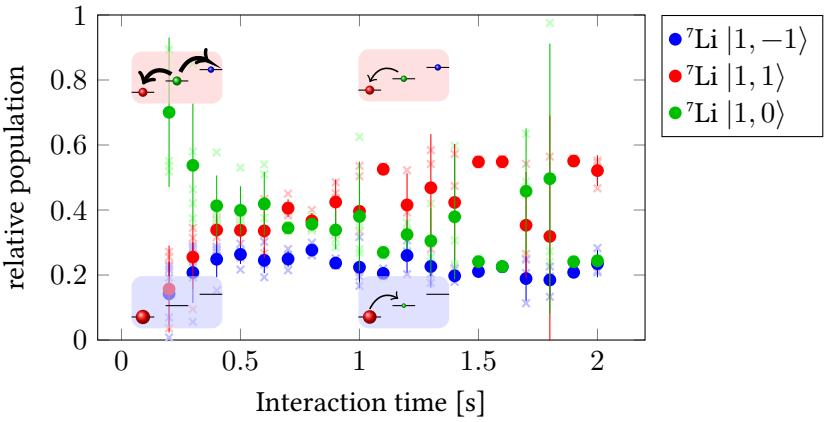

Figure 5.32: Homo- and heteronuclear spin dynamics in ^{7}Li at 820 mG. Sodium atoms are present in $|1,1\rangle$; Na atoms in $|1,0\rangle$ are not detectable. ^{7}Li is prepared in $|1,0\rangle$ and shows a rather fast dynamic into the side modes, which after about 1 s becomes strongly imbalanced as the population of $|1,1\rangle$ rises. This violation of the magnetization can only be explained by the influence of Na.

Unfortunately, the strong atom number imbalance does not allow to detect any changes of state population in sodium which could give an important check to exclude any other external influences on the lithium magnetization.

This type of measurement is similar to the domain formation during the equilibration of the single-species setups, since the whole system can evolve into its ground state with spin-conserving processes.

The second type of experiments, aiming at the observation of coherent oscillations, was done by starting in the $|1,1;1,1\rangle$ state and coupling to a superposition of $|1,0\rangle$ and $|1,1\rangle$ for both species. This is directly analog to the mesurements in the NaRb case of [62]. A typical result of such a measurement is shon in Figure 5.33.

The only feature indicating heteronuclear oscillations in the initial decrease of $|1,1\rangle$ and corresponding increase of $|1,0\rangle$ in ^{7}Li. Again, the large imbalance of more than a factor of ten does not allow to verify this on the sodium populations. Also, the data scatter very strongly, so no clear statement about the spin exchange can be made here.

A problematic feature in this dataset is also the evolution of the $|1,-1\rangle$ state in both species: While for ^{7}Li, a small increase in the relative population can be observed, for Na this increase is very strong. This increase is on a time scale that is in accordance with the observations during the spin domain formation discussed above. Basically this means that one has to look for faster heteronuclear oscillations to reduce the effects of the relaxation into the homonuclear spinor equilibrium states.

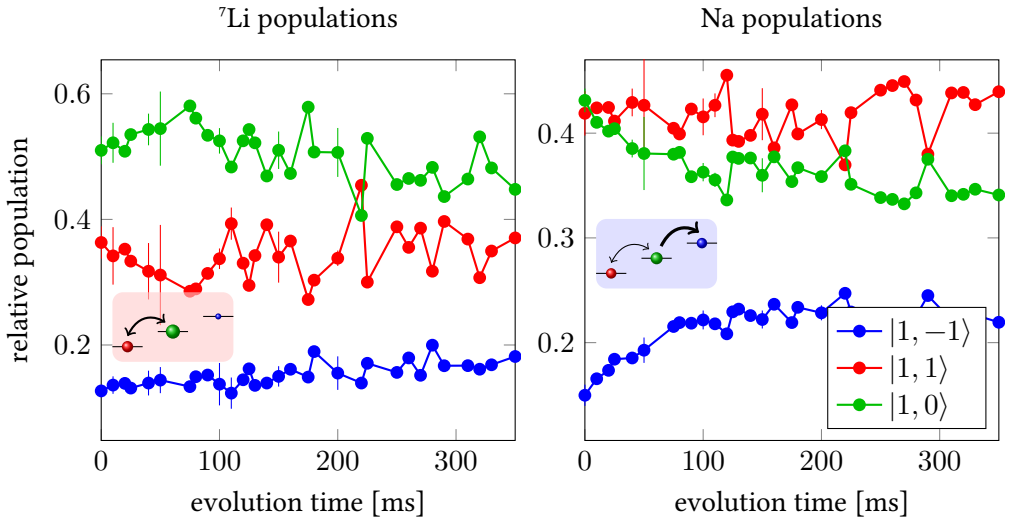

Figure 5.33: Heteronuclear spin dynamics starting from a coherent superposition of both species. ^{7}Li shows for about 100 ms an increase in the $|1,0\rangle$ mode with corresponding decrease in $|1,1\rangle$. In sodium, $|1,0\rangle$ decreases, but also the $|1,-1\rangle$ mode increases, which should not take part in the heteronuclear process. Mean sodium number is 1.3×10^6, mean ^{7}Li number 9.1×10^4. The strong imbalance does not allow to resolve possible influence of the ^{7}Li onto the Na atoms.

5.4.2 Fermi-Bose Mixture ^{6}Li-Na

One of the main challenges in the study of Fermi-Bose spin interactions is the very high energy scale of the differential linear Zeeman shift compared to all other relevant energy scales. While the linear shift cancels in both homonuclear and heteronuclear systems with the same total spin, it does not in the Fermi-Bose mixture. This is due to the different g factors, as detailed in . Note again that it is not just the difference of the nuclear g_i factors, which is the case for the heteronuclear bosonic case, but that due to the different total spin the g_f factor contains different numbers.

As a reminder, Figure 5.34 shows again the energy difference of several spin exchange channels. The scale now is suited to fully show the ^{6}LiNa channel; for comparison, all other channels for the bosonic combinations are also shown.

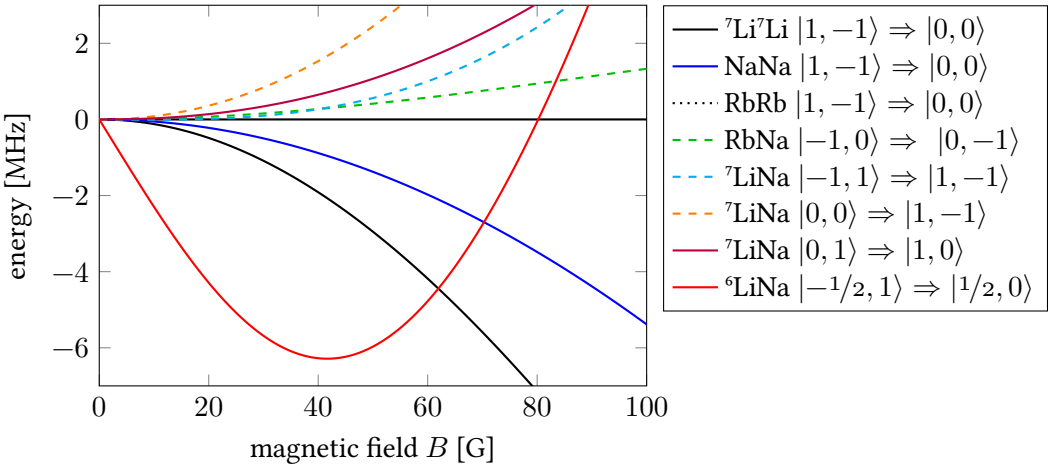

Figure 5.34: Energy differeneces of spin combinations for high fields. As in Figure 5.2, a negative value in the graph means an exotherm process. Note the energy scale which is now in MHz instead of Hz! For the ^{7}LiNa mixture, there is a zero-crossing in the $|1,-1;1,1\rangle$ channel at 16.1 G. This could be an interesting point to study the exchange of $\Delta m_f = 2$.

Similarly to the heteronuclear bosonic case, there are two magnetic fields where the spin combinations are energetically degenerate: At zero field, trivially, but also at higher field, where the differential Zeeman shifts cancel again. This offers another possibility to study the spin dynamics; however, at the required field of about 70.2 G, there is no comercially available sensor with the required resolution, and also the field stabilization at this high offset is difficult. Also, the scattering properties are not given anymore by the low-field scattering lengths, which could make the small coupling even smaller at high fields.

Due to these reasons, the Fermi-Bose mixture was studied at low fields and the main reason for the extension of experimental tools to use the very low offset fields below 10 mG. Only in this range, the detuning gets close to the homonuclear cases, where the spin dynamics could be investigated successfully.

Spin Dynamics with Differen Sodium Backgrounds

Figure 5.35 shows the time development of a spin mixture where spin relaxation is possible (full circles) compared to the case where the process is suppressed both energetically as well as due to spin conservation. The second case therefore acts as the reference where no dynamics should happen and shows the state preparation reliability as well as the stability over time.

In the spin combination that allows SCC, Na is prepared in the ground state $|1,1\rangle$, while Li is transferred by a RAP into the $|1/2,-1/2\rangle$ energetically higher state. In the forbidden case, Li is prepared in the same state, while Na is in $|1,-1\rangle$. Since then Na is in the energetically highest state in the $|F=1\rangle$ manifold, Li cannot transfer energy inelastically. Also, there is no allowed spin transfer possible due to spin conservation.

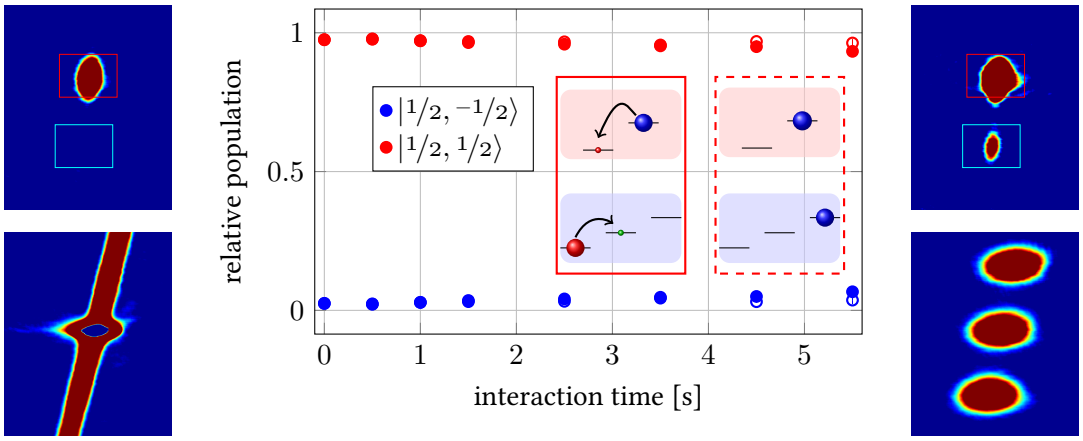

Figure 5.35: Heteronuclear Fermi-Bose spin dynamics at 302.95(85) mG, scanning the hold time. Closed circles indicate Na in $|1,1\rangle$ (left case of the population sketches), while open circles indicate Na in $|1,-1\rangle$ after a 45 µs RF pulse with 212.8 kHz. Only after about 5 s of hold time, the data sets can be clearly distinguished. The absorption pictures show ^{6}Li atoms after time of flight with Stern-Gerlach mapping (upper pictures) and Na in-situ (lower left) and after Stern-Gerlach mapping (lower right). The latter picture was taken for a preparation of Na in a superposition, see below for details.

Due to the very small population of Li in the $|1/2,1/2\rangle$ state, great care has been taken to prevent any systematic errors. Therefore, the sequence for lithium was always identical, with the same hold time, while the Na atoms were removed in-situ with a resonant light pulse which was also used to image the atoms. This procedure makes it impossible to track the sodium spin development over the time as the in-situ imaging is not spin-dependent.

The real space images show the spin mapping of sodium and lithium; the left pictures correspond to removal of Na directly after the final field is reached. The in-situ Na pictures clearly show a large remaining thermal part which is not trapped in the dimple, but stays in the waveguide. These atoms are lost during the hold time, only leaving the atoms in the dimple. The hole in the middle indicates an optically dense sample where no sufficient amount of light reaches the camera.

The right-hand pictures show the mapping of Li and Na after the full interaction time, where also sodium is spin-mapped. The presented data show sodium in a distribution over all three spin states, as the Na seeding was scanned, too. The results of these data are shown below. An important information here is the comparison with the sodium evolution to equilibrium discussed above, which happens on a similar time scale. This process does not seem to have an impact on the heteronuclear processes here.

The effect of any spin changes that might be caused by lithium cannot be resolved in sodium, also not in a clear state preparation, since the imaging sensitivity for Na is not sufficient, as it was designed for high atom numbers so far.

The lithium picture clearly shows the small population in the lower hyperfine state, which seems more convincing than the small counted number. The color scales are chosen to emphasize small atom numbers.

Coherent Coupling of Sodium

As can be seen by the example picture, not only the pure $|1,1\rangle$ state preparation of sodium causes spin dynamics in lithium, but also mixtures of sodium states. Further investigations of this are presented in Figure 5.36, where sodium is driven with Rabi pulses of different length to populate all accessible spin combinations from purely $|1,1\rangle$ over all mixtures to a pure $|1,-1\rangle$ state. See Figure 3.18 as reference for the spin populations and magnetization during the 3-level Rabi coupling.

This dataset shows two important features: The more obvious is that the lithium spin can change only if there is a sufficient amount of sodium atoms in the two lower states, since both the processes $|1/2,-1/2;1,1\rangle \Rightarrow |1/2,1/2;1,0\rangle$ and $|1/2,-1/2;1,0\rangle \Rightarrow |1/2,1/2;1,-1\rangle$ are possible, conserving the spin and releasing energy. Therfore, up to about 25 µs coupling pulse, where the $|1,1\rangle$ and $|1,0\rangle$ states dominate, the Li populaton in $|1/2,-1/2\rangle$ rises by roughly a constant amount. For larger populations of $|1,-1\rangle$ of Na, the Li population in the lower state is reduced, since less possible spin exchange partners are available.

The second feature regards the seeding: For both Na and ^{7}Li the seeded spin changing collisions show a much faster dynamics than any process without seeding. This is consistent with the theoretical description, where the spin flip rate rises with the final state population.

For the data of ^{6}LiNa, there is no corresponding observation, if only Na is seeded: Since $|1,0\rangle$ is one possible final state for the dynamics, the population in this state should influence the spin flips. But this is not observed, of course, since the sodium $|1,0\rangle$ population is only one part of the seeding, similar to the homonuclear case if a spinor $(00.50.5)$ would be prepared: The second part of seeding is missing, thus suppressing the spin exchange. Therefore, ^{6}Li would have to be seeded simultaneously so that a superposition of $|1/2,1/2;1,0\rangle$ and $|1/2,1/-2;1,1\rangle$ would pe present.

Forbidden Spin Population

The influence of the final state population of ^{6}Li was studied by populating both states in different parts. The results of this are plotted in Figure 5.37, where the lithium atoms were transferred to the different state populations using an RF sweep of varied duration.

A full transfer of lithium from the $|1/2,1/2\rangle$ initial state to the upper $|1/2,-1/2\rangle$ state was achieved with an adiabatic sweep of 2000 µs from 2.223 MHz to 2.623 MHz . Reducing this

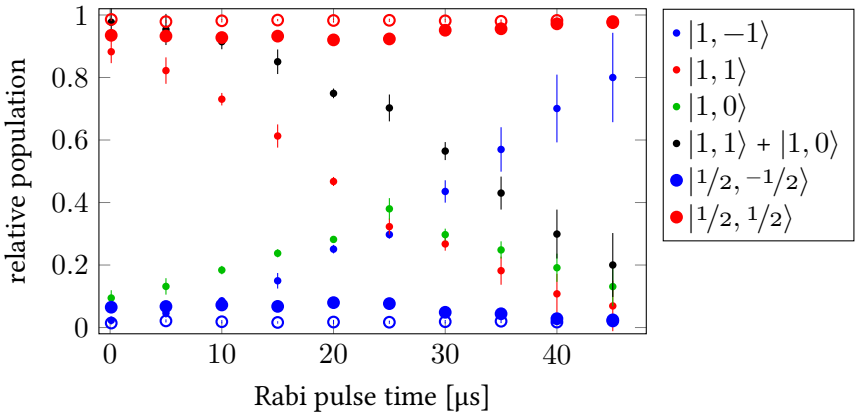

Figure 5.36: Heteronuclear Fermi-Bose spin dynamics at 302.95(85) mG. Hold time for all data was 5.5 s. Na atoms were driven with 212.8 kHz for Rabi coupling. As long as a sufficient amount of Na atoms in either $|1,1\rangle$ or $|1,0\rangle$ are present, spin exchange can be seen. The seeding of Na does never increase the spin exchange rate.

sweep time leads to Landau-Zehner tunnelling, leaving atoms in the ground state. This transfer was done at a higher magnetic offset field of 2.6 G, before the field was ramped to the final settings, leaving the Li atoms in interaction with sodium for about 200 ms. We assume that the state coherence of the ^{6}Li states then is already decayed due to spin-conserving collisions with sodium and a non-coherent, thermalized mixture of the ^{6}Li states is prepared.

The case of a full transfer to the upper state is depicted with the full circles in Figure 5.37 and shows the same behaviour as in the data presented above. For a faster sweep of 375 µs, only around 80% of the atoms are transferred. The observed behaviour is similar, but the difference in populations is larger, which could be interpreted as an amplification of the spin change process.

However, for an even faster sweep with 250 µs and only 60% state transfer, the dynamics show an unexpected behaviour: For 2 to 3 s, the population of the excited state decreases, but *increases* afterwards, reaching nearly the same value as the preparation. But here one has to take the error bars into account which are also consistent with a strictly constant population.

The most striking feature therefore appears for the shortest sweep time of 125 µs, where the excited state population increases for longer interaction times. This is also observed in the case of no RF sweep (0 µs). Here it is important to keep in mind that the ^{6}Li hold time was the same for all points, just the removal time of Na changed. These two lower lines therefore have to be interpreted in the way that the immersion of ^{6}lithium in the sodium condensate for over 4 s leads to a rise of the $|1/2,-1/2\rangle$ population, while without sodium the initial population stays constant.

This observation raises several questions, since the process $|1/2,1/,2;1,1\rangle \Rightarrow |1/2,-1/2;1,x\rangle$ to any sodium state with $x = 0, \pm 1$ is energetically forbidden and violates spin conservation. This double-forbidden process therefore requires further investigation.

To exclude systematic misinterpretation of the data, Figure 5.38 shows the absolute atom numbers detected in the two states. These numbers clearly reproduce the trends seen in Figure 5.37, especially the increase of atoms in the upper state for the ground state preparation

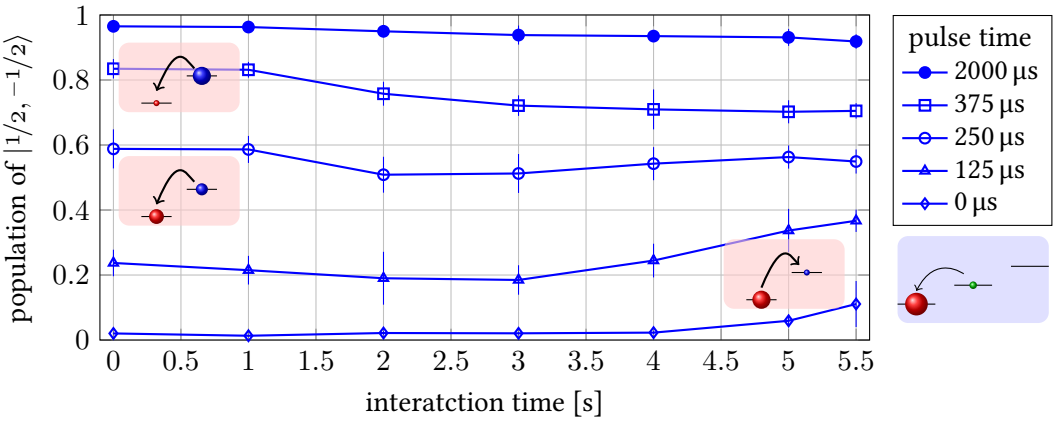

Figure 5.37: Heteronuclear spin dynamics at 302.95(85) mG, scanning the hold time. Lithium is prepared in different populations; the preparation is done with an RF sweep of the indicated length. Sodium is present in the $|1, 1\rangle$ state, allowing lithium atoms to undergo spin relaxations into the $|1/2, -1/2\rangle$ state. The Na atoms are removed at the indicated times; hold time for Li is always 5 s. The striking feature is the increase of Li in the *upper* state after a few seconds interaction time.

(diamond markers). However, the strongly fluctuating sum of atoms due to unstable performance of the experiment makes it necessary to always look at the relative populations, for example the case of 125 µs sweep (triangle markers) where for the last time step, the population in both states increases. It is interesting to note that only in two cases there is a significant amount of losses of total atom number, which is the case of no transfer (starting with all atomn in the ground state, diamond markers) and full transfer (all atoms in the upper state, cirle markers). The latter one makes sense if one assumes that each spin flip of a lithium atom releases about 77 kHz of energy, leading to possible trap losses. In the former case of ground state preparation, there is no obvious reason for stronger losses.

First, one has to check the sodium state preparation. As detailed in subsection 3.4.3, we observe a not well understood transfer of sodium into other states during the hold time without any obvious reason. This is attributed to stray RF fields in the lab that could not be isolated. For the presented date here, we observe a sodium population of the $|1, 0\rangle$ state after the full interaction time of up to 10% , independent of the lithium populations. The total sodium atom numbers are between 1×10^5 to 3×10^5 atoms, which is about 3 to 5 times the lithium atom number.

Unfortunately, the sodium state population cannot be tracked during the hold time, in the same scan as the in-situ imaging again is not state-dependent. Therefore it cannot be detected whether the $|1, 0\rangle$ state population was present from the beginning or was influenced by any lithium spin flips.

The population of $|1, 0\rangle$ atoms in sodium would allow the observed rise of lithium atoms in the upper state, following the spin-conserving process $|1/2, 1/2; 1, 0\rangle \Rightarrow |1/2, -1/2; 1, 1\rangle$. The energy that is necessary for this process could partly be taken from the Fermi energy: A lithium

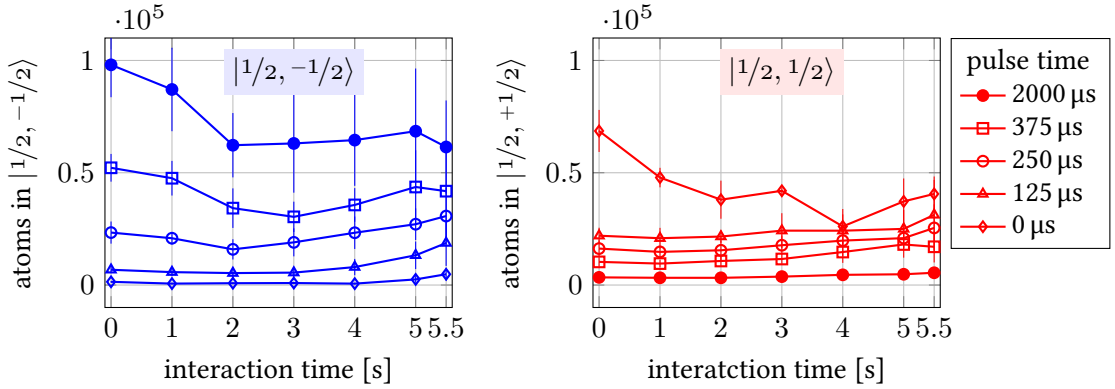

Figure 5.38: Heteronuclear Fermi-Bose spin dynamics at 302.95(85) mG. Same dataset as above, showing the absolute lithium numbers of the upper (right) and lower (left) state. For the case of ground state preparation (diamond markers), a clear increase in the atom number of the excited state can be seen; also the increase in the measured ground state population for the preparation in $|1/2, -1/2\rangle$ (cirle markers) is visible. This shows that the observed effects in the relative population are not just due to a relative loss.

atom from above the Fermi edge could reduce its total energy by changing the internal degree of freedom and undergoing a transition to a low-lying motional state, as sketched in Figure 5.39.

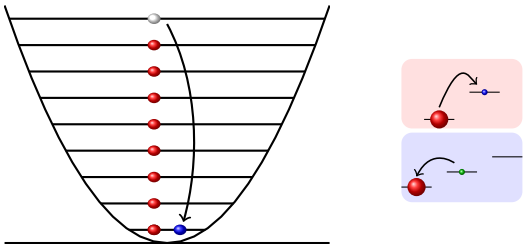

Figure 5.39: Sketch for the explanation of the energy conservation for a spin flip due to large Fermi energy.

The scattering length between the ^{6}Li $|1/2, 1/2\rangle$ and $|1/2, -1/2\rangle$ is less then 1 a_B for $B < 1$ G [112], therefore the interaction does not add a large energy scale; for higher magnetic fields, the interaction could lead to a blockade as the energy of the lowest motional state would be raised by the interaction with the large Fermi sea.

5.5 Remaining Challenges and Opportunities

The main goal of this thesis was the preparation of investigations of coherent heteronuclear spin changing collisions in the Fermi-Bose mixture. This challenging task was tackled in several steps, according to this roadmap:

Coherent oscillations in a thermal Bose gas Although presented in a different order in this thesis, the thermal oscillations were the first scans that really showed oscillatory behaviour. Comparison of the oscillation period with the predicted dependence on the magnetic field shows a qualitative and quantitative agreement.

Coherent oscillations in a BEC of sodium For the second step, the most important change was going to a condensate with lower particle numbers and very low trap frequencies, getting closer to the single mode approximation, so that at least the initial dynamics could be observed. Again, taken the sine curves as indicators for the oscillation period, at least a qualitative agreement with the expected behaviour could be observed. Also multimode dynamics were observed in the oscillations.

Coherent oscillations in a BEC of ^{7}lithium In ^{7}Li, it was not possible to observe coherent dynamics, as it was not extensively studied. In principle, ^{7}Li is an interesting candidate for studies of spin changing collisions due to the large difference in the $F = 0$ and $F = 2$ scattering length with a small total value of both.

Coherent oscillations in the ^{7}Li-Na mixture In the ^{7}LiNa mixture, no coherent oscillations could be observed, but a definite incoherent spin exchange. This system is a very hard choice since the intraspecies couplings are much stronger than the interspecies coupling. A careful choice of magnetic field, densities of both species and controlled overlap might allow to observe oscillations. An important point here is the positive heteronuclear scattering length which leads to a repulsion of the ^{7}Li out of the Na cloud. A thermal gas in one of the components can increase the overlap; this was also the ansatz for the successful bosonic heteronuclear NaRb spin oscillations. [62]

Coherent Oscillations in the ^{6}Li-Na mixture As for the bosonic mixture, in ^{6}LiNa no coherent oscillations could be observed. However, in this case the simultaneous coupling of both species was not yet achieved. The overlap is less limiting for ^{6}LiNa due to the negative scattering length.

Without the coherent coupling, only a slight drift of the populations due to heteronuclear spin exchange could be observed and some additional, partly surprising effects, due to the high Fermi energy and the parasitic coupling. All dynamics were observed on a time scale of several seconds.

Coherent Superposition of ^{6}Li and Na

This work paved the road for the final observation of ^{6}LiNa oscillations by providing the most important experimental features:

- Reliable state read out
- Stable magnetic fields at very low offset ($< 10\,\mathrm{mG}$)
- Coherent Rabi coupling at these fields for both ^{6}Li and Na

Putting these techniques together might allow to observe coherent spin dynamics, since the most promising setup was not yet realised: Both ^{6}Li and Na in their mixture were prepared in a coherent superposition individually, but no oscillations could be observed. However, in analogy to the experiments by [62], one needs to prepare a coherent superposition of *both* species simultaneously. This is also the reason why a very low magnetic field is needed, since only when the differential linear Zeeman shift is smaller than the Rabi frequency of the driving, it will be possible to produce this state combination with a single pulse, which is desirable for a reliable coupling.

Sich, nû hab ich dich gelêret,
des ich selber leider nie gepflac.
ungelücke mir verkêret,
daz ein sælic man volenden mac.

(Walther von der Vogelweide)

6 Conclusion and Outlook to Possible Future Experiments

This thesis has investigated the spin-dependend interactions in sodium and sodium-lithium mixtures, and provided the experimental conditions for this.

The experimental work enabled the control of precise magnetic fields which allow the study and possible application of Feshbach resonances. Spanning nearly six orders of magnitude, also very low magnetic fields could be realized which are an important step for future studies of the Fermi-Bose spinor mixtures. For the coupling of the states, an equal range of frequencies for hyperfine transitions was realized, which allows the preparation of all relevant state combinations.

In the last years, the improved Feshbach spetroscopy of sodium and lithium-sodium mixtures allowed a more precise determination of the interaction potentials and thus a more rigorous prediction for the coupling parameters which is needed for the spin dynamics.

The first observation of coherent spin dynamics in our system clearly shows the experimental limitations that have to be overcome, but also opens the road to many interesting physical models that can be realized in the different spinor mixtures. The homonuclear coherent spin dynamics are already a well-studied process with a still very active field of further investigation, but also application, especially in the prospect of quantum-enhanced metrology or precision tests of fundamental constants.

Extending this field of spinor physics to the heteronuclear case can allow for more degrees of freedom. Especially interesting is the Fermi-Bose case which could allow the production of entangled states of fermionic and bosonic atoms. One possible prospect to use the heteronuclear spin exchange is the simulation of one-dimensional dynamical gauge fields, as discussed in [50].

The realization of this sophisticated model requires a well-working combination of all experimental tools developed so far in our experiment: First, the ultracold Fermi-Bose mixture has to be produced, which is done routinely. Species-dependend lattices have already been used successfully in previous experiments [83, 89].

Due to the new frequency source setup, the state preparation does not pose major challenges, and the same is true for the magnetic field stabilization, where a cancelling of the gradient fields is the remaining task.

The spin-exchange process has also been investigated, but for the Fermi-Bose case it is far from the level of control needed for the implementation of the Schwinger model as introduced in [50].

A final remark regarding possible future improvements in the experiment shall discuss the change to another fermionic species instead of ^{6}Li. Since the scattering properties in the ^{6}LiNa

system are not very fortune for neither interaction tuning nor strong spin exchange coupling, a substitution of ^{6}Li with ^{40}K might be an advantage: The ^{40}K^{23}Na mixture has a large difference of singlet and triplet scattering lengths, promising for spin dynamics, and provides a broad Feshbach resonance suitable for tuning and the production of fermionic molecules, as shown in [110, 76]. The change to potassium would require a change in the oven design, since the mixing, as done in our experiment so far, is not suitable for the K+Na mixture. [110]

A Arduino & Electronics

A.1 Electronic Parts Used in the Microwave Setup

Table A.1: List of parts used in the microwave setup.

device	function	frequency limits
Arduino Due[1]	Microcontroller	84 MHz clock speed
AD9959/PCBZ[2]	4 channel DDS evaluation board	0.3 MHz to 200 MHz
AD9958/PCBZ[2]	2 channel DDS evaluation board	0.3 MHz to 200 MHz
FE 5680 A[3]	Rb atomic frequency standard	10 MHz
E4421B[4]	MW source	0.25 MHz to 3000 MHz
EVAL-ADF4350EB2Z[2]	Wideband PLL Synthesizer	137.5 MHz to 4400 MHz
KU PA BB 233 BBA[5]	3 W MW amplifier	500 MHz to 2500 MHz
ZHL-100W-52X[6]	100 W RF amplifier	50 MHz to 500 MHz
ZHL-3A[6] (2*)	1 W RF amplifier	0.4 MHz to 150 MHz
ZKL-2R5[6] (2*)	20 mW pre-amplifier	10 MHz to 2500 MHz
ZAPDQ-2-S[6]	Splitter/Combiner 90°	1000 MHz to 2000 MHz
ZX10Q-2-3-S+[6]	Splitter/Combiner 90°	220 MHz to 470 MHz
ZX05-C24-S+[6]	Level 7 mixoer	300 MHz to 2400 MHz
ZX05-1L-S+[6]	Level 3 mixer	2 MHz to 500 MHz
ZX10-2-252-S+[6]	Splitter/Combiner 0°	500 MHz to 2500 MHz
ZX10-2-12-S+[6]	Splitter/Combiner 0°	2 MHz to 1200 MHz
ANNE-50L[6]	50 Ω terminator	0 GHz to 12 GHz
SLP-250+[6]	Low pass	0 MHz to 225 MHz
ZASWA-2-50DR+[6]	RF swtich	0 GHz to 5 GHz

Manufacturers: [1]Arduino, [2]Analog Devices, [3] Frequency Electronics, [4]Agilent,[5]Kuhne Electronic, [6]Minicircuits.

A.2 Arduino Program Code

This section lists the Arduino Microcontroller Codes for the magnetic field control, the microwave setup and the cooling water temperature stabilization. Only relevant parts are listed.

A.2.1 Microwave Setup

The code for the microwave setup is split into several files for easier maintenance. The main file defines the channel settings and variables and initiates communication in the main loop. The Interrupt Functions file contains the time critical code which is executed after a trigger pulse is received and controls the timing of the chopped ramps.

Main File DDS_6channel.ino

```
const int P1            =  6; // C24
const int P2            =  7; // C23
const int P3            =  8; // C22

const int updatepin     =  9; // C21
const int cs_dds_1      = 10; // C29/A28
const int power_down    = 11; // D7
const int resetpin      = 12; // D8
const int NOT_USED      = 13; // B27

const int ext_tr_GND    = 24; // A15
const int ext_trigger   = 25; // D0
const int ext_trig2_GND = 34; // C2
const int ext_trig2     = 35; // C3
//        not used      = 36; // C4
//        not used      = 37; // C5
const int ext_50Hz_GND  = 38; // C6
const int ext_50Hz      = 39; // C7

const int switch1_GND   = 40; // C8
const int switch1       = 41; // C9
const int calc_LED      = 42; // A19
const int power_LED     = 43; // A20
const int switch2_GND   = 44; // C19
const int switch2       = 45; // C18
const int switch3_GND   = 46; // C17
const int switch3       = 47; // C16
//        not used      = 48; // C15
const int CLK_GND       = 49; // C14
const int CLK_ref       = 50; // C13
const int MOSI_ref      = 51; // C12
const int ref_clk_cs    = 52; // B21
const int CLK_GND2      = 53; // B14

const double sys_clk    = 500e6;
const double sync_clk   = 0.25*sys_clk;
const int    max_ramp   = 400;
const double cut_time   = 0.297;

//read in data from SDFF variables
int           ramp_num = 0;
double        freq_0[2][max_ramp],    freq_1[2][max_ramp
      ], time_array[2][max_ramp];
unsigned long carrier[2][max_ramp], ampl_int[2][max_ramp
      ], phase_int[2][max_ramp];

// values for PLL frequency, initialized here, set in
      setup()
int R0[2000], R1[2000], R4[2000];

//precompiled data to be written to the DDS
byte    freq_0_c[2][max_ramp][4], freq_1_c[2][max_ramp
      ][4], freq_step[2][max_ramp][4];
byte    ramp_t_step[2][max_ramp], phase_c[2][max_ramp
      ][2],  ampl_c[2][max_ramp][2], bits;
int     ch_select[max_ramp], switch_select[max_ramp],
      switch_shift; // selects the DDS board and RF
      switch to use
double  time_array_c[2][max_ramp];
boolean rampdown_bool_c[2][max_ramp];

//variables for calculation
int     ramp_parts_num[2][max_ramp], ramp_first_part[2][
      max_ramp], ramp_last_part[2][max_ramp], k;
double  freq_start, freq_end, rem_time, steepness,
      start_time, end_time, cutted_time, minimum, multi,
      temp = 0;
boolean finished, rampdown[2][max_ramp];
unsigned long multi_int = 0;

//byte caculation functions
const double min_t_step          = 1/sync_clk;
const double freq_steps_possible = 4294967295.0;
const double min_freq_step       = sys_clk/
      freq_steps_possible;
const double inv_min_freq_step   = freq_steps_possible/
      sys_clk;
unsigned long min_ind, min_ind_index, freq_step_mult;
boolean found;
double delta_fges, min_t_slope, sweep_sync_step, slope,
      f_wanted, f_dds, end_dds = 0, check[256] =
      {999999};
double time_step_freq_step[5];

//min Index function
unsigned long min_index;
double min_value;

//phase function
unsigned long phase_bits;

//amplitude function
double f, norm, corrected_scaling_fac, A_des;

//trigger loop
volatile int all_ramps_counter      = 0;
volatile int SDFF_ramp_counter      = 0;
volatile int this_ramp_chop_counter = 0;
volatile int ramp_in_dds_buffer     = 0;

// temporary variables for serial read
char   ramp_num_char[2], tmpchar, mode;
String tmpstring;

//interrupt
boolean start_up = true;

// variable for selecting the slave DDS. Defaults to the
       first one.
int cs_dds = cs_dds_1;

void setup(){
  R0[ 175] = 0x8C0000; R1[ 175] = 0x8008011; R4[ 175] =
       0xC5003C;
  R0[ 200] = 0xA00000; R1[ 200] = 0x8008011; R4[ 200] =
       0xC5003C;
  R0[ 220] = 0xB00000; R1[ 220] = 0x8008011; R4[ 220] =
       0xC501E4;
  R0[ 230] = 0xB80000; R1[ 230] = 0x8008011; R4[ 230] =
       0xC5003C;
  R0[ 400] = 0xA00000; R1[ 400] = 0x8008011; R4[ 400] =
       0xB501FC;
  R0[ 410] = 0xA40000; R1[ 410] = 0x8008011; R4[ 410] =
       0xB501FC;
  R0[ 500] = 0xC80000; R1[ 500] = 0x8008011; R4[ 500] =
       0xB5003C;
  R0[ 850] = 0xAA0000; R1[ 850] = 0x8008011; R4[ 850] =
       0xA5002C;
  R0[ 851] = 0xAA0010; R1[ 851] = 0x8008029; R4[ 851] =
       0xA5002C;
  R0[1600] = 0xA00000; R1[1600] = 0x8008011; R4[1600] =
       0x95002C;
```

```
108   R0[1772] = 0xB10010; R1[1772] = 0x8008029; R4[1772] =
          0x580005;
      R0[1950] = 0xC30000; R1[1950] = 0x8008011; R4[1950] =
          0x95003C;
110
      // initialize serial communication at 115200 baud (yes
          , we are that fast!)
112   Serial.begin(115200);
      //Serial.println("Arduino Due; DDS_6channel, updated
          around sept. 18 2015");
114   //SPI setup for DDS
      SPI.begin(cs_dds_1);
116   SPI.setDataMode(cs_dds_1,SPI_MODE3);
      SPI.setBitOrder(cs_dds_1,MSBFIRST);
118   SPI.setClockDivider(cs_dds_1,20);

120   SPI.begin(cs_dds_2);
      SPI.setDataMode(cs_dds_2,SPI_MODE3);
122   SPI.setBitOrder(cs_dds_2,MSBFIRST);
      SPI.setClockDivider(cs_dds_2,4);
124
      //pinmode set, start output low
126   pinMode(ext_trigger,  INPUT);
      pinMode(ext_trig2,    INPUT);
128   pinMode(ext_50Hz,     INPUT);

130   pinMode(ext_tr_GND,   OUTPUT); digitalWrite(ext_tr_GND
          ,    LOW);
      pinMode(ext_trig2_GND,OUTPUT); digitalWrite(
          ext_trig2_GND, LOW);
132   pinMode(ext_50Hz_GND, OUTPUT); digitalWrite(
          ext_50Hz_GND,  LOW);

134   pinMode(power_down,   OUTPUT); digitalWrite(power_down
          ,    LOW);
      pinMode(resetpin,     OUTPUT); digitalWrite(resetpin,
          LOW);
136   pinMode(P0,           OUTPUT); digitalWrite(P0,
          LOW);
      pinMode(P1,           OUTPUT); digitalWrite(P1,
          LOW);
138   pinMode(P2,           OUTPUT); digitalWrite(P2,
          LOW);
      pinMode(P3,           OUTPUT); digitalWrite(P3,
          LOW);
140   pinMode(updatepin,    OUTPUT); digitalWrite(updatepin,
          LOW);
      pinMode(ref_clk_cs,   OUTPUT); digitalWrite(ref_clk_cs
          ,    HIGH);
142   pinMode(CLK_ref,      OUTPUT); digitalWrite(CLK_ref,
          LOW);
      pinMode(CLK_GND,      OUTPUT); digitalWrite(CLK_GND,
          LOW);
144   pinMode(CLK_GND2,     OUTPUT); digitalWrite(CLK_GND2,
          LOW);
      pinMode(MOSI_ref,     OUTPUT); digitalWrite(MOSI_ref,
          LOW);
146
      pinMode(switch1,      OUTPUT); digitalWrite(switch1,
          LOW);
148   pinMode(switch1_GND,  OUTPUT); digitalWrite(
          switch1_GND,   LOW);
      pinMode(switch2,      OUTPUT); digitalWrite(switch2,
          LOW);
150   pinMode(switch2_GND,  OUTPUT); digitalWrite(
          switch2_GND,   LOW);
      pinMode(switch3,      OUTPUT); digitalWrite(switch3,
          LOW);
152   pinMode(switch3_GND,  OUTPUT); digitalWrite(
          switch3_GND,   LOW);
      pinMode(power_LED,    OUTPUT); digitalWrite(power_LED,
          HIGH);
154   pinMode(calc_LED,     OUTPUT); digitalWrite(calc_LED,
          LOW);

156   attachInterrupt(ext_trig2,   interrupt_func, RISING);
      attachInterrupt(ext_trigger, interrupt_func, RISING);
158
      Serial.println("Arduino ready");
160
      write_PLL(1950);
162   reset_DDS();  //reset DDS (both bords are reset)
  }
164
```

```
void loop(){
166   if(Serial.available()>0){ // check for data available
          in the buffer
      delay(500);             // wait for all data to
          arrive
168   mode = Serial.read();   // set mode of operation
      if(mode == 't'){        // single tone mode
170   cs_dds = 10;
        read_in_freqdata();   //read in data from buffer
172   }

174   if(mode == 'r' ){           // start ramp mode
        digitalWrite(calc_LED,HIGH);
176     read_in_rampdata();       // read in ramping data
            from buffer
        ramp_calculation();       // pre-calculate all
            bytes to be written to the DDS during the
            sequence
178     reset_DDS();              // reset DDS to bring it
            into a defined state
        write_PLL(carrier[0][0]);
180     cs_dds = ch_select[0];    // selects the DDS board
            for the first ramp
        switch_shift = switch_select[0];
182     ramp_write(0);            //write first ramp to
            the DDS
        start_up = false;
184     digitalWrite(calc_LED,LOW);
      }
186   }
  }
```

Interrupt Functions

interrupt_stuff.ino

```
  // -- start of help functions -- \\
2 //this function gets called by the interrupt on pin
        ext_trigger (experiment control)
  //it starts the first part of each ramp defined in the
        SDFF, if the ramp is chopped the following
4 //parts are started by the timer interrupt
  void interrupt_func(){
6   if(!start_up ){        //workaround (otherwise this
        function runs when arduino is reset, due to all
        pins high)
  // the following means that D4.6 is low and the trigger
        comes from the D3.26 channel only. By this, we
        decide which pin triggered the interrupt!!
8 // why only one interrupt? reduces error probability
  // the 2nd trigger is ~500µs slower. Issue with
        different registers?
10 // But does not matter as we use this for the 50Hz
        trigger anyways.

12 if(REG_PIOC_PDSR & 8){while(!(REG_PIOC_PDSR & 128))
        {};};//delayMicroseconds(5000);};  // this adds a
        delay. Find out what exactly by yourself.
      TC_Stop(TC1, 0);     //disable timer (if running)
14    SDFF_ramp_counter++; // FIXME: could be done
          afterwards if implemented cleverly!
      all_ramps_counter = ramp_first_part[0][
          SDFF_ramp_counter]; //correct the
          all_ramps_counter if necessary
16
      REG_PIOD_ODSR &= ~1 << 7; // set Pin 11 LOW (power
          up)
18    REG_PIOC_ODSR  = 1 << 21;  // set Pin 9 HIGH,
          updatepin
  //    NOP;NOP;                          // wait for two
        clock cycles (not needed)
20    REG_PIOC_ODSR  = 00 << 22;
      REG_PIOC_ODSR  = 15 << 22;
22    REG_PIOC_ODSR  = (9*(!rampdown_bool_c[1][
          all_ramps_counter]) + 6*(!rampdown_bool_c[0][
          all_ramps_counter])) << 22;   // set SDIO Pins
          low if necessary for down ramps

24 NOP;NOP;NOP;NOP;NOP;NOP;NOP;NOP;NOP;NOP;
  REG_PIOC_ODSR  = 1 << switch_shift;  // set switch HIGH
26
      PIOC->PIO_CODR =  1 << 21;       //set Pin 9 LOW  //
          set updatepin low  // FIXME: maybe not
          necessary any more, set by REG_PIOC_ODSR = ...
```

```
28                                                          80
      if(time_array[0][SDFF_ramp_counter] < 0.001){
30      delayMicroseconds(time_array[0][SDFF_ramp_counter  82
            ]*1e6-6);
        PIOD->PIO_SODR=1<<7;      //set Pin 11 HIGH //
            power down if the ramp is not chopped, for
            very short ramps/pulses!
32      REG_PIOC_ODSR  = 0 << 9;                            84
      }
34
//    REG_PIOC_ODSR =   1 << 21;  // set Pin  9 HIGH  //
      set updatepin, brings data into active registers //
       FIXME: test wether this is faster/slower/equal to 86
      setting REG_PIOA_ODSR explicitely
36  /*
// TEST FOR DOUBLE PULSES  // 230t500000f500000F1000aSz
38 REG_PIOD_ODSR  = 1 << 7; // set Pin 11 HIGH (power down) 88
delayMicroseconds(100);
40 REG_PIOD_ODSR  = 0 << 7; // set Pin 11 LOW (power up)    90
   REG_PIOC_ODSR  = 00 << 22; // set all SDIO pins low (
       prepare)
42 REG_PIOC_ODSR  = 15 << 22; // set all SDIO pins high (   92
       start ramps)
   REG_PIOC_ODSR = (9*(!rampdown_bool_c[1][
       all_ramps_counter]) + 6*(!rampdown_bool_c[0][      94
       all_ramps_counter])) << 22;   // set SDIO Pins low
       if necessary for down ramps
44 if(time_array[0][SDFF_ramp_counter] < 0.001){
       delayMicroseconds(time_array[0][SDFF_ramp_counter
       ]*1e6-6); PIOD->PIO_SODR=1<<7;} //set Pin 11 HIGH
       //power down if the ramp is not chopped, for very  96
       short ramps/pulses!
// ********************
46 */
      //start timer, which will start next part of chopped
           ramp or turn off
48    startTimer(TC1, 0, TC3_IRQn, time_array_c[0][        98
          all_ramps_counter]);
      ramp_write(all_ramps_counter+1); //write next ramp
          into buffer
50  }                                                       100
}
52
//Black magic, do not mess with this
54 void startTimer(Tc *tc, uint32_t channel, IRQn_Type irq,
       double wait_time){
  pmc_set_writeprotect(false);          // Enable or
      disable write protect of PMC registers.
56  pmc_enable_periph_clk((uint32_t)irq); // Enable the
      specified peripheral clock.

58  TC_Configure(tc, channel, TC_CMR_WAVE|
      TC_CMR_WAVSEL_UP_RC|TC_CMR_TCCLKS_TIMER_CLOCK4);
  uint32_t rc = VARIANT_MCK/128*wait_time;
60  TC_SetRA(tc, channel, rc/2);
  TC_SetRC(tc, channel, rc);
62  TC_Start(tc, channel);

64  tc->TC_CHANNEL[channel].TC_IER = TC_IER_CPCS;
  tc->TC_CHANNEL[channel].TC_IDR = ~TC_IER_CPCS;
66  NVIC_EnableIRQ(irq);
}
68
//called by timer interrupt, function name must not be
     changed
70 void TC3_Handler(){
  TC_GetStatus(TC1, 0);
72  TC_Stop(TC1, 0); //disable timer (or it will call this
       function again)
  all_ramps_counter++;
74  if(ramp_last_part[0][SDFF_ramp_counter] >
      all_ramps_counter - 1){ // -1
    //this is a fix, without this the ramp chopping does
        /not/ work  // FIXME: but - why?
76    for(int i=0;i<10000;i++){NOP;}  // wait for 10000
        clock cycles (120µs)

78    PIOC->PIO_SODR =  1 << 21;     // set Pin 9 HIGH  //
        set updatepin, brings data into active
        registers // FIXME: test wether this is faster/
        slower/equal to setting REG_PIOA_ODSR
        explicitely
      NOP;NOP;                       // wait for two clock
       cycles
  REG_PIOC_ODSR  = 00 << 22;     // I/O Pins LOW
  REG_PIOC_ODSR  = 15 << 22;     // I/O Pins HIGH
  REG_PIOC_ODSR  = (9*(!rampdown_bool_c[1][
      all_ramps_counter]) + 6*(!rampdown_bool_c[0][
      all_ramps_counter])) << 22;   // set SDIO Pins
      low if necessary for down ramps

  PIOC->PIO_CODR =  1 << 21;       //set Pin 9 LOW  //
      set updatepin low  // FIXME: maybe not
      necessary any more, set by REG_PIOC_ODSR = ...
  REG_PIOC_ODSR  =  1 << switch_shift; // turn on
      switch
  startTimer(TC1, 0, TC3_IRQn, time_array_c[0][
      all_ramps_counter]);
  ramp_write(all_ramps_counter+1); //write next ramp
      into buffer
  ramp_in_dds_buffer = all_ramps_counter+1;
}
else {
  PIOD->PIO_SODR =  1 << 7;            //set Pin 11
      HIGH              // power down
  REG_PIOC_ODSR  = 00 << switch_shift; // set switch
      low

  REG_PIOC_ODSR  = 00 << 22; // set all SDIO pins low
      (prepare) // appareantly necessary when working
       with two boards!
  cs_dds = ch_select[SDFF_ramp_counter+1];
                  // set the slave select to the
      value for the next ramp
  switch_shift = switch_select[SDFF_ramp_counter+1];
  ramp_write(ramp_first_part[0][SDFF_ramp_counter+1]);
       // write proper ramp into buffer  // FIXME:
      Changed place here instead of setting it on
      start of ramp. Suppresses a 100µs delay. But
      does it work reliably here?
  write_PLL(carrier[0][SDFF_ramp_counter+1]);
              // set the carrier to the value for
      the next ramp
}
}
```

Frequency Ramps

ramp_freq_functions.ino

```
// -- start of help functions -- \\
2 //writes the bytes for a single ramp to the DDS (but no
      I/O Update!)
void ramp_write(int ramp){
4 //select ch 1/2 for frequency and amplitude (MW)
  // 0x00
6 SPI.transfer(cs_dds,              B00000000,
      SPI_CONTINUE);
  SPI.transfer(cs_dds,              B01100000,
      SPI_CONTINUE);
8 //write frequency word 0 0x04 (lower frequency)  //
      for ch 1/2
  SPI.transfer(cs_dds,              B00000100,
      SPI_CONTINUE);
10 SPI.transfer(cs_dds,   freq_0_c[0][ramp][0],
      SPI_CONTINUE);
  SPI.transfer(cs_dds,   freq_0_c[0][ramp][1],
      SPI_CONTINUE);
12 SPI.transfer(cs_dds,   freq_0_c[0][ramp][2],
      SPI_CONTINUE);
  SPI.transfer(cs_dds,   freq_0_c[0][ramp][3], SPI_LAST)
      ;
14 //write frequency word 1 0x04A(higher frequency)
  SPI.transfer(cs_dds,              B00001010,
      SPI_CONTINUE);
16 SPI.transfer(cs_dds,   freq_1_c[0][ramp][0],
      SPI_CONTINUE);
  SPI.transfer(cs_dds,   freq_1_c[0][ramp][1],
      SPI_CONTINUE);
18 SPI.transfer(cs_dds,   freq_1_c[0][ramp][2],
      SPI_CONTINUE);
  SPI.transfer(cs_dds,   freq_1_c[0][ramp][3],
      SPI_CONTINUE);
20 //set 0x06 amplitude control
  SPI.transfer(cs_dds,              B00000110,
      SPI_CONTINUE);
22 SPI.transfer(cs_dds,              B01010111,
      SPI_CONTINUE);
```

```
    SPI.transfer(cs_dds,     ampl_c[0][ramp][0],
         SPI_CONTINUE);
24  SPI.transfer(cs_dds,     ampl_c[0][ramp][1],
         SPI_CONTINUE);

26 // ramp parameters for ch 1/2
    if(rampdown_bool_c[0][ramp]){
28    // DOWNWARDS RAMP
      //enable linear sweep 0x03
30    //enable no dwell when ramping up
      SPI.transfer(cs_dds,            B00000011,
           SPI_CONTINUE);
32    SPI.transfer(cs_dds,            B10000000,
           SPI_CONTINUE);
      SPI.transfer(cs_dds,            B01000011,
           SPI_CONTINUE);
34    SPI.transfer(cs_dds,            B00000100,
           SPI_CONTINUE);
      //set 0x07 Linear Sweep Ramp Rate (time between
           frequency steps)
36    SPI.transfer(cs_dds,            B00000111,
           SPI_CONTINUE);
      SPI.transfer(cs_dds, ramp_t_step[0][ramp],
           SPI_CONTINUE);
38    SPI.transfer(cs_dds,            B00000001,
           SPI_CONTINUE);
      //set 0x08  Rising Delta Word (one large set because
           must first ramp up before a ramp down is
           possible)
40    SPI.transfer(cs_dds,            B00001000,
           SPI_CONTINUE);
      SPI.transfer(cs_dds,            B11111111,
           SPI_CONTINUE);
42    SPI.transfer(cs_dds,            B11111111,
           SPI_CONTINUE);
      SPI.transfer(cs_dds,            B11111111,
           SPI_CONTINUE);
44    SPI.transfer(cs_dds,            B11111111,
           SPI_CONTINUE);
      //set 0x09  Falling Delta Word
46    SPI.transfer(cs_dds,            B00001001,
           SPI_CONTINUE);
      SPI.transfer(cs_dds,freq_step[0][ramp][0],
           SPI_CONTINUE);
48    SPI.transfer(cs_dds,freq_step[0][ramp][1],
           SPI_CONTINUE);
      SPI.transfer(cs_dds,freq_step[0][ramp][2],
           SPI_CONTINUE);
50    SPI.transfer(cs_dds,freq_step[0][ramp][3],
           SPI_CONTINUE);
    }else{
52    // UPWARDS RAMP
      //enable linear sweep 0x03 FOR THE NO DWELL BITS IN
           RAMP UP
54    SPI.transfer(cs_dds,            B00000011,
           SPI_CONTINUE);
      SPI.transfer(cs_dds,            B10000000,
           SPI_CONTINUE);
56    SPI.transfer(cs_dds,            B11000011,
           SPI_CONTINUE);
      SPI.transfer(cs_dds,            B00000000,
           SPI_CONTINUE);
58    //set 0x07 Linear Sweep Ramp Rate (time between
           frequency steps)
      SPI.transfer(cs_dds,            B00000111,
           SPI_CONTINUE);
60    SPI.transfer(cs_dds,            B00000001,
           SPI_CONTINUE);
      SPI.transfer(cs_dds, ramp_t_step[0][ramp],
           SPI_CONTINUE);
62    //set 0x08  Rising Delta Word
      SPI.transfer(cs_dds,            B00001000,
           SPI_CONTINUE);
64    SPI.transfer(cs_dds,freq_step[0][ramp][0],
           SPI_CONTINUE);
      SPI.transfer(cs_dds,freq_step[0][ramp][1],
           SPI_CONTINUE);
66    SPI.transfer(cs_dds,freq_step[0][ramp][2],
           SPI_CONTINUE);
      SPI.transfer(cs_dds,freq_step[0][ramp][3], SPI_LAST)
           ;
68  }

70 //select ch 0/3 for frequency and amplitude (RF)
      // 0x00
72    SPI.transfer(cs_dds,            B00000000,
           SPI_CONTINUE);
      SPI.transfer(cs_dds,            B10010000,
           SPI_CONTINUE);
74    //write frequency word 0 0x04 (lower frequency) // for
           ch 0/3
      SPI.transfer(cs_dds,            B00000100,
           SPI_CONTINUE);
76    SPI.transfer(cs_dds,   freq_0_c[1][ramp][0],
           SPI_CONTINUE);
      SPI.transfer(cs_dds,   freq_0_c[1][ramp][1],
           SPI_CONTINUE);
78    SPI.transfer(cs_dds,   freq_0_c[1][ramp][2],
           SPI_CONTINUE);
      SPI.transfer(cs_dds,   freq_0_c[1][ramp][3], SPI_LAST)
           ;
80    //write frequency word 1 0x04A(higher frequency)
      SPI.transfer(cs_dds,            B00001010,
           SPI_CONTINUE);
82    SPI.transfer(cs_dds,   freq_1_c[1][ramp][0],
           SPI_CONTINUE);
      SPI.transfer(cs_dds,   freq_1_c[1][ramp][1],
           SPI_CONTINUE);
84    SPI.transfer(cs_dds,   freq_1_c[1][ramp][2],
           SPI_CONTINUE);
      SPI.transfer(cs_dds,   freq_1_c[1][ramp][3],
           SPI_CONTINUE);
86    //set 0x06 amplitude control
      SPI.transfer(cs_dds,            B00000110,
           SPI_CONTINUE);
88    SPI.transfer(cs_dds,            B01010111,
           SPI_CONTINUE);
      SPI.transfer(cs_dds,     ampl_c[1][ramp][0],
           SPI_CONTINUE);
90    SPI.transfer(cs_dds,     ampl_c[1][ramp][1],
           SPI_CONTINUE);

92 // ramp parameters for ch 0/3
    if(rampdown_bool_c[1][ramp]){
94    // DOWNWARDS RAMP
      //enable linear sweep 0x03
96    // enable no dwell when ramping up
      SPI.transfer(cs_dds,            B00000011,
           SPI_CONTINUE);
98    SPI.transfer(cs_dds,            B10000000,
           SPI_CONTINUE);
      SPI.transfer(cs_dds,            B01000011,
           SPI_CONTINUE);
100   SPI.transfer(cs_dds,            B00000000,
           SPI_CONTINUE);
      //set 0x07 Linear Sweep Ramp Rate (time between
           frequency steps)
102   SPI.transfer(cs_dds,            B00000111,
           SPI_CONTINUE);
      SPI.transfer(cs_dds, ramp_t_step[1][ramp],
           SPI_CONTINUE);
104   SPI.transfer(cs_dds,            B00000001,
           SPI_CONTINUE);
      //set 0x08  Rising Delta Word (one large set because
           must first ramp up before a ramp down is
           possible)
106   SPI.transfer(cs_dds,            B00001000,
           SPI_CONTINUE);
      SPI.transfer(cs_dds,            B11111111,
           SPI_CONTINUE);
108   SPI.transfer(cs_dds,            B11111111,
           SPI_CONTINUE);
      SPI.transfer(cs_dds,            B11111111,
           SPI_CONTINUE);
110   SPI.transfer(cs_dds,            B11111111,
           SPI_CONTINUE);
      //set 0x09  Falling Delta Word
112   SPI.transfer(cs_dds,            B00001001,
           SPI_CONTINUE);
      SPI.transfer(cs_dds,freq_step[1][ramp][0],
           SPI_CONTINUE);
114   SPI.transfer(cs_dds,freq_step[1][ramp][1],
           SPI_CONTINUE);
      SPI.transfer(cs_dds,freq_step[1][ramp][2],
           SPI_CONTINUE);
116   SPI.transfer(cs_dds,freq_step[1][ramp][3],
           SPI_CONTINUE);
    }else{
```

```
    // UPWARDS RAMP
    //enable linear sweep 0x03 FOR THE NO DWELL BITS IN RAMP UP
    SPI.transfer(cs_dds,            B00000011,          SPI_CONTINUE);
    SPI.transfer(cs_dds,            B10000000,          SPI_CONTINUE);
    SPI.transfer(cs_dds,            B11000011,          SPI_CONTINUE);
    SPI.transfer(cs_dds,            B00000000,          SPI_CONTINUE);
    //set 0x07 Linear Sweep Ramp Rate (time between frequency steps)
    SPI.transfer(cs_dds,            B00000111,          SPI_CONTINUE);
    SPI.transfer(cs_dds,            B00000001,          SPI_CONTINUE);
    SPI.transfer(cs_dds, ramp_t_step[1][ramp],          SPI_CONTINUE);
    //set 0x08  Rising Delta Word
    SPI.transfer(cs_dds,            B00001000,          SPI_CONTINUE);
    SPI.transfer(cs_dds,freq_step[1][ramp][0],          SPI_CONTINUE);
    SPI.transfer(cs_dds,freq_step[1][ramp][1],          SPI_CONTINUE);
    SPI.transfer(cs_dds,freq_step[1][ramp][2],          SPI_CONTINUE);
    SPI.transfer(cs_dds,freq_step[1][ramp][3], SPI_LAST);
  }
//phase offset for ch 0 and 1:
  // 0x00  // channel 1 (MW)
  SPI.transfer(cs_dds,              B00000000,
       SPI_CONTINUE);
  SPI.transfer(cs_dds,              B00100000,
       SPI_CONTINUE);
  //write offset to 0x05
  SPI.transfer(cs_dds,              B00000101,
       SPI_CONTINUE);
  SPI.transfer(cs_dds,    phase_c[0][ramp][0],
       SPI_CONTINUE);
  SPI.transfer(cs_dds,    phase_c[0][ramp][1],
       SPI_CONTINUE);

  // channel 0 (RF)
  SPI.transfer(cs_dds,              B00000000,
       SPI_CONTINUE);
  SPI.transfer(cs_dds,              B00010000,
       SPI_CONTINUE);
  //write offset to 0x05
  SPI.transfer(cs_dds,              B00000101,
       SPI_CONTINUE);
  SPI.transfer(cs_dds,    phase_c[1][ramp][0],
       SPI_CONTINUE);
  SPI.transfer(cs_dds,    phase_c[1][ramp][1],
       SPI_CONTINUE);

  //select ALL channels again  // FIXME: NOT needed (?)
  SPI.transfer(cs_dds,              B00000000,
       SPI_CONTINUE);
  SPI.transfer(cs_dds,              B11110000, SPI_LAST);
}

//calculates the best possible frequency step size and time between those steps
byte ramp_para(double sweep_time, double freq_0, double freq_1, int para_select, int which_byte) {
  //user sweep parameters
  delta_fges = abs(freq_0-freq_1);    //frequency difference of the sweep
  min_t_slope = min_t_step*delta_fges/sweep_time;
  sweep_sync_step = sweep_time*sync_clk*min_freq_step;
  found      = false;
  //in the loop for all 256 different time steps possible the best fitting freq step is calculated
  //then of all these ramps the one which ends most closely to the desired end frequency is chosen
  for (int i=1; i<256;i++){    // FIXME: double- and triple check the result of this!!
    f_wanted = i*min_t_slope;
    f_dds    = round(f_wanted*inv_min_freq_step);
    end_dds  = sweep_sync_step*f_dds/i;  // 1/sync_clk = min_t_step
    check[i] = abs(end_dds-delta_fges);
  }
  min_ind        = minIndex(check,256);
  f_dds          = round(min_ind*min_t_slope*inv_min_freq_step)*min_freq_step;
  freq_step_mult = round(f_dds*inv_min_freq_step);

  // all return values, i.e. all bytes needed for one ramp are stored in the global variable and read directly after the function call
  time_step_freq_step[0]   = dec1bin(min_ind,1);
  for (int i=1;i<5;i++){
    time_step_freq_step[i] = dec4bin(freq_step_mult,i);
  }
}
//============================
//read in data for ramping mode
void read_in_rampdata(){
  int i = -1;
  tmpchar = Serial.read();

  while (!(tmpchar == 'z')){  // input is not finished
    tmpstring = "";
    if (tmpchar == 'R'){
      i++;
      ampl_int[0][i]  = 1000;  // standard: full power
      ampl_int[1][i]  = 1000;  // standard: full power
      phase_int[0][i] = -1;    // standard: not defined, will be overwritten later
      tmpchar = Serial.read();
    }
    if (tmpchar == 't'){while(tmpchar = Serial.read()){
        if (tmpchar < 58){tmpstring += tmpchar;} else {
        time_array[0][i] = tmpstring.toInt()/1e6;
        tmpstring = ""; break;}}}
    if (tmpchar == 'f'){while(tmpchar = Serial.read()){
        if (tmpchar < 58){tmpstring += tmpchar;} else {
        freq_0[0][i]     = tmpstring.toInt();
        tmpstring = ""; break;}}}
    if (tmpchar == 'F'){while(tmpchar = Serial.read()){
        if (tmpchar < 58){tmpstring += tmpchar;} else {
        freq_1[0][i]     = tmpstring.toInt();
        tmpstring = ""; break;}}}
    if (tmpchar == 'a'){while(tmpchar = Serial.read()){
        if (tmpchar < 58){tmpstring += tmpchar;} else {
        ampl_int[0][i]   = tmpstring.toInt();
        tmpstring = ""; break;}}}
    if (tmpchar == 'p'){while(tmpchar = Serial.read()){
        if (tmpchar < 58){tmpstring += tmpchar;} else {
        phase_int[0][i]  = tmpstring.toInt();
        tmpstring = ""; break;}}}
    if (tmpchar == 'c'){while(tmpchar = Serial.read()){
        if (tmpchar < 58){tmpstring += tmpchar;} else {
        carrier[0][i]    = tmpstring.toInt();
        tmpstring = ""; break;}}}
  }
  ramp_num = i+1;
  SDFF_ramp_counter = -1;

  for (int i = 0; i < ramp_num; i++){ // post processing
    if (abs(freq_0[0][i] - 1600e6) < 200e6) {carrier[0][i] = 1600; ch_select[i] = cs_dds_1;} // MW mix setting // take care that the right carrier is used!!
    if (abs(freq_0[0][i] - 1950e6) < 200e6) {carrier[0][i] = 1950; ch_select[i] = cs_dds_1;} // MW mix setting
    if (abs(freq_0[0][i] -  850e6) < 200e6) {carrier[0][i] =  850; ch_select[i] = cs_dds_1;} // MW mix setting

    // RF/no carrier
    if (abs(freq_0[0][i] -  410e6) < 200e6) {carrier[0][i] =  410; ch_select[i] = cs_dds_1;} // RF mix setting
    if (abs(freq_0[0][i]         ) < 200e6) {carrier[0][i] =    0; ch_select[i] = cs_dds_2;} // direct RF setting

    if (carrier[0][i] == 0){   // no mixer setup
```

```
      if (freq_0[0][i] > 20e6){switch_select[i] = 18;}
           // D18, switch selection for RF (100W)
           amplifier
//      else                    {switch_select[i] = 16;}
     // D16, switch select for direct RF: leave switch
     low for DDS-connection, but it high for external HP
      input.
      else {if (freq_0[0][i] > 0.4e6) {switch_select[i]
           = 15;} // D15, NOT CONNECTED!, switch select
           for direct RF: leave switch low for DDS-
           connection, put it high for external HP input
           .
            else {switch_select[i] = 16;}  // D16,
                 switch select for direct RF: leave
                 switch low for DDS-connection, but it
                 high for external HP input.
    }
      phase_int[0][i]  =  0;   // phase relation for
           direct RF - ATTENTION: ONLY SET ON ONE
           CHANNEL due to poor implementation!
      freq_0[1][i] = freq_0[0][i];
      freq_1[1][i] = freq_1[0][i];
      ampl_int[1][i] = ampl_int[0][i];
    }

    if (carrier[0][i] > 100){  // RF mixer setup
      switch_select[i] = 18;   // D18, switch selection
           for RF (100W) amplifier
      if (phase_int[0][i] == -1){  // no explicit phase
           given
        if (freq_0[0][i] > carrier[0][i]*1e6) {phase_int
             [1][i] = 270;} else {phase_int[1][i] =
             90;} // phase relation for RF channel
      }
      freq_0[1][i] = abs(carrier[0][i]*1e6 - freq_0[0][i
           ]);
      freq_1[1][i] = abs(carrier[0][i]*1e6 - freq_1[0][i
           ]);
      ampl_int[1][i] = ampl_int[0][i];
    }

    if (carrier[0][i] > 500){  // MW mixer setup
      switch_select[i] = 9;    // D9, switch selection
           for MW
      if (phase_int[0][i] == -1){  // no explicit phase
           given
        if (freq_0[0][i] > carrier[0][i]*1e6) {phase_int
             [0][i] =  90;} else {phase_int[0][i] =
             270;} // phase relation for RF channel
      }
      freq_0[0][i] = abs(carrier[0][i]*1e6 - freq_0[0][i
           ]); // change channel for MW
      freq_1[0][i] = abs(carrier[0][i]*1e6 - freq_1[0][i
           ]);
      freq_0[1][i] = 1;  // set dummies for RF channels
      freq_1[1][i] = 1;
    }
  }

  for (int i=0;i<ramp_num;i++){
    Serial.print("ramp i = ");  Serial.println(i);
    Serial.print("time = ");    Serial.println(
         time_array[0][i]*1000000);
    Serial.print("carrier = "); Serial.println(carrier
         [0][i]);
    Serial.print("ch select = ");  Serial.println(
         ch_select[i]);
    for (int j=0;j<2;j++){
        Serial.print("channel j="); Serial.println(j);
        Serial.println(freq_0[j][i]);
        Serial.println(freq_1[j][i]);
        Serial.println(ampl_int[j][i]);
        Serial.println(phase_int[j][i]);
    }
  }
}

//calculate data for all ramps
void ramp_calculation(){
  //precalculate all ramps to be written the DDS
  for(int j=0;j<2;j++){// do everything twice for both
       channel sets
    //exchange frequencies if necessary: lower frequency
         MUST be in register 0x04!

//for loop over all ramps given by control server
k = 0; // initialize loop variable
for(int i=0;i<ramp_num;i++){
  if(freq_0[j][i]>freq_1[j][i]){
    rampdown[j][i] = true; //upward or downward ramp
    temp           = freq_1[j][i];
    freq_1[j][i]   = freq_0[j][i];
    freq_0[j][i]   = temp;
  }
  //variables used in the while loop over a single
       ramp
  finished   = false;
  steepness  = abs(freq_0[j][i]-freq_1[j][i])/
       time_array[0][i]; //slope of frequency ramp
  rem_time   = time_array[0][i]; //length of
       frequency ramp
  start_time = 0;
  end_time   = time_array[0][i];
  ramp_parts_num[j][i]  = 0;
  ramp_first_part[j][i] = k;

  //In this loop ramps that are longer than cut_time
       are chopped into several ramps
  //with a maximum length of cut_time. This
       increases the frequency accurancy.
  while(!finished){
    if(rampdown[j][i]){
      //chop downward ramps
      if(rem_time  >= 1.3*cut_time){//remaing lenght
           of ramp is greater than cut_time
        start_time  = end_time - cut_time;
        freq_start  = freq_0[j][i] + start_time*
             steepness;
        freq_end    = freq_0[j][i] + end_time  *
             steepness;
        cutted_time = cut_time;
        rem_time   -= cut_time;
        end_time   -= cut_time;
      }else{//last part of the ramp
        start_time  = end_time - rem_time;
        freq_start  = freq_0[j][i] + start_time*
             steepness;
        freq_end    = freq_0[j][i] + end_time  *
             steepness;
        cutted_time = rem_time;
        finished    = true;
        ramp_last_part[j][i] = k;
      }
    }else{
      //chop upward ramps
      if(rem_time  >= 1.3*cut_time){//remaing lenght
           of ramp is greater than cut_time
        end_time    = start_time   + cut_time;
        freq_start  = freq_0[j][i] + start_time*
             steepness;
        freq_end    = freq_0[j][i] + end_time  *
             steepness;
        cutted_time = cut_time;
        rem_time   -= abs(cut_time);
        start_time += cut_time;
      }else{//last part of the ramp
        end_time    = start_time   + rem_time;
        freq_start  = freq_0[j][i] + start_time*
             steepness;
        freq_end    = freq_0[j][i] + end_time  *
             steepness;
        cutted_time = rem_time;
        finished    = true;
        ramp_last_part[j][i] = k;
      }
    }
    //all the data that will be written to the
         arduino during this sequence
    ramp_para(cutted_time, freq_start,freq_end, 1,
         0);
    for (int m=0;m<4;m++){
      freq_0_c[j][k][m]   = frequency(freq_start, m
           +1);
      freq_1_c[j][k][m]   = frequency(freq_end,   m
           +1);
      freq_step[j][k][m]  = time_step_freq_step[m
           +1];
    }
    for (int m=0;m<2;m++){
```

```
            ampl_c[j][k][m]     = amplitude(ampl_int[j][i
                ],(freq_start+freq_end)/2, m+1);
336         phase_c[j][k][m]    = phase(phase_int[j][i], m
                +1);
          }
338       time_array_c[j][k]    = cutted_time;
          rampdown_bool_c[j][k] = rampdown[j][i];
340       ramp_t_step[j][k]     = time_step_freq_step
              [0];//ramp_para(cutted_time, freq_start,
              freq_end, 0, 1);
          k++; //saving position of each ramp in the
              arrays above
342       ramp_parts_num[0][i]++;
        } // while chopper loop end (over one ramp)
344   }   // for loop over all ramps given by control
          server
    }
346 }  // end of ramp_calculation()
```

Clock and PLL

set_clock_and_PLL.ino

```
    //this function resets the DDSs, sets phase autoclear
        and programms the reference clock
 2  void reset_DDS(){
      //reset DDS
 4    digitalWrite(resetpin, HIGH); delayMicroseconds(10);
      digitalWrite(resetpin, LOW);  delayMicroseconds(10);
 6    //set 0x02, function register 2 (all channels auto
          clear phase accumulator)
      SPI.transfer(cs_dds_1, B00000010, SPI_CONTINUE);
 8    SPI.transfer(cs_dds_1, B00100000, SPI_CONTINUE);
      SPI.transfer(cs_dds_1, B00000000, SPI_LAST);
10    delayMicroseconds(10);
      SPI.transfer(cs_dds_2, B00000010, SPI_CONTINUE);
12    SPI.transfer(cs_dds_2, B00100000, SPI_CONTINUE);
      SPI.transfer(cs_dds_2, B00000000, SPI_LAST);
14
      //I/O Update
16    delayMicroseconds(1);
      digitalWrite(updatepin, HIGH);
18    delayMicroseconds(1);
      digitalWrite(updatepin, LOW);
20  }

22  // preparing the reference clock
    void write_PLL(int freq){
24    ref_clk_spi(R0[freq]);  // R0
      ref_clk_spi(R1[freq]);  // R1 // same for all but
          1772, so we have to add this
26    ref_clk_spi(0x4042);    // R2 // same for all
      ref_clk_spi(0x4B3);     // R3 // same for all
28    ref_clk_spi(R4[freq]);  // R4
      ref_clk_spi(0x580005);  // R5  // same for all
30  }

32  // ultra high speed interface to the clock, allowing to
        set the clock in 60µs (!!)
    void ref_clk_spi(unsigned int data) { // SPI tranfer out
          function begins here
34    PIOB->PIO_CODR = 1 << 21;  // sets slave select
          channel LOW
      for(int i=1;i<33;i++) {         // setup a loop of 32
          iterations, one for each bit
36      if (data > 2147483647){PIOC->PIO_SODR = 1 << 12;} //
            sets data channel HIGH
        else {PIOC->PIO_CODR = 1 << 12;}
                                  // sets data channel LOW
38      PIOC->PIO_SODR = 1 << 13; // sets CLK_ref HIGH
        data  = data << 1;  // shift data to next bit
40      PIOC->PIO_CODR = 1 << 13; // sets CLK_ref LOW
      }
42    PIOB->PIO_SODR = 1 << 21;  // sets slave select
          channel HIGH
    }
```

A.2.2 Magnetic Field Control With Passbank

```
1 boolean INT_HIGH_var = LOW;
```

```
  static int GND          = 14; // Logic Ground
3 static int CLK          = 13; // Serial Clock Line
  static int DIN          = 11; // Master Out Slave In
        Line
5 static int SYNC         = 10; // SYNC
  static int SYNC_POTI    =  9; // sync signal for digital
        poti to control total gain
7 static int INT_OPTO_P   =  7;
  static int INT_OPTO_GND =  6;
9
  static int input            = 3;  // digital input pin
11 static int optocoupler_plus = 4;
  static int optocoupler_gnd  = 2;
13
  static long int maximum = 1048575;
15 static long int halfval = 500000;

17 int  i=0;
  char buffer[8];
19 long int voltage     = 0;
  long int starttime   = 0;
21 long int nowtime     = 0;
  long int val         = 0;
23 long int ramptovalue = 0;
  float    valtime     = 0;
25
  int      rampphase   = 0;
27 long int value       = 0;
  long int PPvalue     = 0;
29 int      prepulselength = 0;
  boolean  num[46];
31
  static byte Poti_byte1 = 6150 >> 8;
33 static byte Poti_byte2 = 6150;
  byte byte_1, byte_2, byte_3, Poti_byte3, Poti_byte4;
35
  int potival       = 0;
37
  float downtime    = 5000.0;
39 long int potival_afterdown = 441;

41 #include <SPI.h>
  // Due to the Optocopplers all SPI signals must be
        inverted!
43 void setup(){
    Serial.begin(115200); Serial.flush();
45  SPI.begin();
    SPI.setBitOrder(MSBFIRST);
47  SPI.setDataMode(SPI_MODE0);
    SPI.setClockDivider(SPI_CLOCK_DIV2);
49  // preparing Pin Modes
    pinMode(GND, OUTPUT);  pinMode(CLK, OUTPUT);
51  pinMode(DIN, OUTPUT);  pinMode(SYNC, OUTPUT);
    pinMode(SYNC_POTI, OUTPUT);
53
    pinMode(INT_OPTO_P, OUTPUT);   pinMode(INT_OPTO_GND,
        OUTPUT);
55  digitalWrite(INT_OPTO_P,LOW);  digitalWrite(
        INT_OPTO_GND,LOW);

57  pinMode (optocoupler_plus, OUTPUT);  pinMode (
        optocoupler_gnd, OUTPUT);
    pinMode (input, INPUT);
59  digitalWrite(optocoupler_plus,HIGH); digitalWrite(
        optocoupler_gnd,LOW);

61  digitalWrite(SYNC_POTI,LOW);

63 // initialize with most negative value
    digitalWrite(SYNC,HIGH);
65    SPI.transfer(~B00100000);
      SPI.transfer(~B00000000);
67    SPI.transfer(~B00010000);
    digitalWrite(SYNC,LOW);
69  set_voltage(0);
  }
71
  void rampup(unsigned long int value, float time){
73  starttime = micros();
    val = 0;    // loop variable
75  ramptovalue = value - 1000;
    valtime = (ramptovalue-halfval)/time;
77  if (valtime < 1){valtime = 1;}
    while (val < ramptovalue){
```

```
    val = valtime*(micros()-starttime) + halfval;
    byte_1 = lowByte(val >> 16);  // first Byte
    byte_2 = lowByte(val >> 8);   // 2bd Byte
    byte_3 = lowByte(val);        // 3rd Byte

    byte_1 = B00010000 ^ byte_1;  // set command to
         write to DAC register

    PORTB = B0100;  // sets SYNC HIGH
    SPI.transfer(~byte_1); SPI.transfer(~byte_2);
    SPI.transfer(~byte_3); PORTB = B0000;
  }
  set_voltage(value);
}

// function for setting the digital poti that controls
     the total gain
void set_poti(int poti_val){
  SPI.setDataMode(SPI_MODE2);
  SPI.setClockDivider(SPI_CLOCK_DIV2);
  digitalWrite(SYNC_POTI,HIGH);
  SPI.transfer(~Poti_byte1);
  SPI.transfer(~Poti_byte2);
  digitalWrite(SYNC_POTI,LOW);
  digitalWrite(SYNC_POTI,HIGH);
  Poti_byte3 = poti_val + 1024 >> 8;
  Poti_byte4 = poti_val + 1024;
  SPI.transfer(~Poti_byte3);
  SPI.transfer(~Poti_byte4);
  digitalWrite(SYNC_POTI,LOW);
  SPI.setDataMode(SPI_MODE0);
  SPI.setClockDivider(SPI_CLOCK_DIV2);
}

// input value must be between 0 and 2^20-1 = 1 048 575
int set_voltage(unsigned long val){
    byte_1 = lowByte(val >> 16);  // first Byte
    byte_2 = lowByte(val >> 8);   // 2bd Byte
    byte_3 = lowByte(val);        // 3rd Byte

    byte_1 = B00010000 ^ byte_1;

    PORTB = B0100;  // sets SYNC HIGH
    SPI.transfer(~byte_1); SPI.transfer(~byte_2);
    SPI.transfer(~byte_3); PORTB = B0000;
}

void loop(){
  if (digitalRead(input)){
    delayMicroseconds(2000); // long pulse for writing,
         short pulses for triggering!
    if(digitalRead(input)){  // identify first pulse for
         reading.
      value = 0;
      delay(30);  // wait until program pulse is over
      for (int i = 1; i < 21; i++){
        num[i] = digitalRead(input); delay(10);
      }
      rampphase = 1;
      digitalWrite(SYNC,HIGH);
        SPI.transfer(~B00100000);
        SPI.transfer(~B00000000);
        SPI.transfer(~B00010000);
      digitalWrite(SYNC,LOW);
    }
    else{
      switch (rampphase) {
      case 1: // start ramp up
        set_poti(884);
        rampup(value,10000.0);
        set_poti(potival-30);
        delay(1);
        for (int i = potival-50; i > 441 ; i = i - 14){
          set_poti(i);
          delayMicroseconds(500);
        }
        set_poti(441); // good value for stable
             reglutaion
        delay(10);
        rampphase = 2;
        break;
      case 2: // start ramp down
        set_voltage(value-1200);//576400);
        delayMicroseconds(5);
        rampdown(value-1600,downtime);
        delay(500);
        set_poti(1000);
        delay(1000);
        set_voltage(halfval);
        rampphase = 1;
        break;
      }
    };
  };
}
```

B Bibliography

[1] Patricia Amara, D Hsu, and JE Straub. *Global energy minimum searches using an approximate solution of the imaginary time Schrödinger equation*. In: The Journal of Physical Chemistry 97 (1993), pp. 6715–6721.

[2] M H Anderson et al. *Observation of Bose-Einstein Condensation in a Dilute Atomic Vapor*. In: Science 269.5221 (1995), pp. 198–201.

[3] Xavier Antoine and Romain Duboscq. *GPELab, a Matlab toolbox to solve Gross-Pitaevskii equations I: Computation of stationary solutions*. In: Computer Physics Communications 185.11 (2014), pp. 2969–2991.

[4] Xavier Antoine and Romain Duboscq. *GPELab, a Matlab toolbox to solve Gross-Pitaevskii equations II: Dynamics and stochastic simulations*. In: Computer Physics Communications 193 (2015), pp. 95–117.

[5] Jens Appmeier. *Immersed Quantum Systems: A Sodium Bose-Einstein Condensate for Polaron Studies*. Dissertation. Universität Heidelberg, 2010.

[6] E. Arimondo, M. Inguscio, and P. Violino. *Experimental determinations of the hyperfine structure in the alkali atoms*. In: Reviews of Modern Physics 49.1 (1977), pp. 31–75.

[7] Weizhu Bao and Qiang Du. *Computing the Ground State Solution of Bose–Einstein Condensates By a Normalized Gradient Flow*. In: SIAM J.SCI. Comput. 25.5 (2004), pp. 1674–1697.

[8] Paul Birk. *High Field Imaging of Sodium*. Bachelor's Thesis. Universität Heidelberg, 2013.

[9] Adam T. Black et al. *Spin dynamics in an antiferromagnetic spin-1 condensate*. In: *Conference on Quantum Electronics and Laser Science (QELS) - Technical Digest Series*. 2007.

[10] Immanuel Bloch. *Ultracold quantum gases in optical lattices*. In: Nature Physics 1.1 (2005), pp. 23–30.

[11] C. C. Bradley, C. A. Sackett, and R. G. Hulet. *Bose-Einstein Condensation of Lithium: Observation of Limited Condensate Number*. In: Phys. Rev. Lett. 78 (6 Feb. 1997), pp. 985–989.

[12] C. C. Bradley et al. *Evidence of Bose-Einstein condensation in an atomic gas with attractive interactions*. In: Physical Review Letters 75.9 (1995), pp. 1687–1690.

[13] Brian Harold Bransden and Charles Jean Joachain. *Quantum mechanics*. Pearson Education, 2000.

[14] Gregory Breit and II Rabi. *Measurement of nuclear spin*. In: Physical Review 38.11 (1931), p. 2082.

[15] G. Cappellini et al. *Direct Observation of Coherent Interorbital Spin-Exchange Dynamics*. In: Physical Review Letters 113.12 (2014), p. 120402.

[16] Lincoln D. Carr et al. *Cold and ultracold molecules: Science, technology and applications*. In: New Journal of Physics 11 (2009).

[17] J. Catani et al. *Quantum dynamics of impurities in a one-dimensional Bose gas*. In: Physical Review A - Atomic, Molecular, and Optical Physics 85.2 (2012).

[18] M. S. Chang et al. *Observation of spinor dynamics in optically trapped 87Rb Bose-Einstein condensates*. In: Physical Review Letters 92.14 (2004), p. 140403.

[19] Cheng Chin et al. *Feshbach resonances in ultracold gases*. In: Reviews of Modern Physics 82.3 (2010), pp. 1225–1286.

[20] Alexander D. Cronin, Jörg Schmiedmayer, and David E. Pritchard. *Optics and interferometry with atoms and molecules*. In: Reviews of Modern Physics 81.3 (2009), pp. 1051–1129.

[21] K. B. Davis et al. *Bose-Einstein condensation in a gas of sodium atoms*. In: Physical Review Letters 75.22 (1995), pp. 3969–3973.

[22] Luis E E De Araujo et al. *Two-color photoassociation spectroscopy of the lowest triplet potential of Na2*. In: Journal of Chemical Physics 119.4 (2003), pp. 2062–2074.

[23] E a Donley. *Dynamics of collapsing and exploding Bose-Einstein condensates* . In: Nature 412 (2001), pp. 295–299.

[24] Tiemann Eberhard. private communication. 2015.

[25] Yuki Endo and Tetsuro Nikuni. *Spin dynamics of a trapped spin-1 bose gas above the Bose-Einstein transition temperature*. In: Journal of Low Temperature Physics 152.1-2 (2008), pp. 21–46.

[26] J. Esteve et al. *Observations of density fluctuations in an elongated bose gas: Ideal gas and quasicondensate regimes*. In: Physical Review Letters 96.13 (2006).

[27] U Fano. *Effect of configuration Interaction on intensities and phase shifts*. In: Physical Review 124.6 (1961), pp. 1866–1878.

[28] P. O. Fedichev, M. W. Reynolds, and G. V. Shlyapnikov. *Three-Body Recombination of Ultracold Atoms to a Weakly Bound s Level*. In: Phys. Rev. Lett. 77 (14 Sept. 1996), pp. 2921–2924.

[29] F. Ferlaino et al. *Efimov Resonances in Ultracold Quantum Gases*. In: Few-Body Systems 51.2-4 (2011), pp. 113–133.

[30] Herman Feshbach. *A unified theory of nuclear reactions. II*. In: Annals of Physics 19.2 (1962), pp. 287–313.

[31] Herman Feshbach. *Unified theory of nuclear reactions*. In: Annals of Physics 5.4 (1958), pp. 357–390.

[32] D G Fried et al. *Bose-Einstein Condensation of Atomic Hydrogen*. In: Physical Review Letters 81 (1998), p. 3811.

[33] Marcell Gall. *Active Magnetic Field Stabilisation for Ultracold Sodium Lithium Mixtures*. Master's Thesis. Universität Heidelberg, 2015.

[34] MR Goosen. *Universal relations between Feshbach resonances and molecules*. Dissertation. Technische Universiteit Eindhoven, 2011.

[35] A Görlitz et al. *Sodium Bose-Einstein condensates in the F=2 state in a large-volume optical trap*. In: Phys. Rev. Lett. 90.9 (2003), p. 4.

[36] Markus Greiner and Simon Fölling. *Optical lattices*. In: Nature 453 (2008), pp. 736–738.

[37] Rudolf Grimm, Matthias Weidemüller, and Yurii B Ovchinnikov. *Optical dipole traps for neutral atoms*. In: arXiv preprint physics/9902072 (1999).

[38] C. Gross et al. *Nonlinear atom interferometer surpasses classical precision limit*. In: Nature 464.7292 (2010), pp. 1165–1169.

[39] EP Gross. *Nuovo Cimento 20 454*. In: J. Math. Phys 4.193 (1961), p. 3.

[40] F. Grusdt et al. *Bloch oscillations of bosonic lattice polarons*. In: Physical Review A - Atomic, Molecular, and Optical Physics 90.6 (2014).

[41] F. Grusdt et al. *Renormalization group approach to the Fröhlich polaron model: application to impurity-BEC problem*. In: Scientific Reports 5 (2015), p. 12124.

[42] Z. Hadzibabic et al. *Fiftyfold Improvement in the Number of Quantum Degenerate Fermionic Atoms*. In: Phys. Rev. Lett. 91 (16 Oct. 2003), p. 160401.

[43] Myoung Sun Heo et al. *Formation of ultracold fermionic NaLi Feshbach molecules*. In: Physical Review A - Atomic, Molecular, and Optical Physics 86.2 (2012).

[44] Tin-Lun Ho. *Spinor Bose Condensates in Optical Traps*. In: Physical Review Letters 81.4 (1998), pp. 742–745.

[45] Jeremy M. Hutson, pavel Soldan, and Pavel Soldan. *Molecule formation in ultracold atomic gases*. In: Reviews in Physical Chemistry 25.4 (2006), pp. 497–526.

[46] S. Inouye et al. *Observation of Feshbach resonances in a Bose-Einstein condensate*. In: Nature 392.6672 (1998), pp. 151–154.

[47] HA Jahn and J Hope. *Symmetry properties of the Wigner 9 j symbol*. In: Physical Review 93.2 (1954), p. 318.

[48] A. S. Jensen et al. *Structure and reactions of quantum halos*. 2004.

[49] S Jochim et al. *Bose-Einstein condensation of molecules*. In: Science 302.5653 (2003), pp. 2101–2103.

[50] V. Kasper et al. *Schwinger pair production with ultracold atoms*. In: arXiv (2015), p. 1506.012238.

[51] W Ketterle, D S Durfee, and D M Stamper-Kurn. *Making, probing and understanding Bose-Einstein condensates*. In: *Proceedings of the International School of Physics "Enrico Fermi"*. 1999, p. 67.

[52] W. Ketterle and M. W. Zwierlein. *Making, probing and understanding ultracold Fermi gases*. In: Rivista del Nuovo Cimento 31.5-6 (2008), pp. 247–422.

[53] S. Knoop et al. *Feshbach spectroscopy and analysis of the interaction potentials of ultracold sodium*. In: Physical Review A - Atomic, Molecular, and Optical Physics 83.4 (2011), pp. 1–10.

[54] S. Knoop et al. *Observation of an Efimov-like resonance in ultracold atom-dimer scattering*. In: Nature Physics 5.3 (2008), p. 12.

[55] Michael Köhl et al. *Fermionic atoms in a three dimensional optical lattice: Observing Fermi surfaces, dynamics, and interactions*. In: Physical Review Letters 94.8 (2005).

[56] M Koschorreck et al. *Attractive and repulsive Fermi polarons in two dimensions*. In: Nature 485.7400 (2012), 619–U111.

[57] T Kraemer et al. *Evidence for Efimov quantum states in an ultracold gas of caesium atoms*. In: Nature 440.7082 (2006), pp. 315–318.

[58] J S Krauser et al. *Giant spin oscillations in an ultracold Fermi sea.* In: Science (New York, N.Y.) 343.6167 (2014), pp. 157–60.

[59] Jan Krieger. *Zeeman-Slower und Experimentsteuerung für das NaLi-Experiment*. Diploma Thesis. Universität Heidelberg, 2008.

[60] LD Landau. *Zur Theorie der Energieübertragung (On the theory of the energy transfer)*. In: Physics of the Soviet Union 2 (1932).

[61] L. J. Leblanc and J. H. Thywissen. *Species-specific optical lattices*. In: Physical Review A - Atomic, Molecular, and Optical Physics 75.5 (2007).

[62] Xiaoke Li et al. *Coherent Heteronuclear Spin Dynamics in an Ultracold Spinor Mixture*. In: Physical Review Letters 114.25 (2015), p. 255301.

[63] J M McGuirk et al. *Normal-superfluid interaction dynamics in a spinor bose gas.* In: Physical review letters 91.15 (2003), p. 150402.

[64] H. J. Metcalf and P. van der Straten. *Laser cooling and trapping of atoms*. In: Journal of Optical Society of America 20.5 (2003), pp. 887–908.

[65] Harold Metcalf and Peter van der Straten. *Cooling and trapping of neutral atoms*. In: Physics Reports 244.4-5 (1994), pp. 203–286.

[66] a. J. Moerdijk, B. J. Verhaar, and a. Axelsson. *Resonances in ultracold collisions of ^{6}Li, ^{7}Li, and ^{23}Na*. In: Physical Review A 51.6 (1995), pp. 4852–4861.

[67] Peter J. Mohr, David B. Newell, and Barry N. Taylor. *CODATA Recommended Values of the Fundamental Physical Constants: 2014*. Aug. 2015.

[68] Oliver Morsch and Markus Oberthaler. *Dynamics of Bose-Einstein condensates in optical lattices*. In: Reviews of Modern Physics 78.1 (2006), pp. 179–215.

[69] W. Muessel et al. *Twist-and-turn spin squeezing in Bose-Einstein condensates*. In: Phys. Rev. A 92 (2 Aug. 2015), p. 023603.

[70] C. Myatt et al. *Production of Two Overlapping Bose-Einstein Condensates by Sympathetic Cooling*. In: Physical Review Letters 78.4 (1997), pp. 586–589.

[71] Stefan S. Natu and Erich J. Mueller. *Pairing, ferromagnetism, and condensation of a normal spin-1 Bose gas*. In: Physical Review A - Atomic, Molecular, and Optical Physics 84.5 (2011).

[72] Stefan S. Natu and Erich J. Mueller. *Spin waves in a spin-1 normal Bose gas*. In: Physical Review A - Atomic, Molecular, and Optical Physics 81.5 (2010).

[73] Tetsuo Ohmi and Kazushige Machida. *Bose-Einstein condensation with internal degrees of freedom in alkali atom gases*. In: Journal of the Physical Society of Japan 67.6 (1998), pp. 1822–1825.

[74] *Oliver. Angular Momentum Coefficients*. URL: www.mathworks.com/matlabcentral/fileexchange/31729-angular-momentum-coefficients.

[75] Yuri B Ovchinnikov, Krzysztof Szymaniec, and Soliman Edris. *Measurement of rubidium ground-state hyperfine transition frequency using atomic fountains*. In: Metrologia 52.4 (2015), p. 595.

[76] Jee Woo Park, Sebastian A. Will, and Martin W. Zwierlein. *Ultracold Dipolar Gas of Fermionic Na²³K⁴⁰ Molecules in Their Absolute Ground State*. In: Physical Review Letters 114.20 (2015).

[77] H. K. Pechkis et al. *Spinor dynamics in an antiferromagnetic spin-1 thermal bose gas*. In: Physical Review Letters 111.2 (2013), pp. 1–5.

[78] Christopher J Pethick and Henrik Smith. *Bose-Einstein condensation in dilute gases*. Cambridge university press, 2002.

[79] Luca Pezzé and Augusto Smerzi. *Entanglement, nonlinear dynamics, and the heisenberg limit*. In: Physical Review Letters 102.10 (2009).

[80] R. Pires et al. *Observation of Efimov resonances in a mixture with extreme mass imbalance*. In: Physical Review Letters 112.25 (2014).

[81] LP Pitaevskii. *Vortex lines in an imperfect Bose gas*. In: Sov. Phys. JETP 13.2 (1961), pp. 451–454.

[82] S. E. Pollack et al. *Extreme tunability of interactions in a Li7 Bose-Einstein condensate*. In: Physical Review Letters 102.9 (2009).

[83] Tobias Rentrop. *Observation of the Phononic Lamb Shift in a Synthetic Vacuum*. Dissertation. Universität Heidelberg, 2016.

[84] K. Riisager. *Nuclear halo states*. In: Reviews of Modern Physics 66.3 (1994), pp. 1105–1116.

[85] Hiroki Saito and Masahito Ueda. *Intermittent implosion and pattern formation of trapped Bose-Einstein condensates with an attractive interaction*. In: Physical Review Letters 86.8 (2001), pp. 1406–1409.

[86] Murray Sargent and Paul Horwitz. *Three-level Rabi flopping*. 1976.

[87] Raphael Scelle. *Cooling, Plugging, Trapping: Exploiting Optical Dipole Potentials For Polaron Experiments*. Diploma Thesis. Universität Heidelberg, 2009.

[88] Raphael Scelle. *Dynamics and Motional Coherence of Fermions Immersed in a Bose Gas*. Dissertation. Universität Heidelberg, 2013.

[89] R. Scelle et al. *Motional coherence of fermions immersed in a bose gas*. In: Physical Review Letters 111.7 (2013).

[90] André Schirotzek et al. *Observation of fermi polarons in a tunable fermi liquid of ultracold atoms*. In: Physical Review Letters 102.23 (2009).

[91] Tobias Schuster. *Feshbach Resonances and Periodic Potentials in Ultracold Bose-Fermi Mixtures*. Dissertation. Universität Heidelberg, 2012.

[92] T. Schuster et al. *Feshbach spectroscopy and scattering properties of ultracold Li + Na mixtures*. In: Physical Review A - Atomic, Molecular, and Optical Physics 85.4 (2012).

[93] Anders S. Sørensen and Klaus Mølmer. *Entanglement and extreme spin squeezing*. In: Physical Review Letters 86.20 (2001), pp. 4431–4434.

[94] Dan M. Stamper-Kurn and Masahito Ueda. *Spinor Bose gases: Symmetries, magnetism, and quantum dynamics*. In: Reviews of Modern Physics 85.3 (2013), pp. 1191–1244.

[95] Dan M. Stamper-Kurn and Masahito Ueda. *Spinor Bose gases: Symmetries, magnetism, and quantum dynamics*. In: Reviews of Modern Physics 85.3 (2013), pp. 1191–1244.

[96] C. A. Stan and W. Ketterle. *Multiple species atom source for laser-cooling experiments*. In: Review of Scientific Instruments 76.6 (2005).

[97] C. a. Stan et al. *Observation of Feshbach resonances between two different atomic species*. In: Physical Review Letters 93.October (2004), pp. 1–4.

[98] Daniel A Steck. *Sodium D line data*. In: Report, Los Alamos National Laboratory, Los Alamos 124 (2000).

[99] J. Stenger et al. *Spin domains in ground-state Bose–Einstein condensates*. In: Nature 396.November (1998), pp. 345–348.

[100] J. Tempere et al. *Feynman path-integral treatment of the BEC-impurity polaron*. In: Physical Review B - Condensed Matter and Materials Physics 80.18 (2009).

[101] T. G. Tiecke et al. *Asymptotic-bound-state model for Feshbach resonances*. In: Physical Review A 82.4 (2010), p. 042712.

[102] Arno Trautmann. *Feshbach Spectroscopy of Sodium and Sodium-Lithium Mixtures*. Diploma Thesis. Universität Heidelberg, 2011.

[103] Shih-Kuang Tung et al. *Observation of geometric scaling of Efimov states in a Fermi-Bose Li-Cs mixture*. In: Physics 7 (2014), p. 51.

[104] K. M R Van Der Stam et al. *Spin-polarizing cold sodium atoms in a strong magnetic field*. In: Physical Review A - Atomic, Molecular, and Optical Physics 73.6 (2006).

[105] M.-S. Chang M S Chapman Wenxian Zhang D. L. Zhou et al. *Coherent spin mixing dynamics in a spin-1 atomic condensate*. In: Phys. Rev. A 72.August 2004 (2005), p. 13602.

[106] CW White et al. *Determination of g-Factor Ratios for Free Rb 85 and Rb 87 Atoms*. In: Physical Review 174.1 (1968), p. 23.

[107] Carl Wieman, David Pritchard, and David Wineland. *Atom cooling, trapping, and quantum manipulation*. In: Reviews of Modern Physics 71.2 (1999), S253–S262.

[108] E. Wigner. *On the quantum correction for thermodynamic equilibrium*. In: Physical Review 40.5 (1932), pp. 749–759.

[109] Sebastian Will et al. *Coherent interaction of a single fermion with a small bosonic field*. In: Physical Review Letters 106.11 (2011).

[110] Haibin Wu and J. E. Thomas. *Optical control of the scattering length and effective range for magnetically tunable Feshbach resonances in ultracold gases*. In: Phys. Rev. A 86 (2012), p. 063625.

[111] Jonas Zeuner. *Theoretical and experimental optimization of evaporative cooling*. Master's Thesis. Universität Heidelberg, 2014.

[112] G. Zürn et al. *Precise characterization of Li6 Feshbach resonances using trap-sideband-resolved RF spectroscopy of weakly bound molecules*. In: Physical Review Letters 110.13 (2013).

[113] M W Zwierlein et al. *Observation of Bose-Einstein condensation of molecules*. In: Physical Review Letters 91.25 (2003), p. 250401.

[114] M W Zwierlein et al. *Vortices and superfluidity in a strongly interacting Fermi gas*. In: Nature 435.7045 (2005), pp. 1047–1051.

[115] Martin W Zwierlein et al. *Direct observation of the superfluid phase transition in ultracold Fermi gases.* In: Nature 442.7098 (2006), pp. 54–58.

C List of Figures and Tables

C.1 List of Figures

C.2 List of Tables

Danksagung

Auch wenn man oft alleine im Labor steht und einem das Schreiben des Textes niemand abnehmen kann, so gibt es doch einige Menschen, ohne die die Entstehung dieser Arbeit nicht möglich gewesen wäre oder die mir außerhalb der Physik zur Seite standen. Diesen Menschen bin ich zu Dank verflichtet, und daher möchte ich mich bedanken bei:

- Prof. Dr. Markus K. Oberthaler, der mich schon vor langer Zeit in seine Gruppe aufgenommen hat und deren Begeisterung für Physik auch lange Durststrecken immer wieder gelockert hat. Sein Bestreben, jedes Detail einer Fragestellung verstehen zu wollen war stets ein wichtiger Prüfstein.
- Prof. Dr. Matthias Weidemüller danke ich für die Bereitschaft, das Zweitgutachten der Arbeit zu erstellen.
- Meinen Eltern, die mich immer unterstützt haben und an mich geglaubt haben. Sie haben mir in jedem Alter das ermöglicht, was mich vorangebracht hat und von frühster Kindheit an den Funken der Neugierde beigebracht. Ich danke euch für alles!
- Dem NaLi verschiedener Generationen: Tobias Schuster und Raphael Scelle für die lange Betreuung und die vielen Lektionen im Labor, vor allem für die Erkenntnisse, dass ich nichts ändern möchte. Steven Knoop danke ich vor allem für seine geduldigen Erklärungen des ABM und dem Interesse, das er in mir für Feshbachresonanzen und Efimovphysik geweckt hat. Besonders danken möchte ich Tobias Rentrop, der mir für den größten Teil der Arbeit ein großartiger Kollege war. Seine bodenständigen, realistischen Ansichten und seine gründliche Arbeit waren stets bewunderswert. Fabián Olivares danke ich für seinen unüberwindbaren Optimismus und seine gute Laune, die auch dann nicht getrübt wurde, wenn ich ihn bat, den Farbstofflaser zu justieren. Marcell Gall hat nicht nur ins Magnetfeld, sondern auch in jede Aufregung Ruhe gebracht. Ich erinnere mich gerne an gemütliche Grillabende bei ihm. JProf. Dr. Fred Jendrzejewski danke ich für seine Unterstützung bei den numerischen Simulationen und vielen Diskussionen im und ums Labor und hoffe und wünsche, dass er die großen Pläne des NaLi erfolgreich umsetzen kann.
- Dem Rest der Matterwave-Gruppe, der jeden Tag aufs Neue vom plötzlichen Auftauchen des Mittagessen überrascht wurde. Viele Grillabende, Radtouren, oder einfach nur Kaffeepausen haben die Arbeit in anstrengenden Zeiten erträglich gemacht und in erfolgreichen Momenten war es schön, diese zu teilen. Besonders danke ich den Mitgliedern des BEC-Experiments für hilfreiche Gespräche und das Ertragen vieler Fragen über Spin Dynamik („Ah stimmt, bei euch ist das ja völlig anders!")
- Prof. Dr. Tiemann für die gute Zusammenarbeit bei den Feshbachresonanzen im LiNa-System und dem geduldigen und ausführlichen Beantworten vieler Fragen zu Streuprozessen.
- Dagmar und Christiane, deren fröhliche Gemüte und Organisationstalent die Gruppe zusammenhalten.

- Der Elektronikabteilung des KIP, für viele Beratungen und Hilfe bei Installationen, vor allem Jürgen Schölles, der immer wieder Fragen zu Schaltunge, Bauteilen und defekten Netzteilen beantwortet hat.
- Den Mitarbeitern der feinmechanischen Werkstatt, die so manches Bauteil präzise, zuverlässig und mitunter auch außerhalb der Arbeitszeiten anfertigten. Besonders Herr Spiegel war stets mit Rat und Tat zur Seite.
- Den Teilnehmern und Trainern der Judo- und JuJutsu-Hochschulsportgruppen, die es immer geschafft haben, meine Laune nach dem Training deutlich zu steigern, vor allem natürlich den Mitgliedern des Matterwave Fight Club!
- All den Menschen, für die ich mir viel zu wenig Zeit genommen habe und die dennoch für mich da waren und sind.